BRABS: Bringing Retired Aircraft Back to the Skies

A circular end-of-life pathway and example case for retired aluminium airframes

Final Report
AE3200 Design Synthesis

Group 32
Q4 2025/2026

Author	Student ID
Philip Benschop	5996902
Pietro Cartocci	5935547
Roos van Duin	5727480
Theo van de Griendt	5481597
Simon Huwaert	5937922
Piotr Krylowicz	5905974
Kees van Meel	5793521
Quinten Nouwens	5076765
Jesper Smits	5788110
Defne Tilkici	5950902

Tutor
Dr. Santiago Garcia Espallargas

Coaches
Max Knoop
Manu Singh

Preface

This report represents the culmination of ten weeks of dedicated effort by a team of ten students for their completion of their Bachelor's degree in Aerospace Engineering. The research was conducted from the 20th of April until the 17th of June 2026 at Delft University of Technology.

When beginning the project, we were all intrigued by aircraft recycling, but started out with little knowledge of the field. Over the course of the project, this passion grew as our grasp of the topic deepened and we figured out how to shape our research. This report is the result of ten weeks of work, and one we could not have achieved alone.

We want to express our sincere gratitude to our responsible tutor, Santiago Garcia Espallargas, and our coaches, Max Knoop and Manu Singh. Your guidance, feedback, and support were instrumental in keeping this project on track and shaping its outcome. Furthermore, we extend our deepest thanks to the following experts who generously shared their expertise, time, and practical insights, helping us along the way:

Albert Dirkzwager (Textron Aviation), Anne Kvithyld (SINTEF), Arjan Otten (KLM), Clive Harper (EcoPro Solutions), Derk-Jan van Heerden (Aethos), Derya Dispinar (SINTEF), Eugene van den Boomen (TOMRA), Ferdy de Smet (Seef B.V.), Joaquin Exalto (Elysian Aircraft), John-Alan Pascoe (TU Delft), Julio Cesar de Luca (IRT Jules Verne), Ligeia Paletti (Aethos), Ludmila 't Hoen (NLR), Marianna Panou (NLR), Philippe Kientzler (Vesuvius), Roelof Vos (TU Delft), Rolf Stein (Socomore), and Yan Ma (TU Delft).

Your willingness to answer our questions and share your professional experience provided us with valuable real-world context to build upon. Thank you all for your time and dedication. Finally, we would like to thank Joris Melkert and the rest of the OSCC organising committee for their guidance and help in the execution of this project.

We hope this design project will help push forward the boundaries in circular end-of-life aircraft recycling today, such that in the future, more and more aircraft can find a second life instead of a scrapyard.

Design Synthesis Exercise Group 32

Supervisor:	Santiago Garcia Espallargas
Coaches:	Max Knoop
	Manu Singh

Cover:	AI generated (ChatGPT)
Conversion rate:	USD/EUR conversion rate is set at \$1 = €0.86 (ECB rate, 22 May 2026)
AI statement:	Generative AI was used to improve grammar, style, and/or spelling, to support coding, and to produce visualisations.

Executive Summary

Every year, hundreds of aircraft are retired and simply parked in boneyards in Australia, Spain, France or the United States. Some are stripped of their most valuable components, such as engines and avionics, which are then repurposed. What's left is an aluminium carcass containing thousands of tonnes of aerospace-grade aluminium, left out in a boneyard somewhere in the world, with no real destination.

Furthermore, Europe in particular is currently facing major challenges with the supply-chain security of critical raw materials for aerospace applications, with bauxite / aluminium being added to the Critical Raw Materials (CRMs) list. With forecasts predicting a wave of more than 13,000 retirements over the next two decades, and aluminium being considered to be infinitely recyclable, with negligible losses in mechanical properties, the case for recycling aluminium alloys (AA) from end-of-life aircraft back into aerospace use is much more than only an environmental one.

This is precisely what this report covers: the design of a full recycling process for aluminium alloys in retired aircraft, starting with a stripped airframe and ending with recycled AA2024 and AA7075 sheets, ready to be used in a new airframe. As an example case to demonstrate the use of these recycled alloys, a Cessna 172 Skyhawk's structure is redesigned and retrofitted with an electric propulsion system, truly making it a fully "green" aircraft.

Why this has not been done before

The reason all that aluminium sits unused is that recovering it at aerospace-grade is difficult, and making it economically viable even more so, requiring a scale no current dismantler possesses. Three main obstacles stand in the way.

First, an airframe is not made of one alloy but of many. The 2xxx and 7xxx families that carry the loads are mixed with other grades and metals, which are held together by thousands of fasteners of different compositions from the parts they join. The few aircraft that are recycled today are simply shredded, segregated by material at best, but still blending together all alloys. Once different alloys are melted together, the material will most likely decay and not be suitable for an aerospace specific use case and can only be sold for less demanding use cases and therefore lower value. This is downcycling and it is current best practice.

Second, every airframe is painted with a primer containing hexavalent chromium, Cr(VI), which is carcinogenic and tightly controlled under EU REACH rules. It has to be removed before melting, and it cannot be removed carelessly. Any process that heats or vaporises the coating puts both workers and the environment at risk.

Third, aerospace-grade aluminium is held to narrow composition limits and must be free of iron contamination, oxide inclusions and dissolved hydrogen. Scrap-based recycling cannot meet these limits, which is why recycled aluminium from outside the manufacturing processes never returns to aircraft.

This project is, to the team's knowledge, the first fully engineered process that takes a retired airframe all the way back to certifiable AA2024 and AA7075 sheet at industrial scale, rather than stopping at downcycled scrap. It does so by keeping the alloys separated and by controlling purity at every step, so the metal that comes out is good enough to fly again.

The recovery process

The process is built around two goals that pull against each other: yield (recovering as much metal as possible) and purity (keeping it at aerospace-grade). The seven main steps are: end-of-life carcass acquisition, bulk diamond-wire dismantling, detail laser cutting, automated XRF sorting, decoating, foundry melt refining, and testing and certification. Most of it can run on-site at the boneyards and airports where the aircraft already are.

The key idea is to split coarse cutting from fine cutting. A mechanical diamond-wire saw sections the airframe outdoors into manageable pieces. It is cheap (around €150,000) and needs only two operators, and it was already shown to work on a real airliner by AELS and Husqvarna in 2014. A laser then does the detail work inside a sealed, extracted enclosure, where a computer-vision system follows the rivet lines and cuts the fasteners out so the alloys are never blended at the source. The laser setup for cutting the wing is shown in Figure 1. The laser is kept enclosed precisely because it would vaporise the coatings, which contain carcinogenics; doing this in a controlled space protects the operators and captures the fumes.

The decoating line strips the paint system in a sequence of chemical baths: an alkaline remover for the organic layers, a caustic etch for the chromate primer, and a nitric-acid step to clear any residue, with rinses and inspections in between. This keeps the Cr(VI) contained and leaves a clean, ready to melt material. Cut parts are then identified by an X-ray fluorescence (XRF) automated sorting line. It is a cost-effective method that reads the alloying elements to about 99.8% accuracy.

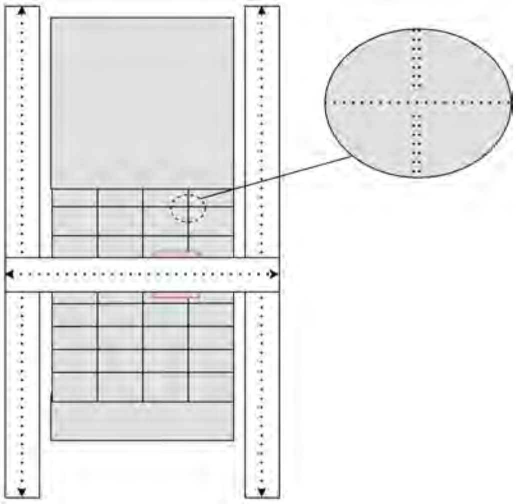

Figure 1: Wing laser cutter

Returning to aerospace-grade

Refining is where the metal is actually brought back to specification. Each melt is nudged back inside the AMS composition limits by adding a small, calculated amount of virgin or alloy aluminium, capped at 7% of the final mass so the product stays mostly recycled. Oxidation losses are limited with cover and dross fluxes, dissolved hydrogen is driven below 0.08 ml/100g of melt with an in-line degasser, and a deep-bed filter removes the last inclusions before casting. When the line switches between alloy families, the leftover metal is cast into blocks and fed back into the dilution step rather than thrown away. The result is rolled AA2024 and AA7075 sheet that meets aerospace standards.

On average based on the retiring fleet, about 8 tonnes of aerospace-grade aluminium (7,536 kg) is recovered per retired aircraft. More than 37% of the aluminium structural weight is recovered overall; the rest is still downcycled into less demanding applications by scrapyards, and foundry melt losses are held low. Today's recyclers upcycle none of an airframe's aluminium back to an aerospace level. This process recovers all of the structural aluminium and returns a large share straight back to aerospace use.

Proof of concept: the electric Cessna 172 Skyhawk

To show the recovered metal really is airworthy, a Cessna 172S is redesigned from it and converted to electric power. To allow for more battery mass, the maximum take-off weight is raised by 10%. A 15% increase in wingspan provides the extra lift at a sensible cruise point while keeping the handling close to the original. The new wing is rolled from the project's own recycled sheet, which closes the loop.

The design is driven by two standard training missions. The 80-minute flight that covers most lessons needs 106 kWh of usable energy and a peak of 147 kW; a cross-country flight needs 90 kWh with a 30-minute recharge between legs. After removing the combustion engine and two seats, about 438 kg of battery can be carried using Amprius SA02 cells. The existing radiator is reused for cooling, including during fast charging.

Results

From an environmental impact perspective, recycling beats primary production by a wide margin on both energy and emissions, because most of the cost of aluminium is the energy used to extract it from ore in the first place.

Table 1: Recycled vs. primary aerospace-grade aluminium, per kg of product

Metric	**Primary**	**Recycled**	**Reduction**
Carbon footprint (Europe, incl. imports)	10.1 kg CO_2e	0.25 kg CO_2e	97%
Process energy (excl. transport)	14.8 kWh	5.99 kWh	60%

The electric Cessna carries the same story to the aircraft level, with a roughly 84% lower lifetime carbon footprint than the original (about 2 million kg of CO_2 saved over 20 years and 17,500 flights) and much lower running costs, since electricity and low maintenance replace fuel.

The business case treats the number of aircraft processed per year as the main unknown and rebuilds the full cost and revenue picture at each level. Cash flows are discounted at a 9% cost of capital against a 5-year payback target. The headline figures are below.

Table 2: Business-case outcomes at the minimum viable throughput.

Quantity	**Value**
Aluminium recovered (sold)	7,536 kg/aircraft
Minimum viable fleet	**77 aircraft/yr**
Total upfront investment	€12.9 M
Discounted payback	5.0 yr
Annual profit (steady state)	€2.71 M
Net margin	29%
20-yr return (cash)	416%

The 29% net margin is far above the roughly 5% of ordinary scrap recycling, because the product is certified aerospace sheet rather than bulk scrap. The result is most sensitive to the sale price of the alloy, and the largest practical risk is not demand but supply: 77 aircraft a year is about 12% of yearly projected retirements worldwide. While the conclusion is that this remains a reasonable number to achieve, securing enough feedstock is the real constraint on this project as retirement rates and the selling price of end of life aircraft cannot be controlled. This could only be mitigated by signing agreements with aircraft owners ahead of time to secure sufficient feedstock.

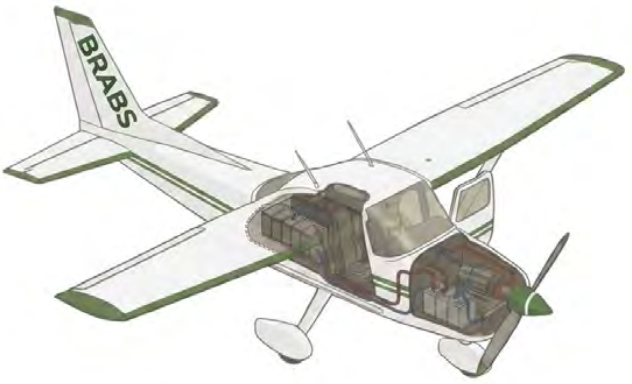

Figure 2: Render of the retrofit Cessna - AI generated (Gemini)

Conclusion

Closing the loop on aircraft aluminium is challenging for a number of reasons: mixed alloys, a toxic coating, and strict purity limits, which is why today's recyclers stop at downcycled scrap. This project shows the full loop can be closed. By making alloy separation a priority, removing the coating system safely and completely, and refining the melt back to material specification, a France-based, low-carbon process can turn retired airframes into certifiable AA2024 and AA7075 sheet at about 97% lower carbon and 60% lower energy than virgin metal, paying back a €12.9 M investment in five years at 77 aircraft per year. The recycled electric Cessna 172 redesign shows the metal can fly again. The main thing standing between the design and reality is securing the supply of retired aircraft. Recycling aircraft aluminium and building a profitable business from it is and will remain a daunting challenge, but this report builds a documented case for why it can become reality.

Table of Contents

Nomenclature

Abbreviations

AA	Aluminium Association (alloy designation system)
AELS	Aircraft End-of-Life Solutions
AFM	Airplane Flight Manual
AGV	Automated Guided Vehicle
AMS	Aerospace Material Specification
AoA	Angle of Attack
AR	Aspect Ratio
ASM	ASM International (American Society for Metals)
ASME	American Society of Mechanical Engineers
AWJ	Abrasive Waterjet (cutting)
BEW	Basic Empty Weight
CAD	Computer-Aided Design
CAGR	Compound Annual Growth Rate
CAPEX	Capital Expenditure
CBAM	Carbon Border Adjustment Mechanism
CBS	Cost Breakdown Structure
CC	Constant Current (charging)
CFF	Ceramic Foam Filter
CFRP	Carbon-Fibre-Reinforced Polymer
CG	Centre of Gravity
CINEA	European Climate, Infrastructure and Environment Executive Agency
CNC	Computer Numerical Control
CRM	Critical Raw Materials
CV	Constant Voltage (charging)
DBF	Deep-Bed Filter
DC	Direct-Chill (casting)
DGFiP	Public Finances Directorate General (France)
DOD	Depth of Discharge
DPA	Defense Production Act
DSE	Design Synthesis Exercise
EASA	European Union Aviation Safety Agency
EC	European Commission
ELV	End-of-Life Vehicles (Directive)
EOL	End-of-Life
EPR	Extended Producer Responsibility
ERP	Equity Risk Premium
ETS	Emissions Trading System
EU	European Union
FAA	Federal Aviation Administration
FAR	Federal Aviation Regulations
FBS	Functional Breakdown Structure
FFD	Functional Flow Diagram
GFRP	Glass-Fibre-Reinforced Polymer
HCB	Hexachlorobenzene
IBC	Intermediate Bulk Container
ICAO	International Civil Aviation Organization
ICAS	International Council of the Aeronautical Sciences
ICCT	International Council on Clean Transportation
ICE	Internal Combustion Engine
IRA	Inflation Reduction Act
IRR	Internal Rate of Return
IRS	Internal Revenue Service
ISA	International Standard Atmosphere
ISO	International Organization for Standardization
LME	London Metal Exchange

LPM	Litres per Minute
MRR	Material Removal Rate
MTOW	Maximum Take-Off Weight
NACA	National Advisory Committee for Aeronautics
NDT	Non-Destructive Testing
NLR	Royal Netherlands Aerospace Centre
NPV	Net Present Value
NREL	National Renewable Energy Laboratory
NVM	Normal force, Shear force and Bending Moment (diagrams)
OEW	Operating Empty Weight
OES	Optical Emission Spectroscopy
OPEX	Operating Expenditure
PBL	PBL Netherlands Environmental Assessment Agency
PCDD/F	Polychlorinated Dibenzo-*p*-Dioxins and Furans
PD&D	Project Design & Development
POH	Pilot's Operating Handbook
PPE	Personal Protective Equipment
PPL	Private Pilot License
RAMS	Reliability, Availability, Maintainability and Safety
REACH	Registration, Evaluation, Authorisation and Restriction of Chemicals
ROC	Rate of Climb
ROI	Return on Investment
SAE	Society of Automotive Engineers
SAM	Serviceable Available Market
SDS	Safety Data Sheet
SNIF	Spinning Nozzle Inert gas Flotation
SOC	State of Charge
SOH	State of Health
SRM	Structural Repair Manual
SWOT	Strengths, Weaknesses, Opportunities, Threats
TAM	Total Available Market
TBD	To Be Determined
TRL	Technology Readiness Level
TSP	Total Suspended Particulates
UAT	User Acceptance Testing
UV	Ultraviolet
WACC	Weighted Average Cost of Capital
WEG	Water–Ethylene Glycol
XRF	X-ray Fluorescence

Chemical Formulae

Cl_2	Chlorine
CO_2	Carbon Dioxide
Cr(VI)	Hexavalent Chromium
NaOH	Sodium Hydroxide

Latin Symbols

A	Area	m^2
b	Wing span / stiffener (boom) spacing	m
B	Boom (lumped) cross-sectional area	m^2
c	Chord length	m
C_{D_0}	Zero-lift drag coefficient	–
C_L	Lift coefficient	–
$C_{L\alpha}$	Lift-curve slope	rad^{-1}
C_p	Pressure coefficient	–
D	Frame diameter	m
e	Oswald efficiency factor	–
E	Young's modulus	Pa

F	Applied force	N
g	Gravitational acceleration	$\mathrm{m\,s^{-2}}$
h	Height (wing box / frame web)	m
J	Propeller advance ratio	–
k	Thermal conductivity	$\mathrm{W\,m^{-1}K^{-1}}$
K_g	Gust alleviation factor	–
L	Lift force	N
L_e	Effective column length	m
l_h	Horizontal tail arm	m
L_w	Diamond-wire loop length	m
m	Mass	kg
M	Bending moment	N m
n	Load factor	–
P	Compressive load	N
P_d	Mechanical power delivered at the wire	W
q	Heat flux	$\mathrm{W\,m^{-2}}$
R	Radius	m
R_e	Cost of equity	–
R_f	Risk-free rate	–
S	Wing reference area	$\mathrm{m^2}$
SP	Small-firm (size) premium	–
t	Thickness	m
t_c	Cut time	h
T	Temperature	K
U_{de}	Derived gust velocity	$\mathrm{m\,s^{-1}}$
v	Wire (cutting) speed	$\mathrm{m\,s^{-1}}$
V	Airspeed	$\mathrm{m\,s^{-1}}$
V_B	Root vertical reaction force	N
W	Weight	N
x_{ac}	Aerodynamic-centre position	m
$\bar{y}$	Spanwise centre-of-pressure location	m

Greek Symbols

α	Thermal diffusivity / angle of attack	$\mathrm{m^2\,s^{-1}}$ / rad
β	Unlevered (asset) beta	–
β_L	Levered (equity) beta	–
δ	Deflection	m
Δp	Pressure differential	Pa
ε	Downwash angle	rad
ε_{grid}	Grid carbon intensity	$\mathrm{kg\,CO_2\,kWh^{-1}}$
η	Efficiency	–
λ	Taper ratio	–
ν	Poisson's ratio / Kinematic viscosity	– / $\mathrm{m^2\,s^{-1}}$
ρ	Density	$\mathrm{kg\,m^{-3}}$
σ	Normal (direct) stress	Pa
τ	Shear stress	Pa
τ_w	Diamond-wire working life	h

Subscripts

alu	Aluminium
cc	Crippling
cr	Critical (buckling)
dr	Electric–hydraulic (drive)
sp	Spar
str	Stringer
u	Cutting utilisation
y	Yield
$\perp$	Perpendicular (transverse to skin)

1

Introduction

The commercial aviation industry is currently facing a dual challenge: an impending wave of aircraft retirements and an increasing global imperative to reduce its environmental footprint. In parallel, the EU faces mounting supply-chain pressure for critical raw materials for aerospace applications. Over the next two decades, approximately 13,000 commercial airliners are expected to be decommissioned [1], creating a massive influx of end-of-life airframes. Currently, the very few aircraft that have a destination other than simply being parked in a boneyard are shredded and downcycled into lower-grade applications. Downcycling can be to automotive or construction materials, due to contamination from fasteners, mixed alloy families, and protective coatings. Simultaneously, the production of high-performance aerospace aluminium alloys from virgin bauxite ore remains highly energy-intensive and environmentally taxing, especially with the phasing out of free carbon allocations in the EU[1].

To address this gap, this report presents a comprehensive engineering and logistical framework for recycling end-of-life aircraft aluminium alloys back into aerospace applications. This project conceptualises a process that meticulously dismantles retired airliners, removes hazardous hexavalent chromium coatings via chemical immersion, accurately sorts the recovered metals using X-ray Fluorescence (XRF), and refines the melts into certifiable, aerospace-grade 2xxx and 7xxx series aluminium alloy sheets. By operating on a low-carbon electrical grid and employing deep-bed filtration and precise dilution techniques, the process preserves the material's properties while significantly undercutting the carbon footprint and energy consumption of primary aluminium production.

As a proof-of-concept for the circularity of these recycled materials, the project also details the preliminary design of a "green" Cessna 172S. This trainer aircraft is structurally composed of recycled alloys and is retrofitted with a battery-electric propulsion system, ensuring zero in-flight emissions and aligning with the operational and economic needs of modern flight schools.

The core motivation and goals of this project are encapsulated in the following statements:

- **Mission Need Statement:** "Establish a viable, profitable, and energy-efficient circular lifecycle for high-performance aerospace aluminium alloys."
- **Mission Objective Statement:** "Design a closed-loop aluminium recycling process for commercial aircraft and a recycled-alloy aircraft at a preliminary design review level."

The subsequent chapters of this report detail the market analysis in Chapter 2, the process overview in Chapter 3, and the disassembly technique from initial diamond-wire sectioning to computer-vision laser cutting in Chapter 4, decoating in Chapter 5. The sorting and refining of the aluminium are discussed in Chapter 6. Then the design of the electrical Cessna is discussed, starting with the structure in Chapter 7, and followed by the electric propulsion system in Chapter 8. Furthermore, potential risks are assessed in Chapter 9, sustainability is too in Chapter 10, and the economic business case is presented in Chapter 11, all to validate the feasibility and profitability of bringing retired aircraft back to the skies. Finally, the project's verification and validation procedure is discussed in Chapter 12 Finally, an outlook on the project's future and implementation is outlined in Chapter 13.

---

[1] URL `https://carboncredits.com/carbon-prices-today/` [cited June 8 2026]

2

Market Analysis

This chapter outlines the market analysis for both the aluminium alloys and the retrofit Cessna. Firstly, a SWOT analysis is performed in Section 2.1. Then, a value proposition for the aluminium alloy is given in Section 2.4, which is followed by a description of the current and future alloy demand in Section 2.5. Then, a green alloy supplement is explained in Section 2.6. The current prices and market fluctuations are described in Section 2.7. Finally, in Section 2.9.

2.1. SWOT Analysis

Firstly, a Strengths, Weaknesses, Opportunities, Threats (SWOT) analysis is performed for both the aluminium alloy and the Cessna market. Strengths and weaknesses are internal, whilst opportunities and threats are external. This analysis can be seen in Table 2.1

Table 2.1: Economical SWOT Analysis of Recycled Aluminium and Green Cessna

STRENGTHS	**WEAKNESSES**
▪ High-value product in contrast to traditional recycled material, the alloys are not downcycled, but retain their aerospace-grade properties. This creates the opportunity for the alloys to compete with the virgin alloy market and even demand a premium due to their green sourcing. ▪ Avoidance of carbon pricing penalties: by producing the alloys using the French green electricity grid, the emissions are kept very low and high carbon penalties are avoided. ▪ Low operating costs for the green Cessna: although the Cessna has a higher upfront cost, by using a battery instead of fuel and low maintenance requirements, the operating costs are low. ▪ Cross-border financial hurdle elimination: the entire process is in the EU (specifically France), so complex international legislation/costs are avoided.	▪ High sensitivity to throughput volume: the process has high upfront costs, and a high turnover is required to be able to achieve a payback period of five years. ▪ Pricing complexity: since the 2xxx and 7xxx aluminium alloy series are not traded on the public market, such as the London Metal Exchange (LME), the pricing is heavily reliant on business-to-business commitments, such as letters of intent. ▪ Regulatory burden: to be able to sell the material as certified aerospace-grade alloys, strict documentation is necessary. ▪ End-product trade-off: to maintain handling characteristics of a standard Cessna 172, while still having sufficient range, the layout of the aircraft is changed. This creates a niche segment in the market.
OPPORTUNITIES	**THREATS**
▪ Capitalising on industry 'green premium': brands are becoming more climate-conscious and are more willing to pay a premium for sustainable materials. This can be motivated by both consumer expectations and legislation. ▪ Phasing out free EU carbon allocations: Since the EU is phasing out the free baseline emissions, the cost of producing virgin aluminium alloys will rise. This creates a price advantage for electrically green recycled aluminium alloy. ▪ Large aircraft retirements: With approximately 13,000 aircraft retiring in the upcoming 20 years, this fleet will create a high volume of feedstock for the project. ▪ Access to EU funding: the EU has increasingly been investing in strategic autonomy. The associated grants could fund the project's initial setup costs.	▪ Competition from established downcyclers: large dismantlers like Tarmac Aerosave and AELS currently have dominant positions in acquiring the aircraft carcasses at European boneyards. If the profit margin of this process is lower, the feedstock volume would become a challenge. ▪ Energy market volatility: the process is partially dependent on the electricity pricing. Sudden increases in price would cut into profit margins. ▪ Long-term shift in aircraft composition: the aircraft retiring in the immediate future have a high aluminium alloy content. However, the percentage of composites in aircraft has risen steadily in recent years, which would threaten the project's long-term viability. ▪ Supply chain risks for batteries: the raw materials for batteries used in the Cessna are mined globally, often in volatile regions and carry the risk of human rights exploitation. This requires thorough and potentially expensive audits under the EU Battery Regulation.

2.2. Stakeholder Analysis

The entire process of recycling aluminium alloys and creating the retrofit Cessna involves many stakeholders. Understanding these stakeholders is essential when assessing the feasibility and viability of the project. In this section, these stakeholders are identified and placed in Figure 2.1, building an influence-interest graph.

The most critical stakeholders are large lessors and aircraft owners. Since these control the end-of-life aircraft, they are essential for the project. The primary interests of these companies are minimising costs and complying with sustainability legislation.

Aircraft dismantling companies such as AELS and Tarmac Aerosave are both partners and competitors. They currently dominate the end-of-life recycling market, but could become strategic partners. Their influence on acquiring these aircraft is strong.

Another key stakeholder group are aerospace manufacturers. As these companies are some of the primary purchasers of aerospace-grade materials, their willingness to pay a low-carbon premium is crucial. Willingness is highly affected by sustainability commitments and regulations. Component suppliers are thus the primary customer segment for recycled alloys.

Regulatory authorities such as EASA, national environmental agencies, the European Commission and national governments have significant influence due to certification and environmental compliance requirements. Getting approval from these organisations is essential before recycled alloys can be sold into the aerospace market. In addition to this, European sustainability initiatives and critical raw material policies can create financial incentives and strategic support for the project.

Another set of important stakeholders is investors and public funding bodies. Since high upfront costs are incurred for the project, access to funding is crucial. The investors are primarily interested in good financial returns, scaling possibilities and sustainability objectives

When looking at the retrofit Cessna, flight schools and general aviation operators are the primary stakeholders. The demand for aircraft is influenced by operational costs, sustainability performance and regulations. The retrofit Cessna is a smaller revenue stream than the aluminium alloy sales, and it serves as a demonstrator for the viability of a closed-loop system concept.

Finally, TU Delft is a key stakeholder in this project. Through supervision, technical expertise and assessment of the project, the university influences the scope, methodology and validation of the project. Although TU Delft would not be directly involved in operations after implementation, it is critical in the design phase.

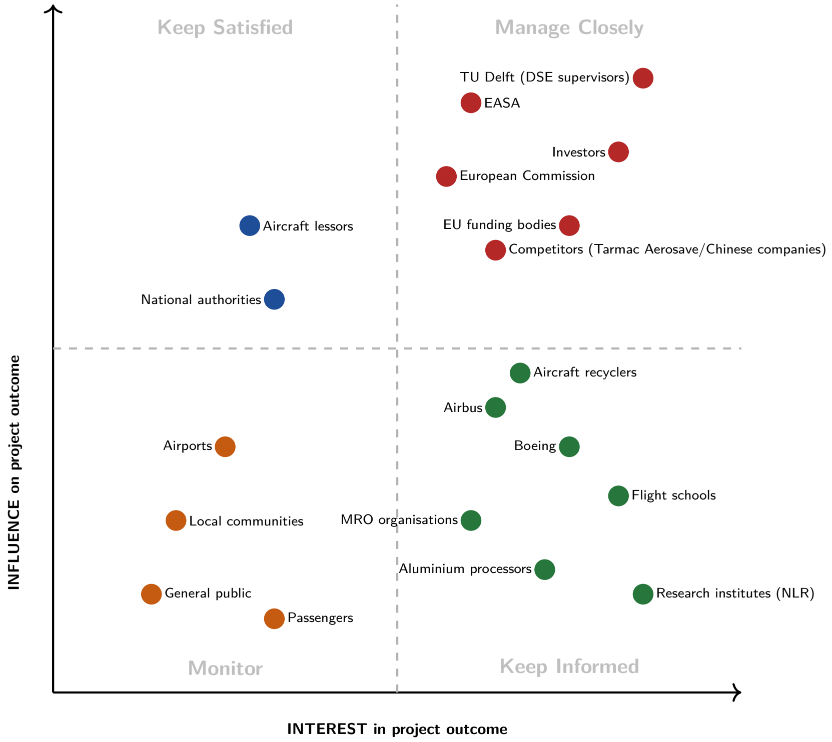

Figure 2.1: Interest-influence (external) stakeholder map for the mission

2.3. Market Segmentation

The business model serves two distinct markets: recycled aerospace-grade aluminium alloys and retrofit electric training aircraft. Thus, market segmentation is done separately for each product.

2.3.1. Recycled Aerospace-Grade Aluminium Alloys

The aluminium market is segmented according to industry application, sustainability requirements, and purchasing volume. Although recycled aluminium alloys are sold to multiple sectors, specifically aerospace and automotive manufacturers purchase high quantities of aerospace-grade 2xxx and 7xxx alloys.

The market is sized using three nested measures. The Total Addressable Market (TAM) represents the total demand if 100% of the market were captured, the Serviceable Addressable Market (SAM) is the portion of that TAM reachable given the business model, geography, and product, and the Serviceable Obtainable Market (SOM) is the realistic share of the SAM that can actually be captured in light of competition and available resources. The three therefore narrow in scope from the theoretical maximum (TAM) to the reachable market (SAM) to the winnable market (SOM).

The Total Available Market (TAM) consists of the global aerospace aluminium market, including aircraft manufacturers, maintenance companies, defence contractors, and aerospace component suppliers. The Serviceable Available Market (SAM) is limited to organisations that are willing to pay for the certified recycled aerospace-grade aluminium alloys. This segment is expected to grow as sustainability targets are becoming increasingly important and primary aluminium production, which is a high-carbon emitter, becomes more expensive under EU regulations. The Serviceable Obtainable Market (SOM) is focused on European manufacturers and suppliers that focus on low-carbon material sourcing. As the project is in the European Union and is located close to the aerospace core of the continent, this creates a competitive advantage within this segment.

The high-priority customer groups are:

1. Aircraft original equipment manufacturers
2. Maintenance, repair and overhaul organisations
3. Defence and government aerospace programmes
4. Manufacturers focus on creating low-carbon supply chains

These customers have high material quality requirements, long-term contracts, and are willing to pay a premium for high-grade sustainable materials.

2.3.2. Retrofit Electric Cessna

The retrofit Cessna market is segmented based on aircraft mission profiles and operator characteristics. This project specifically targets pilot training operations.

The TAM consists of all globally sold single-engine piston aircraft. The SAM is limited to aircraft used primarily for pilot training and flight instruction; this creates flight duration expectations to align with current battery limitations. Finally, the SOM comprises environmentally conscious flight schools.

This segment is especially attractive because flight training missions are predictable, relatively short, and repetitive. Operators in this segment benefit significantly from fuel cost elimination, reduced maintenance requirements, and lower noise emissions. These advantages create a convincing value proposition regardless of the limitations of current battery technology.

The market segmentation shows that both products are focused on specialised, high-value niches rather than high scale, mass-market applications. This strategy enables the project to maximise margins, differentiate itself and establish a strong position within circular supply chains.

2.4. Value Proposition Aluminium Alloys

The value proposition of the recycled aluminium alloys is centred on a premium for the low-carbon production and creating a closed-loop process. This process performs well on both environmental and economic criteria. By recycling aluminium alloys from retired aircraft, the energy required to process the metal is extremely low. This directly appeals to downstream manufacturers that aim to meet environmental and social targets. Unlike general scrap aluminium alloys, this material is sourced only from decommissioned aircraft, ensuring that it retains the properties required for 2xxx or 7xxx series. This high material integrity allows the material to yield a higher sale price than standard recycled scrap, which directly supports the financial feasibility of the project. If the volume of disassembled aircraft fluctuates, the higher margins protect the project in paying back non-recurring capital costs much faster. Since the reclaimed material undergoes a strict certification process, buyers are certain that it is aerospace-grade.

2.5. Current and Future Alloy Demand

The current aluminium market is estimated to be at \$243.02 billion in 2025. The Asia-Pacific region was dominant with a market revenue share of over 66%[1]. The market is expected to grow to \$406.39 billion in 2033 with a compounded annual growth rate (CAGR) of 7.4%. The dominant drivers behind this growth are the automotive and aerospace sectors. Construction and infrastructure development, especially in Asia and the Middle East, also contribute to market growth[2]. These alloys can also be reused in the aerospace industry, as they maintain their high quality.

The recycled alloys are predominantly 2xxx, 6xxx and 7xxx series. The 6xxx series is changed to the 2xxx series during the refining process, so only the 2xxx and 7xxx series are further developed with regard to their current market.

2xxx series (Al-Cu alloys) The global 2xxx series was valued at \$8.4 billion in 2025[2]. It is expected to reach a value of \$13.6 billion by 2034 with a CAGR of 5.5%. Drivers of this growth are the aerospace, defence and automotive sectors. There is a current global aviation backlog of more than 13,000 aircraft. The aerospace sector accounts for more than 40% of the global consumption. The automotive sector is adopting more lightweight materials to decrease fuel use, and defence programmes are expanding worldwide[3]. Ingots are often not the final traded commodity; secondary smelters cast the recycled material into raw extrusion billets or rolling ingots. These intermediate shapes are subsequently transferred to downstream processors, where critical solution heat treatments and artificial ageing are done. The product type in which the alloy is sold can be seen in Figure 2.2. The dominant products are clearly identified as plates and sheets.

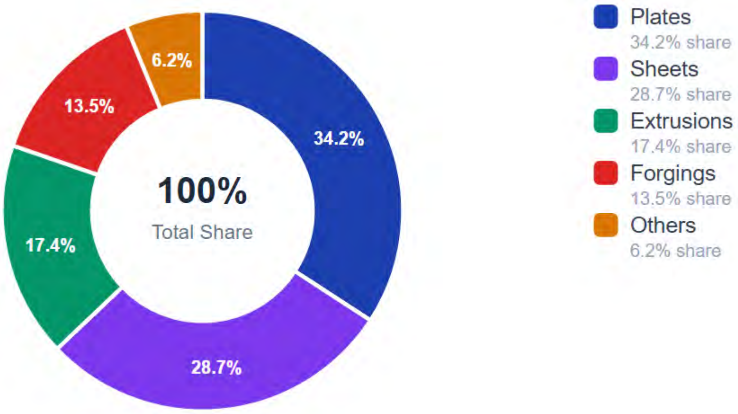

Figure 2.2: Market distribution for 2xxx series aluminium alloys products[2]

7xxx series (Al-Zn alloys) The 7xxx series is the highest-strength aluminium family currently available. Although its current market share is below 5%[3], it has the highest projected CAGR. Processing this alloy family is energy-intensive, and its use is difficult since fusion welding drastically reduces its strength. Some market drivers are the automotive applications due to their high ultimate tensile strength[4].

2.6. Green Alloy Supplement

Since carbon accounting was introduced, the pricing structure of the aluminium market has changed. Instead of paying the single commodity price, the buyer pays a 'green premium'. The difference in greenhouse emissions between virgin aluminium and recycled material can be up to 95%.

Firstly, these differences in carbon footprint can result in a premium of \$400-800 (€344-688) per tonne for the 7xxx and 2xxx series [2]. The influence of this increase can be seen in the second column of Table 2.3. This increase ties back to brand commitments: large companies in industries that depend on public opinion can reduce their environmental impact by swapping primary aluminium alloys for recycled aluminium alloys, thereby appealing to consumers.

In 2005, the EU introduced the ETS (Emissions Trading System)[5]. This increased the cost of producing virgin aluminium alloys, since companies pay for all CO_2 emissions above their allocated free allowance. This increases the

---

[1] URL `https://www.grandviewresearch.com/industry-analysis/aluminum-alloys-market` [cited 10 June 2026]
[2] URL `https://www.grandviewresearch.com/industry-analysis/aluminum-alloys-market` [cited 10 June 2026]
[3] URL `https://dataintelo.com/report/global-2xxx-series-aluminum-alloy-market` [cited 10 June 2026]
[4] URL `https://www.mordorintelligence.com/industry-reports/high-strength-aluminum-alloys-market` [cited 10 June 2026]
[5] URL `https://climate.ec.europa.eu/eu-action/carbon-markets/about-eu-ets_en` [cited 15 June 2026]

competitiveness of electrically produced recycled aluminium, which comes with fewer emissions. Initially, the cleanest primary aluminium smelters were exempt from paying for their emissions and functioned as a baseline. Smelters with lower levels of cleanliness paid for all CO_2 exceeding this lower limit. However, since the first of January 2026, the EU is scaling down these free permits. All smelters pay for 2.5% of the initial baseline on top of everything exceeding it. In Table 2.2, the increase per year can be seen. The amount of CO_2 produced in primary aluminium production is approximately 1.45 tonnes for 1 tonne of aluminium. As a carbon credit for one tonne of CO_2 costs approximately €78 Euro as of June 2026, this would cause a significant cost increase in 2034 when all free permits are phased out[6]. These carbon credits have been increasing in price since their introduction; thus, the effect is assumed to be more influential over time. This directly increases the competitiveness of the recycling process, as it emits less carbon dioxide and thus incurs lower permit costs.

Table 2.2: EU ETS Free Permit Phase-Out Schedule

Timeline Year	Free Permit Reduction (%)	Remaining Allocation (%)
2026	2.5%	97.5%
2027	5.0%	95.0%
2028	10.0%	90.0%
2029	22.5%	77.5%
2030	48.5%	51.5%
2034	100.0%	0.0%

2.7. Current Prices and Fluctuations

Finding prices is challenging since specialised aluminium alloys such as the 2xxx and 7xxx series are rarely traded publicly on exchanges like the London Metal Exchange (LME) or the Shanghai Futures Exchange. Instead, companies such as Alcoa and Rio Tinto work on the basis of letters of intent; aluminium alloys are sold before they are produced. An estimation of prices can be found in Table 2.3[7].

Market fluctuations also impact the price. The three changes are: scrap availability, energy usage and regulation changes. Scrap availability is crucial for this project. If scraps become scarce, prices increase and cut into the profit margin. Then energy usage is also important; variations in price are directly linked to production costs, potentially increasing them drastically. Finally, regulation changes have an impact. This is already evident in the implementation of carbon border adjustment mechanism (CBAM). These regulation changes can potentially also cause price disconnects between European and other markets.

Table 2.3: Pricing of Recycled Aluminium

Alloy Series	Rolled Sheet (without premium)	Price Including Green Premium
AA2024	€9.03 /kg	€9.37-9.72 /kg
AA7075	€10.97 /kg	€11.31-11.66 /kg

2.8. Competitor Analysis and Market Share

Downcyclers are the primary market competitor at this moment. Established companies such as Tarmac Aerosave and AELS already process retired aircraft into sorted scrap and sell it to remelters. Since there is currently no alternative, these companies have a massive market share in European decommissioned aircraft. The country that recycles the most aluminium is China, at 40% of the total market. The country is also making progress in upcycling, instead of solely downcycling.[8]. This makes Chinese companies a significant current and future competitor.

Selling bulk material scrap is based on a high-volume and low-margin business model. This scrap aluminium alloy is sold to secondary markets like the automotive sector. To compete for aircraft carcasses, the recycling process needs to have a similar or higher profit margin, as the opportunity costs otherwise are too high to divert the material. Recycling has the distinctive advantage that the material is not degraded into mixed material. Recycled aerospace-grade aluminium alloys can compete with virgin aluminium alloys and thus demand a higher price. Aside from being high quality, a low-carbon premium can be asked for the material, increasing profit margins.

The number of retiring aircraft in the upcoming years is approximately 13,000 aircraft [3]. Assuming this happens linearly, this would mean 650 aircraft retire each year. However, currently approximately 500 large aircraft are decommissioned per year[9]. Of these aircraft, most are stored rather than disassembled, reducing the value of

---

[6] URL `https://carboncredits.com/carbon-prices-today/` [cited June 8 2026]

[7] URL `https://solitairesteelllp.com/aircraft-aluminum-sheet-supplier` [cited 10 June 2026]

[8] URL `https://www.aluminiumchina.com/en-gb/news-center/industry-news/2025/12/9.html` Visited on 23 June, 2026

[9] URL `https://simpleflying.com/how-many-aircraft-scrapped-every-year/` [cited 15 June 2026]

available aircraft for recycling. For this project to break-even, 77 aircraft need to be disassembled, which is equal to approximately 12% of the total market, assuming 650 aircraft. This is a challenging goal for a start-up, especially looking at the current retirement rate, but by focusing on long-term contracts with current aircraft owners, it would become more achievable.

2.9. Market Analysis Retrofit Cessna

Market analysis of the green retrofit Cessna contains a value proposition in subsection 2.9.1, competitor analysis and market share in subsection 2.9.2 and finally economics, market fluctuations and barriers in subsection 2.9.3.

2.9.1. Cessna Value Proposition

The value proposition for the green retrofit Cessna centres around three advantages: operational cost reduction, zero in-flight carbon emissions and reduced noise emissions.

Firstly, the aircraft is not reliant on aviation fuel, as it is powered by electrical energy. Since the lifetime costs of electricity are significantly lower than those of fuel, operational costs are low. This calculation is shown in subsection 8.8.2. Also, an electric motor has very few moving parts, thus maintenance and downtime costs are limited. Secondly, the electric Cessna emits no direct greenhouse gas emissions during flight. Consequently, the environmental impact is limited compared to that of conventional aircraft. Indirect emissions can be limited by using a low-carbon electricity grid. Finally, the electric propulsion system generates less noise than conventional engines[10]. These noise reductions are especially beneficial when the aircraft are flown near noise-sensitive locations. This makes community acceptance higher and expands potential training times.

2.9.2. Competitors, Segmentation and Market Share

Currently, only one electric aircraft model has been sold in 2025, the Pipistrel Velis Electro [4]. This aircraft has an endurance of 50 minutes, which is significantly lower than the endurance of conventional aircraft. Although it is a competitor of the electric retrofit Cessna, it commands a very small market share due to its limited use. The conventional single-engine piston aircraft are thus the main competitors. The designed retrofit Cessna is able to do standard training flights, as described in Section 8.3, which makes it a suitable substitute for the current aircraft options.

The target market is the single-engine propeller aircraft market. The size of this market is roughly 1,600 sales a year [4]. This represents the total addressable market (TAM). A big segment of this market is the flight schools. This is sized by around 35% and 560 aircraft[11].This segment is especially attractive because flight training missions are predictable, relatively short, and repetitive. Operators in this segment benefit significantly from fuel cost elimination, reduced maintenance requirements, and lower noise emissions. These advantages create a convincing value proposition regardless of the limitations of current battery technology. Therefore this is the serviceable available market (SAM).

The serviceable obtainable market (SOM) for the first three to five years will be 5% of the SAM. An overview can be found in Figure 2.3. The primary driving force in capturing this market is the substantial operational cost advantage of green electric Cessna.

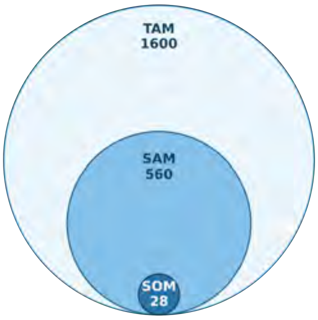

Figure 2.3: TAM, SAM, SOM calculation of the green retrofit Cessna

---

[10] URL `https://uwaterloo.ca/sustainable-aeronautics/blog/noisy-neighbours-do-electric-aircraft-reduce-airport-noise` [cited 16 June 2026]

[11] URL `https://www.snsinsider.com/reports/piston-engine-aircraft-market-10114` [cited 16 June 2026]

2.9.3. Economics, Market Fluctuations and Barriers

The cost of the Green Cessna is similar to the original Cessna 172S. The cost advantage is created during the operational lifetime of the aircraft. If the price of the AVgas (aviation gasoline) goes up, the retrofit Cessna benefits from this, as it is not reliant on fuel. Aside from fuel fluctuations, the battery prices are also important to the business case. If these go up, the battery replacement expenses increase. The expectation for the upcoming years is that the price of these batteries will decrease [5]. This works favourably for the Green Cessna. As geopolitical tensions have been increasing over the last five years, a battery shortage could become an issue. China is the dominant producer of materials used in battery production, so European dependence is high[12].

The introduction of electric retrofit Cessnas to the market is hindered by several barriers: infrastructure, battery capabilities and strict certification regulations. Currently, the electric infrastructure is not implemented on a large scale at most airports. Also, the battery capacity is a limiting factor. For flight schools, this battery capacity is sufficient, but for general aviation, it severely limits flight time compared to the combustion-powered Cessna 172S. Finally, the aircraft has to be certified. Certifying a CS-23 / Part 23 aircraft can cost up to €50,000,000[13][14].

---

[12] URL `https://www.iea.org/reports/global-ev-outlook-2024/trends-in-electric-vehicle-batteries` [cited 16 June 2026]

[13] URL `https://generalaviationnews.com/2012/09/09/the-cost-of-certification/` [cited 22 June 2026]

[14] URL `https://files.gao.gov/reports/GAO-26-107816/index.html`[cited 16 June 2026]

3

Process Overview

3.1. Operations and Logistics Concept Description

To better understand the recycling process, a block diagram for the operations & logistics was made in Figure 3.1. The process starts with sourcing a scrapped airliner. Existing retired aircraft could be taken from boneyards, such as Teruel airport, for disassembly. Retired airliners could also be purchased from lessors and airlines, or from other recycling companies such as TARMAC and AELS. After an airliner is acquired, it will be disassembled at a boneyard or central hub into workable pieces measuring no more than 80 cm by 30 cm. This process also ensures that no rivets are included in the recovered scrap, as their high iron content would ruin the sheet's mechanical properties.

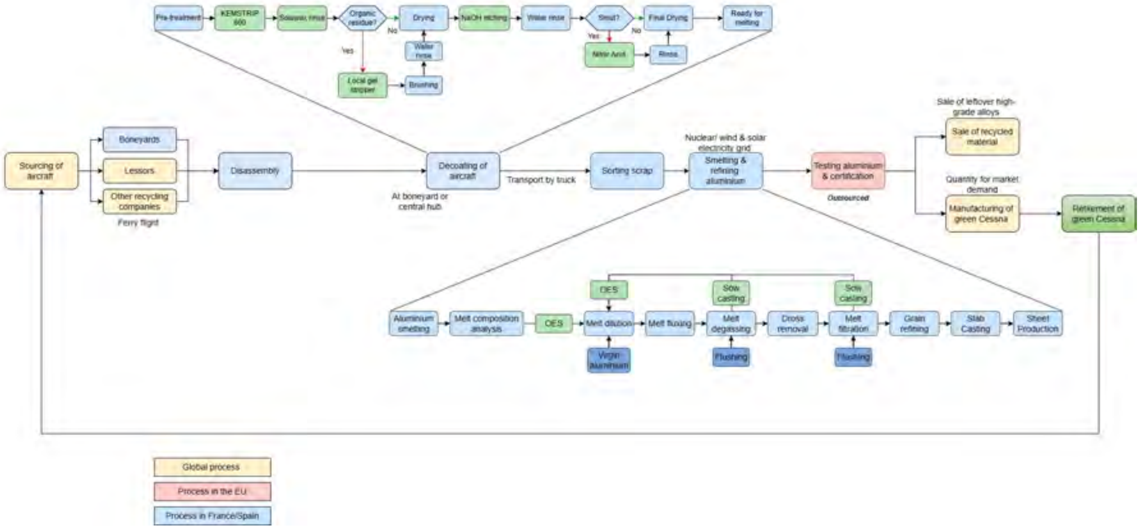

Figure 3.1: Detailed general overview of the process

Then the pieces follow a rigorous sequence of stripping using chemical baths, followed by drying to remove their coatings. This removes the dangerous Cr(VI) containing coatings and any other coatings present on the pieces. After which the decoated metal parts are brought by truck to the refining facility, where they are first sorted. This sorting is based on the alloy families that can be melted into batches aimed at producing AA2024 and AA7075, respectively, and the two sorting groups are shown in Table 3.1. These follow the guidelines published by the Aluminium Association [6], i.e. AA2219 will not be recycled because of its high Zirconium content. The sorted batches then go through the refining process, where the metal is melted, and contaminants such as excess iron, oxides, hydrogen, alkalis and dirt are removed. During the refining process, the melt is repeatedly analysed with Optical Emission Spectroscopy (OES), to check if it achieves the required chemical composition.

At the end of the refining process, the melt is cast into aluminium slabs, which are then sent to a specialised mill to be turned into sheets. These sheets are third-party tested and certified and are now ready for production in the aerospace industry. Part of the certified AA2024 and AA7075 sheets will be used to manufacture a green Cessna 172S, which will also be electrically powered, resulting in zero in-flight emissions. Most of the metal, however, will be sold to OEMs as the project would otherwise flood the general aviation market, bringing the Cessna's price down.

The goal of the project is again to close the loop in the aerospace industry. Thus, the Cessna will be designed with recyclability in mind. When the green Cessnas reach the end of their operational life, they will be recycled into new aircraft parts, thus closing the aircraft aluminium loop.

Table 3.1: Table showing the alloy families that are melt-compatible with AA2024 and AA7075, respectively

AA2024 Group		AA7075 Group	
AA2014	✓	AA2014	✗
AA2017	✓	AA2017	✗
AA2024	✓	AA2024	✗
AA2219	✗	AA2219	✗
AA5083	✓	AA5083	✗
AA6061	✓	AA6061	✗
AA7050	✗	AA7050	✗
AA7150	✗	AA7150	✗
AA7075	✗	AA7075	✓
AA7178	✗	AA7178	✓
AA7475	✗	AA7475	✓

3.2. Communications Flow Diagram

Another way of looking at the process overview is through a communications diagram. It shows the flow of data through a certain system, as well as the flow to and from its environment. To achieve this, all elements are treated as blocks and connected by arrows annotated with the flow content. A notable section is the refining section, where the OES analysers have to communicate with the dilution calculator to know how much virgin material to add. Furthermore, the flushing of the degassing and filtration systems needs to be communicated to other subsystems, as it does not happen at regular intervals. The vehicle controls section is separate; this is because the system is only relevant for the standalone green Cessna that the design team will produce. Communications with ATC were left out of that section, as it involves the pilot, which is not an automatic process.

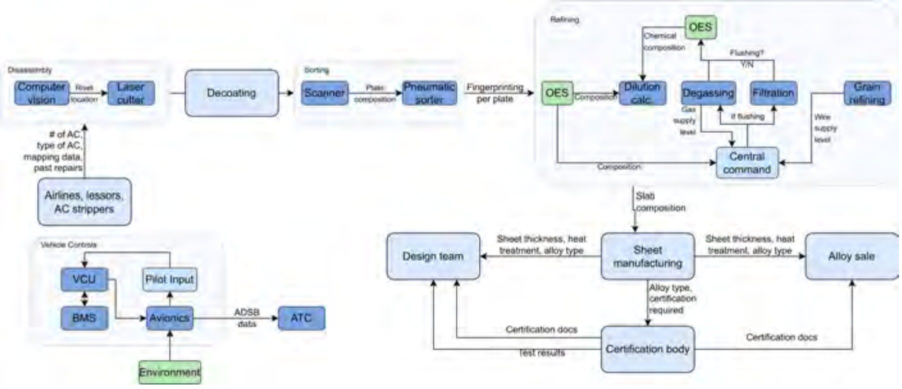

Figure 3.2: The process communication flow diagram

3.3. Aircraft Sourcing

Within this section, three aspects of aircraft sourcing are explored: sourcing considerations in subsection 3.3.1, the location in subsection 3.3.2 and state of aircraft and costs in subsection 3.3.3.

3.3.1. Sourcing Considerations

The sourcing of aircraft takes into account four aspects: geopolitical and regulatory risk, green energy, strategic funding, logistics and proximity.

Regulations

Firstly, regulations are currently unpredictable in the US. Changes in tariffs and withdrawals from international agreements create risks for long-term investments. The EU is historically stable and consistent with legislation. Furthermore, the EU enforces Carbon Border Adjustment Mechanisms (CBAM); importing and selling carbon-heavy materials from outside the EU increases costs and reduces economic viability. Also, sourcing within the EU structurally aligns the project with potential future structural shifts in European aerospace asset accountability. Currently, the automotive sector enforces Extended Producer Responsibility (EPR) under the End-of-Life Vehicles (ELV) directive. The EU is actively seeking to apply these cradle-to-cradle principles to the aviation industry, too. Under the strategic direction of the EU's Circular Economy Action Plan and new initiatives such as the European Climate, Infrastructure and Environment Executive Agency's (CINEA) Green Assist advisory framework, future capital distribution will heavily weigh lifecycle transparency, material traceability, and non-destructive alloy recovery[1].

---

[1] URL `https://cinea.ec.europa.eu/news-events/news/green-assist-supporting-circular-solutions-aircraft-recycling-2026-05-04_`

Green Energy
Sustainable, high-energy processes require a low-carbon power grid to keep greenhouse gas emissions low. France has a highly stable and sustainable grid due to its high amount of nuclear power production; approximately 95% of its energy is produced with zero carbon emissions[2]. Spain makes use of solar and wind energy production, making 75% of its electricity low-carbon emissions and 57% zero emissions generated[3]. Conversely, the United States derives around 43% of its energy from zero-emissions sources, with the majority of its energy still dependent on fossil fuels[3].

Strategic Funding
Strategic Funding is also a significant consideration. The Critical Raw Materials (CRM) Act has significantly improved the EU's funding landscape. Direct grants, such as the Innovation Fund and Horizon Europe, become possible as the process directly reduces bauxite import dependency[4]. Also, by introducing the "Green Deal" and "Circular Economy Action Plan", more funding opportunities have been created, and the aim for circularity is clear.

In addition, obtaining strategic project status would fast-track permits, reducing the traditionally strict legislative hurdles faced in the EU. The US, by contrast, uses tax cuts and national security funding rather than centralised project designations. Under the Inflation Reduction Act (IRA) and the Defence Production Act (DPA), the US provides a 10% advanced manufacturing tax credit for domestic processing of critical minerals like bauxite and alumina[5]. The US is more focused on fast scale-ups, whilst the EU is more tailored to start-ups[6]. Since the project is still in its initial phase and relatively low-scale, the current EU landscape is assumed to be more beneficial.

Logistics and Proximity
Finally, most of the boneyards in the US are in remote locations such as deserts. Transatlantic or domestic transport would significantly increase both logistics costs and supply chain emissions. The United States is highly effective at disassembling and has a large maintenance-driven infrastructure; however, it treats the materials as low-value by-products, which can lead to alloy mixing[7]. Spain and France, on the other hand, are slower at disassembling, but these countries have more advanced thermal decoating systems integrated into the smelting process, which gives the EU an edge in closed-loop production[7]. In addition, sourcing within the EU would create a small loop, with the entire process within a radius of a few hundred kilometres. Based on these four considerations, the sourcing will be done within the EU.

3.3.2. Sourcing Location & State of Aircraft

Finding a primary aircraft source within the EU narrows down to a few geographical locations. Currently, the largest aircraft storage and decommissioning sites are in Spain and France. These are in Teruel Airport (TEV) and Tarbes-Lourdes-Pyrénées Airport (LDE), these locations are predominantly due to both climate and sufficient room to park the aircraft. Both locations provide extensive dismantling capabilities and are operated by Tarmac Aerosave. They can achieve a material recovery rate of over 92% per airframe[8]. However, the coatings and primers force the material to be downcycled, as Tarmac does not remove them.

Since a significant part of the current commercial fleet is scheduled to be decommissioned over the coming years, securing contracts with large aircraft lessors such as AerCap or Avolon is crucial to maintaining a steady aircraft supply. Providing a stable supply chain is especially important when applying for EU circularity grants[9].

Aircraft are assumed to be sourced from storage locations within the European Union, including airports and dismantling sites. For this project, France is used as a representative case due to its prominent aerospace industry, infrastructure and low-carbon electricity grid.

3.3.3. Costs

The process starts at acquisition of the aircraft. When purchasing aircraft from lessors or other owners, the cost of an aircraft carcass is primarily determined by its residual scrap-metal value and operational condition. Once the aircraft is at the dismantling location, the stripping can begin. Complete stripping includes defueling, draining, removing toxic fluids, and removing the non-metal interior. This costs approximately €110,000 per aircraft [3]. This process also creates revenue for the stripper as the removed material, such as engines, can be sold. Then, the stripped airframe is

---

en [cited June 11 2026]

[2] URL `https://lowcarbonpower.org/region/France` [cited 10 June 2026]

[3] URL `https://ember-energy.org/countries-and-regions/spain/` [cited 10 June 2026]

[4] URL `https://single-market-economy.ec.europa.eu/sectors/raw-materials/areas-specific-interest/critical-raw-materials/critical-raw-materials-act_en` [cited 10 June 2026]

[5] URL `https://www.irs.gov/inflation-reduction-act-of-2022` [cited June 10 2026]

[6] URL `https://kpmg.com/ch/en/insights/esg-sustainability/eu-green-deal-vs-us-inflation-reduction-act.html` [cited 10 June 2026]

[7] URL `https://www.strategicmarketresearch.com/market-report/commercial-aircraft-disassembly-dismantling-and-recycling-market` [cited 10 June 2026]

[8] URL `https://www.tarmacaerosave.aero/about-us` [cited 8 June 2026]

[9] URL `https://cinea.ec.europa.eu/programmes/innovation-fund/calls-regular-grants_en` [cited 10 June 2026]

left as the carcass of a Boeing 747; the scrap value is approximately €55,000[10]. It is assumed that this is the price of acquiring the carcass. Assuming 19% is recovered from the aircraft, approximately 31 tonnes of aluminium alloy are retrieved[11].

If the aircraft is not at the boneyard yet, a ferry flight causes additional costs. A flight can cost between €25,000 and €60,000[12]. This is mainly due to fuel, permits, landing fees, and crew day rates. If the aircraft are sourced at the airports/boneyards, these emissions and expenses are eliminated completely.

For this project, stripping and ferry flights are ignored as these are not part of the business. The processes are performed by other companies. This process assumes the carcass is bought on-site at a price of €55,000, costing a price of €1.77 per kg aluminium alloy.

3.4. Transport

Since the transport of the material is kept within France, transport costs and carbon emissions are kept relatively low. It is assumed that the entire process requires a maximum of 1,000 km of transportation. This is done by road freight, similarly to the approach of TARMAC Aerosave. Although Railway infrastructure is well developed across Europe, it does not fit for this specific recycling loop due to the 'last mile'. The smaller airports or regional smelting facilities are typically not directly connected with railways. Using these would require loading the scrap onto trucks, transportation to the train and then reloading onto trucks to transport it to its final destination. The additional handling would increase labour costs, handling time and risk of material contamination.

Road freight is the most efficient option, the scrap would be packed into trucks and transported 'gate-to-gate'. Since aluminium has a fairly high density, volume should not be an issue, and the trucks will be filled up to the maximum weight limit. A legal payload of 24 tonnes per trip is assumed. Since the alloys are in scrap, tipper trucks are used. France has many toll roads, which increases the price per kilometre. As a base rate, €1.50-2.20 per kilometre is assumed[11]. This would result in a total cost per 24-tonne payload batch between €1,500-2,200.

The fuel consumption is assumed to adhere the following relationship $fuel/km = 0.1 + 0.01 \cdot GVW$ [7] where GVW is the gross vehicle mass or the total mass of the vehicle. This gives a fuel consumption of 0.5 l/km for a 40 tonne vehicle, the maximum allowed on French roads. For the assumed 1,000 km, this would result in 1,238 kg of CO_2 or 0.0516 CO_2/kg of aluminium. Using 2.91 kg of CO_2 per kg and a density of 0.85 kg/l for diesel [7]. It also gives an energy consumption of 0.207 kWh/kg. Using a lower heating value of 35.8 MJ/l.

3.5. Interface Definition

Figure 3.3 An interface definition shows the subsystems and their interactions in an N^2 chart, as shown in Figure 3.3. The subsystems are placed in the blue boxes on the diagonal. The subsystems in the foundry part are enclosed in a red box, and those in the aircraft design process are in a green box. If a box is on the right or left of a subsystem, it is an output, and if it is below or above, it is an input of that subsystem. For example, the disassembly subsystem determines the size of the parts that are supplied to the sorting system. In the reverse direction, the sorting subsystem determines what alloys cannot be distinguished accurately enough and therefore need to be presorted when disassembling.

---

[10] URL `https://www.flexport.com/blog/decommissioned-planes-salvage-value/` [cited 1 June 2026]

[11] URL `https://www.flexatrans.eu/details-tarif+transport+routier+au+km+votre+devis+en+deux+minutes-1745` [cited 10 June 2026]

[12] URL `https://mhcaviation.com/blog/aircraft-ferry-services-explained-costs-process-and-global-operations` [cited 9 June 2026]

Figure 3.3: N-Squared (N^2) dependency chart

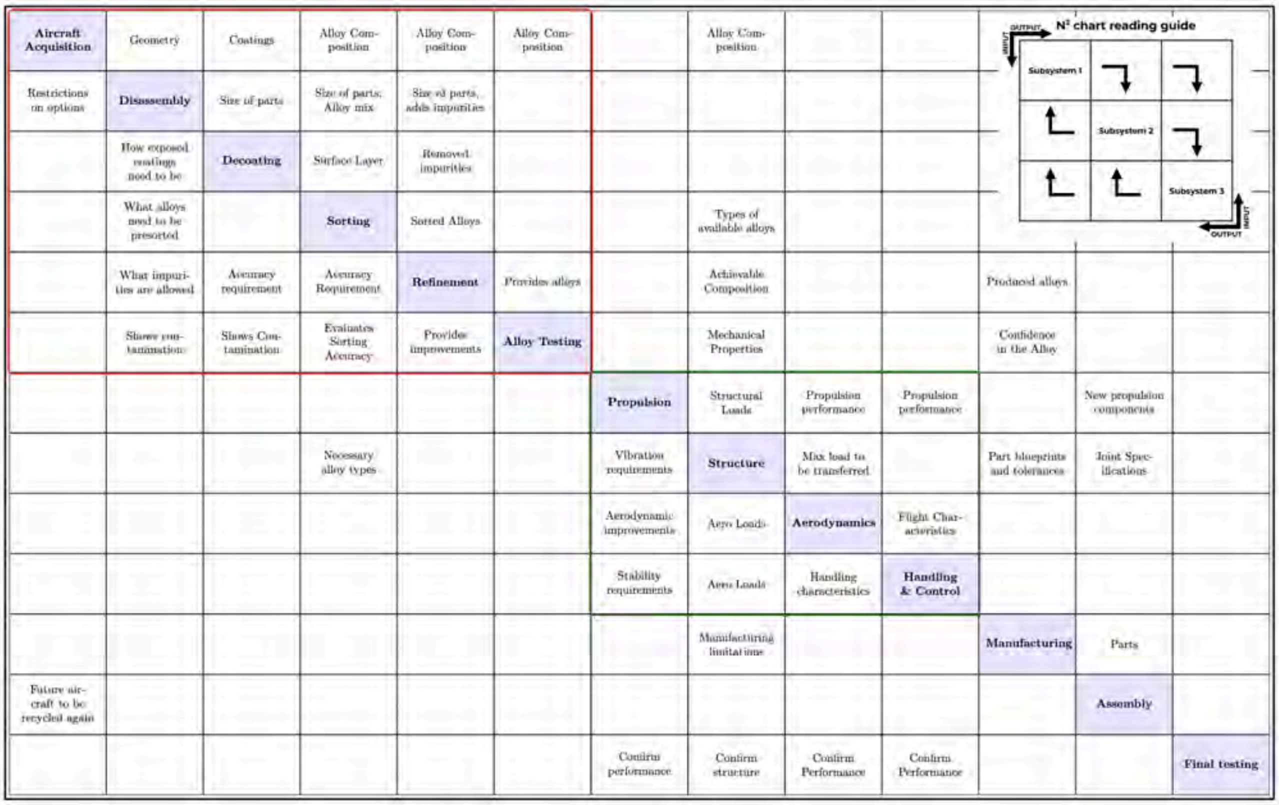

Aircraft Acquisition	Geometry	Coatings	Alloy Composition	Alloy Composition	Alloy Composition		Alloy Composition					
Restrictions on options	**Disassembly**	Size of parts	Size of parts; Alloy mix	Size of parts, adds impurities								
	How exposed coatings need to be	**Decoating**	Surface Layer	Removed impurities								
	What alloys need to be presorted		**Sorting**	Sorted Alloys			Types of available alloys					
	What impurities are allowed	Accuracy requirement	Accuracy Requirement	**Refinement**	Provides alloys		Achievable Composition			Produced alloys		
	Shows contamination	Shows Contamination	Evaluates Sorting Accuracy	Provides improvements	**Alloy Testing**		Mechanical Properties			Confidence in the Alloy		
						Propulsion	Structural Loads	Propulsion performance	Propulsion performance		New propulsion components	
			Necessary alloy types			Vibration requirements	**Structure**	Max load to be transferred		Part blueprints and tolerances	Joint Specifications	
						Aerodynamic improvements	Aero Loads	**Aerodynamics**	Flight Characteristics			
						Stability requirements	Aero Loads	Handling characteristics	**Handling & Control**			
							Manufacturing limitations			**Manufacturing**	Parts	
Future aircraft to be recycled again											**Assembly**	
						Confirm performance	Confirm structure	Confirm Performance	Confirm Performance			**Final testing**

3.6. Functional Breakdown and Flow

The functional breakdown structure (FBS) and functional flow diagram (FFD) are part of the functional analysis, which describes what the system will do, but not how it will do it. The purpose of this functional analysis is to demonstrate the system's desired capabilities and functions before implementing the solution.

3.6.1. Functional Breakdown Structure

The goal of the FBS is to define what functions are in scope. The main system functions (shown in blue) are at the top level of the FBS. These top-level functions are:

- "Disassemble an EOL aircraft"
- "Decoat aluminium alloy plates"
- "Sort and decoat aluminium alloy plates into sheets"
- "Manufacture green retrofit Cessna 172S with recycled aluminium alloy sheets"
- "Perform training flight operations of the green retrofit Cessna 172S"
- "Decommission green retrofit Cessna 172S at EOL"

These functions are further broken down into middle-level functions (shown in green), which represent the subsystems. Lastly, the middle-level functions are split into low-level functions. If the system can complete all of these functions, the requirements will be met. Each function has its own unique identifier (ID), and the top and middle-level functions are labelled with their respective system and subsystem.

3.6.2. Functional Flow Diagram

All of these functions are also represented in the FFD. This places the functions in an operational flow, which gives insights into their operational flow, providing useful information on parallel or sequential processing of the functions. Logical operators such as AND and OR are also included in the FFD to show these paths. To maintain clear consistency across both diagrams, the IDs specified for the FBS are exactly the same as the IDs used in the FFD.

Figure 3.4: Functional breakdown structure

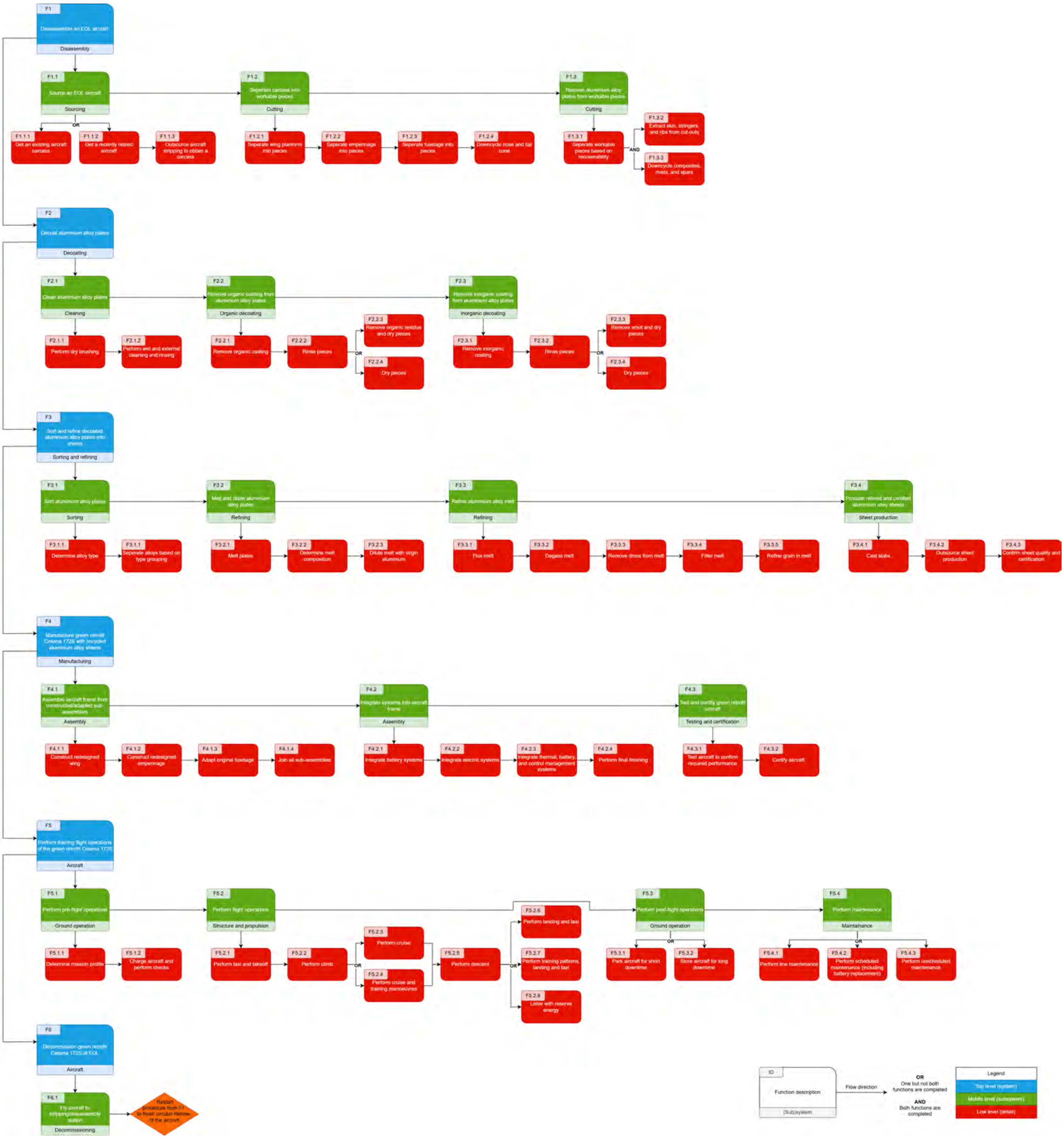

Figure 3.5: Functional flow diagram

4

Disassembly

After the aircraft carcass has been acquired, which was discussed in Chapter 3, it needs to be processed into smaller pieces, which can be processed. First, the aircraft will be rough cut with the help of a wire saw. The technique used for the rough cutting is described in Section 4.1, and lastly, the detailed design of the saw is done in Section 4.2. The rough cut does not have accuracy as its primary objective; it is intended to break the structure into smaller sections that can be easily and safely handled around the facility. This process will take place outdoors to accommodate the large structure. Next, the aircraft is cut into small plates as a final product. This secondary cutting is done with the help of a laser, as can be seen in Section 4.4. The cuts will be made to remove rivets with the help of computer vision. This process is done in an enclosed room to capture all chromium fumes which might be released during the process. The entire disassembly process can be seen in Figure 4.1. The starting point is taken as a completely stripped aircraft carcass.

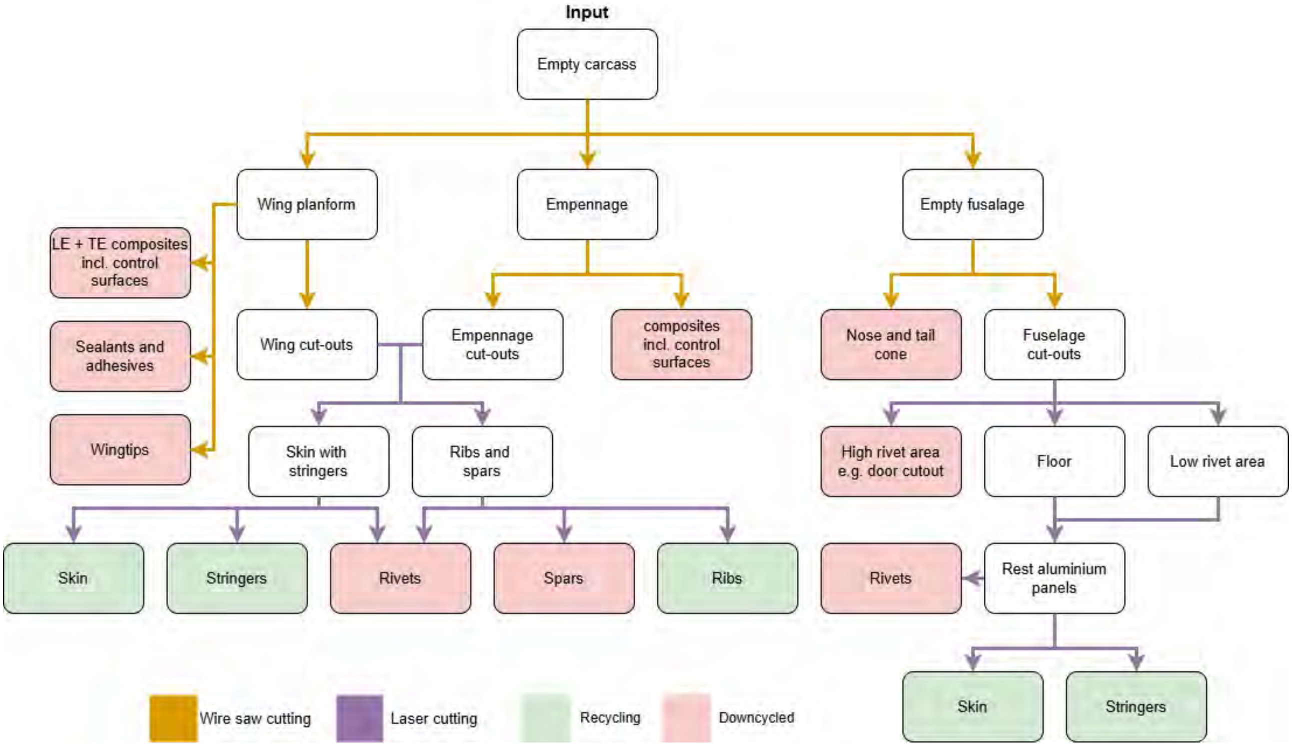

Figure 4.1: The flow of the disassembly

A conceptual sketch of the full facility is shown in Figure 4.2, which showcases the various elements and buildings that a recycling plant needs and an order of magnitude of its dimensions. The facility would have to be located next to an airstrip (shown at the top of the sketch) in order to receive end-of-life aircraft, and should be able to host a few carcasses awaiting dismantling to account for uneven retirement rates throughout the year and absorb periods of more frequent retirements. The open-air wire sawing area is also located sufficiently far from the runway to avoid potential flying debris posing a severe risk of ingestion by the engines of incoming aircraft.

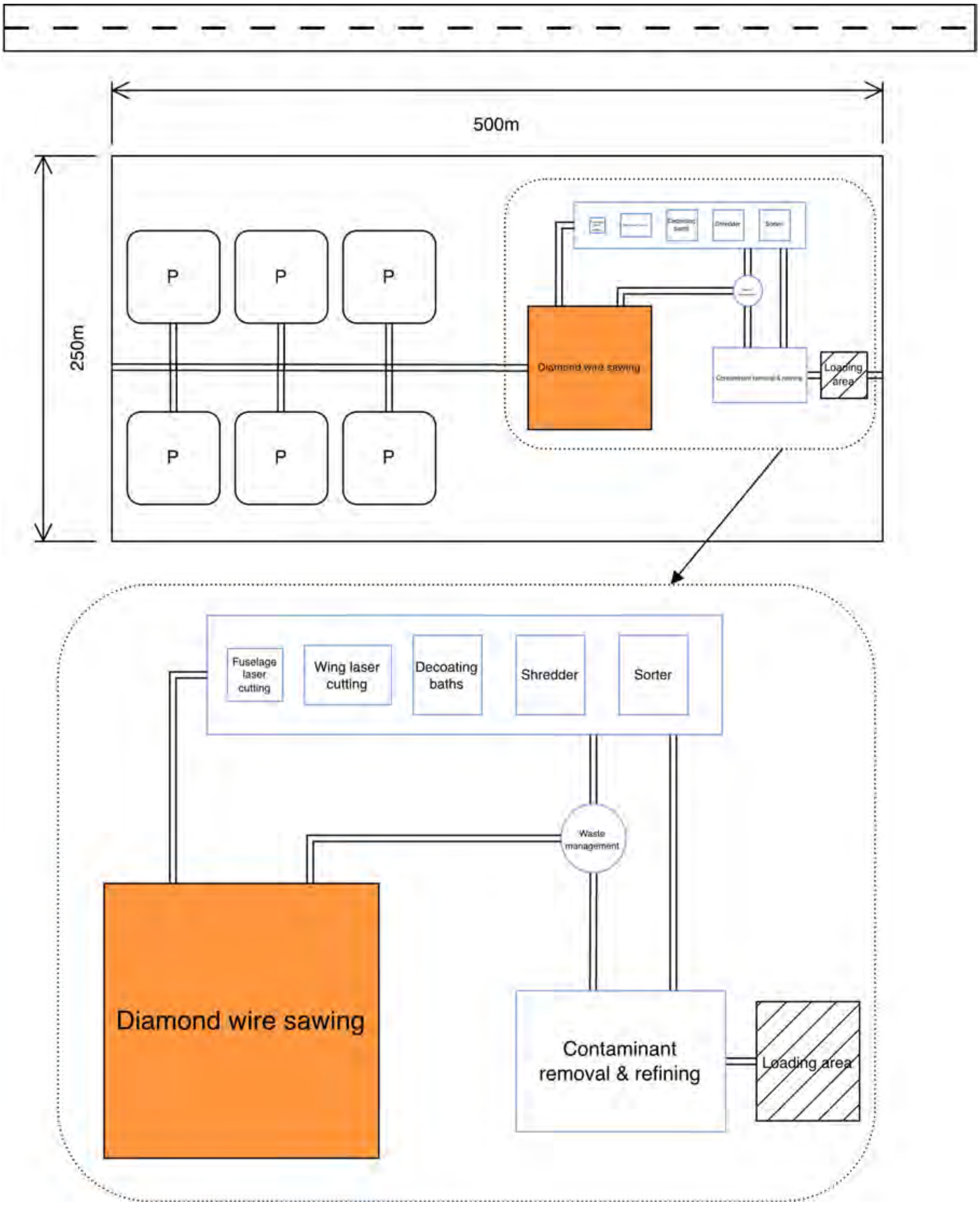

Figure 4.2: Facility sketch. In orange, the outdoors working areas, outlined in blue, the indoors working areas. "P" denotes a parking space for aircraft waiting to be dismantled. At the top of the sketch, a runway for inbound retiring aircraft.

The upfront expenditure for such a facility is estimated to be €12,000,000, and its annual operating costs are set at 5% of the initial investment, i.e., €600,000. The orange area on Figure 4.2 must be vacated when the wire saw is running, and if any operators approach the cutting zone soon after the saw has been stopped, they must wear appropriate PPE to avoid inhaling any produced dust.

4.1. Rough Cutting Technique

Diamond wire sawing is selected as the bulk sectioning technique. The technique works by drawing a continuous loop of diamond-coated wire across the workpiece and has been demonstrated on aluminium alloy structures [8]. Furthermore, in November 2014, AELS and Husqvarna demonstrated that slicing through an airliner's wings and fuselage using a diamond wire is not only possible but also relatively fast and cost-effective[1]. For this demonstration,

---

[1] URL `https://www.youtube.com/watch?v=rag4nSoMlNQ` [cited 4 June 2026]

the tools used were Husqvarna's CS2512 wire saw equipped with a C1000 diamond wire and the hydraulic power pack PP455E, all shown in Figure 4.3 and the company's global applications manager Patrick Meeremans said that "with this setup only two people are needed to get the job done"[2]. Therefore, as this is the only publicly demonstrated and sufficiently well-documented use of diamond wire sawing to dismantle an aircraft, these machines and the number of operators are used in this report for reference numbers in sizing the process.

(a) CS2512 diamond wire saw **(b)** C1000 diamond wire **(c)** PP455E hydraulic pack

Figure 4.3: Husqvarna tools used as references

Capital and consumable costs are low, with machinery costing roughly €150,000 and wire replacement needed only roughly every 100 hours for use on soft metals like aluminium. Although cutting is performed by diamond grit, the wire substrate is steel, and progressive wear deposits iron debris directly onto the cut face. This Fe contamination risk is critical for 2xxx and 7xxx alloy remelting and will require subsequent steps to cut away the kerf edges for downcycling to avoid melt contamination.

Other options were also considered for this purpose, namely abrasive waterjet cutting (AWJ), fibre laser cutting, and reciprocating nibbling, but were discarded. Waterjet cutting was rejected mainly on the grounds of the complex infrastructure required to process water that would be significantly contaminated with Cr(VI), as it is highly soluble in water. Laser cutting was discarded because the high temperatures would cause the coatings to vaporise over a large portion of the skin around the cut [9], as aluminium is a good heat conductor. These toxic vapours would have been released into the air with no possibility to reliably capture them, infringing the strict Cr(VI) regulations in place. Finally, nibbling was mainly discarded due to its insufficient speed and the complexity of the cutting process. It must be noted that if lubricant or coolant is used for the diamond wire cutting, then liquid contamination could still be an issue. This is addressed in subsection 4.2.2

4.1.1. Disassembly Sequence and Cut Plan

The aircraft arrives already stripped of its interior, wiring, insulation and windows, and depolluted, with the fluids drained and the hazardous and valuable components taken off before any structural cutting starts.

Cutting is done in two stages that use different tools. The diamond wire saw in Figure 4.3a does the coarse work only. It breaks the airframe into a small number of large pieces that can be lifted and trucked away. The fine work, which is separating each piece into clean single-alloy parts, is done afterwards by a laser shown in Figure 4.14 and covered later in Section 4.4.

Splitting the job this way suits each tool. The wire does not care what it runs through, and the cut line does not have to be cleared of any one material first. It is, however, not very accurate, so it is only used for the few long cuts that actually break the structure apart. The many fine cuts needed to sort the materials are left to the laser, where accuracy and access matter.

The cut is run dry, with no coolant. A dry cut makes no slurry, so there is no contaminated liquid to collect and dispose of, and the work can be done outdoors in the open air. However, the downside is the dust produced by the cutting process. A dry cut throws off fine dust that carries the coating metals, such as Cr(VI) and some aluminium and titanium particles, so it needs breathing protection for the operators if they approach the cutting area while the saws are active. The open-air setting helps to keep the dust concentration down, and most particles settle to the ground in a few minutes.

The wings and tail come off before the fuselage is cut up. Taking them off frees up access to then longitudinally cut the fuselage. How many cuts are made in each area comes down to one number: the longest section $L_{\max}$ that can still be handled and transported. This is set by what is deemed practical for transport around the facility and the working envelope of the laser cell. Each area is then split into as few sections as possible while keeping every piece under that length, with the cuts spaced evenly. Fewer cuts also mean less metal lost to the saw kerf. The full plan is shown in Figure 4.4.

---

[2] URL `https://pdworld.com/articles/view/how-to-cut-an-airplane/1000` [cited 4 June 2026]

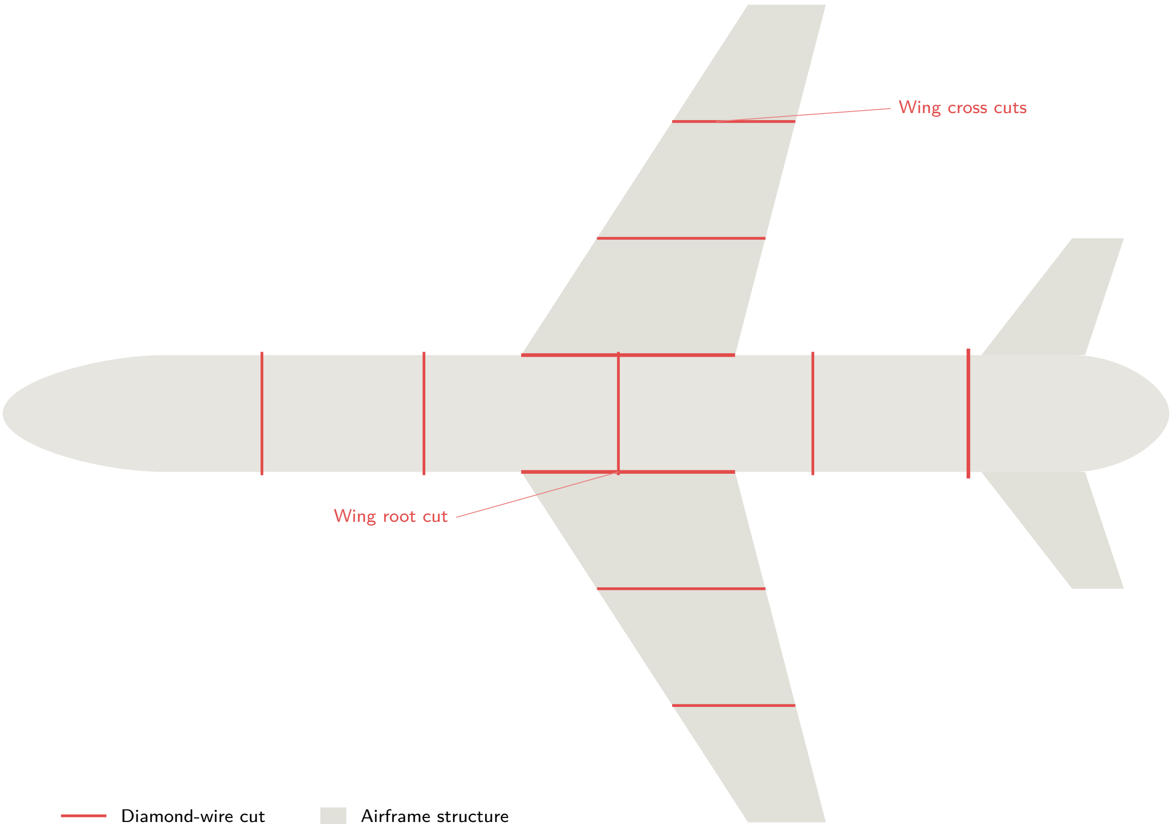

Figure 4.4: Overall coarse cut plan. The diamond wire makes a small number of long cuts that break the airframe into large, transportable pieces. Not to scale.

4.1.2. Wings and Empennage

The tail is removed first, with a single cut straight across the rear fuselage at the tailcone. This takes off the whole tail, both stabilisers and the tailcone, as one piece, which is then cut down further away from the main line in the same way as the wings.

Each wing is then cut into shorter sections, starting at the tip, by a row of cuts across the wing, spaced to keep every section under $L_{\max}$, with one last cut at the wing root. Figure 4.6 provides a visualisation for this. Nothing inside the wing is taken apart at this point; the spars, ribs, skins and the composite leading and trailing edges all stay together inside each section and are separated by the laser. The wing box is mostly aluminium, but the leading and trailing edges often contain composites as can be seen in Figure 4.5a, and how much varies from one aircraft to another. The upper and lower skins can also be a different alloy from the structure underneath, and in the end all of these have to go to different melt streams. Sorting those boundaries out cleanly is finer work that suits the laser better, so the wire just keeps them whole inside sections that are easy to move.

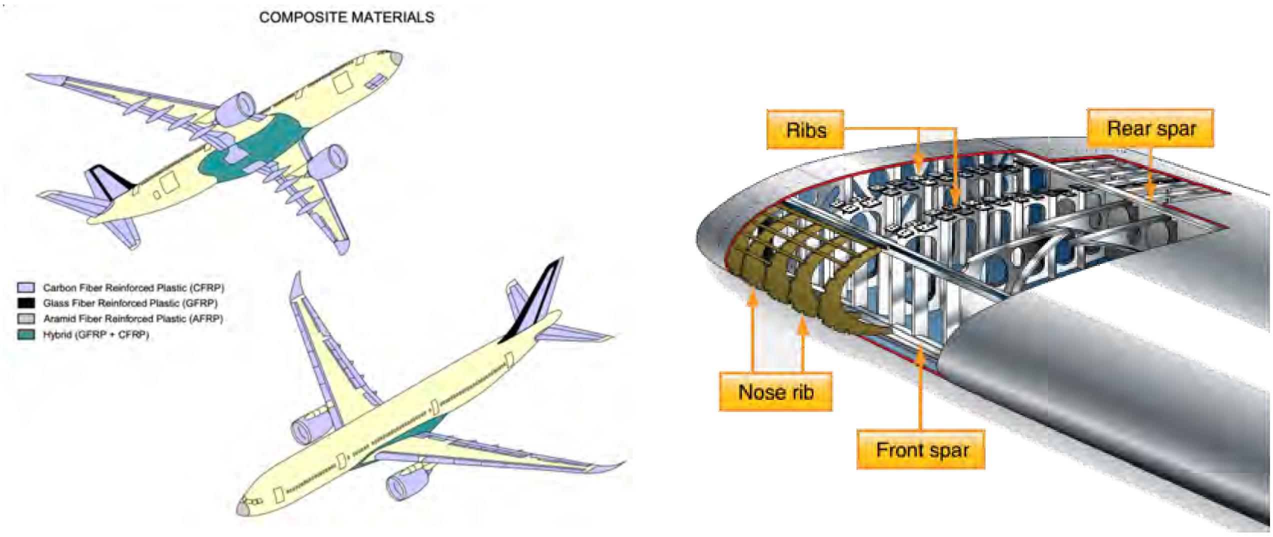

(a) Composites Map A330 (Figure 10-0-0-991-005-A01 of the A330 Airport Planning Manual [10]). Coloured purple CFRP, black GFRP, grey AFRP, green hybrid GFRP + CFRP and yellow metallic parts.

(b) Wing internal structure sketch (FAA) showing an aluminium skin and wing box with composite leading edge structures.

Figure 4.5: Aircraft wing structures and materials.

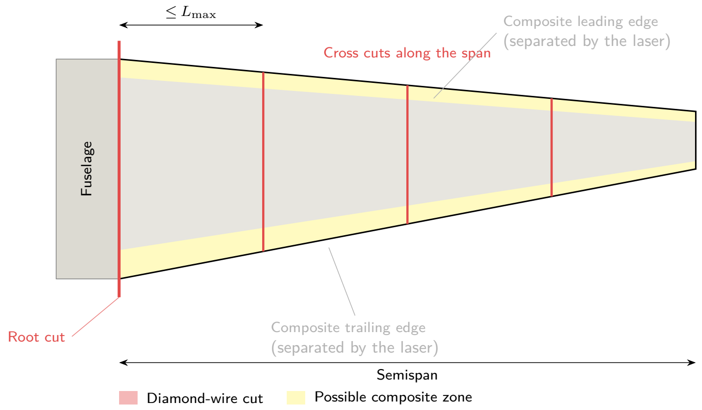

Figure 4.6: Wing cutting scheme. Not to scale.

4.1.3. Fuselage

The part of the fuselage that gets cut up is bounded by two cuts, a cut behind the nose section and the tailcone cut that was already made to remove the empennage. Between these two, the fuselage is cut straight across at intervals, as seen in Figure 4.7. Each piece is a cylinder of length $L_{\max}$, and the number of slices follows from the length of the fuselage.

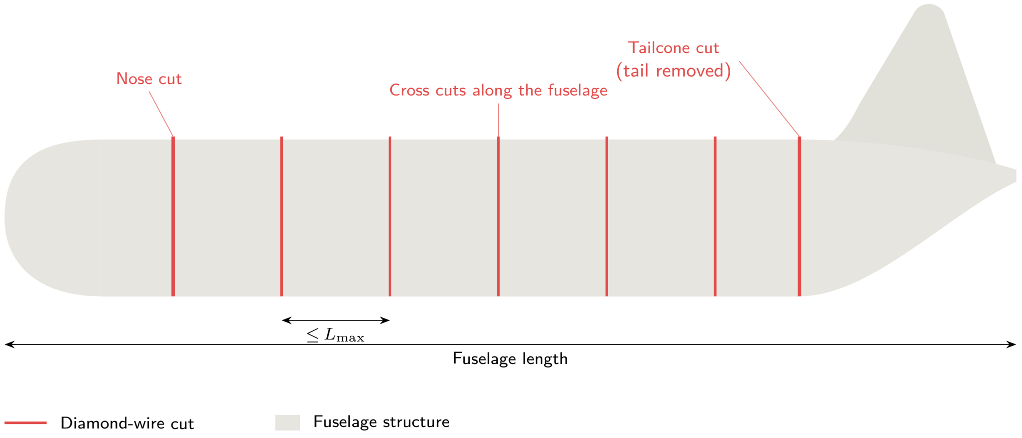

Figure 4.7: Fuselage cutting scheme. Not to scale.

4.2. Design and Sizing

The sectioning step is sized with a parametric model that takes the aircraft's key dimensions and the saw/wire specification and returns the cut time, the number of saws required, and the per-aircraft cost and emissions.

4.2.1. Throughput and Cutting Mechanics

For a wire saw, the limiting quantity is the *cut-face area*, which is the cross-section of solid metal the wire saws through, not the path length. The disassembly makes one tailcone cut, a set of transverse fuselage slices (nose cut to tailcone, each section $\leq \ell^f_{\max}$), and per wing a root cut plus spanwise slices (each $\leq \ell^w_{\max}$) up to the last rib. The areas are

$$A_{\text{fus-tail}} = \pi D t_s f_{\text{str}},$$

$$A_{\text{wing}}(c) = \left[2 c t_{\text{skin}} + n_{\text{sp}} h_{\text{box}} t_{\text{sp}}\right] f^w_{\text{str}}, \qquad h_{\text{box}} = \left(\frac{t}{c}\right) c,$$

where f_{str} is a structure factor lumping frames, stringers and floor beams into the thin-shell ring (f^w_{str} does the same for wing stringers/spar caps), t_{skin} is the skin thickness, n_{sp} is the number of spars (often equal to 2) and t_{sp} their thickness, h_{box} is the height of the wingbox calculated using t/c the thickness-to-chord ratio of the wing, and the wing chord c tapers linearly from root to tip. The total area is $A_{\text{tot}} = A_{\text{fus-tail}} + \sum A_{\text{wing}}(i)$, where the variable i takes the value of the chord length at all cut locations along the wing.

The saw is assumed to auto-feed the wire to its power ceiling, so the material removal rate is limited by available power rather than wire speed ($P = F_t v$, so v cancels). With a specific material cutting energy u_s and kerf width k, the volumetric and areal removal rates are

$$\dot{V} = \frac{P_d \eta_u}{u_s}, \qquad \dot{A} = \frac{\dot{V}}{k},$$

where P_d is the mechanical power at the wire and η_u is the fraction actually delivered to the cut. The cut time per aircraft is then

$$t_c = \frac{A_{\text{tot}}}{\dot{A}}.$$

Each saw can only cut for a limited amount of time each year, and a cap is set at $H_{max} = 2{,}000$ hours per year (8h per day, 250 working days per year). For a throughput N_{ac} the annual demand is $H_d = N_{\text{ac}} t_c$, giving

$$N_{\text{saw}} = \left\lceil \frac{H_d}{H_{max}} \right\rceil$$

as the required number of saws.

4.2.2. Thermal Analysis

Diamond wire cutting can be performed both dry and wet, that is, with or without a cooling liquid. If coolant use can be avoided, operations are greatly simplified, eliminating the need for infrastructure to channel spent coolant. Cost would also benefit from a dry cut, eliminating the expense of this coolant. However, while aluminium melts around 600-650°C, it tends to soften and become "gummy" around only 200°C. This behaviour must be avoided as it causes the metal to stick to the wire, severely hindering cutting performance. To prevent this, a thermal analysis of the cutting process is performed, ensuring the aluminium stays below the 200°C threshold during the sawing.

In abrasive cutting, essentially all the mechanical work is converted to heat [11, 12], so the total heat generated equals the cutting power, which by definition of the specific cutting energy u_s is

$$Q = u_s \cdot \text{MRR} = P_d \eta_u,$$

The cutting heat is shared between the two bodies in sliding contact in proportion to their thermal *effusivity* $e = \sqrt{k \rho c}$, which measures how readily a body absorbs heat at a contact [13, 14]:

$$f_{wp} = \frac{e_{Al}}{e_{Al} + e_{\text{tool}}}, \qquad f_{\text{tool}} = 1 - f_{wp}.$$

Here, f_{wp} and f_{tool} are the fractions of total heat energy picked up by the workpiece and cutting wire, respectively. The body sharing the contact is the abrasive that does the cutting, so e_{tool} is taken for the diamond grit.

Diamond's very high conductivity gives it a large effusivity of $e_{\text{grit}} =\approx 59{,}900\ \mathrm{Ws^{1/2}/m^2K}$ [15], so it carries the majority of the contact heat away from the aluminium, whose effusivity is only $e_{Al} \approx 19{,}400\ \mathrm{Ws^{1/2}/(m^2K)}$ [16]. This results in only

$$f_{wp} = \frac{19,373}{19,373+59,920} \approx 0.24 = 24\%$$

of the heat entering the aluminium, which is consistent with the grinding result obtained by Rowe that high-conductivity grains keep the workpiece cool [14], and with dry diamond-wire sectioning working in practice as demonstrated by AELS.

The peak surface temperature at the contact point follows Jaeger's moving heat-source solution for a semi-infinite solid [13, 17]. The Péclet number, which measures the ratio of advective heat transport to diffusive transport, is defined as

$$\mathrm{Pe} = \frac{v l_c}{2\alpha} \qquad \text{with } \alpha = \frac{k}{\rho c},$$

and is $\gg 5$ due to the large wire speed v. Here, α is the thermal diffusivity, k the thermal conductivity, ρ the density, c the specific heat, and l_c the length of the cut in the direction of movement of the heat source (thus equal to the skin thickness here). Therefore, the peak (flash) temperature is given by Jaeger's high-speed sliding temperature equation:

$$\Delta T_{\text{flash}} = \frac{2}{\sqrt{\pi}}\frac{q}{k}\sqrt{\frac{\alpha l_c}{v}}, \qquad q = \frac{f_{wp}Q}{\mathrm{k_w} \cdot l_c}. \tag{4.1}$$

Since the heat is power-limited, q is independent of the wire speed and $\Delta T_{\text{flash}} \propto \frac{1}{\sqrt{v}}$: a *faster* wire gives a *cooler* peak temperature at the contact, because each point is heated for less time. Here, q is the heat flux into the aluminium at the contact surface, with k_w the kerf width (which equals the diamond bead diameter in this case).

The wire circulates and sheds its share of the heat over the whole loop by convection and radiation. The loop period (≈ 0.8s) is far shorter than the cut, so a steady-state balance can be used:

$$f_{wire}Q + Q_{\text{bow}} = hA(T_w - T_\infty) + \sigma\varepsilon A(T_w^4 - T_\infty^4)\text{with} \qquad A = \pi d L.$$

It is also of interest to map how far the heat reaches around the cut and how skin temperature evolves over time, mainly to monitor the areas potentially sensitive to coating decomposition and to ensure safe handling. To achieve this, the in-plane temperature field of the skin of thickness t is solved as a thin plate losing heat from both faces, with a Gaussian source advancing along the cut at the feed speed $v_f = \mathrm{MRR}/(k_w \cdot t)$, the classical moving heat-source problem as solved by Rosenthal [18]:

$$\frac{\partial T}{\partial t} = \alpha \nabla^2 T + \frac{q_{\text{src}}}{\rho c t} - \frac{2h(T - T_\infty)}{\rho c t}. \tag{4.2}$$

It is integrated with an explicit finite-difference scheme (stable for $\Delta t < \Delta x^2/4\alpha$) and the source magnitude is calibrated so the peak equals the flash temperature of Equation 4.1, so the simulation supplies the spatial field while the analytical model supplies the peak.

4.2.3. Cost and Emissions

The per-aircraft cost aggregates four contributions: energy, wire, labour and machine amortisation. Each is written as a rate multiplied by the quantity that drives it, and all are referred to a single aircraft so they can be summed and scaled to annual figures through the throughput N_{ac}.

Energy

While cutting, the hydraulic pack draws power continuously from the grid. The electrical draw is the wire power P_d divided by the electric–hydraulic efficiency η_{dr}, so the energy cost is the draw multiplied by the cut time and the electricity price c_{el}:

$$C_{\text{energy}} = \frac{P_d}{\eta_{\text{dr}}}\, t_c\, c_{\text{el}}.$$

Wire

The diamond wire is treated as a consumable with a working life τ_w (cutting hours per wire), after which the full loop of length L_w is replaced. Each aircraft therefore consumes the fraction t_c/τ_w of a wire, or $(t_c/\tau_w)L_w$ metres, charged at the wire price c_w per metre. The cost associated with the wire is thus:

$$C_{\text{wire}} = \frac{t_c}{\tau_w} L_w c_w.$$

Labour

Labour is modelled as a *fixed crew* rather than a per-cut cost: a team of $n_{\mathsf{op}=2}$ operators is paid for $h_d = 10$ hours per day over 250 working days per year at an hourly rate r_{op} (h_d is set to larger than the saw running hours per day to account for set-up, rigging and handling overheads). This annual labour bill is divided over the throughput and is *not* scaled by the number of saws, as the same crew can oversee multiple ones:

$$C_{\mathsf{labour}} = \frac{n_{\mathsf{op}} h_d d_y r_{\mathsf{op}}}{N_{\mathsf{ac}}}.$$

Machine

The saws are assumed to be dedicated to the dismantling line (no other uses), so each unit of capital K is depreciated over the number of aircraft it processes during its service life Y. Since they are industrial equipment, the saws are depreciated over a standard $Y = 7$ years [19]. With N_{saw} saws required to meet capacity, the amortised capital per aircraft is

$$C_{\mathsf{machine}} = \frac{N_{\mathsf{saw}} K}{Y N_{\mathsf{ac}}}.$$

Totals

The per-aircraft and annual costs are then

$$C_{\mathsf{ac}} = C_{\mathsf{energy}} + C_{\mathsf{wire}} + C_{\mathsf{labour}} + C_{\mathsf{machine}}, \qquad C_{\mathsf{yr}} = N_{\mathsf{ac}} C_{\mathsf{ac}}.$$

Emissions

Operational $\mathrm{CO_2}$ emissions follow the same grid draw as the energy cost, with the electricity tariff replaced by the grid carbon intensity $\varepsilon_{\mathsf{grid}}$ to give the mass of $\mathrm{CO_2}$ emitted both in total terms and per year:

$$m_{\mathrm{CO_2}} = \frac{P_d}{\eta_{\mathsf{dr}}}\, t_c\, \varepsilon_{\mathsf{grid}}, \qquad m^{\mathsf{yr}}_{\mathrm{CO_2}} = N_{\mathsf{ac}} m_{\mathrm{CO_2}}.$$

The model carries two efficiencies that act at different stages and must not be confounded. The cutting utilisation η_u governs the removal rate given by subsection 4.2.1: it is the fraction of the wire power that does useful cutting, the rest being lost to wire bow and friction. The electric-hydraulic efficiency η_{dr} governs the *grid draw* P_d/η_{dr} used for energy and emissions: it accounts for the electric-motor and hydraulic-pump losses of the power pack. The overall grid-to-cut efficiency is then the product $\eta_u \eta_{\mathsf{dr}}$.

4.2.4. Cutting Rig

The diamond wire is carried on a mobile portal frame that straddles the workpiece shown in Figure 4.8. The wire runs as a horizontal loop between two pulleys at the top of the two columns, with a height control translating the pulleys vertically to draw the wire down through the section, while a width control sets the column spacing. The width adjustment lets one rig serve aircraft of different sizes and cut the wings as well as the fuselage, rather than being fixed to a single geometry. This will also introduce the need for a tensioning system, allowing the wire length to be adjusted as needed. The frame also stands on omnidirectional wheels, which both move and rotate it freely around the facility for repositioning between cuts and provide the lateral travel that drives the width control.

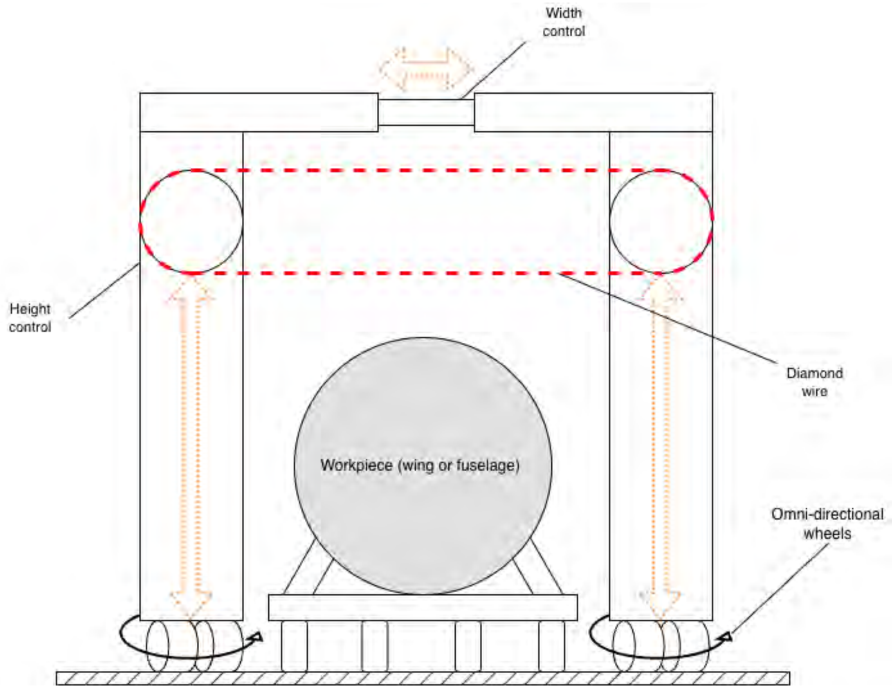

Figure 4.8: Diamond wire saw rig sketch

However, the tangential cutting (friction) force the wire exerts as it abrades the section could pose a tipping risk for the rig. This force and its impact must therefore be quantified, at least as a high-level estimate, to evaluate the severity of this risk and mitigate it. From the cutting power, the force is approximately:

$$F_{\text{cut}} = \frac{P_{\text{drive}}}{v_{\text{wire}}} = \frac{20\text{kW}}{20\text{m/s}} \approx 1\text{kN}.$$

, The feed force is vertical (reacted by the workpiece) and the wire tension acts inward on both columns, so neither contributes to tipping. The wheels are assumed to have brakes applied, and that these are able to resist the forces at play without allowing the wheels to spin. Treating the broken rig as a rigid body, the Free Body Diagram (FDB) of Figure 4.9 can be drawn, and the sum of moments about the pinned support is (counter-clockwise direction is positive)

$$\sum M = W \cdot b - W \cdot b/2 - F_{\text{cut}} h_{\text{cut}} = 0, \tag{4.3}$$

with W the rig weight, b the wheel base and h_{cut} the cut height.

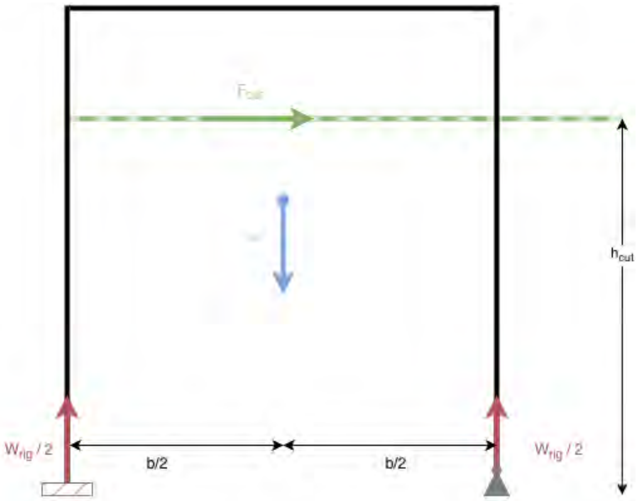

Figure 4.9: Diamond wire saw Free Body Diagram

To size for the worst-case scenario, the wire is assumed to be at its highest position; therefore $b \approx h_{cut}$ for circular fuselages.

Equation 4.3 simplifies to $W\,b/2 = F_{\text{cut}} h_{\text{cut}}$, and solving for the weight of the frame gives that it must weigh at least

$$W = \frac{2\,F_{\text{cut}}\,h_{\text{cut}}}{b} = 2\cdot 1\text{kN} = 2\text{kN},$$

i.e. a mass of only $m = W/g \approx 0.2\text{t}$. This is the weight at the verge of tipping; including a safety factor of two against overturning raises the requirement to 0.4 tonnes. Both values are roughly an order of magnitude smaller than the mass of any such steel portal frame, so the cutting force cannot realistically overturn the rig.

4.2.5. A310 Example

Applying the model to the A310 (Husqvarna C1000 wire[3] on a CS 2512 saw[4], $P_d = 20$ kW, $\eta_u = \eta_{\text{dr}} = 0.60$, $u_s = 17.38$ J/mm^3, $k = 10.3$ mm, at $N_{\text{ac}} = 77\text{a}^{-1}$) gives the results in Table 4.1. The cut is relatively slow (0.24 m^2/h), so each aircraft needs about 10.7 h of cutting and the line requires three dedicated saws. The cost is dominated by labour, making the operator crew the input that controls the result, accounting for 81% of the total cost-per-aircraft.

Table 4.1: Diamond-wire sectioning of an A310 (base case)

Quantity	**Value**
Cut-face area (wing / fuselage / tail)	2.29 / 0.27 / 0.02 m^2
Total cut area	2.57 m^2
Number of cuts	23
Areal cutting rate $\dot{A}$	0.24 m^2/h
Cut time t_c	10.7 h/aircraft
Saws required (41% utilised)	1
Energy / wire / labour / machine	€71 / 171 / 2,272 / 278
Cost per aircraft	€2,793
Annual cost (77 aircraft)	€215,070
CO_2	9.6 kg/aircraft, 0.74 t/yr

The dry cut generates $Q = u_s \mathrm{MRR} = 12$ kW. With the contact length equal to the member thickness ($l_c = t$) and the effusivity partition of $f_{wp} = 0.24$ as computed in subsection 4.2.2, the contact (flash) and wire temperatures are given in Table 4.2 and Figure 4.10.

Table 4.2: Dry-cut temperatures (A310 / C1000, $v = 20$m/s).

Member (l_c)	T_{contact}	**vs. 200°C**
Fuselage skin (1.8 mm)	107°C	safe
Spar web (8 mm)	62°C	safe
Wing skin (10 mm)	58°C	safe
Wire bulk	91°C	safe

The contact surface reaches only 107°C on the thinnest member to be cut, well below the 200°C softening onset, and the wire sits at 91°C. Therefore, no additional cooling is required to prevent gumming behaviour, and the dry cut can be performed.

Both trends in Figure 4.10 stem from the same cause: because the cut is power-limited, the heat Q, the contact length l_c and hence the heat flux are fixed, so the contact temperature is governed only by how concentrated the heat is (in space) and how long each point is exposed to it (in time), as described by the equations in subsection 4.2.2. A faster wire spreads the fixed heat over more grit passes, shortening the time each surface point dwells under the moving contact, so it runs cooler, with $T_{\text{contact}} \propto v^{-1/2}$. The CS2512 saw offers two gears, allowing for some control over the maximum speed of the wire. Raising the wire from gear 1 (max. 20m/s) to gear 2 (max. 25m/s) lowers the skin contact from 107 to 96°C as shown in Figure 4.10a at no throughput cost; only the mechanical penalties (thin-chip loading, wire wear) limit the speed. Conversely, since $l_c = t$, a thinner member concentrates the same heat onto a smaller contact patch and so runs hotter, with $T_{\text{contact}} \propto l_c^{-1/2}$. The fuselage skin is therefore the design case (Figure 4.10b), while the thicker spars and wing skins spread the heat and stay well below the limit. The worst case (the thinnest member cut at the lowest speed) still reaches only 107°C, leaving a comfortable margin to the softening onset.

---

[3] URL `https://www.husqvarnaconstruction.com/us/diamond-tools/diamond-wires/elite-wire-c1000/` [cited 15 June 2026]

[4] URL `https://www.husqvarnaconstruction.com/us/wire-saws/cs2512/` [cited 15 June 2026]

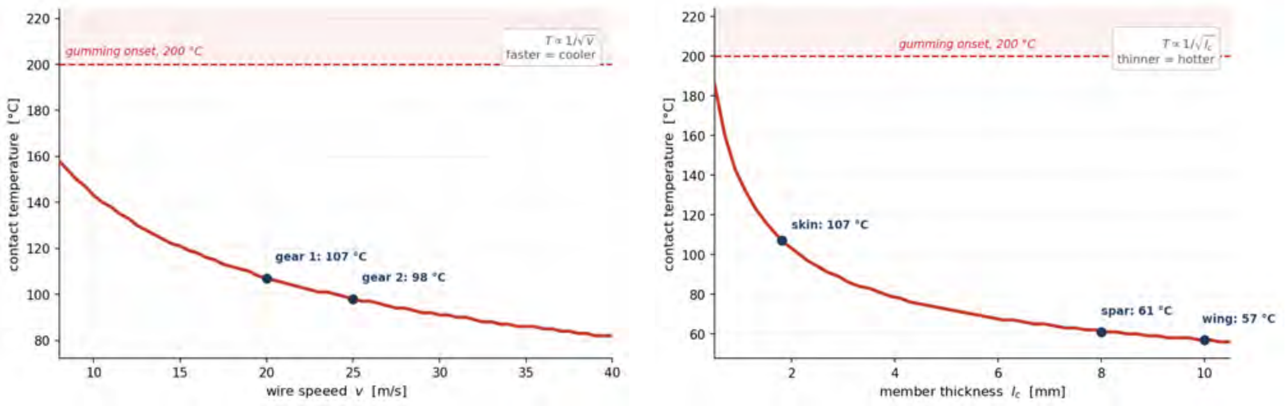

(a) Versus wire speed

(b) Versus member thickness

Figure 4.10: Dry-cut contact temperature

The transient 2-D conduction solution shown in Figure 4.11 sees the heat travelling with the cut as a short comet-shaped zone with a cooling wake, obtained by numerically solving Equation 4.2 with respect to time. The region above $100^\circ\mathrm{C}$ is only a few millimetres across and the warm halo $(> T_\infty + 10^\circ\mathrm{C})$ extends $\sim 1\mathrm{cm}$ either side of the kerf. The heat thus remains local and moderate, posing no risk of excessive vaporisation of the coatings, which only start degrading at higher temperatures, around 500°C [9].

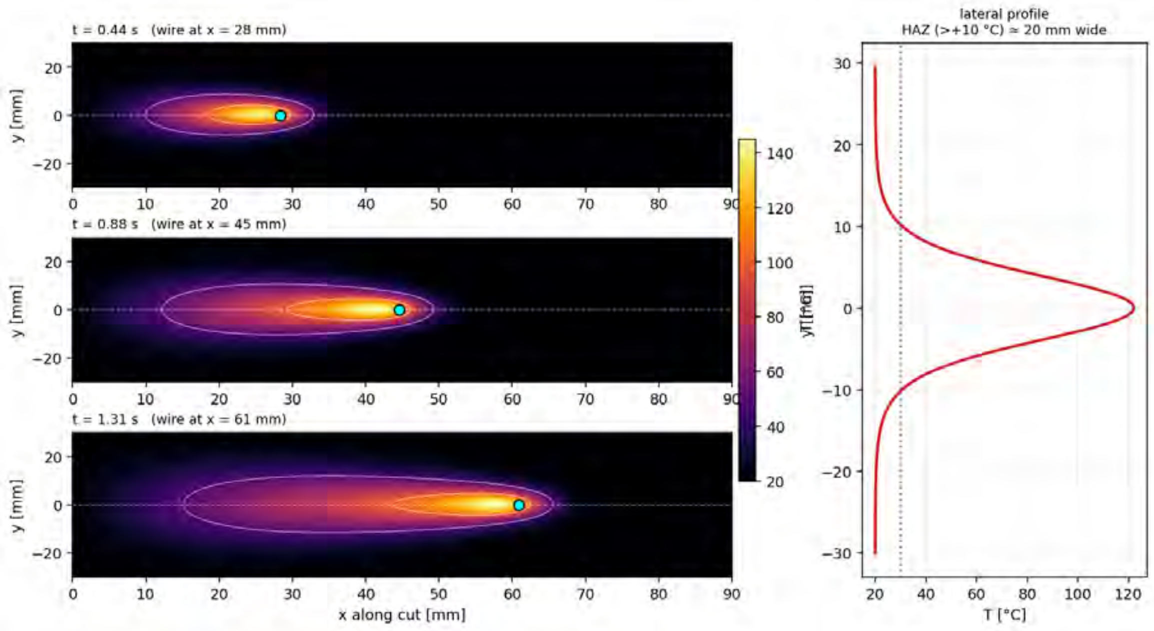

Figure 4.11: Transient heat field around the moving cut

4.3. Supporting Infrastructure

The diamond-wire sawing also requires some surrounding infrastructure to support the cutting process.

Cutting Bay and Loading

The cutting is done outdoors on a level, reinforced hardstanding. The surface carries the weight of the supports, the saw rig, and the loaded transporters, and is drained for rain. When an aircraft arrives, it is lifted off its landing gear with hydraulic jacks and set down onto the supports before cutting starts.

Workpiece Support

During cutting, the airframe sits on a set of shaped supports to prevent it from yielding under its own weight. One support goes under each fuselage section, with gaps left for the wire to pass through. The supports press on the internal frames rather than the thin skin, so the skin is not crushed. Each one carries only a few tonnes, except the one under the wing box, which is heavier while the wings are still attached and is sized for that load. A section stays on its support until its cut is finished, so it cannot fall. The wings rest on their own supports to avoid excessive flexure during cutting.

Autonomous Transport

Once a piece is cut free, it is moved by an electric autonomous transporter: a heavy automated guided vehicle (AGV) that lifts the support and carries it, such as the one shown in Figure 4.12. The piece stays on the same supporting structure from the cut to the next station, so no crane or re-gripping is needed. The transporters are sized for the heaviest load, from a few tonnes for a single section up to tens of tonnes for a whole fuselage or wing. They drive themselves between the cutting area and the laser cutters, and because they need no driver, operators are able to stay away from danger zones.

Figure 4.12: Electric heavy-duty AGV (Voitto Crane)

4.4. Secondary Cutting

After the preliminary cutting, the aircraft pieces are cut into more detail. Here, the objective is to extract recyclable plates and separate the stringers, ribs and spars. This is done by a laser cutter

4.4.1. Placement

Before being able to cut the large cut-outs into smaller pieces, first the fuselage part needs to be placed correctly so that it is possible to cut it down into smaller pieces. For this, it was chosen to rotate the fuselage 90° in order to put it onto the circular side, which would improve the ability to accurately cut. An important consideration here is the self-weight buckling; if the mass of the part is too large, it might collapse under its own weight. To find if this is the case, the critical buckling stress formula is used:

$$\sigma_{cr} = \frac{E}{\sqrt{3(1-\nu^2)}}(\frac{t}{R}) \tag{4.4}$$

Here, E is the Young's modulus, which is taken to be 70 GPa for aluminium [20], and ν is the Poisson's ratio, which is taken to be 0.33 for aluminium [21]. The radius R and thickness t for a cut-out piece of fuselage are 2.82 m and 0.002 m, respectively. With this, the critical buckling stress can be calculated to be:

$$\sigma_{cr} = \frac{70,000,000,000}{\sqrt{3(1-0.33^2)}}(\frac{0.002}{2.82}) = 29.32\,\text{MPa}$$

The next step to understand whether the structure might buckle is to determine the stress it experiences. The total mass of a single cut-out piece was estimated to be 853 kg. So the total force experienced by the cut-out is $853 \cdot 9.81 = 8,210.97$ N. Lastly, to find the stress, the total area on which the cut-out stands needs to be found. The total area can be found by $2\pi\text{Rt} + \text{A}_{\text{stringers}}$; the total area of the stringers is equal to that of the skin, making the formula for the area: $2\pi\text{Rt} \cdot 2$. Giving a total area of $2\pi \cdot 2.82 \cdot 0.002 \cdot 2 \approx 0.071$ m^2. With this, the total stress on the cut-out can be calculated as:

$$\sigma = \frac{F}{A} = \frac{8,210.97}{0.071} \approx 0.12\,\text{MPa}$$

where F is the force applied on the cut-out, and A is the total area on which that force is applied. As the calculated stress on the cut-out is much lower than the critical buckling stress, it will not buckle under its own load. Meaning it is possible to place the cut-out onto the cut edge. After knowing that it is possible to let the cut-out stand independently without failing, the method for rotating the cut-out needs to be determined. The method chosen is the use of an upender. This is an industrial machine normally used for the rotation of steel coils. But it can be

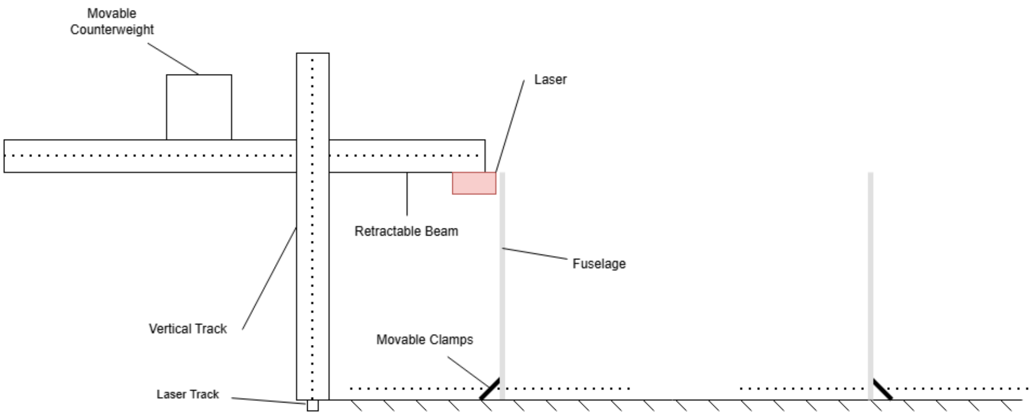

Figure 4.13: Side view of the fuselage cutting station

adapted to rotate different types of materials, e.g. aircraft cut-outs. A typical upender costs around €25,000[5] when bought second-hand and with a typical rotating capacity of 2,000 lb. These machines will take around 40 seconds to complete a cycle while at the same time consuming 3 kW.

4.4.2. Computer vision

In order to cut correctly, the laser cutter needs to correctly identify where to cut. Rivet identification is a lot more difficult than bolt identification, mainly due to most rivets having a button head. This has weaker and fewer exterior features than bolts have, making it difficult for algorithm identifications [22]. Because of this difficulty, a computer vision system needs to be used. More specifically, a YOLO-V5 and MobileNet V3 Large model based on the research done by O. Amosov et al [23], which analyses pictures taken by a high-definition camera. An important assumption that is made to use this method is that every rivet is visible to the surface. This assumption needs to be made, as the camera needs to see the rivet for the model to correctly identify it. This assumption is made reasonably as all rivets that need to be removed are used to connect the aircraft skin to reinforcement structures. Therefore, all rivet heads are shown on the outside of the skin and can be identified by a camera. While using this method, an accuracy rate of 98% is achieved [23]. For the accuracy, there is an important note. In the study done by Amosov et al [23], a training, testing and validation set of 375 images are used, where some of these images are deliberately made vague and blurry to better train and test the model. In the case of the cutting of the aircraft, here there are generally only straight lines of rivets placed in a repetitive manner, thus it might be possible to achieve an even higher accuracy rate.

4.4.3. Laser Cutter

Two laser cutters are needed for the secondary cutting. The first is used for the fuselage, with a thickness of around 2 mm, and the second for the wing skin, with a thickness of up to 20 mm. This means the first laser can be a relatively low-power laser of around 4 kW. The laser used for the wing must be a 30 kW high-power laser. Both lasers will use micrometre wavelengths, as these are most commonly used for metal cutting. The lasers will be produced by a stationary laser source and transferred via a fibre-optic cable to a nozzle that applies the laser to the part to be cut. The nozzle also requires cutting gas.

The cutting gas is different between the two lasers. The fuselage cutter only needs to cut through 2 mm of aluminium. This can be done with compressed air and is the cheapest solution available. The air, however, will react with the aluminium, forming an aluminium oxide melt. This oxide melt will be a problem when the thicknesses get too large. The oxide layer will clog up the cut and will prevent deep cuts. The wing has a thick skin and therefore requires a gas that does not react strongly with aluminium. For this, nitrogen is chosen. This will be more expensive than compressed air, but it is the only available option without resorting to the really expensive noble gases.

4.4.4. Fuselage Cutter

The laser for the fuselage will be mounted on a rotating gantry that can move around the fuselage. This is done so that the laser has a line of sight on the rivet lines in the fuselage sections. The laser cutting setup must be able to cut fuselage diameters from 3.76 m for the 737 up to 7.14 m for the A380 [24]. Furthermore, the laser needs to be close to the aluminium to cut effectively, so the laser must be able to move closer and further away from the centre. This has to be done even if a single aircraft type is cut with this machine, since fuselage sections also become smaller when they are more aft. The laser also needs to make vertical cuts to cut the stringers.

---

[5] URL `https://surplusrecord.com/search/?q=upender&top-search=1` [cited 10 June 2026]

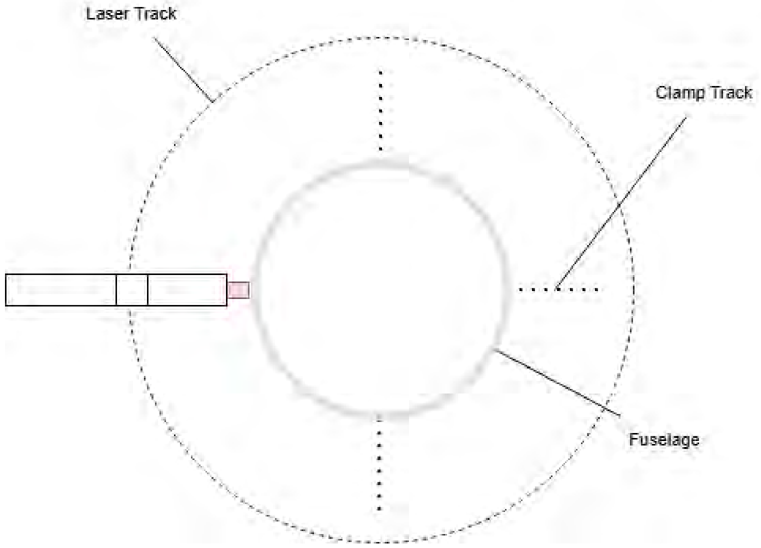

Figure 4.14: Top view of the fuselage cutting station

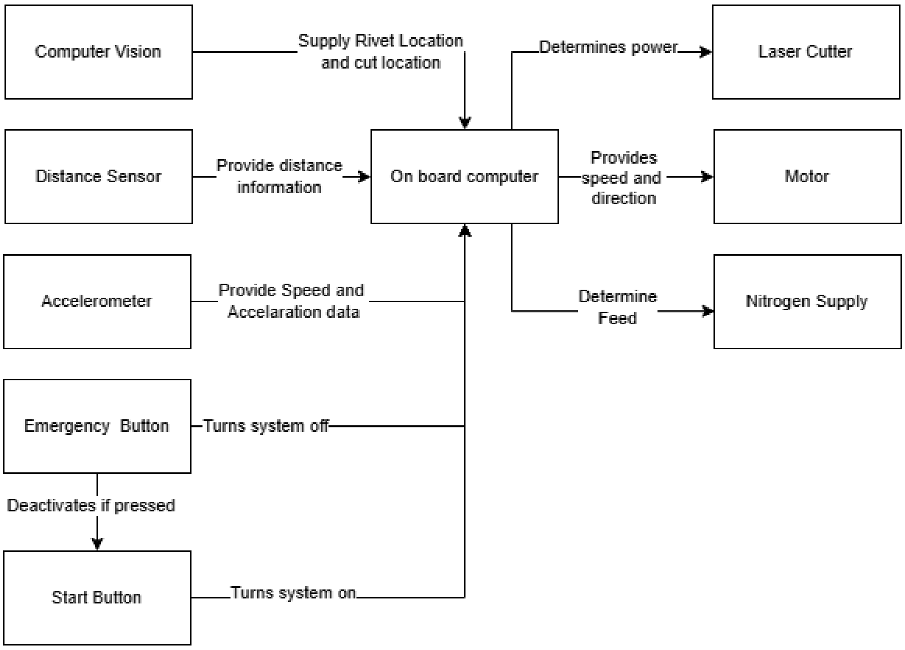

Figure 4.15: Hardware / Software Diagram of the laser cutting

A sketch of the side view of the fuselage cutting setup is shown in Figure 4.13. It shows that the laser can both be moved up and down and move towards and away from the fuselage. There are movable clamps in the ground to keep the fuselage in place during the cutting process. A movable counterweight is placed on the opposite side of the vertical track to reduce the vibrations and deflections caused by the movement of the machine. The whole gantry is put on a track that goes around the fuselage, so that cuts around the full circumference can be made.

Figure 4.14 shows the top view of this setup. It shows that the fuselage is in the middle and the track around the entire fuselage on which the gantry can be moved. It also shows the tracks of the movable clamps that are placed on four places across the fuselage. This makes sure the fuselage is clamped even if, for example, the doors are missing and the fuselage is not complete. On the laser, multiple sensors are placed that measure the distance between the laser and the fuselage and a computer vision system that detects the rivet lines and decides where to cut. Figure 4.15 shows the sensors and the interactions with the onboard computer.

The secondary cutting process of the fuselage is shown in Figure 4.16. First, the fuselage is cut into sections of roughly three metres. This was discussed in the previous section. Once the machine is clamped on the working area, the machine is turned on and will look for the rivet lines of the stringers. These rivet lines will be removed up until the next frame. After this, there is a cut above the rivet line of the next frame. This causes the skin panels that are above the frame and between the stringers to fall off. Then the frame web is cut to remove the material of the frame.

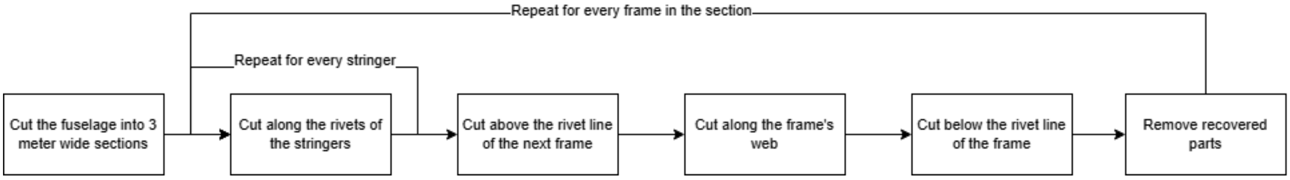

Figure 4.16: The procedure of the fuselage cutting process

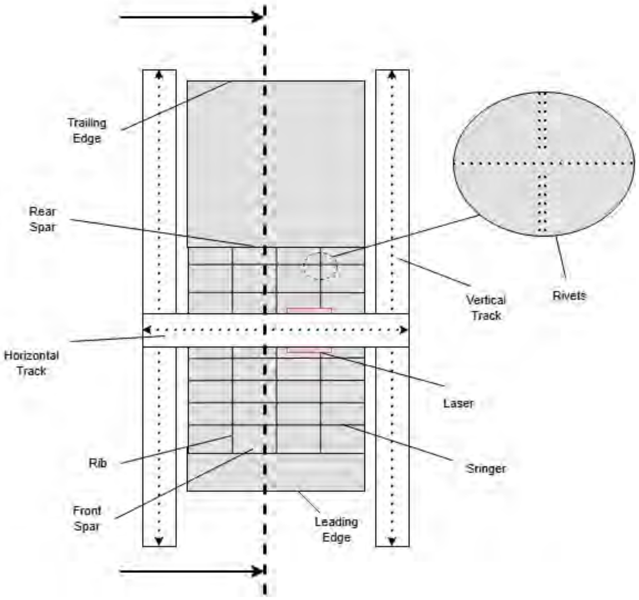

Figure 4.17: A schematic top view of the wing cutting setup

Lastly, a cut will be made below the rivet line of the frame. This will make the frame get off and therefore, will start the process over. This will be repeated until the final frame is cut out and then the final stringers and plates are separated.

4.4.5. Wing Cutter

For the wing, a different setup is needed. This is due to the fact that the wing is more like a rectangular box than a cylinder. The wing also has a higher thickness than the fuselage. This requires a more powerful laser and an inert cutting gas, as explained in subsection 4.4.3. For this, a more conventional CNC machine setup is chosen.

Figure 4.17 shows a schematic top view of the wing cutting setup. It shows that the laser is mounted on a set of tracks that allow the laser to be moved both horizontally and vertically. This way, it can cut both the stringer lines and the rib lines. It also shows the typical rivet lines of a wing.

Figure 4.18 shows a schematic side view of the wing cutting setup. It shows that the laser is also able to move up and down with respect to the cutting bed. The machine needs to be able to do this due to fact that the wing is curved and gets thinner the further away it is from the fuselage.

Figure 4.19 shows the cutting procedure of the wing. First cuts are made along the stringers, then along the ribs.

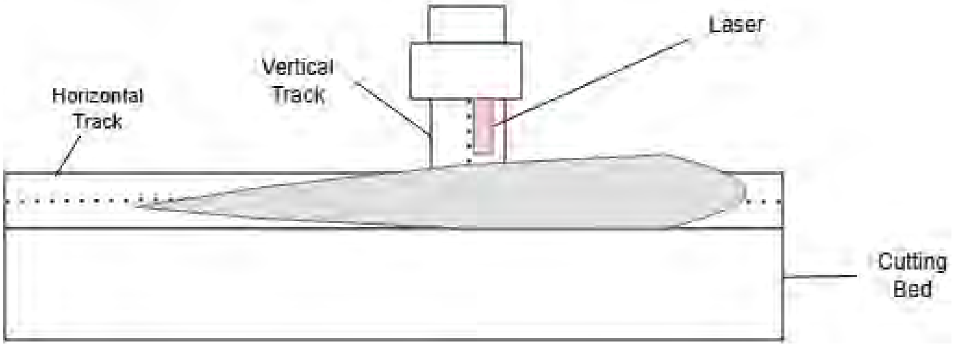

Figure 4.18: A schematic side view of the wing cutting setup

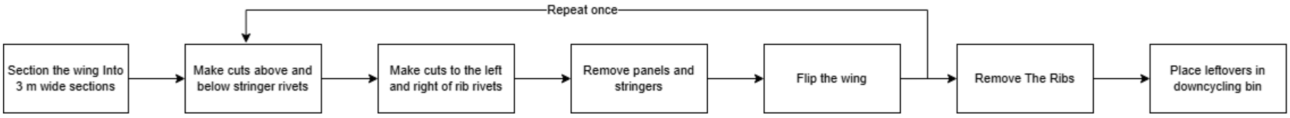

Figure 4.19: The cutting procedure of the wing

This removes the fasteners of the wing skin to the stringers and the ribs. Therefore, allowing them to be removed from the wing box. After the panels on the top are removed, the wing is flipped, and the panels on the bottom are removed. Since the wing skin is now removed, the ribs can be cut, and this material can be retrieved. The stringers are only connected to the wing skin and can thus be removed once the panels are removed. All the leftover material is downcycled.

4.4.6. Retrieval Calculation

Now that the setup and cutting procedures are known, the amounts of aluminium from the intersections and the stringers at every rib are determined. If the stringer has a value for one rib but does not have one for the next rib, it is assumed to have stopped halfway between those ribs. Some stringers will stop close to the ribs, and others will stop far away from the ribs, but it is assumed that this averages out over all the stringers. The stringers are also assumed to be equally spaced.

The wingbox is assumed to have a width of 45% of the chord. This is based on the fact that the front spar is usually between 12% and 17%, and the rear spar is usually at 60% [25]. It is also assumed that the chord length decreases linearly from the wing root to the wing tip.

The average thickness of the skin on a rib is determined by the sum of the thicknesses of the skin at each intersection with a stringer divided by the number of stringers. This is shown in Equation 4.5, where $t_{avg,r}$ is the average thickness at a rib, n_{str} is the number of stringers and $t_{s,r}$ is the thickness at an intersection of a stringer and a rib.

$$t_{avg,r} = \frac{\sum_{s=0}^{str} t_{s,r}}{n_{str}} \tag{4.5}$$

The chord length is going down linearly as you go from the root to the tip. The chord length at some point along the rib is given by Equation 4.6. The chord length at some distance from the root c_d is given by subtracting the rate of change across the wing multiplied by the distance along the wing d from the root chord length c_r. The rate of change is determined by the root chord length c_r, the tip chord length c_l and the length of the wing measured from the wing root l_w. The length of a rib l_r is then given by the chord length at the location of the rib c_r multiplied by 45%.

$$c_d = c_r - \frac{c_r - c_t}{l_w} \cdot d \tag{4.6}$$

$$l_r = 45\% \cdot c_r \tag{4.7}$$

The weight of the wing skin can now be determined. To get the weight of the skin, first, the area of a certain wing section needs to be determined. This is calculated by Equation 4.8. This is determined by calculating the trapezoidal area of the wing section. This is done by adding the lengths of the two ribs surrounding the section l_r and l_{r+1} together, dividing them by two and multiplying this by the distance between the ribs, where d_{r+1} and d_r are the distances of the ribs from the wing root. When the area is calculated, the weight can be calculated as shown in Equation 4.9. The average thickness across the section is calculated by averaging the two thicknesses at the ribs $t_{avg,r}$ and $t_{avg,r+1}$, multiplying this by the wing area A_{ws} and the density of aluminium ρ_{alu}.

$$A_{ws} = \frac{l_r + l_{r+1}}{2} \cdot (d_{r+1} - d_r) \tag{4.8}$$

$$W_{ws} = A_{ws} \cdot \frac{t_{avg,r} + t_{avg,r+1}}{2} \cdot \rho_{alu} \tag{4.9}$$

The total cutting length required for the wing cutting is given by Equation 4.10. It sums up the four different cuts required. The first are the cuts to the left and right of the ribs. This cut length is determined by summing all the rib lengths l_r together and doubling that. The same is done for the stringers with the stringer length l_{str}. Then the cuts along the front and rear spar l_{spar} are added. Finally, the cuts that need to be added are the cuts along the wire saw cut to remove the impurities created by the wire saw l_{cut}.

$$l_c = 2\sum_{r=1}^{n_{rib}} l_r + 2\sum_{s=1}^{n_{str}} l_s + 2\cdot l_{spar} + 2\sum_{c=1}^{n_{cuts}} l_{cut} \tag{4.10}$$

The weight and cutting calculation is also done for the bottom of the wing. The bottom of the wing is fairly similar to the top of the wing in the way the cuts are done. One major difference between the bottom and the top is that the bottom contains manholes. This means that the section where the manholes are reinforced is therefore likely to be complexly fastened. For these calculations, the manhole section is assumed not to have recoverable material.

For the fuselage, a different calculation needs to be done. The part of the fuselage that is going to be cut consists of two parts. The first part is a tube that starts after the nose and runs until the next part. The next part is the part that runs until the nose cone. In the second part, the diameter of the fuselage gets smaller. Both fuselage sections consist of frames, stringers, skin and floors. The frames are circular rings that are placed at a constant pitch throughout the fuselage. The stringers run from the nose cone to the tail cone to provide structural integrity to the skin.

The amount of skin recovered per frame section depends on a number of factors. The length of the skin recovered per frame section l_{fs} is shown in Equation 4.11. This depends on the diameter of the fuselage section D and on the amount of material that is removed by the removal of the stringer rivets. This is calculated by multiplying the amount of stringers n_{str} and the width of the cut w_c. It is assumed that when the diameter of the fuselage gets smaller in the second part, the stringer pitch will remain the same. This relation is shown in Equation 4.12. It shows that the ratio of stringers $n_{str,x}$ to the circumference of a section D_x stays the same. Lastly, it depends on the distance between two frames, the frame pitch p_{frame}. This is calculated by dividing the length of the fuselage that is going to be cut l_f, by the number of frames in that section n_{fr}. It is assumed to stay constant over the area to be cut. This assumption is verified with the SRM of the A310 [26].

$$l_{fs} = \pi D - n_{str}\cdot w_c \tag{4.11}$$

$$\frac{n_{str,1}}{\pi D_1} = \frac{n_{str,2}}{\pi D_2} \tag{4.12}$$

$$p_{frame} = \frac{l_f}{n_{fr}} \tag{4.13}$$

Now the weight recovered can be calculated. The weight of the fuselage skin w_{fs} is shown in Equation 4.14. This depends on the length of the skin l_s, the thickness of the fuselage t_f, the frame pitch p_{frame} and the density of aluminium ρ_{alu}. The weight of the stringers is calculated by Equation 4.15. The weight of the stringers w_{str} depends on the area of the stringer profile A_{str}, the frame pitch p_{frame} and the number of stringers n_{str}. Finally, the weight of the frames w_{frame} is considered in Equation 4.13. Here D is the diameter of the frame, t_{frame} is the thickness of the frame, h_{frame} is the height of the frame web, and ρ_{alu} is the density of aluminium.

$$w_{fs} = l_s\cdot t_f\cdot p_{frame}\cdot \rho_{alu} \tag{4.14}$$

$$w_{str} = A_{str}\cdot p_{frame}\cdot n_{str} \tag{4.15}$$

$$w_{frame} = t_{frame}\cdot D\pi\cdot h_{frame}\cdot \rho_{alu} \tag{4.16}$$

The length of the cuts is then calculated. For the fuselage, the length of the cut l_c depends on four factors. First, all stringer rivets will be removed. This consists of one cut below and one cut above the rivet line, so two times the stringer length l_s. For the frames, three cuts will be made. One on both sides of the frame on the outside of the fuselage and one cutting the web of the frame on the inside of the fuselage. These depend on the length of the frame cut l_f. Then the edges made by the wire-saw cutting need to be cut with the laser, defined by the lengths of those cuts, l_{cut}. Finally, the frame web needs to be cut into pieces so that the size is similar to the skin panels. These cuts are named the frame cuts, and their length is called l_{fc}.

$$l_c = 2\sum_{s=1}^{n_{str}} l_s + 3\sum_{f=1}^{n_{fr}} l_f + l_{cut} + \sum_{fc=1}^{n_{fc}} l_{fc} \tag{4.17}$$

Table 4.3: The weight retrieval results for the A310

Component	**Weight**
weight wing skin recovered	3,251 kg
weight wing stringers recovered	1,477 kg
weight wing ribs recovered	1,064 kg
fuselage skin weight recovered	2,156 kg
fuselage stringer weight recovered	979 kg
fuselage frame weight recovered	1,768 kg
total weight recovered	**10,694 kg**
OEW	79,166 kg
Structural Weight	41,166 kg
Aluminium Structural Weight	28,816 kg
Percentage of aluminium structure recovered	**37.1%**

Table 4.4: Length of cuts required to cut the a310

Cuts type	**Length**
Cuts along the wing stringers top	353 m
Cuts along the ribs top	136 m
Cuts along the spars top	37 m
Cuts along the wire saw cuts	29 m
Cuts along the wing stringers bottom	143 m
Cuts along the ribs bottom	199 m
Cuts along the spars bottom	37 m
Cuts along the wire saw cuts	29 m
Total cuts wing	**1,926 m**
Cuts along the fuselage stringers	6,989 m
Cuts along the fuselage frames	3,081 m
Cuts along the wire saw cuts	371 m
Cuts to make frame webs smaller	296 m
Total cuts fuselage	**10,737 m**

Table 4.5: Costs and Energy calculations

Parameter	**Value**
Cutting speed for fuselage and wing	20 m/min
Wing	
Total cut time wing	1.93 h
Laser output wing	30 kW
Price per hour wing cutting	€80 /h
Price per kilo recovered	€0.0256 /kg
Cutting time percentage	25%
Total time machine occupied	7.71 h
Fuselage	
Total cut time fuselage	8.95 h
Laser output fuselage	4 kW
Price per hour fuselage cutting	€20 /h
Price per kilo recovered	€0.0365 /kg
Cutting time percentage	25%
Total time machine occupied	35.79 h
Power Required and Energy usage	
Power usage wing cutter	100 kW
Power usage fuselage cutter	20 kW
Energy usage wing cutter	0.0408 kWh/kg
Energy usage fuselage cutter	0.0365 kWh/kg

A310 Example

The SRM of the A310 provides thickness values for the thickness of the skin of the wing at every stringer and rib intersection [26]. It also shows the location of all the ribs measured from the fuselage. This was used to calculate the weight of the aluminium to be retrieved and the length of the cuts required.

Now that the general overview of the process has been presented, the results for the A310 are calculated. Table 4.3 shows the amount of aluminium recovered from the A310are. It shows that roughly 10.7 tonnes is recovered and where the recovered material comes from. It also shows what percentage of the aluminium structure is recovered. This value is assumed to be the same for all aircraft. It is based on the assumption that 52% of the OEW [27] comprises structures of which 70% is aluminium [1]. For the A310 specifically, it was found that all the recovered material comprised 2024 and 7075 aluminium alloys. This is, however, not assumed to be the same for all aircraft. The total length of cuts required to recover this material is shown in Table 4.4.

Table 4.5 shows an overview of the costs and energy usage. The total cut time is calculated by dividing the cut length by the cutting speed. With this,are the costs per kg of aluminium recovered is calculated. For the total time machine occupied, the amount of time the machine is not cutting, due to, for example, changing the fuselage sections or scanning the section, is considered. This downtime is estimated by multiplying the cutting time by 4, and therefore, the cut time is estimated at 25% of the total time the machine is occupied.

5

Decoating

5.1. Coating Removal

After disassembly and fastener removal, the coating layers on the aluminium parts must also be removed before melting. The purpose of this stage is to remove the layered coating structure and prepare the parts for the melting stage by reducing melt contamination from organic coatings, oxides, and pretreatment residues. The coating includes a highly carcinogenic Cr(VI) layer[1], which should be handled with care, and the possible risk of exposure should be minimised [28]. Following a detailed trade-off process that compared the options for coating removal methods, including their effectiveness and potential safety hazards, chemical stripping methods were chosen as the most optimal. In the following chapter, the detailed process of the coating removal stage will be elaborated on.

5.1.1. Chemical Structure of Aerospace Coatings

The coating removal process should remove the paint and coating layers above the aluminium substrate. The primer layer consists of the epoxy polyamide and strontium chromate mixtures and is approximately 20-40 μm thick. Finally, for the topcoat, usually polyurethane, polyol or polyester paints are used to prevent the exposure of the external surface to ultraviolet (UV) light and corrosion [29]. The topcoat layer is usually 40-70 μ m. The removal process should treat each layer individually, considering the chemical composition.

Additionally, in some areas, sealants that make the structure air- or water-tight are present and should also be removed during the decoating process. Sealants are mostly composed of epoxy-cured polythioether polymer [30], and can be removed during organic layer stripping; thus, the sealants will also be removed in this stage.

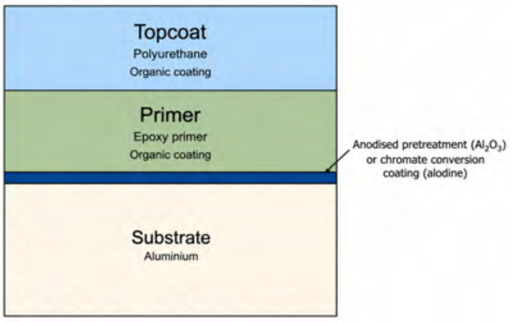

Figure 5.1: Exterior Coating Layered Structure- AI Generated (ChatGPT)

5.1.2. Organic and Inorganic Coating Structure

A typical aerospace coating system on aluminium consists of several layers. The aluminium substrate is first treated with an inorganic surface treatment, such as anodising or chromate conversion coating. This layer improves corrosion resistance and provides an active surface for paint adhesion. Above this layer, an organic primer is applied, commonly an epoxy-based primer [31]. Finally, a polyurethane topcoat is applied to provide the external layer UV resistance and weather protection.

The organic coating layer consists of two layers, the primer and the topcoat layer, each with different compositions. The primer layer is applied above the pretreatment layer. The epoxy primer layer is used to enhance the adhesion between the topcoat and the pretreatment layer and to prevent the corrosion of the aluminium substrate [32]. The epoxy layer is also added with strontium chromate to increase its corrosion protection properties. The epoxy layer consists of a cross-linked structure, which is used for its resistive properties against external conditions. This, however, poses a challenge for the coating removal process. Thus, to effectively remove the primer layer, strong chemicals such as hydrogen peroxide or alkali-activated alcohol strippers can be used.

---

[1] URL `https://www.nlr.org/newsroom/case/rd-case-neutralising-hazards-and-risks-for-chromated-aircraft-scrap-handling/` [cite 16 June, 2026]

The polyurethane layer is the topcoat painted layer. This is the first layer in contact with the external environment. Thus, this layer is used as a protection against degrading environmental factors such as UV, moisture and chemicals [33]. Removal of the organic layer requires longer immersion times and stronger chemicals to break the cross-linked polymer bonds.

The inorganic coating layer is the pretreatment layer applied under the primer and top coat layers. The pretreated layer can be in an alodine or anodised coating layer [34]. Different parts of the aircraft structures can include alodine or anodised pretreatments. This depends on the specific surface requirements on the part. For instance, for parts that require a higher corrosion resistance, anodised pretreatments are used; for anodised layers, the electrical conductivity can be very low. For the parts that require high electrical conductivity and corrosion resistance less than the anodised layers, an alodine pretreatment layer can be used [2].

The process of forming alodine and anodised layers differs significantly. Firstly, the alodine layers are formed through a chemical reaction between the aluminium surface and the chemical solution. The chemical solution contains chromium salt or chromic acid. Thus, these layers can also be called chemical conversion coatings. This reaction produces a thin oxide conversion layer containing aluminium and chromium compounds [35]. This layer is usually very thin, with a thickness of a maximum of 0.5 μm. Industrially, Alodine 1200S solutions are used as a hexavalent chromium-based chemical conversion coating used in the chemical solution [36].

Anodised pretreatments are applied through an electrochemical process. The aluminium parts are submerged into an acidic electrolyte bath and exposed to voltage [34]. This causes the surface of the aluminium to oxidise. Causes aluminium to form an aluminium oxide (Al_2O_3) layer. The oxide layer protects the aluminium beneath it from further corrosion and exposure to oxygen [37]. Such pretreatments are thicker when compared to the Alodine pretreatment. The approximate thickness of an anodised pretreatment can be 20-25 μm.

However, as it forms a strong bond with the aluminium substrate, it cannot be removed with organic coating strippers. The removal of this coating requires a caustic alkaline stripping step, which is commonly done using NaOH. [38].

Selection of Industrial Chemical Strippers

The industrial chemicals can be classified according to their pH levels and according to their aimed coating level, such as the organic or inorganic levels [39]. an Aluminium alloys are usually protected by a oxide layer that stays stable in a near-neutral pH range, between pH 4 and 9. When the solution goes beyond this range, especially in strong alkaline conditions, that protective layer can break down. This makes the aluminium underneath more vulnerable to chemical damage. This is also evident in the Pourboix diagram of aluminium. During the coating removal stage, effective coating removal is achieved when the cross-linked structure of the polyurethane and epoxy layers is impacted such that the layer is removed [39]. For the inorganic coating layers, the strong alkaline solutions can dissolve the anodised and chromium conversion coatings by attacking these layers.

To remove the coating effectively and thoroughly, sequential baths that include chemical solutions for the removal of organic, inorganic, and deoxidising smut layers are selected based on available industrial chemical solutions for each step. The immersion solutions are efficient in removing the coating from both sides of the panel, unlike gel solutions, where the application should be done homogeneously and applied to both sides. Thus, in terms of efficiency and effectiveness in removing coatings, immersion solutions are considered. For more resistant and local coating layers, hydrogen peroxide-based gel solutions will be used as a secondary treatment. The following section elaborates on the solutions analysed for the chemical stripping process.

Organic coating removal solutions:

- **Alkaline-activated benzyl alcohol stripper** For the removal of organic layers. Mainly used for polyurethane topcoats, epoxy primers, and aged aircraft paint layers. Benzyl alcohol penetrates the organic coating layer. It weakens the adhesion between the coating and the aluminium surface [40]. Alkaline acts as an activator in the solution by breaking chemical bonds in epoxy and polyurethane coatings. In some cases, highly cross-linked coatings may require local treatment. It can also be used to remove sealants from some parts [41]. The main safety concerns of alkaline-activated benzyl alcohol strippers are related to direct exposure and inhalation of vapour. Although these compositions are generally safer alternatives to methylene chloride-based paint strippers, they still require controlled bath conditions.
- **Methylene chloride stripper** For the removal of organic layers. Methylene chloride-based strippers are very effective at removing paint and topcoat. They have been commonly used in history for resistant coatings because they can quickly penetrate cross-linked polymer structures [42, 43]. This is not a preferred solution for paint removal processes due to its severe health concerns. The main concerns are its toxicity, carcinogenic risk, strict regulatory restrictions, and hazardous waste generation [44].
- **Phenolic acidic stripper** For the removal of the organic layers. It is also one of the most aggressive industrial stripping formulations used for very resistant or aged coatings. Such solutions are mainly used for the coatings

---

[2] URL `https://www.gd-prototyping.com/alodine-vs-anodize/` [cited 22 June 2026]

that require highly effective strippers [45]. They can provide high stripping effectiveness, but they introduce major safety risks related to toxicity and fume exposure. Therefore, they are not ideal as the main chemical stripping solution for a sustainable process.

Inorganic coating removal:

- **Caustic alkaline stripper (NaOH)** Used for inorganic coating layers. It can remove the natural aluminium oxide, anodised aluminium oxide, and some coating residues. This makes it effective for removing oxide-based inorganic layers [46]. Useful both for the chromium conversion coatings and oxide pretreatments by attacking the bonding between the oxide structure and surface. Hydrogen gas formation during the process is important from a safety point of view because it requires good ventilation [47].

Oxide and smut cleaner solutions:

- **Nitric acid deoxidiser** A nitric acid deoxidiser is used as a cleaning step after NaOH treatment. It removes the smut layer, oxide residues, hydroxides and other residues that might remain on the aluminium surface after alkaline etching [48]. The main concerns are corrosivity, acid fumes, and dissolved metal waste. Proper rinsing is required before this step to prevent NaOH from contaminating the acid bath.
- **Fluoride deoxidiser** A fluoride deoxidiser is a stronger oxide-removal solution than a standard nitric acid bath. Fluoride ions help dissolve stable aluminium oxide films, making these solutions useful for stronger oxide residues, which won't be necessary after treatment with NaOH immersion [44]. Fluoride deoxidisers have higher safety risks due to their toxicity, corrosiveness, and difficult waste treatment. They require strict ventilation and waste handling. Because of these concerns, they are less suitable as a solution for a sustainable aluminium alloy recycling process.

After considering their effectiveness and their safety implications for the organic coating layers, alkaline-activated benzyl alcohol strippers were chosen. For the persistent coatings local removal, hydrogen peroxide-activated gel benzyl alcohol strippers were selected. For the inorganic layer, caustic alkaline strippers (NaOH) were selected. To treat the possible smut layer, a nitric acid deoxidiser was selected.

5.2. Chemical Coating Removal Process

The parts that are cut in panel-shaped batches will be delivered for the decoating process. The following section elaborates on each step required for the pre-chemical treatment and chemical treatment processes.

Pre-chemical treatment cleaning: Before the chemical immersion process, any loosely attached exterior surface contamination should be removed. This step is to ensure that the topcoat exterior layer will be in direct contact with the organic coating stripper. To do so, dry and wet cleaning methods are used[3]. Such that loose contaminations are not carried over to the separate baths. To remove grease or dirt on the surface, parts are cleaned with a mild alkaline cleanser, then rinsed with water.

Dry brushing: Uses hard-bristle brushes to remove the loose paint, dust or dirt that might be attached to the surface. Such physical contaminants should be removed before immersion in the chemical baths to ensure surface particles are not carried over to the rinsing baths.

Wet external cleaning: Uses mild alkaline water-based cleaners, such as SOLUWAX water-based surface cleaner[4]. This step is important for the attached contamination on the surface, such as grease and more persistent surface contaminants that can't be removed with brushing.

Water rinsing: Dips the cleaned parts in a water bath to remove the excess cleaning substance that might remain on the surface.

Chemical Treatment
Organic coating removal: For organic coating removal, an environmentally and labour-safe but also a very effective option should be selected. As coating structures include cross-linked bonding, the removal requires strong chemicals. Industrial solutions utilise strong acids, activators, or methylene solutions, which can be effective but are dangerous to use. Thus, utilising an amino-ethanol (alkaline) activated benzyl alcohol stripper can be effective in removing the coating and allowing the chemical stripping to be safely applied. KEMSTRIP 600 solution can be a suitable choice for bath immersion and removal of polyurethane and epoxy layers.
Rinsing: Parts should be rinsed in a clean water bath to remove the surface from possible solution residue [49].
Dry: Parts should be dried before applying a secondary treatment.
Inspect: After the immersion process, parts can be inspected for the remaining coating. If there are local areas

---

[3] URL `https://www.socomore.com/en/paint-stripper-kemstrip-600-10001-p.html` [cited 5 June 2026]
[4] URL `https://www.socomore.com/en/waterbased-cleaner-synclair-a-c-2101-55gal-plast-drum.html` [cited 2 June 2026]

where coating is not removed with immersion, gel hydrogen peroxide-activated benzyl alcohol strippers will be applied. During application, the product's safety standards should be complied with.

Industrially, Eldorado PR-5044 or Cee-Bee E-3000[5] can be used as local strippers. This step should be followed with dry brushing or squeegeeing the coating off the surface [50].

Inorganic coating removal: For the inorganic coating layers of anodised chromate pretreatment, caustic alkaline (NaOH)[6] solutions will be used in stainless steel baths.

Rinse: Parts should be rinsed in clean water to remove any caustic alkaline solution residue.

Inspect: After alkaline etching, aluminium alloys can leave a black residue called smut. This residue can consist of alloying particles, oxides, hydroxides, and intermetallic residues that were not dissolved during the alkaline etch.

Deoxidising: Smut layers that remain on the aluminium surface can be removed by utilising a nitric acid deoxidiser [51]. This step will be applied only if the parts include smutting.

Rinse: Rinse the parts that were immersed in the deoxidiser bath to remove any desmutting agent.

Dry: Leave the parts to dry.

The proposed decoating sequence is summarised in the following diagram. The flow diagram shows the main process steps from pre-treatment to final drying. This ensures that organic coatings, inorganic pretreatment layers, and remaining surface residues are removed before the parts are transferred to the melting process.

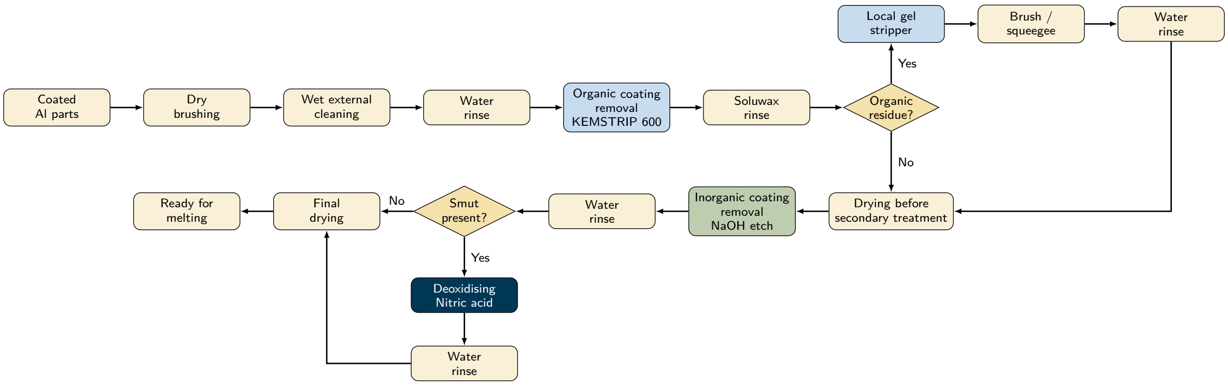

Figure 5.2: Proposed chemical coating removal process flow

The sequence separates organic coating removal, inorganic oxide removal, pretreatment removal, and smut removal into different chemical stages. This prevents the whole stage from relying on a single aggressive chemical to remove each layer, reducing the risk of incomplete removal and of excessive attack on the aluminium substrate. Thus, it can be assumed that during the decoating process, the aluminium alloy mass loss is negligible. Intermediate rinsing and drying steps are included to prevent chemical carryover between incompatible baths. Inspection steps are included mid-process to increase the reliability of the process.

---

[5] URL `https://www.cee-bee.com/product/eldorado-pr-5044/` [cited 2 June 2026]

[6] URL `https://www.anodizing.org/chemical-treatment` [cited 2 June 2026]

5.3. Proposed Sequential Chemical Immersion Bath System

The following table specifies the required specifications for each bath. The Table 5.1 summarises the required solution, bath temperature, and drying station specifications. Since the wait times for each solution are dependent on the bath and coating conditions, an exact wait time cannot be given. Using the process time ranges given by the suppliers, an estimate for the best-case and worst-case time limits is presented. For the following calculations, the maximum time taken for each process will be used to implement a safety margin for the overall process time. Bath temperatures for the chemical baths will be maintained within the required limits. The following table presents individual requirements for each bath.

Table 5.1: Process stations for the chemical coating removal process

Station	Chemical solution / process	Temperature	Dilution / preparation	Time
Tank 1	Mild alkaline water-based cleaner. (SOLUWAX)	Ambient temperature	Diluted according to supplier instructions.	10–30 min
Tank 2	Clean water rinse	Ambient	No dilution.	Until residue removal, approx. 2–5 min.
Tank 3	KEMSTRIP 600, benzyl-alcohol-based alkaline-activated immersion paint remover	80–110°C; up to 115°C for persistent layers	Two-phase bath: 85% KEMSTRIP 015 and 15% oil seal layer using ADDICAP 2.	1–4 h, depending on coating thickness.
Tank 4	Rinse with SOLUWAX after organic stripping	Ambient or warm	No dilution.	Approx. 5–10 min.
Tank 5	Clean water rinse	Ambient	No dilution.	Approx. 5–10 min.
Dryer 1	Drying station after organic coating removal and rinsing	Warm air	No chemical preparation. Parts are dried through an industrial drying unit before the inorganic removal step.	Approx. 15–30 min.
Tank 6	Caustic alkaline sodium hydroxide (NaOH) [52]	60–80°C	Concentration selected based on trials and required oxide removal thickness.	Approx. 5 min.
Tank 7	Clean water rinse	Ambient	No dilution.	Approx. 5–10 min.
Dryer 2	Drying station after NaOH immersion and rinse	Warm air	Parts are dried before the deoxidising stage to prevent chemical carry-over.	Approx. 15–30 min.
Tank 8	BONDERITE C-IC (Nitric acid solution)	20–30°C	10% nitric acid	0.5–5 min.
Tank 9	Clean water rinse	Ambient	No dilution.	Until acidic residue removal, approx. 5–10 min.
Dryer 3	Final drying station after the last rinse	Warm air	Final drying is required before transfer to the next melting process.	Approx. 15–30 min.

5.3.1. Bath Sizing and Immersion Cycles

For the industrial chemical immersion system, nine chemical immersion tanks and an immersion basket will be used. This is to ensure controlled and safe immersion of the parts. Each bath line-up includes nine baths for chemical stripping, rinsing, deoxidising, and cleaning steps. Chemical baths require a bath heater to ensure each bath is within the required temperature limit throughout the immersion process. They also include a pumping, agitation and filtering system to maintain a constant solution flow and to ensure homogeneous removal on each part. Across the baths, a vertical overhead rack is included to move the basket between baths.

According to Proceco, an industrial chemical immersion bath supplier, the selected bath has approximate internal dimensions of 2,150 mm · 1,500 mm · 2,100 mm, and the immersion basket has approximate dimensions of 1,850 mm · 1,000 mm · 850 mm. The basket holds the parts with a vertical rack arrangement. The necessary clearance for the sides of the immersion bath and immersion rack will be established to ensure all parts are in contact with the solution. Figure 5.3 shows the basic layout for the bath arrangement and basket immersion:

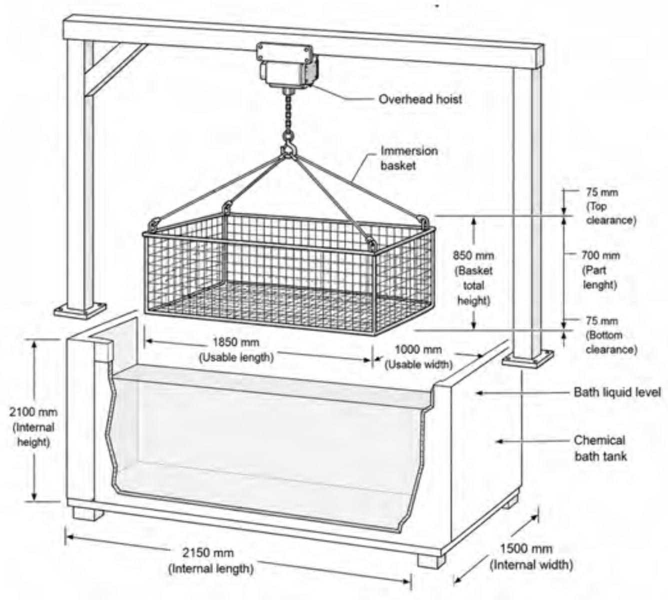

Figure 5.3: Immersion bath setup and dimensions - AI Generated (ChatGPT)

Following the given setup, the optimal positioning of each part will be organised. The clearances are for considering the solution flow between the racks and the end sections of the stringers. Since each stringer is assumed to have a thickness of 2 mm and a 15 mm clearance gap is assigned between adjacent stringers, each stringer position requires 17 mm of rack length.

The following calculations determine the number of parts that can be immersed simultaneously, considering the horizontal and vertical side clearances. Where p_{slot} is the given slot for the part, t_{part} is the thickness of the part and c_{part} is the clearance of the part from the other parts. Two configurations for immersion will be considered: Type A and Type B. Type A rack configuration includes 3 rows and will be used for mid-sized parts with a width up to 150 mm. Type B rack configuration includes 2 wider rows for larger-sized parts that have a width between 250 mm and 300 mm. Figure 5.4 and Figure 5.5 illustrate the sizing of each row and corresponding clearances.

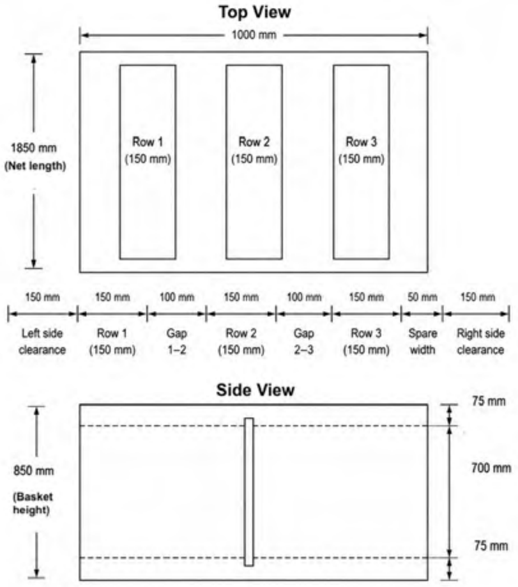

Figure 5.4: Rack A immersion basket arrangement

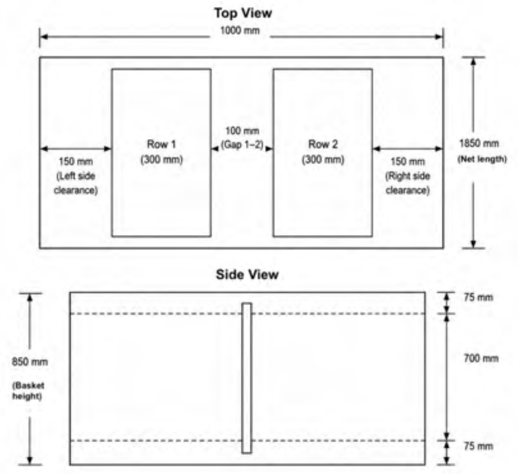

Figure 5.5: Rack B immersion basket arrangement

Batch Number Calculation

The bath size is constant for each parallel line for both KEMSTRIP and the rest of the processing lines. Each bath has a common size of 2,150 · 1,500 · 2,100 mm. The baskets used to immerse the parts simultaneously in the bath are also common in size, and considering the required right and left clearances for the parts to have full contact, a clearance gap of 150 mm is used. The net length to place the parts remains as 1,850 · 1,000 mm.

The number of parts per row, considering a net side length (L_{usable}) of 1,850 mm, with the clearances, will follow Equation 5.1:

$$N_{\text{row}} = \left\lfloor \frac{L_{\text{usable}}}{p_{\text{slot}}} \right\rfloor = \left\lfloor \frac{1,850}{17} \right\rfloor = 108 \text{ parts/row}. \tag{5.1}$$

For the type A rack, three narrow rows are used. Where the $N_{\text{batch,A}}$ is the number of parts per batch A, N_{row} number of parts per row and $n_{\text{rows,A}}$ number of rows in rack Type A, and $n_{\text{rows,B}}$ number of rows in rack Type B thus, the number of parts per batch will follow Equation 5.2:

$$N_{\text{batch,A}} = N_{\text{row}} \cdot n_{\text{rows,A}}, N_{\text{batch,A}} = 108 \cdot 3 = 324 \text{ parts/batch}. \tag{5.2}$$

For the type B rack, two wide rows are used. Where, $N_{\text{batch,B}}$ is the number of parts per batch B, $n_{\text{rows,B}}$ is the number of rows in Type B rack, and N_{row} is the number of parts per row thus, the number of parts per batch will follow Equation 5.3:

$$N_{\text{batch,B}} = N_{\text{row}} \cdot n_{\text{rows,B}} \tag{5.3}$$

$$N_{\text{batch,B}} = 108 \cdot 2 = 216 \text{ parts/batch}. \tag{5.4}$$

The part size, number of parts and batch grouping with their corresponding rack arrangement are summarised in Table 5.2

Table 5.2: Batch calculation for the part-size distribution

Quantity	**Part size [cm]**	**Rack type**	**Rack capacity (parts per batch)**	**Required batches**
580	$30 \cdot 25$	Type B	216	$\lceil 580/216 \rceil = 3$
580	$70 \cdot 30$	Type B	216	$\lceil 580/216 \rceil = 3$
584	$70 \cdot 30$	Type B	216	$\lceil 584/216 \rceil = 3$
1,168	$70 \cdot 15 \cdot 15$	Type A	324	$\lceil 1,168/324 \rceil = 4$
5,700	$50 \cdot 15$	Type A	324	$\lceil 5,700/324 \rceil = 18$
5,700	$50 \cdot 2 \cdot 2$	Type A	324	$\lceil 5,700/324 \rceil = 18$
1,680	$50 \cdot 15$	Type A	324	$\lceil 1,680/324 \rceil = 6$
Total	–	–	–	**55 batches per aircraft**

Using the final values for batch numbers and total parts per aircraft, the required addition of baths, and the overall process time can be calculated.

5.3.2. Parallel Bath Setup

To optimise the time efficiency of the coating removal process, the immersion time for each process step and the corresponding total processing time per basket will be approximated. The basket capacity is then used together with the estimated number of parts required for one aircraft to calculate the total number of immersion batches. The batch number and process time will then be used to estimate the required number of sequential bath lines needed to satisfy the selected processing time limit. Finally, a time and cost analysis will be performed to select the most suitable bath line configuration for the decoating process.

The objective is to determine an optimal number of sequential bath lines that reduces the processing time while keeping the total process cost within acceptable limits. Adding more bath lines increases throughput and decreases the processing time per aircraft, but it also increases the recurring and non-recurring costs due to additional tanks, ventilation, waste collection equipment, and solutions used. Therefore, the number of bath lines must be selected based on a time-cost trade-off.

First, a process time breakdown is calculated for the individual immersion, rinsing, drying, inspection, and deoxidising steps. The organic coating removal bath is treated separately because the KEMSTRIP immersion step is the bottleneck of the decoating process, due to its long immersion time. Thus, through adjusting the number of KEMSTRIP baths used and the rest of the sequential bath layout, a configuration that optimises the cost and process time can be obtained. To obtain the optimal configuration, the number of KEMSTRIP baths and the remaining baths are initially adjusted for each scenario to meet the target aircraft to be processed. To ensure a safety margin for the capacity of aircraft processed per year, a higher target of 100 aircraft has been selected. This also ensures that the decoating section can comply with the higher throughput from other sections.

An effective process time for the rest of the process and for the organic coating removal process is calculated in Equation 5.5. K is the number of KEMSTRIP 600 baths used for the process, and R is the number of parallel sequential baths for the rest of the steps. Through using the individual process times for the KEMSTRIP 600 bath, which is for four hours and the effective remaining bath time, which is approximately 1.33 hours.

$$\text{Effective remaining bath time} = \frac{1.33}{R}, \ \text{Effective KEMSTRIP bath time} = \frac{4}{K} \tag{5.5}$$

Table 5.3 summarises the required processing time for each bath and supplementary steps such as local treatment. The process times to be scaled and the aircraft capacity for each configuration is presented.

To calculate the required effective time for processing per aircraft, the number of parts that need to be processed in a day has been calculated. By using the target amount for aircraft to be decoated, the configurations that satisfy this requirement are selected.

The target aircraft for this process is selected as 100 aircraft to be processed per year. The higher target applied for this process aims to add a margin for operational unavailableness or possible pauses for the process.

Table 5.3: Estimated process time and selective bath scaling cases for chemical stripping

(a) Process times excluding KEMSTRIP

Process step	Time
Wet alkaline cleaning	5–15 min
Water rinse after cleaning	2–5 min
Drying before KEMSTRIP	10–15 min
Rinse after KEMSTRIP	5–10 min
Inspection for coating residues	5–10 min
NaOH etching	5–20 min
Water rinse after NaOH	2–5 min
Smut inspection	3–5 min
Optional deoxidising	1–10 min
Final water rinse	2–5 min
Final drying before melting	10–15 min
Total excluding KEMSTRIP	**50–115 min**
Nominal value used	**83 min**

(b) Scaled Process Time

Process part	Base time	Scaled time
Remaining baths	83 min	$1.33/R$ h
KEMSTRIP	4 h	$4/K$ h
Effective time per batch	5.33 h	$\mathbf{1.33/R + 4/K}$ h

(c) Aircraft processing capacity for variable bath numbers

KEMSTRIP	R = 1	R = 2	R = 3	R = 4	R = 5
4 baths	70.9	**99.2**	114.5	124.0	130.5
5 baths	77.5	112.6	132.9	145.9	155.0
6 baths	82.6	124.0	148.7	165.3	177.0
7 baths	86.7	133.4	162.7	182.7	197.3
8 baths	90.1	141.7	175.0	198.4	215.5
9 baths	93.0	148.7	185.9	212.5	232.5
10 baths	95.4	155.0	195.7	225.4	247.9
12 baths	**99.2**	165.3	212.5	247.9	275.5

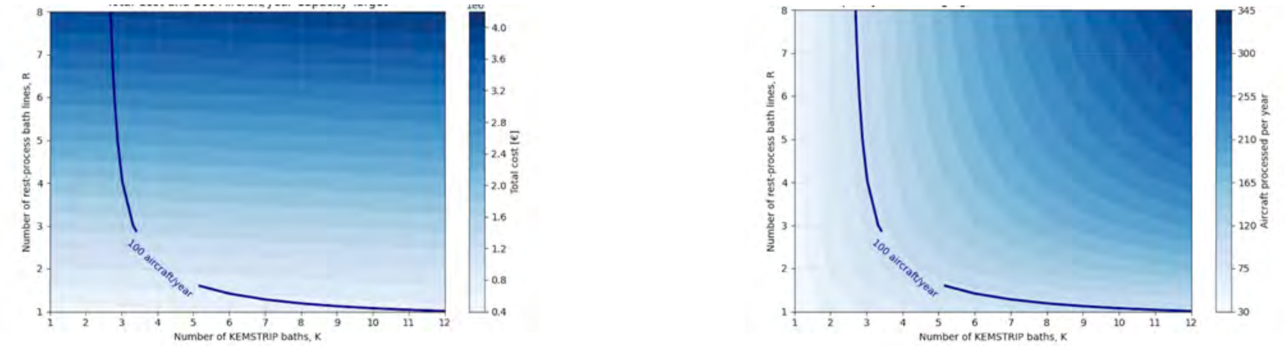

(a) Process capacity

(b) Total cost and capacity target

Note: A configuration consisting of four parallel KEMSTRIP baths and two parallel lines for the remaining non-KEMSTRIP process steps was selected.

Figure 5.6: Process capacity and cost-capacity target comparison

To determine the most time and cost-efficient bath configuration, two Python calculation scripts were used. The first script evaluates the annual processing capacity by varying both the number of KEMSTRIP baths and the number of parallel lines used for the remaining bath processes. The effective process time per batch is calculated by the remaining process time and the number of remaining bath lines, and dividing the KEMSTRIP time by the number of KEMSTRIP baths given in equation Equation 5.5. This allows the annual aircraft capacity to be plotted for different combinations and compared against the target aircraft to be processed per year in Figure 5.6a.

The second plot in Figure 5.6b adds the corresponding cost of each configuration. The cost of the remaining bath system scales with the number of parallel bath lines, while the KEMSTRIP cost only scales with the number of KEMSTRIP baths. By combining the capacity result with the total estimated cost per year, the most optimal configurations can be obtained.

Using the given plots and Table 5.3, a configuration consisting of four parallel KEMSTRIP baths and two parallel lines for the remaining non-KEMSTRIP process steps was selected.

5.4. Chemical Waste Management

To safely manage the chemical waste produced at the end of each immersion step, the waste treatment steps have been analysed for each chemical and rinsing bath. The waste handling process should separate suspended solids, paint sludge, and used chemical solutions [49]. The waste treatment process has been implemented in the following section.

The bath solutions are not replaced after each basket cycle. The process will aim to be reused over multiple immersion cycles. The bath conditions should be maintained by regular monitoring of pH, chemical concentration, and stripping performance. Thus, for this stage, the replacement will be considered dependent on the bath condition rather than a timed schedule. For the preliminary design, the baths are assumed to be checked daily or per batch, with filtration applied when possible and full replacement only when the bath is no longer within the required operating conditions.

To determine the time at which the solution should be changed, pH and temperature monitors are added to ensure the solution is within the required range. The control of the bath conditions ensures that the usable time for the solution is extended and reduces the changing times for the baths [53]. The reduction of contamination due to paint layers can also contaminate the solution further; this can be tackled with the following measurements.

Each tank includes a different type of chemical contamination. This is due to solutions introduced at each step, externally extracted waste and the chemical waste due to Cr(VI) and polyurethane, epoxy coatings. Thus, each bath should be treated individually and carefully after batches are immersed.

To effectively remove the paint and sludge layers, the draining section of each tank will be formed in a conical shape. Industrial chemical immersion tanks include a bottom outlet connected to an IBC discharger. An IBC discharger is used to transfer spent chemical solutions and rinse-water waste from the process tanks into labelled containers. They enable controlled storage, waste separation, and safe transport for treatment or disposal. This setup allows the chemical waste to be collected safely and without requiring manual collection. Each chemical bath requires a separate IBC collector unit and conical attachment to prevent cross-contamination and to collect the solid and liquid waste separately [49]. The sketch of the waste collection method can be seen in Figure 5.7.

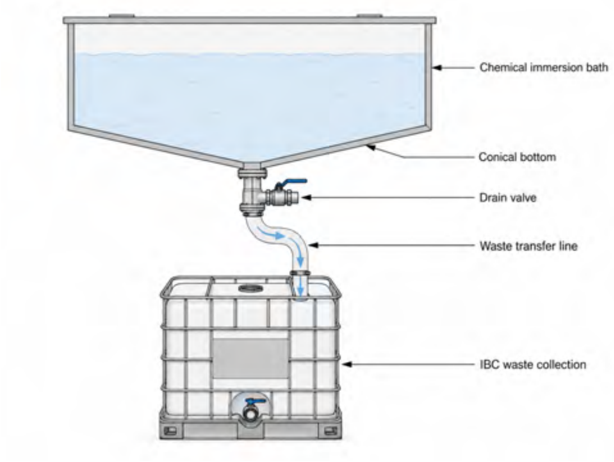

Figure 5.7: Waste Treatment Process for Chemical Baths - AI Generated (ChatGPT)

Acidic, alkaline, solvent, and rinse water chemical waste must be segregated to avoid reactions that might occur due to cross-contamination [54]. To do so, different classes of waste should be collected separately and treated before being sent to waste treatment facilities, in accordance with the safety manual for each solution. Table 5.4 identifies the required collection method and treatment.

Table 5.4: Waste streams and treatment routes for the chemical immersion process

Waste stream	**Collection method**	**Treatment**
Used organic stripper[7]	Collected separately in an IBC tank through a controlled drain system.	Filtration or settling to remove paint sludge, followed by chemical waste treatment.
Paint flakes and coating sludge [55]	Removed from the conical tank bottom and stored in a hazardous solid waste container.	Disposed of hazardous solid waste, especially if chromate primer or conversion coating residues may be present [56].
Used NaOH waste	Collected separately in an IBC tank.	Neutralisation, to reduce the pH of the alkaline before the treatment, and filtration.
Nitric acid deoxidiser waste	Collected separately in an acid-resistant IBC or waste tank.	Neutralisation, filtration, and treatment of the remaining acidic wastewater and sludge.
Contaminated rinse water [57]	Collected in a separate wastewater tank or IBC after each rinse step.	pH control and filtration of suspended solids.
Cr(VI) residues	Segregated in labelled hazardous waste containers and kept separate from general chemical waste.	Hazardous waste treatment.

The hazardous waste and contaminated water treatment will be outsourced. For transfer to an external waste or wastewater treatment facility in France, the chemical waste collected from the immersion process should first be classified, then the specific treatment processes should be applied, and the documentation of the treatment and source of waste should be addressed[8].

---

[7] URL `https://www.socomore.com/en/paint-stripper-kemstrip-600-201-5-3gal-plast-pail.html`[cite 4 June 2026]

[8] URL `https://entreprendre.service-public.gouv.fr/vosdroits/F37830?lang=en` [cite 10 June, 2026]

5.5. Economic Cost Assessment

For the economic cost assessment, considering that the Chromium(VI) contaminated parts cannot be transported between facilities [49], an in-house decoating facility will be used. Therefore, the assessment considers a dedicated chemical immersion line located within the dismantling facility. Since the exact pricing for the capital and operational expenditures is not present, best and worst case estimates presented in the Metal Surface Treatment Market Analysis report have been used to approximate the cost for a given expenditure [58]. A representative value that considers the higher margin was then selected from this range and used in the cost table. Therefore, the values can be interpreted as preliminary estimates rather than final costs.

The costs are divided into CAPEX, fixed annual cost, and OPEX. CAPEX includes the immersion baths, heaters, circulation and filtration systems, baskets, handling equipment, and ventilation infrastructure. Fixed annual costs include labour and facility rent. Operating costs include electricity, water consumption, chemicals, waste treatment, and waste handling. The cost estimates for single-line bath layup and for additional KEMSTRIP baths have been calculated separately to scale up the additional KEMSTRIP baths. To do so, CAPEX, fixed annual costs, and operating costs are recorded in their respective categories. The following table summarises the final cost for each bath system. Both bath line prices are given as a single CAPEX cost and a possible scale-up cost for both CAPEX and OPEX.

For the parts that use electricity, their yearly electricity usage and corresponding emissions are obtained. The electricity usage and emission summary is presented in Table 5.5.

For the final configuration with four KEMSTRIP baths with their corresponding rinsing baths and two lines for the remainder stripping and rinsing baths, the final cost estimation can be summarised by scaling up the single line costs. The summary of each cost item is presented in the following table.

Table 5.5: Estimated cost, KEMSTRIP scaling cost, and electricity budget for the chemical immersion bath system

(a) Estimated single line cost

Cost category	Item	Estimated cost
CAPEX		
Immersion system	9 immersion baths	€200,000
Heating system	Tank heater	€40,000
Circulation system	Pump, filtering and agitation	€50,000
Basket system	Baskets with vertical racks	€20,000
Handling equipment	Overhead crane	€8,000
Ventilation and extraction	Fume scrubber	€95,000
	Total CAPEX per line	**€413,000**
Fixed annual cost		
Labour	Operators and inspectors	€150,000/year
Facility cost	Rent	€240,000/year
	Total fixed annual cost per line	**€390,000/year**
Operating cost		
Electricity	Heated tanks	€13,000/year
Electricity	Pumps	€3,000/year
Electricity	Ventilation	€6,500/year
	Electricity subtotal per line	**€22,500/year**
Water consumption	Rinsing baths	€12,000/year
Chemical treatment		
Organic coating removal	KEMSTRIP 600	€20,000/year
Inorganic coating removal	NaOH	€3,000/year
Deoxidising	Deoxidiser	€7,000/year
Secondary treatment	CEEBEE hydrogen peroxide	€4,000/year
Pre-cleaning	Alkaline surface cleaner	€4,000/year
	Chemical treatment subtotal per line	**€38,000/year**
Waste disposal		
Waste treatment	Neutralisation and waste treatment	€20,000/year
Waste handling	IBC cost and waste transfer	€12,000/year
	Waste disposal subtotal per line	**€32,000/year**
	Total annual OPEX per line	**€104,500/year**

(b) KEMSTRIP scaling cost

Cost category	Item	Cost per additional KEMSTRIP bath
CAPEX		
Bath tank	Chemical bath and rinsing bath	€400000
Heating system	Tank heater	€4,444
Circulation system	Pump, filtering and agitation	€5,556
Basket system	Baskets with vertical racks	€2,222
	Total KEMSTRIP scale-up CAPEX	**€12,222**
OPEX		
Electricity	Heated tanks	€1,444/year
Electricity	Pumps	€333/year
Electricity	Ventilation	€722/year
	Electricity subtotal	**€2,500/year**
Water consumption	Rinsing baths	€1,333/year
Chemical treatment	KEMSTRIP 600	€20,000/year
Waste treatment	Neutralisation and waste treatment	€2,222/year
Waste handling	IBC cost and waste transfer	€1,333/year
	Total KEMSTRIP scale-up OPEX	**€27,388/year**

(c) Final selected configuration cost

Cost item	OPEX/year	CAPEX
Rest line, $R = 2$	€169,000/year	€826,000
KEMSTRIP baths, $K = 4$	€139,111/year	€412,222
Subtotal	**€308,111/year**	**€1238,222**
Final cost		**€1,546,333**

(d) Electricity and emission summary

Parameter	Value
Annual electricity consumption [kWh/year]	440,190
Energy cost per aircraft [€/aircraft]	1,143.35
CO_2 emissions per aircraft [kg CO_2/aircraft]	154.35
Specific electricity consumption [kWh/kg Al]	0.736

The current estimate of the cost items and their approximate values imposes limitations on the analysis. First, the values are based on industry standards, are derived by averaging the upper and lower limits, and reflect representative cost assumptions. As the exact cost values are supplier-dependent, they were not provided. Furthermore, chemical solution consumption, rinsing water consumption, and wastewater treatment may depend on coating conditions and change for each case, so the end values for electricity, water, or chemical usage would change. Finally, the overall electricity costs do not include downtime and assume the facility will operate autonomously 24 hours a day; thus, this provides an upper bound for the approximated costs. Finally, legislative costs, such as facility certifications, were not included in the initial level cost estimate. Therefore, the given values are preliminary estimates.

6

Sorting and Refining

The next steps are melting and refining the aluminium alloys. The objective of the foundry is to produce AA2024 and AA7075 high-grade alloys. To simplify the process, it first needs to be determined whether alloy types can be mixed during smelting, as described in Section 6.1. Next, all alloys need to be sorted so that no contamination is introduced into the melt streams; this is described in Section 6.2. Lastly, some refining still needs to be done after the melt is made to meet the characteristics of aerospace-grade aluminium alloy, as critical contaminants such as excessive iron and aluminium oxides need to be removed. The methodology used to do this is given in Section 6.3.

6.1. Alloy Mixing

A typical aircraft contains around 80% of aluminium by mass [59]. Of the total aircraft mass, around 40% by weight is made of AA2024 alloy and 30% by weight is made of AA7075 alloy [59]. Meaning that approximately 10% of the total aircraft mass is made up of different alloy types. In this section, it will be investigated whether these alloys can be mixed during the refining process. The main advantage of combining the melt streams into a single stream is cost savings. As described later in Section 6.3, switching between smelting different alloy types during refining costs a lot of money and time, making it beneficial to minimise this and thus create single-melt streams. With the help of Table 6.1, where the chemical compositions of all common aerospace alloys are laid out, it is possible to calculate whether it is acceptable to mix alloys in the melt stream. Here, the average value of the composition can be found in brackets.

Table 6.1: Chemical composition of common aerospace aluminium alloys (wt%) [60]

Alloy	Cu	Mg	Zn	Mn	Si
AA2014	3.9-5.0 [4.45]	0.2-0.8 [0.5]	0.25_{max}	0.4-1.2 [0.8]	0.5-1.2 [0.85]
AA2017	3.5-4.5 [4]	0.4-0.8 [0.6]	0.25_{max}	0.4-1.0 [0.7]	0.2-0.8 [0.5]
AA2024	3.8-4.9 [4.35]	1.2-1.8 [1.5]	0.25_{max}	0.3-0.9 [0.6]	0.50_{max}
AA2219	5.8-6.8 [6.3]	0.02_{max}	0.10_{max}	0.2-0.4 [0.3]	0.20_{max}
AA5083	0.10_{max}	4.0-4.9 [4.45]	0.25_{max}	0.4-1.0 [0.7]	0.40_{max}
AA6061	0.15-0.4 [0.275]	0.8-1.2 [1]	0.25_{max}	0.15_{max}	0.4-0.8 [0.6]
AA7050	2.0-2.6 [2.3]	1.9-2.6 [2.25]	5.7-6.7 [6.2]	0.1_{max}	0.12_{max}
AA7075	1.2-2.0 [1.6]	2.1-2.9 [2.5]	5.1-6.1 [5.6]	0.3_{max}	0.4_{max}
AA7150	1.9-2.5 [2.2]	2.0-2.7 [2.35]	5.9-6.9 [6.4]	0.10_{max}	0.12_{max}
AA7178	1.6-2.4 [2]	2.4-3.1 [2.75]	6.3-7.3 [6.8]	0.30_{max}	0.4_{max}
AA7475	1.2-1.9 [1.55]	1.9-2.6 [2.25]	5.2-6.2 [5.7]	0.06_{max}	0.10_{max}

To calculate whether it is acceptable to intermix different alloys, it is assumed that when smelting, there will be a melt with all AA7075 and another with all AA2024 alloy. When mixed, it will have the average composition of all elements. Lastly, it is assumed that, when checking for compliance of a certain alloy, the remaining 10 wt% will be only a single alloy type added to the stream to simplify the chemical composition calculation. This assumption is valid as this is the maximum amount of that alloy that could be in the aircraft.

With this approach concluded, it is possible to calculate the minimum and maximum composition for each element. For example, the maximum copper composition when AA2014 alloy is mixed in. The maximum composition is then given as:

$$\text{Cu}_{\text{new, max}} = \frac{\text{Cu}_{\text{2014, max}} \cdot \text{m}_{\text{rest}} + \text{Cu}_{\text{2024, avg}} \cdot \text{m}_{2024}}{\text{m}_{2024} + \text{m}_{rest}} = \frac{5 \cdot 8,000 + 4.35 \cdot 32,000}{32,000 + 8,000} = 4.48\,\text{wt\%}$$

Where $\text{Cu}_{\text{2014, max}}$ is the maximum concentration of copper that can be found within a 2014 aluminium alloy and $\text{Cu}_{\text{2024, avg}}$ is the average copper content in the 2024 aluminium alloy. Next, m_{rest} is the amount of aluminium alloy that can be 2014, which is 10% of the aircraft's total mass, totalling 8,000 kg. Lastly, m_{2024}, which is the amount of 2024 aluminium alloy found in the aircraft, which is 40% of the total aircraft mass, giving 32,000 kg. With these numbers, it can be seen that the maximum copper concentration will be 4.48 wt% for the mixing of 2014 and 2024 aluminium alloy, which is within the allowable range of AA2024 alloy. This is also done for the minimum copper concentration. From this, a minimum concentration of 4.26 is found. Thus, the total range of copper in the new AA2024 and AA2014 melts is 4.26-4.48, which is within the correct range for an AA2024 alloy, set at 3.8-4.9. All other elements found in the alloy, such as Cr and Ti, will remain within the correct range due to the defined boundaries of the original alloys.

Magnesium and Silicon

Within the AA2024 melt stream, two elements might pose a problem, the first is magnesium. The problem lies with AA5083; this alloy has a very high magnesium content, which can disrupt the melt stream. Fortunately, magnesium evaporates during alloy melting [61]. In other words, the magnesium content of the alloys does not need to be considered. Next, there is silicon. When combining a high amount of AA2014 into the AA2024 mix, it could disrupt the melt stream due to too-high silicon concentration. Here, the risk is taken; assuming the average silicon concentration in 2024, the melt will be safe. However, when all maximum silicon concentrations in 2024 and 2014 are considered, the melt will be out of bounds. Thus, in the worst-case scenario, silicon can fall outside the specified ranges. Several mitigative techniques can be used to prevent this alloy from being produced with an incorrect elemental range in a sheet. Firstly, an internal counter is implemented in the sorting machine to estimate the wt% of each aluminium alloy type and to issue a warning to the refining processes if there is a risk of incorrect element quantities. In addition, OES tests are used to determine whether all element ranges are within AMS bounds. Finally, if a batch has an element that falls outside of range, a portion of the recycled melt can be used as dilution for later batches. An example is shown below:

- A melt composed of 80% AA2024 with a silicon concentration of 0.5 wt%, with 20% of the mass being AA2014 with a silicon concentration of 1.2 wt%, exceeds the maximum silicon wt% for AA2024 by 0.14 wt%. The sorting machine realises that a big portion of a certain batch is AA2014 and sends a warning to the refining process. The OES, right before dilution, analyses the melt. Upon discovering that the silicon concentration is too high, it will signal for the melt to be cast into ingots and used in the dilution melt.

This is done for all alloys and elements. From this, it can be concluded that AA2024 can be produced from a mixed stream of AA2024, AA2014, AA2017, AA5083, and AA6061. With the exception that, if only AA5083 or AA6061 is added to the stream, some extra copper must be added to achieve the correct composition. For the AA7075 mix stream, it is possible to add AA7178 and AA7475 into a shared stream without any difficulty.

Lastly, zirconium is found in three main alloys. Namely, in AA2219, AA7050 and AA7150. In the appropriate alloy, zirconium increases heat resistance, strength, and the recrystallisation temperature [62]. When it is mixed into the standard AA2024 alloy, it creates dispersions within the microstructure of the alloy, significantly reducing the fracture toughness of the material [63]. Because of zirconium, these aluminium alloys must be separated from the melt stream to avoid contamination.

6.2. Sorting

After it is decided which alloys can be mixed, the alloy plates must be sorted into their respective groups using an X-ray fluorescence sensor, also known as an XRF sensor. XRF works by firing X-rays at a material. The material then converts this radiation into a fluorescent X-ray that can be detected by the XRF scanner and used to identify the material[1]. The technique was mainly chosen for its low cost and ease of use. Another note is that it is possible to scan through paint and coatings [64]. Meaning the sorting process could take place right after cutting and before the decoating. However, the current process sorts after decoating. For the sorting, there is only a need for a distinction in the concentration of zinc and zirconium to correctly sort the alloy. This is due to the different melt streams as described in Section 6.1. This is something XRF does well, as it excels at identifying heavier elements such as zinc and zirconium. According to the manufacturer, the XRF machine has an accuracy of 99.8%.

For this specific use case, an XRF line scanner made by LLA-Instruments is used. More specifically, using a single sensor XRF configuration, three streams of plates can be sorted in parallel. From the contact with the manufacturer, it is known that the sensor takes approximately five seconds per plate to correctly identify the material. The XRF sensor is mounted above a motorised roller belt, where the plates are placed after laser cutting. Once the scanner has determined whether it is a 2xxx melt-stream alloy, a 7xxx melt-stream alloy, or a zirconium alloy, it is sorted using a simple pneumatic diverter that directs it to the appropriate stack. A schematic layout of the process can be seen in Figure 6.1.

---

[1] URL `https://www.vrxrf.com/blog/detector-of-xrf-analyzer-working-principle-and-types/` [cited on 22 June 2026]

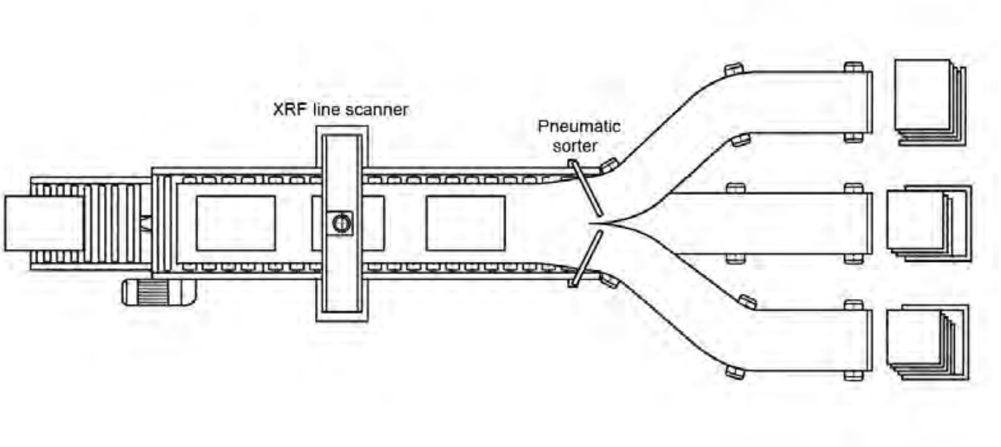

Figure 6.1: Sorting sketch - AI Generated

6.2.1. Sorting Costs

After direct communication with the manufacturer of the XRF sensors, the cost of this machine is set to be €98,031. It also consumes around 1 kW of energy. For the motorised roller belt, a standard €100 per foot is taken in the automotive industry[2], and can thus also be taken in this application. In this system, there is no need for very long conveyor belts; a maximum of 50 m of belt will be used. So, to be conservative, an approximation of €15,000 will be taken for the total cost of the conveyor belt. The energy consumed by these belts will be around 10 kW[3]. From Chapter 4, it is known that every aircraft produces around 16,000 parts that need to be sorted. Each scan takes 5 seconds to complete, and you can scan three plates sequentially. Thus, scanning the entire aircraft will take:

$$\frac{16,000}{3} \cdot 5 \ \div 3,600 = 7 \text{ hours } 24 \text{ minutes}$$

6.3. Melt Refining

Even with a 99.8% sorting accuracy, our aluminium melt is not yet aerospace-grade. Firstly, metallic impurities such as iron and titanium, resulting from improper removal of airliner fasteners, contaminate the melt. Iron specifically forms into needle-like crystal structures [65], reducing the ductility and fracture toughness of the final alloy. Furthermore, aluminium oxide forms upon melting [66]. It is essential to recover this lost aluminium to meet our strict material recovery requirements. Dissolved gases generated during oxidation can interact with atmospheric moisture and affect the fatigue life of aircraft components. Environmental species, including gases and moisture-related electrolytes, can generate atomic hydrogen at crack surfaces, accelerating fatigue-crack growth in aluminium alloys and reducing component life [67]. As the last concern, alkaline contaminants such as sodium and calcium can reduce the corrosion resistance of aluminium alloys and must therefore be carefully controlled [68].

6.3.1. Objective

There are different contaminants, and unfortunately, there is no single technique that can remove all of them efficiently without destroying the alloy composition. Therefore, a five-step purification procedure was engineered as follows: metallic removal, fluxing, gas removal, byproduct removal, and filtration. This procedure, which will be explained in the next subsections, is visually presented in Figure 6.2.

---

[2] URL `https://www.vitrans-conveyor.com/2025/04/02/how-much-does-a-conveyor-belt-cost-per-foot-in-2025/` [cited 10 June 2026]

[3] URL `https://www.szsunqit.com/how-much-electricity-does-the-conveyor-belt-consume-per-hour.html` [cited 10 June 2026]

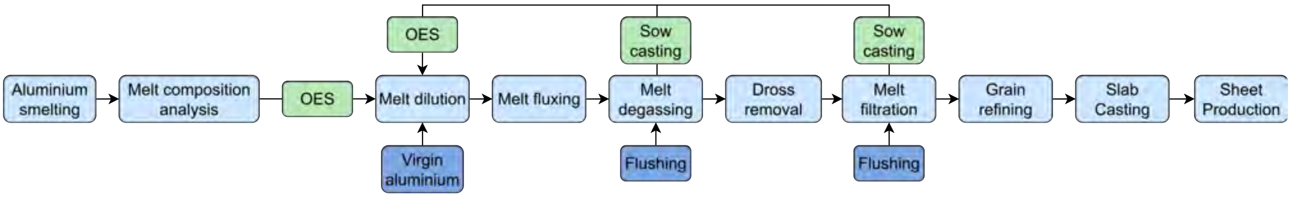

Figure 6.2: Process flow diagram of the melt refining

6.3.2. Melting

Before the first refining step, the metal must be melted. The aluminium industry usually uses gas furnaces[4], as aluminium smelting requires enormous amounts of power, which creates up to 2 kg of CO_2 [69]. Induction furnaces are expensive but effective in small foundry settings, thanks to their high efficiency and minimal contamination[5]. As the furnace should be able to process 604 tonnes per year according to Section 2.8, Luoyang Ruixinsheng Industrial Technology Co. was chosen[6]. Their RXS induction furnace can melt two tonnes of aluminium alloy scrap in an hour, with a peak power consumption of 1,500 kW, and costs less than €44,000.

6.3.3. Metallic Removal

The first step in the refining process is to reduce metallic contaminants, such as iron, to levels below the AMS limits for each alloy, as shown in Table 6.1. For this purpose, two main options were considered: dilution and intermetallic precipitation. This method adds neutralisers, such as manganese or chromium, to force iron and silicon to form dense sludge crystals. It was not chosen because of its slow speed, and it traps a lot of valuable alloy at the bottom of the furnace.

The other option, dilution, scored much higher, as it is a fast and safe way to reduce the amount of iron and other tramp elements in an aluminium alloy, while controlling the melt composition and not affecting material recovery. The downside to this method is that it is slightly more expensive due to the use of virgin materials, and that it slightly compromises the closed-loop aspect of the project by allowing up to 15% of the final melt mass to be composed of virgin aluminium.

During the preliminary design phase, pure aluminium was used to dilute the iron until its level was low enough, e.g. an AA2014 recycled melt with an iron content of 1.0 wt% was diluted to 0.7 wt% or lower [6]. Unfortunately, two major flaws were found with this technique:

- There exists no such alloy as 100% pure aluminium that is cheap enough to be used in our process
- Even by using quasi-pure aluminium, some alloy elements such as copper could potentially be diluted below the limits set by the Aluminium Association [6].

So the recycled melt, whose composition is currently unknown, must be diluted with a virgin melt to obtain an alloy within the alloy's allowed limits. To solve this, a calculated dilution with a mix of virgin pure aluminium and virgin alloy is used. The pure aluminium used should be cheap and contain a low level of alloying elements such as iron, silicon, and titanium. This is why the 1xxx-series AA1090 was chosen, with a market price of $2,950[7] or €2,538 per kg. For the virgin alloy, non-quenched, non-heat-treated ingots will be used, with prices varying by alloy.

A Python dilution calculator was then made. The user selects the relevant alloy type from 11 options and manually enters the chemical composition of the recycled melt. Please note that the last step could also be automated using packages such as pandas and by connecting the calculator to an OES composition detector. OES was chosen for composition analysis due to its high accuracy and low upfront and operating costs. The Ametek Spectro MAXx LMM04 model was chosen, with a second-hand model found for €8,950[8], and a budget of €10,000 is allocated for any aluminium software needed, as the machine is currently calibrated for steels and high-purity aluminium. From this information, the code outputs precisely how much pure and alloy aluminium are needed to ensure all elements are within the limits. A key assumption that the code makes is that the virgin alloys have element compositions around the upper half of the ranges. This technique is used by manufacturers to ensure that the composition falls within

---

[4] URL `https://new.abb.com/metals/abb-in-metals/references/optimised-ems-in-aluminium-melting-and-holding-furnaces` [cited 10 June 2026]

[5] URL `https://www.okonrecycling.com/industrial-scrap-metal-recycling/steel-and-aluminum/aluminium-scrap-melting/` [cited 10 June 2026]

[6] URL `https://www.alibaba.com/product-detail/RXS-Direct-Factory-Supply-Induction-Furnace_1600705340096.html` [cited 10 June 2026]

[7] URL `https://dmjdmetal.en.made-in-china.com/product/rGbUaIoKgjcT/China-Supply-A91090-American-Standard-Pure-Aluminum-Al1090-Aluminum-Plate-1090-Industrial-Aluminum-Bar.html` [cited June 4 2026]

[8] URL `https://www.machinio.com/listings/111345553-ametek-spectro-maxx-lmm04-oes-metal-spectrometer-material-analysis-complete-with-pc-accessories-in-borken-germany` [cited 12 June 2026]

the AMS range, even if slight contamination occurs downstream. Let's see an example of the code in action. When selecting the AA2024 alloy with Fe and using a normal alloy composition for the melt, the output of the code can be seen in Figure 6.3. As can be seen, the dilution only uses pure aluminium until iron reaches 0.76 wt%, after which virgin AA2014 alloy melt, marked with the orange colour, shall also be used until a maximum iron concentration of 0.81% is reached. It can thus be concluded that if the recycled melt has a concentration above 0.81 wt%, it cannot be diluted while remaining below the 15% virgin material limit. The results of two element contaminants, iron and titanium, are summarised in Table 6.2. As discussed previously, magnesium and zinc tend to evaporate during melting, and to account for this possibility, the dilution calculator will be adjusted in the future to allow adding pure magnesium or other pure ingots to the melt.

After completing the energy breakdown in subsection 6.3.12, it was discovered that only 7% of the total melt mass can be virgin aluminium, as the high energy required to produce virgin aluminium, 15 kWh/kg [70], limits the total dilution mass. This is a quick change to make in the dilution calculator, and the code will be adapted at a later stage of the project.

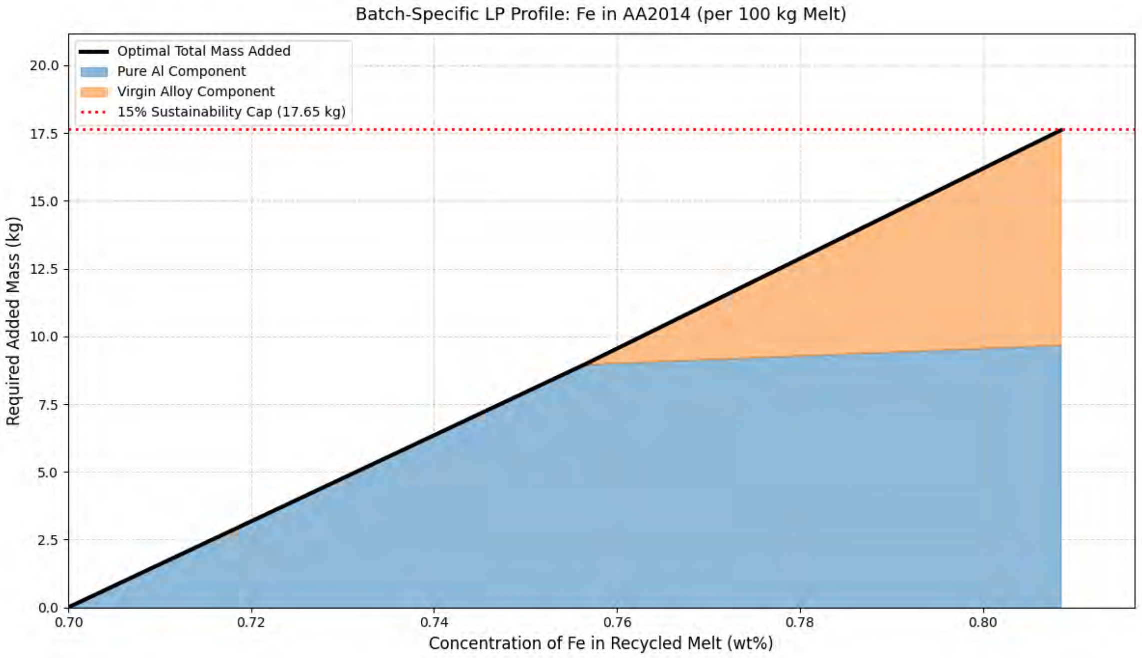

Figure 6.3: Graph showing how much virgin pure and alloy aluminium should be added to a recycled AA2014 melt to counter a rising iron proportion.

Table 6.2: The maximum amount of iron and titanium allowed in different wrought alloys

Alloy	Fe [wt%]	Ti [wt%]
AA2014	0.8085	0.1675
AA2017	0.7945	0.1710
AA2024	0.5745	0.2920
AA2219	0.3330	0.1115
AA5083	0.4485	0.1710
AA6061	0.8110	0.1745
AA7050	0.1630	0.0670
AA7150	0.1625	0.0665
AA7075	0.5645	0.2315
AA7178	0.5590	0.2295
AA7475	0.1410	0.0665

To dilute the melt, virgin aluminium ingots will be added. The amount to be added will be calculated by the code, and the machine will add the correct dilution amount. The maximum amount of dilution that can be added is 0.1765% of the original mass, as this is 15% of the total melt mass. To estimate the price, 0.1765 will be multiplied by the market price of AA1090, and the price to melt this metal will also be calculated. The code firstly follows the upper and lower limits of all elements, such that for element i in Equation 6.1, where c is the concentration of, and m is the mass of the initial recycled melt 0, the pure aluminium added subscript p, and the virgin alloy added subscript v, respectively.

$$(c_{min,i} - c_{p,i})m_p + (c_{min,i} - c_{v,i})m_v \leq c_{min,i}(m_0 + m_p + m_v), \tag{6.1}$$

The code also ensures that the sustainability cap of 15% of the final mass, dictated by the maximum allowable added fraction f_{max}, is respected at all times in Equation 6.2:

$$\frac{m_p + m_v}{m_0 + m_p + m_v} \qquad m_p + m_v \leq (\frac{f_{max}}{1 - f_{max}})m_0. \tag{6.2}$$

And lastly, the sum of the added masses, $m_p + m_v$, is minimised.

6.3.4. Oxide Removal

The aluminium scrap that will be melted in subsection 6.3.2 comes mostly from alloy sheets. These thin sheets have a high surface area-to-volume ratio, leading to significant oxidation during melting. To prevent more oxidation from occurring, cover fluxing will be used, and dross fluxing will be used to recover as much aluminium as possible from the white dross formed partially by aluminium oxides.

The cover fluxing salts will form a protective layer on the melt surface [71, 72]. This prevents further oxidation and prevents the melt from absorbing more atmospheric moisture. The cover fluxes from Vesuvius will be used for this. The manufacturer specifically recommended the Flussum SW2 powder flux [73], with an addition rate of 20 to 30kg of powder per tonne of melt. Furthermore, a lot of aluminium is lost due to oxidation. This aluminium oxide mass is called "white dross". Through a process called dross fluxing, up to 83% of the trapped aluminium can be recovered [74]. Again, a drossing flux was recommended by a product manager at Vesuvius. The team will use the Flussum 111 [75] for the melt batch of batches destined for AA2024, and will use the sodium-free Flussum 21Z for the magnesium-containing melt batch destined for AA7075 sheets. Up to three kg per tonne of the dross flux will be added to the melt. Assuming a typical price of €0.5/kg for cover fluxes[9] and €2.5/kg for cover fluxes[10], the total cost per kg of aluminium produced will be €0.0225/kg.

6.3.5. Dissolved Gas Removal

Hydrogen is actually a natural byproduct of oxidation and is also present in the melt through atmospheric moisture. Dissolved gases in the melt, such as hydrogen, can cause microscopic porosity, thereby reducing the fatigue life of the aircraft part. In the aluminium refining industry, the Spinning Nozzle Inert gas Floatation system (SNIF), trademarked by Pyrotek Inc.[11], introduces a microscopic vortex of inert gas bubbles into the melt. These bubbles, usually made of Argon or Nitrogen, catch and carry nitrogen bubbles out of the melt. As a bonus, they also sweep up a part of the melt's non-metallic dirt particles. A key requirement of this subsystem is that it shall reduce the hydrogen concentration to 0.08 ml/100g of melt or lower.

The Adtech EC-1R-6 [76] on-line degassing machine will be used for this purpose. This type of degasser sits directly between two refining stages, connected by aluminium launders, a gravity-led metal transfer system[12]. With a work rate of 6 tonnes per hour, a power usage of 24 kW, and the ability to degas with both Argon and Chlorine gas until a concentration of 0.12 ml/100g of melt or lower, it is a great candidate for this refining process, and the additional usage of chlorine gas will assist with the removal of alkalis such as sodium and calcium. The price of the EC-1R-6 model is not published anywhere, but can be estimated at $60,000 or €51,546 based on the price of a 45 kW on-line degassing unit from Hydeb[13].

During the detailed design of this subsystem, a problem arose: a significant amount of metal would remain behind when switching between alloy types, potentially leading to cross-alloy contamination. The standard industry practice is to flush the degassing bath with a pure aluminium melt twice the bath's volume, which then carries away any contaminants left behind, making the bath ready for the next alloy type. With the EC-1R-6 having a bath capacity of 720 kg, 1,440 kg of aluminium would be wasted every time the casthouse switches between incompatible alloy types. Our project's sustainability limits prevent this, so it was decided to cast this melt into low-cost sows. These sows, large rectangular aluminium blocks[14], are then analysed with an OES machine and used in the dilution process from subsection 6.3.3 together with the dilution calculator code. The melting of this flushing P1020 aluminium will

---

[9] URL `https://www.indiamart.com/proddetail/foseco-coverall-11-foundry-flux-2855770198012.html` [cited 15 June 2026]

[10] URL `https://www.indiamart.com/proddetail/foseco-coverall-gr-2516-foundry-flux-2855778566933.html` [cited 15 June 2026]

[11] URL `https://www.pyrotek.com/products/casthouse/show/Product/snif-in-line-degassing-and-furnace-treatment-systems` [cited June 5 2026]

[12] URL `https://www.aluminiumceramicfiber.com/launder-system-for-aluminum/` [cited June 5 2026]

[13] URL `https://www.aluminiumfurnaces.com/sale-14393510-45kw-process-of-refining-aluminum-degassing-on-line-unit-750-deg-launder-type.html` [cited June 5 2026]

[14] URL `https://www.ntruddock.com/product/aluminium-supply-ingot-sows/` [cited 10 June 2026]

use 1,080 kWh of energy, and will cost €4,176[15], and will be performed once per month to switch from 2xxx to 7xxx alloys or vice-versa. Furthermore, the system will use up to 143 l/min of Argon and 7 l/min of Cl_2. Argon is priced at €0.033/L[16] and Cl_2 at €0.01697 /l [77][17], so combining this with the degassing system's 6 tonnes per hour capacity yields a gas cost of €0.04837/kg of aluminium.

6.3.6. Dross Removal

All oxidation, fluxing, and degassing create a foam-like substance called dross on the melt surface. It is now called black dross, as one of the fluxing steps recovered most of the aluminium from it. This dross needs to be physically removed from the melt to ensure that the slab created at the end of the refining process is as good as possible. This will be achieved with specialised dross rakes, followed by placing the dross in cast-iron dross pans. The pan will cost around €1,500[18], with rakes starting at €200[19]. A total material cost of €4,000 will be used to cover spares and to fund the purchase of top-of-the-line equipment, with an additional €500 per year in maintenance costs.

The dross still has some aluminium content, which could be recovered using a dross press[20]. However, most of the aluminium has already been recovered from the dross during the fluxing stage, so investing in an expensive dross press is not worth it in our case.

6.3.7. Filtration

However, compared to other industry standards such as ceramic foam filters (CFF), there are some notable drawbacks[21]:

- DBF is a huge financial investment compared to the cheaper CFFs, but a CFF filter has to be replaced much more often[22].
- Swapping a CFF filter should not take more than five minutes and can be done by one person, but changing the filter media on a DBF requires up to 40 minutes from trained personnel. This has to be managed carefully on a continuous refining line, such as the line in this project[23].
- Alloy changes represent a significant challenge, as, similarly to the degassing system, the tank has to be flushed to prevent alloy cross-contamination of elements such as zinc and copper.

To achieve the required flow rate, together with an affordable price, the $20,000 or €17,282 DBFF-5 filter by Hydeb[24] was selected. It offers a flow rate of up to 8 tonnes per hour and a storage capacity of 500 kg. This rate meets the yearly capacity requirements, and the smaller tank minimises material loss during flushing when switching between alloys. Furthermore, the system will use a material recovery technique similar to the one described in the degassing step. When flushing the system, the aluminium melt will be cast into cheap sows, analysed with an OES machine, and sent back to the dilution stage, ensuring higher sustainability on the refining floor. Lastly, the DBF system requires significant energy to preheat, preventing cracking from heat shock. It uses 30 kW of power for 48 hours to preheat the system, then 15 kW to maintain the aluminium in a melted state, totalling over 130,000 kWh of energy per year. The more this system is used, the more economical and sustainable it becomes.

6.3.8. Slab Casting & Sheet Manufacturing

The melt cannot simply be cast into a sheet; it requires a specialised casting technique, along with other processes, to ensure the resulting sheet has the desired microstructure. Firstly, an automated wire feeder equipped with Al-Ti-B or Al-Ti-C wires feeds the alloy into the melt. This step happens right before the melt is cast into slabs. approximately 0.1 wt% of alloy is added [78], and this is done with a rod feeding unit from Hydeb[25] priced at $6,500 or €5,584.

Furthermore, specialised casting equipment, such as a hydraulic direct-chilling (DC) pit that cools the slab from the outside, is required to ensure proper casting. This expensive equipment, costing around €1.3 million from companies such as Wagstaff [79], can cast slabs weighing up to 15 tonnes with their innovative Airslip and APEX

---

[15] URL `https://www.alibaba.com/product-detail/Inox-Premium-Production-Standard-Competitive-Price_1601425253562.html` [cited 10 June 2026]

[16] URL `https://eziswapgas.co.nz/product/argon/` [cited 9 June 2026]

[17] URL `https://businessanalytiq.com/procurementanalytics/index/chlorine-price-index/` [cited June 10 2026]

[18] URL `https://htelite.en.made-in-china.com/product/XYzrHBGynDhS/China-Dross-Pan-V-Method-for-Aluminum-Casting.html` [cited 10 June 2026]

[19] URL `https://www.dykast.com/products/rakes/2782` [cited 10 June 2026]

[20] URL `https://www.drosspress.com/complete-guide-to-aluminum-dross-press-machines-everything-you-need-to-know-in-2025/` [cited 10 June 2026]

[21] URL `https://www.aluminiumceramicfiber.com/principle-of-deep-bed-filters/` [cited 11 June 2026]

[22] URL `https://www.adtechamm.com/deep-bed-filter/` [cited 11 June, 2026]

[23] URL `https://www.alalloycasting.com/deep-bed-filter/` [cited 11 June, 2026]

[24] URL `https://www.aluminiumfurnaces.com/sale-36754740-aluminium-foil-production-machine-deep-bed-filtration-box-dbff-10.html` [cited 11 June 2026]

[25] URL `https://www.aluminiumfurnaces.com/sale-54172082-used-for-the-production-of-aluminum-alloy-bars-applied-aluminum-casting-using-altib-rod.html` [cited 8 June 2026]

casting technology. This will be combined with electromagnetic stirring equipment, which forces the microstructure to become round and uniform [80], and high-shear melt conditioning with a spinning rotor to control both the cast microstructure and defect formation [81]. Lastly, strict superheat control will ensure that the melt is not too hot. This will result in the melt freezing instantly when hitting the mould, trapping the grains into a fine, tightly packed structure.

After the slab is cast, it will be sent to a specialised plant such as the Constellium Issoire plant, specialising in aerospace sheets[26]. The plant will heat the slabs for up to 24 hours to release elements trapped at the grain boundaries. Then, hot-rolling followed by cold-rolling will physically shape the slab into a thin sheet, with pancake-shaped grains aligned with the rolling direction. The sheets are then heat-treated and quenched, followed by a stretching and multi-stage ageing process to increase the sheet's resistance to stress-corrosion cracking. It is really hard ot estimate the cost of outsourcing this sheet manufacturing, as costs are hidden behind non-disclosure agreements and companies are not willing to disclose this information. But based on engineering estimates and rough differences between aluminium ingots and sheets on online marketplaces, the cost was estimated at €3.5/kg. The cost increases to €3.545, taking into account that 30% of the material is wasted during sheet production and needs to be remelted. Lastly, to calculate the energy required to produce sheets from AA2024 and AA7075 ingots, a paper by Kore et al. [82] was used. The paper estimates the life-cycle energy for AA2024 and AA7075 to be 120 MJ/kg and 140 MJ/kg, respectively, and that recycled alloys only use 5% to 10% of this energy. This means that their average energy usage is 3.7862 kWh/kg. Subtracting the total kWh/kg used for the refining process (without diluter production), that can be found in subsection 6.3.12, the sheet production uses a total of 2.612 kWh/kg of energy.

6.3.9. Material Recovery Rate

The material recovery rate is predominantly determined by dross creation and removal. Dissolved gas removal uses SNIF, which removes hydrogen gas, but does not deal with recovery rates. Finally, the material goes through deep bed filtration; due to losses incurred by the material not passing through, the loss is approximately 0.8%[27]. However, the material that does not pass through is flushed out using virgin aluminium/alloy and can be reused in the diluting process, thus it does not incur any losses. Oxidation and dross removal will thus be the only part of the refining process considered for the material recovery rate.

Since the aluminium is decoated, it is assumed to be clean. Typically, secondary processing of aluminium creates 30-50 kg of white dross per tonne [74]. Aluminium scrap remelting produces approximately 80-100 kg of dross per tonne [74]. Since the aluminium is in scraps, but clean, a value between 40-70 kg dross is assumed. The created dross consists of approximately 60-70% aluminium. Assuming a recovery rate of 83% with salt fluxing, the material recovery rate (MRR) is between 99.1-99.6% [74]. The example calculation for the upper end can be seen in Equation 6.3. This value assumes pure aluminium, since the material is not pure aluminium, but an alloy, the dross creation is different. Below, for the 2xxx and 7xxx series, a brief explanation is given.

$$MRR = 1 - \frac{40}{1000} \cdot 0.6c \cdot (1 - 0.83) = 1 - 0.005 = 99.6 \tag{6.3}$$

2xxx series Copper has very little impact on dross formation. The previously found value of 99.1-99.6% is kept as the value for this alloy [83].

7xxx series The magnesium content is highest in this alloy family. It consists of 1.9-3.1 wt% magnesium. In addition to this, it consists of 5.1-7.3 wt% zinc. Some zinc is lost due to evaporation [84]. Although it increases the dross quantity, it has less of an impact than the magnesium. The total increase of dross formation is 2-3 percentage points, creating 60-100 kg of dross per tonne [83]. This results in a recovery rate between 98.8-99.4%.

Finally, the ratios of these three alloy families are used to find an average MRR. The 2xxx series is approximately 45% of the aircraft, and 38% is 7xxx series. The other alloys are not remelted, so the ratio 45/38 is used. The total MRR is thus between 98.9-99.5%. The calculation for the lower bound follows Equation 6.4, using the lowest possible recovery rates for both series. The converse is done for the high end; this uses the highest values for both series.

$$MRR_{tot} = \frac{99.1 \cdot 45 + 98.8 \cdot 38}{38 + 45} = 98.9\% \tag{6.4}$$

This calculation is performed assuming the aluminium is completely cleaned and does not produce black dross before extracting metal from the white dross. However, if the material is not decoated, the dross mass generation in weight percentage can be up to 2-3 times higher [85]. Ignoring the effect on microstructure and the massive increase in toxic waste, skipping the decoating step would decrease the material recovery rate to 96.7-97.8%.

---

[26] URL `https://www.constellium.com/fr/sites-de-production/issoire` [cited 5 June 2026]

[27] URL `https://www.aluminiumceramicfiber.com/principle-of-deep-bed-filters/` [cited 28 May 2026]

6.3.10. Material Fingerprinting

As was just mentioned in subsection 6.3.9, the metal recovery rate is the ratio of useful output aluminium recovered to the input aluminium. To verify the recovery rate of the batches, a batch certification software such as Katana[28] can be utilised to trace the material losses during the recycling process, and obtain the final material recovery rate. This process would be called material fingerprinting and would ensure that clear material batches are tracked to ensure traceability and ease of certification. Another requirement that will be tracked is if the percentage of virgin aluminium added to the batch remains within the required 7 wt% range.

6.3.11. Testing and Certification

To certify the recycled aluminium alloys, the remelting facility must be an 'approved supplier'. This requires AS9100 certification and Nadcap accreditation. Nadcap is necessary for specific heat treatment and remelting processes. During the process, several tests are used for preliminary in-house verification. These include OES, hardness and ultimate/yield strength tests.

For each batch that is produced, it is required that an independent verification company complete certification tests. These labs need both ISO/IEC 17025 and Nadcap accreditation. The verification includes both a chemical and a mechanical analysis. Initial chemical composition analysis is done in the remelting plant while the material is still molten to allow for adjustments in composition. Then, a spectrochemical analysis is done of the solidified batch by an external party. Mechanical testing is done on the cooled and processed alloy [86]. The results are then linked to the unique batch via a batch number. Finally, this information is encoded into a digital material passport.

The amount of material that has to be tested is approximately 10-15 kg. This is consists of chemical testing (0.5-1kg), mechanical testing (5-10kg) and microstructure analysis (1kg). Since only pristine metal can be tested, crop ends are cut off. These can weigh around 50-100 kg [87]. However, this material is not wasted, but can be remelted into the next batch. Costs per batch are approximately €2,500 [88].

6.3.12. Refining Energy & Emissions Breakdown

With the process now set in stone, the energy required, along with the emissions produced and costs required, are calculated and tabulated in Table 6.3, Table 6.4 and Table 6.5. Firstly, the energy usages, mainly referring to electricity used by all subsystems, are tabulated in Table 6.3. Some subsystems, such as filtration, run continuously to avoid costly, lengthy pre-heating periods. The energy usage of other subsystems, such as the melting tank, which melts 2 tonnes of aluminium in an hour at 1,500 kW, is calculated on a per-kg basis. To get the energy used during the foundry processes, covering the entire refining process, to produce 1 kg of recycled aluminium, the numbers in the third column will be divided by the total amount of kg of aluminium processed per year, as shown in Equation 6.5:

$$E[kWh/kg] = \frac{E[kWh/year]}{n \cdot m}, \tag{6.5}$$

with n being the number of aircraft recycled and m the recyclable mass recovered per aircraft. Assuming 7,536 kg of aluminium can be recovered per aircraft, this number falls exactly on 2.5 kWh/kg of energy outputted by the foundry per kg of aluminium produced, and thus meets the requirement SYS-USR04-REC01-SUS-03 in Section 12.3. A notable figure in the table is the energy required to produce the virgin aluminium used in the dilution process. It was previously allowed to add up to 15% of the total melt mass in virgin material, but this will now be lowered to 7% to stay under 2.5 kWh of energy used per kg of recycled aluminium produced as a kg of virgin aluminium requires up to 15 kWh to produce [70]. Furthermore, the energy required for the sheet manufacturing is included in the table, even though it is not a part of the requirement SYS-USR04-REC01-SUS-03.

---

[28] URL `https://katanamrp.com/features/inventory-management/batch-lot-tracking/` [cited 10 June 2026]

Table 6.3: Energy breakdown of the refining process

Process Subsystem	Energy use [kWh/kg]	Energy use [kWh/year]
Forklift	0.004	2,600
Melting	0.75	-
OES	0.0017	1,000
Dilution	0.132	-
Production of Diluter	1.326	-
Fluxing	0	0
Degassing	0.026	12,960
Sow Casting	0	0
Dross Removal	0	0
Deep Bed Filtration	0.235	140,400
Grain refining	0	0
Slab Casting	0.025	-
Total	**2.500**	-
Sheet Production	2.612	-

Furthermore, SYS-USR04-REC01-SUS-02 requires the foundry processes to have 90% lower greenhouse gas emissions than their virgin counterparts. The foundry processes of virgin aluminium (melting, casting, heat treatment) produce an approximate amount of 0.4 to 0.8 kg of CO_2e/kg of aluminium [89].

Firstly, the electricity emissions are calculated by multiplying the energy used to produce a kg of aluminium by 0.027 kg CO_2/kWh, which is the average for France, the major place of operations, in 2025[29]. Furthermore, the European Environment Agency compiled all emissions from the production of secondary aluminium [90], and, combining this information with CO_2e emission factors according to the city of Winnipeg [91], the total emissions are presented in Table 6.4.

Table 6.4: Emissions breakdown of the refining process

Pollutant	Upper value	Conversion factor	CO_2e [kg/kg Al]
Energy in France	2.500 [kWh/kg]	0.027	0.068
TSP	2 [kg/t Al]	-	-
PM_{10}	1.4 [kg/t Al]	-	-
$PM_{2.5}$	0.55 [kg/t Al]	-	-
BC	2.3 [% of $PM_{2.5}$]	2.38	0.0055
PCDD/F	35[μg/t Al]	-	-
HCB	5 [g/t Al]	-	-
Total	-	-	**0.073**

Pollutants such as Total Suspended Particulates(TSP), PCDD/F, Hexachlorobenzene(HCB), and particulate matter (PM_{10} and $PM_{2.5}$) cannot be converted to CO_2e, as they do not contribute to global warming. They do, however, impose a safety risk to workers, and this should be addressed in the future to avoid dangerous working conditions in the casthouse.

6.3.13. Refining Cost Breakdown

Lastly, the costs of all refining subsystems will be broken down in Table 6.5. The costs are described in their respective subsection and then are divided into three categories. It should be noted that OPEX costs are per kg of aluminium sold to the recycled market or used in the green Cessna, and the fixed costs per year are long-term recurring costs such as the daily use of a forklift to lift heavy sows, or the 10 OES tests that will be performed per day to analyse the recycled melt composition as well as the composition of dilution sows.

---

[29] URL `https://www.nowtricity.com/country/france/` [cited 10 June 2026]

Table 6.5: Cost breakdown of the refining process

Process Subsystem	CAPEX [€]	OPEX [€ /kg]	Fixed costs per year [€]
Forklift	11,717	0	520
Melting	43,763	0.19	0
OES	18,950	0	5,561
Dilution	0	0.474	0
Fluxing	4,296	0.026	0
Degassing	51,546	0.049	50,112
Sow Casting	10,000	0	1,000
Dross Removal	4,000	0.005	500
Deep Bed Filtration	17,282	0	65,580
Grain refining	5,584	0.020	0
Slab Casting	1,300,000	0.025	0
Sheet Production	0	3.545	0
Total	**1,467,138**	**4.334**	**126,526**

7

Cessna Wing Structure

Reusing the recycled aluminium alloys in the aerospace industry is the primary objective of this section. Thus, the chosen product to reuse these alloys is a retrofitted Green Cessna 172S with a new design of the wing. This requires redesigning the conventional Cessna. These design changes involve using the recycled 7xxx series aluminium alloys. The new aircraft design will have a higher maximum take-off weight (MTOW) to account for the heavy electric propulsion system required to achieve an acceptable flight range. Specific range and endurance improvements are quantified in Chapter 8. The 7xxx series is used in the wing structure, which is a deviation from the material choice in the conventional Cessna. The material for the structural section of the fuselage is kept the same, the 2xxx alloys. The 6xxx series is applied to non-structural components. Therefore, the structural redesign focuses on designing the wing of the retrofit Cessna using the 7xxx series.

7.1. Increase in Wing Span

To achieve the required range and endurance for the retrofit Cessna, the maximum take-off weight of the conventional Cessna is insufficient. Therefore, the MTOW is increased by $+10\%$. This increase allows for the wing lifting surface area to be enlarged.

This change is chosen due to a relatively small change in the handling characteristics of the aircraft compared to the conventional Cessna 172S. The updated MTOW also allows for a substantial addition of battery cells, and places a smaller weight penalty on the wings' lift-to-weight ratio. The lift-to-weight ratio scales at different rates; the lift scales linearly. The weight increases quadratically as a result of increasing internal moment characteristics. As such, a preliminary aerodynamic wingspan sizing is done, which would provide the $+10\%$ in MTOW. With room for a margin for the increase in wing weight, choose an optimal increase in wingspan.

For this preliminary aerodynamic sizing, the increase in wingspan was treated as the primary method for increasing the lifting surface, while keeping the general Cessna 172S wing layout and handling characteristics relatively similar. Increasing the range span was evaluated under the assumption that the cruise velocity, air density, airfoil section and aerodynamic characteristics of the NACA 2412 profile remain unchanged, while the reference wing area increases proportionally with span. The lift produced by the redesigned wing is estimated using the standard lift relation from the given lift coefficient (C_L) values of the profile, while the drag coefficient (C_D) of the whole aircraft is evaluated with several assumptions. The first is the Oswald efficiency factor, which is assumed to be 0.8, and the drag contribution of the fuselage and landing gears is taken as approximately 0.025 [92]. Calculations based on the series of these assumptions have been done for the L/D fraction evaluation. The equations followed for those calculations have been provided in Equation 7.1. The aspect ratio ($AR = b/a$) is left in this format due to the wingspan being subject to constant iterations.

$$C_{Dwing} = (C_{D0} + \frac{C_L^2}{\pi e \frac{b}{a}}) \qquad C_{D_{fuselage}} = 0.025 \qquad C_D = C_{D_{wing}} + C_{D_{fuselage}} \tag{7.1}$$

The baseline aircraft weight used in this comparison is $W_0 = 11,277.65\,\mathrm{N}$ from 1,157 kg of the MTOW of the original Cessna 172S [93]. The additional mass that could be supported by the redesigned wing and the corresponding MTOW increase was then evaluated with the help of the following formula:

$$m_{\text{add}} = \frac{L - W_0}{g}, \tag{7.2}$$

The results show that the 15% wingspan increase provides enough lift capability to suffice the 10% MTOW increase when the aircraft operates close to the optimal cruise condition of the NACA 2412 airfoil, as depicted in Table 7.1. The 5° cruise condition was therefore selected as the most suitable design point, since it provides approximately 116.7% of the original MTOW while maintaining an efficient lift-to-drag ratio of about 13.15. This corresponds to an additional supported mass of approximately 192.8 kg, of which around 115 kg satisfies the required 10% MTOW increase, while the remaining margin is available to account for the increased structural mass of the enlarged wing, spar reinforcement, ribs, skin, strut attachment and manufacturing tolerances. As a baseline, the values and configuration of the wing for lower angles of attack (AoA) are also provided, due to the more suitable drag characteristics but worse lift-capable performance.

Table 7.1: Preliminary aerodynamic sizing results for the $(+15\%)$ wingspan increase

Cruise angle	(L/D)	Additional supported mass [kg]	Supported MTOW	Margin above MTOW
(4°)	13.13	112.71	109.74 %	-0.26%
(4.5°)	13.16	152.90	113.21%	3.21%
(5°)	13.15	192.82	116.67%	6.67%

Having chosen the increase of 15% in wingspan (b) the visualisation of this change has been presented in Figure 7.1.

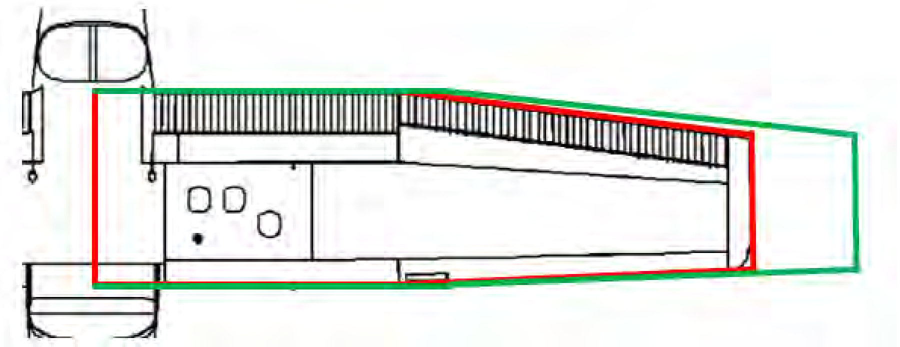

Figure 7.1: Increase of 15% in wingspan. New wing planform shown in green, compared to the original in red.

7.2. List of Requirements and Design-Constraining Assumptions

From the derivation of the driving requirement for the increase of the wing span, the design team had to update and create further design driving requirements. From the requirements, the list of design-constraining assumptions is also presented. These assumptions limit the scope of the analysis given to optimise the design.

Design Requirements

The wing redesign shall satisfy the following subsystem requirements:

1. The outer wing skin between stiffeners shall not buckle before the limit load.
2. The wing skin stiffened panels shall not cripple before the ultimate load.
3. None of the wing box components shall yield, due to axial stress, before the limit load.
4. None of the wing box components shall fail due to axial stress before the ultimate load.
5. The aircraft shall retain a high-wing, strut-braced wing configuration.
6. The wing shall be resized to support a 10% increase in maximum take-off weight (MTOW).
7. The redesigned wing shall provide sufficient lift for an electrically propelled trainer aircraft.
8. The design shall consider the use of recycled aluminium alloys supplied by the team foundry, with particular consideration given to 7xxx-series aluminium alloys.
9. The wing design shall define the required sizing, dimensions, and locations of the main wing structure and strut attachment points.
10. The redesigned wing structure shall be stronger and larger than the baseline configuration while remaining compatible with the selected high-wing strut-braced layout.
11. The assembly method shall minimise stress concentrations in regions experiencing the largest stress amplitudes. In particular, the use of rivets and bolts in or near the upper caps of Section 2 shall be minimised where possible.
12. Local load introduction at the strut attachment shall be accounted for through suitable structural reinforcement, but will not be designed in detail due to structural complexity.

Structural Assumptions

The following assumptions are made for the structural analysis:

1. The wing-box cross-section and its second moment of area, I_{xx}, shall be evaluated from the wing-box centreline rather than from the neutral axis of the mean-chord NACA 2412 airfoil section.
2. Combined loading shall be considered between the wing root and the strut attachment due to the axial load transferred from the strut into the wing spars, together with the distributed internal bending moment.
3. The wing section between the wing root and the strut attachment is modelled as a beam with a fixed support at the wing root and a pinned support at the strut attachment.
4. The wing weight, serving as the weight moment relief, is not considered in the structural load evaluation due to the preliminary stage of the design and the weight providing a moment relief.
5. Buckling evaluation shall be performed using Johnson's parabolic formula and Euler buckling theory, depending on the applicable slenderness range.
6. The fraction of the load carried by the front spar relative to the rear spar is assumed to depend on spar placement within the airfoil and the resulting spar heights.
7. A clearance criterion of $0.85(d/2)$ is assumed for the upper spar caps, while for the bottom caps, the spar-to-skin clearance criterion is $0.85(d/2)$. The exact application of this criterion shall be defined in the detailed design stage.
8. Inter-rivet failure is not considered in the current design stage.
9. The rib spacing, denoted by g, is used as the effective column length for local buckling checks. Because the skin and stiffeners provide partial-to-full rotational restraint at each rib intersection, the effective length factor is assumed to lie between $K = 0.5$ and $K = 0.7$. A conservative value of $K = 0.7$ is used.
10. Plates between wing stringers are assumed to behave as flat plates.

Aerodynamic Assumptions

The following assumptions are made for the aerodynamic analysis:

1. A Schrenk lift distribution is assumed over the wing span.
2. A zero-lift drag coefficient of $C_{D0} = 0.025$ is assumed, based on reference aircraft data and expected aerodynamic improvements from electric propulsion integration.
3. The NACA 2412 airfoil section is used, and the relationship between sectional lift coefficient, c_l, and wing lift coefficient, C_L, is evaluated accordingly.
4. An initial Oswald efficiency factor of $e = 0.8$ is assumed for the wing planform, which consists of a rectangular and slightly tapered chord distribution.

7.3. Use of Recycled Aluminium Alloys

This section elaborates on the use of AA2024 and AA7075 in the aircraft structure. The specific properties of both alloys are presented, and allocations for all components are concluded. The components of the wing are: spar, ribs, skin, stringers and the strut. The alloys are chosen based on their suitability for loading and design requirements.

7.3.1. Material Properties

The material properties of the two pristine aluminium alloys used in the structure are listed in Table 7.2. The AA7075 aluminium alloy is much stronger than the AA2024 alloy and would be suited to resist high peak stresses. The AA2024 aluminium alloy is much more ductile, thus suited to components with high manufacturability. It is also resistant to fatigue and can sustain high load cycles. The design took the approach of using the lower range end values. This decision has been made since the designed components are made with recycled aluminium alloys that have an increased risk of more imperfections, impurities and as such a larger range of deviation from the nominal range values. The decision was then made on the choice of lower-end values being taken, since the recycled aluminium alloys are to be refined to the level of aerospace-grade. The impacted design values, for instance, of the lowest yield strength, σ_y, and the highest densities, provided from the ranges, are used in the design.

Table 7.2: Typical mechanical properties of common aerospace aluminium alloys [60, 94]

Alloy	**Temper**	**Density** (g/cm^3)	**Elastic modulus** (GPa)	**Tensile properties**			**HCF limit** (MPa)	**Fracture toughness** ($MPa\sqrt{m}$)	**Poisson's ratio,** v
				Yield σ_y (MPa)	**Tensile** (MPa)	**El (%)**			
AA2024	T3	2.74-2.8	72-77	248-330	359-445	6-20	133-147	38-40	0.33
AA7075	T6	2.77-2.83	69-76	460-530	530-580	2-10	152-168	26.6-26.8	0.33

7.3.2. Material Allocation

The material allocation identifies where the high strength of AA7075 aluminium can be used effectively. This is done by accounting for its lower ductility and fatigue performance. This section lists the parts for which the use of AA7075 is beneficial.

The disadvantages of using AA7075 in aircraft structures are mainly related to its lower ductility. The following disadvantages can be summarised as:

- Poorer fracture toughness
- Notch sensitive
- Less formability than AA2024
- More susceptible to stress corrosion cracking
- Reduced fatigue crack growth resistance compared with AA2024
- Less forgiving around rivet holes

The four primary structural components of the wing are ribs, stringers, spars and wing skin. The ribs, stringers and wing skin are eliminated as options for the AA7075 alloy. The AA7075 is avoided in the wing skin because the skin contains many rivet holes and is exposed to fatigue cracking. This makes AA2024 more suitable due to its better damage tolerance, fracture toughness and fatigue crack growth resistance. Ribs are commonly thin, formed sheet-metal components, so the poorer formability and notch sensitivity of AA7075 make it less appropriate for these parts than the AA2024. Stringers also require good manufacturability, fatigue resistance and tolerance to fastener hole stress concentrations. Since the AA7075 does not perform well on these requirements, it is not used.

The spar has a simple design and is consistently subjected to the high unidirectional stress in its caps. Therefore, the high static strength of AA7075 can be used for the spar caps, where the dominant requirement is carrying high axial bending loads. However, another section of the spar web is a crack-sensitive region because it is exposed to heavily varying shear loads. This makes it more susceptible to high-cycle fatigue. Moreover, the spar web has:

- Many rivet holes
- Potential cutouts and lightning holes
- Local stress concentrations

Therefore, considering these design points, the caps shall be made with AA7075, utilising the high strength of this alloy, and the web will be made of AA2024.

For preliminary analysis, the assumption is made that the AA7075 spar caps carry the normal bending stresses, while the AA2024 web carries the shear flow. In a more detailed analysis, the web may carry some normal stress and local bearing loads. The structural analysis would treat the caps as carrying bending/direct stress and the web as carrying shear flow. This is used as a baseline to check for web buckling, fastener shear/bearing and cap crippling/buckling.

7.4. Loading on the Electric Cessna

Aerodynamic load evaluation will be done within this section. Initially, a velocity load factor diagram will be produced for the newly updated wing configuration. Then, a strut force evaluation and the reactive diffusion of this force into the spar will be evaluated with the energy method for this statically indeterminate problem. Lastly, a series of NVM diagrams shall be presented, creating the baseline for the structural design.

7.4.1. V-n Diagram

The requirements and set flight conditions are made at set values of the MTOW, V_C, AR, S wing surface and $C_{L,Max}$, which flow down from the NACA 2412 airfoil of the aircraft. Those values have a direct influence on the allowable load factors and flight regimes the aircraft is required to fly at.

The V-n diagram, Figure 7.2, presents the structural and aerodynamic service envelope by combining the manoeuvre envelope with the gust load limits. The green shaded region defines every permissible combination of airspeed and load factor, bounded on the left by the stall speed (V_s = 26.64 m/s), above by the positive stall curve rising to the maximum load factor of +4.6 g, and below by the negative gust boundary down to 2.6 g. The right edge closes vertically at the dive speed (V_D = 85 m/s), beyond which the aircraft's operation might be dangerous for the structure and for which the aircraft is not certified or even considered in any flight condition. Placed on the manoeuvre envelope are the gust load lines, where blue dashed for cruise gust (U_{de} = 15.24 m/s), and red dashed for dive gust (U_{de} = 7.62 m/s). Those lines have been computed using the Federal Aviation Regulations (FAR) gust alleviation factor K_g, which accounts for the aircraft's mass ratio and wing geometry. The green area is the design region that shall be considered for the retrofit of the Cessna.

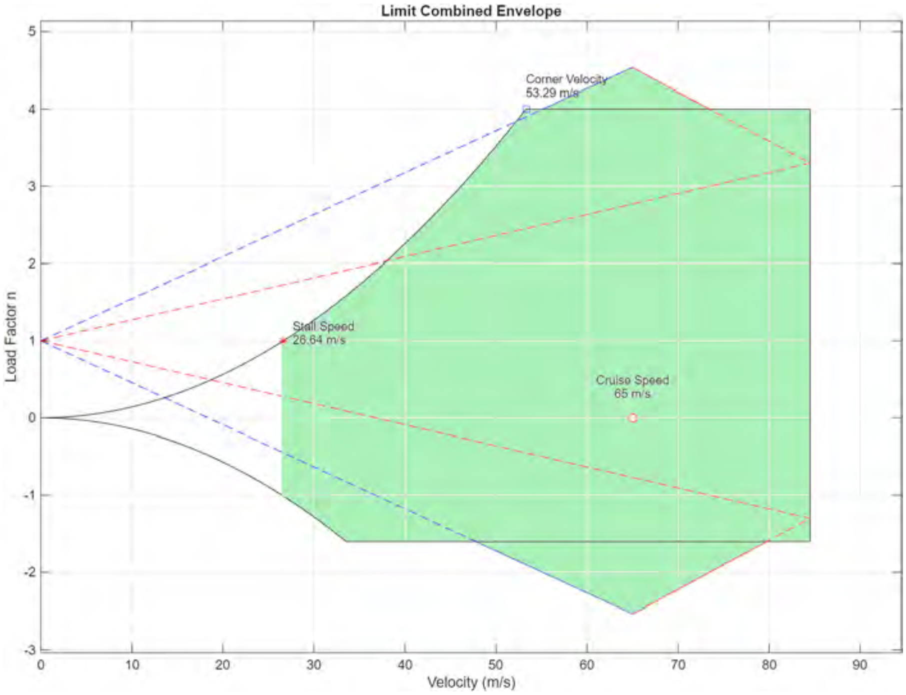

Figure 7.2: Flight envelope for the retrofitted Cessna 172S

7.4.2. Strut Load Path and Support Reactions via Castigliano's Second Theorem

The wing, together with the strut and the corresponding fuselage hard point it reacts against, is idealised as a planar structure viewed from the front in the yz plane. A body axis system is fixed at the wing root, with x pointing toward the nose, z measured spanwise toward the tip, and y vertical and positive downward. The lift therefore acts in the negative y direction, and the bending of the spar is taken about the chordwise x axis. The wing root joint B, the strut attachment C, the tip D and the fuselage hardpoint A lie at $B = (0,0)$, $C = (z_s,0)$, $D = (L,0)$ and $A = (0,h_s)$ in the $y - z$ plane, where the hardpoint sits at a positive y value because y is positive downward, as can be seen in Figure 7.3

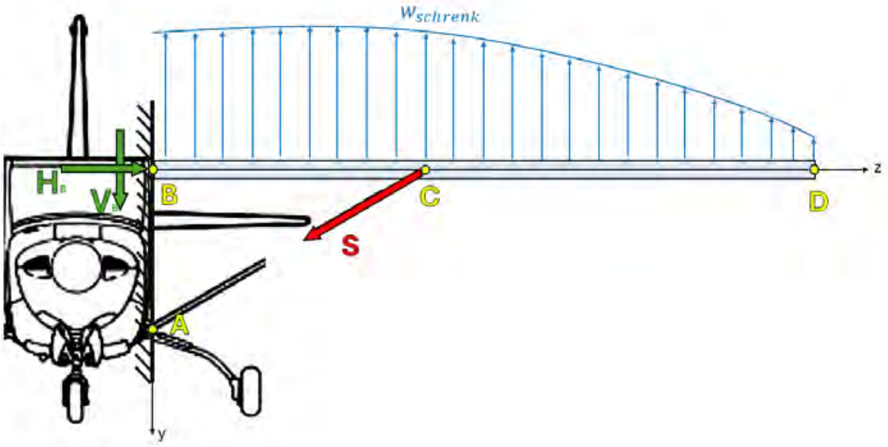

Figure 7.3: Front view of the Electric Cessna from the y-z plane

Using the planform geometry of the new design, facilitating the increase in $+10\%$ MTOW with $S = 18.461\,\mathrm{m}^2$ and $AR = 8.668$, the span is $b = \sqrt{S \cdot AR} = 12.65$ m and the semi-span is $L = b/2 = 6.325$ m. The strut attaches at $z_s = 0.6L = 3.795$ m and drops $h_s = 1.2$ m to the hardpoint, which fixes the strut length and inclination given in Equation 7.3. The purpose of the present analysis is to quantify the support reactions and the internal loads introduced by the strut.

$$L_s = \sqrt{z_s^2 + h_s^2} = 3.980 \text{ m}, \tag{7.3}$$

The attachment station at $0.6b/2$ is chosen because it is in the range of strut locations that minimises $\int |M(z)|$ over the span, which permits the high degree of mass optimisation in the spar structures of Section 7.5. This was made by using a range of strut locations. The decision was made on the basis that $0.6b/2$ connects at the last half wing span length before tapering occurs and still provides a great moment relief with the minimisation of $\int |M(z)|$ with the further analysis at subsection 7.5.3.

The wing is sized by the ultimate symmetric manoeuvre load, which is the limit load factor acting on the aircraft's weight, shared between the two wings and factored to ultimate. The corresponding value is given below:

$$W = mg = 12.87 \text{ kN}, \quad n = 4.6, \quad L_{\text{ult}}^{\text{semi}} = 1.5\left(\tfrac{1}{2} n W\right) = 44.39 \text{ kN},$$

The spanwise running load $w(y)$ is estimated using Schrenk's approximation, which takes the mean of a chord-proportional loading and an elliptical loading with the same total lift. This is appropriate for the investigated wing because the planform is not a simple, fully tapered trapezoid. As shown in Figure 7.1, the inboard part of the wing has a constant chord, while the outer part is tapered towards the tip. The resulting Schrenk loading is written in Equation 7.4.

$$w_{\text{Schrenk}}(y) = \frac{1}{2}\left[w_c(y) + w_e(y)\right], \tag{7.4}$$

where the chord-proportional loading is

$$w_c(y) = L_{\text{half}} \frac{c(y)}{\displaystyle\int_0^L c(y)\,\mathrm{d}y}, \tag{7.5}$$

and the elliptical loading is

$$w_e(y) = \frac{4L_{\text{half}}}{\pi L}\sqrt{1 - \left(\frac{y}{L}\right)^2}. \tag{7.6}$$

Here, y is the spanwise coordinate measured from the wing root to the tip, $L = b/2$ is the semi-span, and L_{half} is the total lift carried by one half-wing. The chord distribution is not expressed using a single root chord c_r and taper ratio λ. Instead, the actual measured $c(y)$ distribution is used directly. This avoids incorrectly assuming that the wing tapers linearly from the root to the tip, whereas the investigated wing has a mostly rectangular inboard section and only tapers over the outboard region. The ideal wing that approaches this distribution is the elliptical planform, and the locally tapered wing resulting in the total half-wing lift distribution at Equation 7.7.

$$\int_0^L w(z)\,\mathrm{d}z = L_{\text{ult}}^{\text{semi}} \qquad w(z) = L_{\text{ult}}^{\text{semi}} \cdot \frac{1}{2}\left(\frac{\sqrt{1-(z/L)^2}}{\displaystyle\int_0^L \sqrt{1-(z/L)^2}\,\mathrm{d}z} + \frac{c(z)}{\displaystyle\int_0^L c(z)\,\mathrm{d}z}\right) \tag{7.7}$$

The resulting centre of pressure of this lift distribution is the mean of the elliptical and trapezoidal centroids, and it sits at $\bar{y} = 2.830$ m from the root, which is 44.7% of the semi-span. While the strut is pinned at both A and C, where C carries no distributed load nor moment, it is treated as a two-force member whose internal force S acts purely along the AC direction. Considering a manoeuvre resulting in a positive $(+n)$ manoeuvre, the wing lifts and rotates upward about the root. The strut is anchored below at A, so it is stretched and acts in tension, and its vertical component reacts to the bulk of the lift while relieving the root of bending, while its spanwise component is fed into the spar as an axial force. In the negative $(-n)$ case, the load reverses, and the strut is driven into compression, which is the condition that governs its buckling design. Because the force is axial, its two components on the spar at C are tied by the strut geometry, as given in Equation 7.8.

$$V_s = S\,\frac{h_s}{L_s}, \qquad H_s = S\,\frac{z_s}{L_s}, \qquad \frac{H_s}{V_s} = \frac{z_s}{h_s}. \tag{7.8}$$

Modelling the root as a joint that resists moment leaves four unknown reactions, which are the root vertical V_B, the root horizontal H_B, the root moment M_B and the strut force S. These act against only three equilibrium equations, so the structure is statically indeterminate to the order of first degree and one further equation is needed. This equation is supplied by Castigliano's second theorem, which is the form of energy method equivalent to the unit load method. With the assumption that the structure does not deform plastically, the displacement conjugate to a force P is recovered from $\delta = \partial U/\partial P$, where the complementary strain energy of the structure is dominated by spar bending with the strut axial term retained, as given in Equation 7.9.

$$U = \int_0^L \frac{M(z)^2}{2EI}\,\mathrm{d}z + \frac{S^2 L_s}{2E_s A_s}. \tag{7.9}$$

The strut force is taken as the redundant because removing the strut reduces the wing to a determinate cantilever beam for which the internal bending moment can be written directly from equilibrium. The unknown strut force is then recovered by enforcing the compatibility condition that the deflection of point (C) along the strut axis is zero. Since the fuselage anchor A is rigid, the displacement of C along the strut axis is zero, and setting $\partial U/\partial S = 0$ applies the principle of least work. This gives the closing condition stated in Equation 7.10.

$$\int_0^{z_s} M(z)\,\frac{\partial M(z)}{\partial S}\,\frac{\mathrm{d}z}{EI} + \frac{S\,L_s}{E_s A_s} = 0. \tag{7.10}$$

In this condition, the inboard bending moment is the cantilever moment due to the lift alone, reduced by the strut vertical reaction, as expressed in Equation 7.11.

$$M(z) = M_w(z) - S\,\frac{h_s}{L_s}\,(z_s - z), \qquad M_w(z) = \int_z^L w(z')\,(z' - z)\,\mathrm{d}z', \qquad \frac{\partial M}{\partial S} = -\frac{h_s}{L_s}(z_s - z). \tag{7.11}$$

If the small strut axial flexibility is neglected, the closing condition reduces to the requirement that the spar deflection at C vanish, and the strut vertical reaction then follows directly from Equation 7.12. The result shows that the strut reacts to the entire lift moment about the root essentially and drives the residual root moment to near zero.

$$V_s = \frac{3}{z_s^3}\int_0^{z_s} M_w(z)\,(z_s - z)\,\mathrm{d}z = 0.746\,L_{\text{ult}}^{\text{semi}}. \tag{7.12}$$

With S fixed by Equation 7.12, the remaining reactions follow from equilibrium through $V_B = L_{\text{ult}}^{\text{semi}} - V_s$ and $H_B = H_s$.

Table 7.3: Summary of ultimate loads and reactions for the strut and root

Parameter	**Symbol**	**Value**
Strut ultimate axial tension	S	109.8 kN
Strut vertical component	V_s	33.1 kN
Strut spanwise component	H_s	104.7 kN
Root transverse shear	V_B	11.3 kN
Root horizontal reaction	H_B	104.7 kN
Root bending moment	M_B	0 kNm
Strut ultimate compression (Pushover)	S_{comp}	62.1 kN

In the pushover case, the same load path reverses, and the strut sees an ultimate compression of 62.1 kN, which is the value that drives the buckling design of the strut. A further evaluation of (-n) manoeuvres is also crucial for the design of the stringers and the wing box.

7.4.3. NVM Diagrams

The internal force diagrams for the normal force, N, the shear force, V and the moment, M are constructed by sectioning the spar from the free tip inward. Outboard of the strut, between the attachment and the tip, the strut does not act on the section, so the axial force is zero, the shear is the integrated lift outboard of the cut, and the bending moment is the first moment of that lift about the section. Inboard of the strut, the spanwise component is reacted at the root and compresses the bay, so the inboard axial force is constant and equal to the value given in Equation 7.13, which is the high compression that the wing box of Section 7.6 must carry in regions 1 and 2.

$$N(z) = -H_s = -104.7 \text{ kN}, \qquad 0 \leq z < z_s. \tag{7.13}$$

The inboard shear is the integrated outboard lift reduced by the strut vertical reaction, as given in Equation 7.14. This produces a root shear of $V(0) = 11.3$ kN and a step of magnitude $V_s = 33.1$ kN at the strut station.

$$V(z) = \int_z^L w(z')\,\mathrm{d}z' - V_s, \qquad 0 \leq z < z_s. \tag{7.14}$$

The inboard bending moment is obtained by integrating this shear, as given in Equation 7.15.

$$M(z) = \int_z^L w(z')(z'-z)\,\mathrm{d}z' - V_s(z_s - z), \qquad 0 \leq z < z_s. \tag{7.15}$$

The moment is zero at the root; it then develops a weak sagging behaviour through the first section from the root, passing back through zero near $z = 2.7$ m, and rises to a hogging peak of 14 kN·m at the strut attachment before decaying to zero at the tip, as shown in Figure 7.4 and Figure 7.5. Therefore, until the $z = 2.7$ point, it is the bottom caps and lower wing section that experience combined compressive forces acting from the internal bending moment and axial force. As it was expected, the region of $z = 2.7$ to $z = 3.8$ serves as the biggest combined compressive loads that the internal wing structure would be subjected to. This confirms that the strut, sized through Castigliano's compatibility condition, relieves the root of bending and establishes the intended load path, in which the lift passes into the wing spar, then through the strut as an axial force, and finally into the fuselage frame.

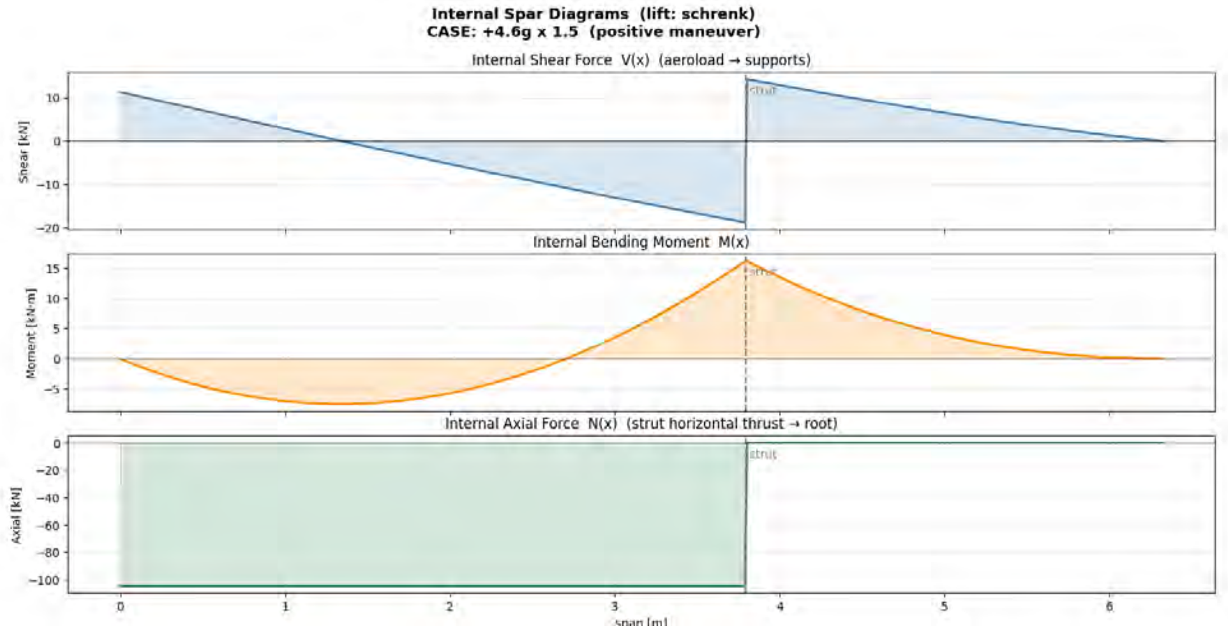

Figure 7.4: Flight envelope for retrofitted Cessna 172S

In contrast, a reversed loading (-2.6 g) (push-off) scenario is worth investigating as well. This loading scenario retains the exact equation characteristics, but with the sign and magnitude change of a factor of $2.6/4.6$. This scenario is worth investigating, especially from the $z = 2.7$ point, the internal bending moment and the produced compressive forces would dictate the cap sizing and against buckling strategies.

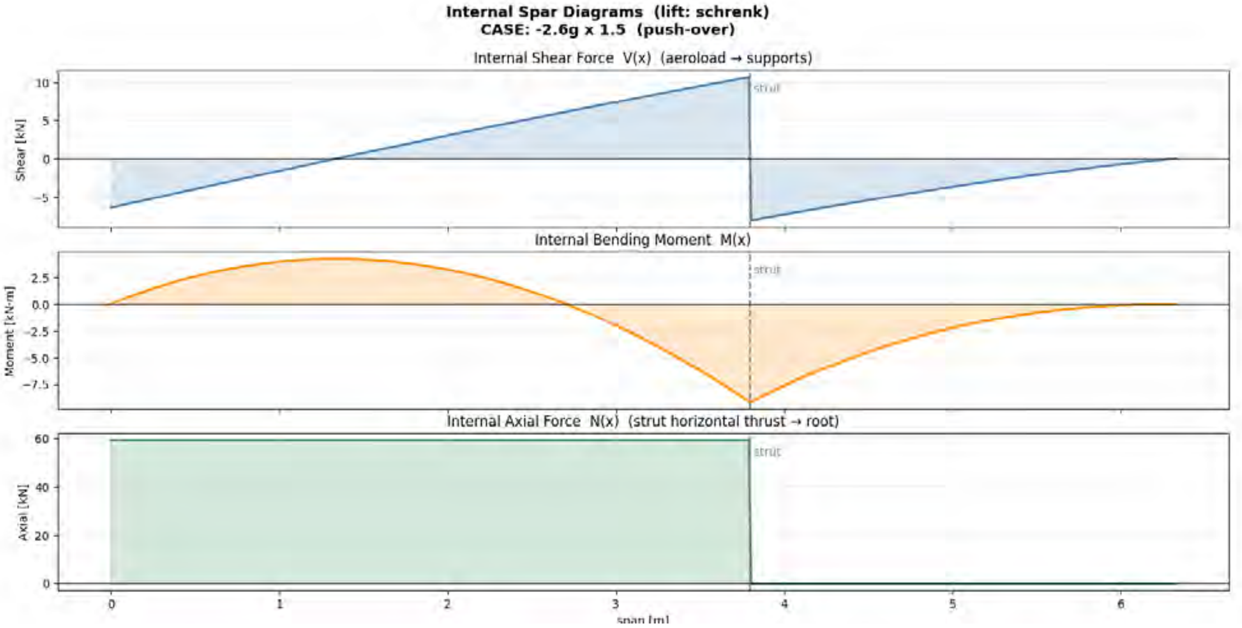

Figure 7.5: Flight envelope for retrofitted Cessna 172S

To obtain the torsional moment (T) about the z-axis, *XFOIL* was used to find the pitching moment coefficient C_m. *XFOIL* requires multiple inputs to find the appropriate value. First, the NACA 2412 aerofoil was selected, and then the Reynolds number, Re = 9.2 million. This is calculated with Equation 7.16, where V is set as the dive speed, c is the chord length, and v is the kinematic viscosity at sea level [95]. Finally, the reference point was set to $0.425 \cdot c$, the centre of the wing box, so that the software accounts for the moment created by the lift force. As a result, C_m at multiple angles of attack is generated, and the largest one is selected at an angle of attack of 15 degrees. Finally, Equation 7.17 can be used to find the magnitude of the torsional moment.

$$Re = \frac{Vc}{v} \tag{7.16}$$

$$T = C_m \frac{1}{2} \rho V^2 S c \tag{7.17}$$

7.5. Internal Structure Wing Design

The structural design approach begins with primary load-carrying elements. The wing spar is a critical part of the wing as it bears the primary internal bending stresses caused by the distributed lift. The highest compressive and tensile stresses occur in the relative upper and lower caps of the spar, with the web being responsible for carrying the internal shear force. To use the maximum load-bearing capability of the spar made of AA7075-T6, the rib spacing is adjusted to maximise the critical column buckling load, which was determined to be the governing constraint.

As shown in this example, the internal wing structure is highly susceptible to iterations. This section will go through the design chronologically.

Initial load design considerations and the subsequent failure modes have been taken into account. The main driving loads acting through the wing structure that shall be supported are:

1. Internal Bending Moment
2. Internal Shear force
3. Internal Axial forces in the Spars and the Strut
4. Internal Torsional Moment

"The reactive axial force transmitted by the strut acts as a compressive load on the wing spar during cruise. Therefore, the simultaneous application of the worst-case internal bending moment and this compressive force yields the driving critical load case for the structure.

The axial force acting as a reaction to the strut, when in cruise, creates a compressive load in the spars. The combination of the worst-case compressive load, combined with the loading scenario for internal moment, results in the driving critical loading scenario.

The considered failure modes are:

1. Column Buckling
2. Plastic Deformation
3. Shear Web Buckling
4. Compression Flange Local Buckling
5. Crippling

The omitted failure modes are:

1. Inter-rivet sheet buckling
2. Fatigue Failure, although minimisation is mentioned, especially for the AA7075-T6 alloy
3. Corrosion Fatigue Failure, although measures to minimise galvanic coupling and the use of a coating for mitigation

7.5.1. Spar Design

The spar design is the baseline for the structural wing design and is subjected to the highest number of design iterations. The spar accounts for a significant mass contribution in the design. Therefore, its structural and weight optimisation is prioritised. The spar design will contain the cross-section type, its dimensions, the number of spars and their respective lengths. The spar design, as well as other parts, is primarily dependent on the NVM diagrams, which serve as the baseline of the structural analysis and part design.

The design of the I-beam has an I_{xy} of zero. As an alternative, a C-shaped strut design was considered due to its higher torsional moment. A C-shape is asymmetrical, meaning its shear centre sits outside the physical shape. This causes the C shape to naturally twist or warp when loaded, which compromises its strength. Due to its configuration, a C-shaped spar has very low inherent resistance to buckling. However, using a properly designed wing box can provide the necessary external support. Due to the added complexity of the C-shape, an I-shaped spar design is chosen.

The AA7075 alloy has a yield stress, σ_y, between 460 and 530 MPa. The spar design uses the lowest value of 460 MPa. This design decision is made to create sufficient margin to account for alloy depreciation in the recycling process. The design also applies a safety factor of 1.5 to the life loading when deriving the internal moment distribution.

$$\sigma_y = \frac{M(z) \cdot d/2}{I_{xx}} \tag{7.18}$$

The conservative assumption is made that all bending stresses are carried by the caps, and the web solely carries the shear stresses. The spar is divided into top and bottom regions, both of which are sized separately, minimising the required total amount of material. In the worst-case scenario of combined loading (internal moment and compressive force), the top cap will experience a significantly higher stress than the lower flange. Moreover, the loading scenarios of the manoeuvres' load factors are disproportionate (4.6 g and -2.6 g); thus, the spar is manufactured with separate top and bottom areas.

The appropriate clearance from the skin needs to be made for the spar caps to be placed. Appropriate clearance to place the spar caps is calculated for both the top and bottom of the profile. The high curvature of the top profile section has a clearance of 0.15 times the half-wing span. The bottom has a relatively flat curvature; thus, it decreases to 0.1 times the half wingspan.

$$I_{xx} = A_{top}(0.85d/2)^2 + A_{bot}(0.9d/2)^2 \tag{7.19}$$

The distance (d) of caps separation and the location where the spar is assigned to be placed is defined by the NACA 2412 airfoil dimensions. As can be seen in Figure 7.6, the curvature is more restrictive at the upper section, and the precise dimensions can be seen for the 0.2 times the cord length location of the front spar.

The NACA 2412 airfoil geometry determines the separation distance between the spar caps, d, and the chordwise location of the front spar. The curvature is more restrictive on the upper surface. The dimensions at the $0.2c$ chord position are shown in Figure 7.6.

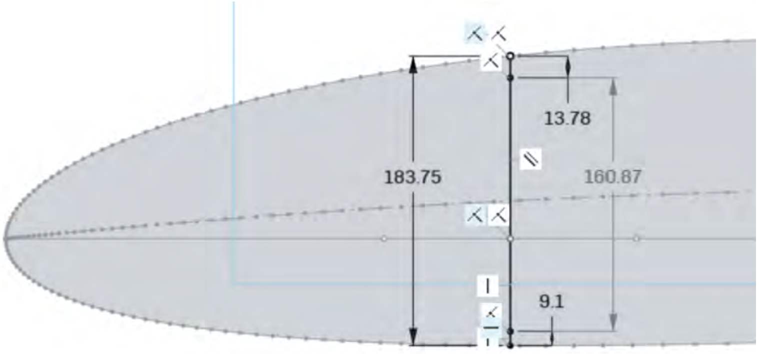

Figure 7.6: Positioning of the spar for the NACA2412 at 0.2c length

The cross sections of the spar caps are governed by comparing their critical local buckling stress to the yield strength (σ_y) of the material. Although the idealised bending model depends mainly on the cap area and cap separation distance, the final cap geometry is defined to satisfy local buckling constraints.

The idealisation assumption is taken out, and the dimensions of the caps are of importance. Thinner caps are more desirable as they can be manufactured to maximise the actual inertia moment; on the other hand, local compression cap buckling restricts slenderness and thinness. The formula Equation 7.20which provides the required ratio between the cap thickness and the cap width, (b). In this equation, (k) is the plate buckling coefficient. A conservative value of $(k = 4)$ is taken, this corresponds to a simply supported rectangular plate. The Young's modulus (E), is taken as the modulus of AA7075-T6 aluminium.

$$\sigma_y = \sigma_{cr} = \frac{k\pi^2 E}{12(1-v^2)}(\frac{t}{b})^2 \tag{7.20}$$

From the transverse shear stress formula, the thickness of the initial spar web is derived.

To find the shear yield allowable for the spar web, the von Mises yield criterion is applied to the pure shear case. This yields $\tau_y = \sigma_y/\sqrt{3}$. However, similarly to the dimensioning of the caps, the web dimensions follow a buckling constraint. Plastic shear is not the design driver of the area of the web. Elastic plate buckling shear stress is found to be more critical, see Equation 7.21. As the height of the web is fixed, the thickness is determined. The value of the Young's modulus, E, is assumed to be 72 GPa, the value associated with AA2024-T6.

$$\tau_{cr} = \frac{k_s \pi^2 E}{12(1-v^2)} (\frac{t}{d})^2 \tag{7.21}$$

Initial sizing positioned a single spar at the 25% chord line $(c/4)$. However, it was found that a double spar configuration provides better torsional stiffness and stress relief for the front spar. This spar is responsible for carrying a significant amount of the normal force stress from the strut. This configuration places the front spar in front of $c/4$, and the rear spar further aft. The rear spar would provide counter-torsional relief. This causes the torsion to be transferred by bending the rear spar upwards and the front spar downwards, where the spars and skin together form an enclosed wing box area, which is the main carrier of torsional loads in the wing Equation 7.22. A_m represents the enclosed area between the spars and the skin of the wing. Therefore, an increase in separation distance between the spars squares the torsional stiffness K_t.

$$K_t = \frac{4A_m^2 G}{\oint ds/t} \tag{7.22}$$

The respective chosen locations are found to be 0.2c and 0.65c. The design decision is dictated by allowing a substantial increase in the enclosed area, and by decreasing the overall wing skin thickness, which has a large contribution to the weight, but also providing at least a fractional carried moment and therefore area relief. The final fraction of moment carried by the rear spar follows the moment to inertia relation, where the caps distance is the governing determinant of the inertia value of $M_r/M_f = I_r/I_f$. Their respective moments of inertia are quadratically proportional to the distance.

$$\frac{113^2}{113^2+161^2} = 0.3301 \tag{7.23}$$

A further design iteration on the wing box, including the design of accompanying stiffeners and chosen wing skin thickness, is shown in Section 7.6; however, another load scenario is taken into account, torsion, which is not the main sizing driver of the spar dimensions.

Lastly, a design approach was chosen following the investigation of the internal moment diagram to split the internal wing structure into four design regions. A conservative approach is chosen for the constant cross-sectional area, determined by the highest combined loading stress condition from the internal axial force and internal moment across regions 1 and 2. While region 3 follows the linear chord taper in the respective height. This taper of the spar is assumed due to the quadratic decrease over the wing span length in that region. Finally, it was decided that region 4 does not include any spars, where the internal moment is primarily carried by the wing skin. The respective region distances have been summarised within Figure 7.7 and quantified in Table 7.4.

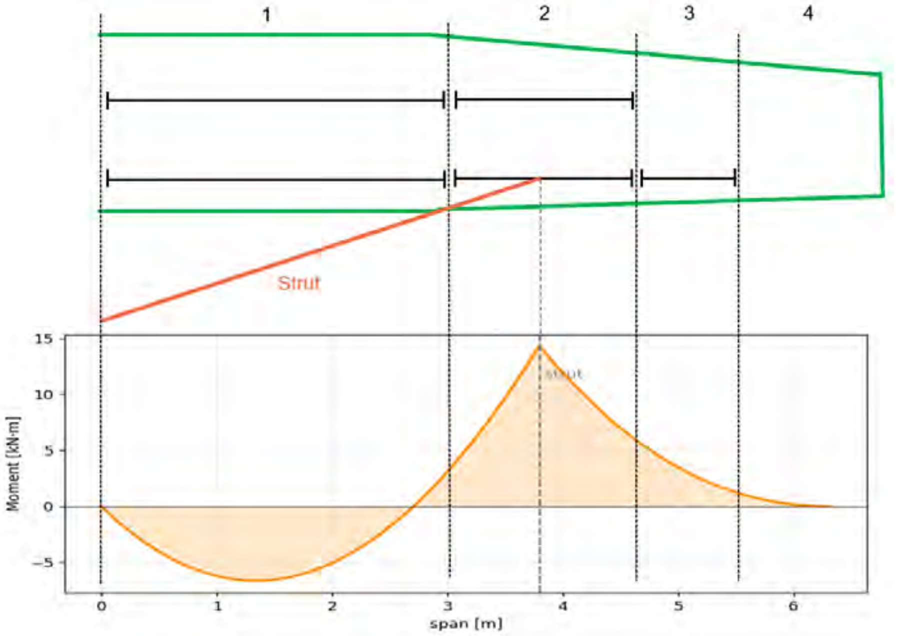

Figure 7.7: Illustration showing the 4 spar zones on the left wing, top view, and their respective bending loads.

Table 7.4: Region length splits

Region	From [m]	To [m]
1	0	3.0
2	3.0	4.6
3	4.6	5.5
4	5.5	6.25

Last Iteration Spar Design

After determining the governing load scenarios, these serve as a baseline for further component design. Design values for thicknesses obtained from the calculation of the web thicknesses are rounded up by 0.2 mm. This is used as the manufacturing tolerance of the produced material. Therefore, the values in Table 7.5 and Table 7.6 are rounded up conservatively.

Table 7.5: Spar dimensions and thicknesses across regions

Region	b_{top} [mm]	b_{bot} [mm]	t_{top} [mm]	t_{bot} [mm]	t_{web} [mm]
1	55	60	3.0	3.3	3.2
2	75	45	3.6	2.3	3.6
3	45	45	2.3	2.3	3.0

Due to no differential between the compressive and tensile strength yield target, the rear spar is symmetric. The dimensions are determined through local flange buckling.

Table 7.6: Rear Spar dimensions and thicknesses across regions

Region	b_{rear} [mm]	t_{rear} [mm]	t_{web} [mm]
1	40	1.8	2.2
2	55	2.5	2.6

7.5.2. Ribs Design and Spacing

During spar design, it is assumed that all strut load is borne by the front spar. However, this is a conservative estimate; in reality, the load would be distributed through the front spar, skin, ribs, rear spar, local strut fitting and the torsional wing box. However, this assumption allows for the preliminary design of the rib spacing. This spacing is determined through the limitation of the effective length of the front spar in column buckling.

The front spar is laterally restrained at each rib station. The ribs connect the front spar to the rear spar and skin structure, forming a braced wing box. Therefore, the effective buckling length is taken as the rib spacing rather than the full strut-root distance. Since Euler's critical load scales with $1/L^2$. This substantially increases the global buckling resistance. The placement of the ribs allows for the sizing of the spar based on its plastic strength regime and the governing failure modes of σ_y. Because the skin and stiffeners provide partial rotational fixing at each rib intersection, the effective length factor typically ranges from $K_r = 0.5$ (fully fixed) to $K_r = 0.7$ (fixed-pinned) for the effective length factor. The conservative factor of 0.7 is considered. An effective length factor of $K_r = 0.5$ is adopted because the spar cap is not idealised as an isolated pin-ended column. At each rib, the spar web, rib, skin and stiffeners provide significant rotational restraint, making the local spar segment closer to a fixed-fixed member rather than to a fixed-pinned one. Euler buckling stress, provided in Equation 7.24, varies with $1/K_r^2$, this assumption will be validated during later design stages by checking the stiffness of the ribs, spar to rib joints and skin attachments.

$$\sigma_{cr} = \frac{\pi^2 E}{(K_r L_{rib}/\rho)^2} \tag{7.24}$$

There is a drawback to introducing the ribs: a discrete mass penalty to the overall wing structure. The design challenge is a trade-off between increasing the number of ribs, raising σ_{cr}, but adding localised mass, and increasing the spar web thickness t_{web}, which increases mass continuously along the span. Too few ribs result in larger unsupported spar lengths, causing buckling and requiring an oversized spar. On the other hand, too many ribs add unnecessary mass. The optimal configuration is therefore minimising total structural mass, while ensuring σ_{cr} remains above the σ_y of the spars. After a third iteration, the rib spacing considered is the design where the cut-off of the rib at a distance of 0.7c is included. Due to small loads induced in the last section and lack of spar in region 4, it would not buckle. As such, for this longer distance its the torsional strength that serves as the main driving load.

Table 7.7: Ribs Count across Regions

Region	Ribs Count	L_{rib} **[mm]**	L_{rib}/d
1	9	375	2.32
2	4	400	2.59
3	3	300	2.33
4	1	800	6.72

Another consideration is the method in which the spars are connected. The selected design approach joins the spar components using riveted connection surfaces between the spar caps and web, while also providing suitable attachment interfaces for the rib supports. Higher stress concentration due to the presence of the rivet holes is of less concern for the less stressed web than the highly stressed cap. The design minimises the number of rivets in the highly stressed sections, and the use of supportive brackets connecting ribs and spars.

The introduction of lightening holes in the ribs presents an opportunity for structural weight reduction. However, these holes cannot be placed arbitrarily, since sufficient solid material must remain between adjacent holes and around the rib boundaries to maintain the load path through the rib web. For preliminary sizing, standard aerospace design guidelines are applied to limit the hole geometry. The hole diameter (D) should generally not exceed 50% to 70% [96] of the local rib web depth (h) giving the preliminary constraint (D $\leq 0.7h$). In addition, the spacing between the centres of adjacent holes (P) must leave an adequate solid web post between them.

Adequate edge distance is maintained between each hole and the spar attachment flanges to avoid local stress concentrations and preserve the load transfer into the spars. These rules provide a conservative basis for the preliminary rib lightening-hole layout, which should be refined in later design stages using detailed analysis. A minimum post width of approximately 0.3D is frequently used in hole spacing as a primary for wing skin clearance and spacing between the holes. For this lightening holes design, it was chosen to keep 0.3D wing skin clearance but increase the spacing between the holes to 0.5D due to the double stress concentration and stress flow from both circles' directions. As such, the spacing used resulted in ($\geq 1.5D$) for the final design. Visualisation of the final lighting hole placement can be seen at Figure 7.8, where the rightmost hole was sized to the nearest rear spar, resulting in 80 mm (113 $\cdot 0.7$ ≈ 80 mm). Thin-walled ribs are often allowed to buckle under high ultimate loads, provided these do not permanently deform or fail. A reference of 1mm thick ribs has been used [97]. The presented drawing of rib design is applicable for ribs located in region 1 and half of region 2 until $3.8m$ corresponding to strut attachment.

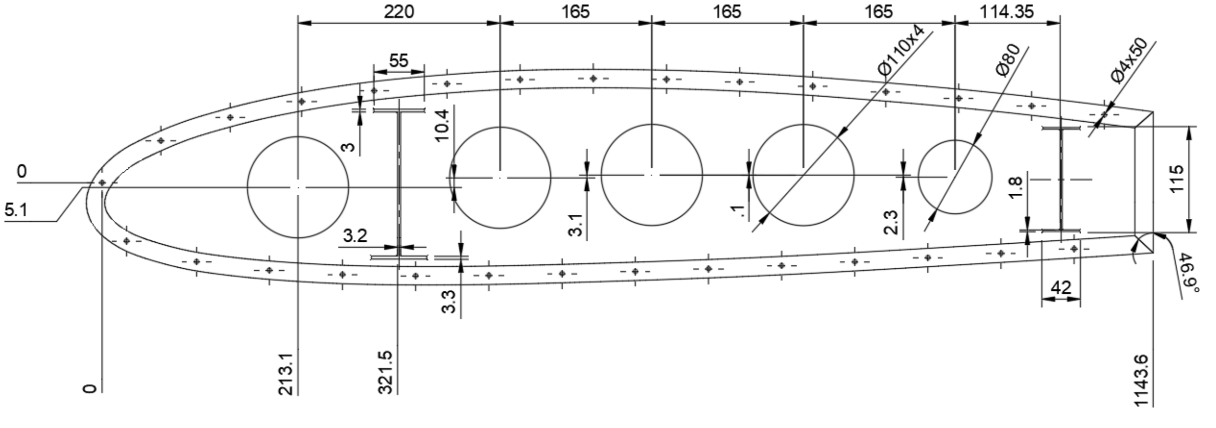

Figure 7.8: Ribs Holes placement along the camber line with 0.3D skin spacing, 0.5D spacing in between, D=0.7h and overall design of the rib in region 1, drawn in engineering E drawing

The engineering drawing is created for the sheet metal forming of the rib. The outer sheet layer is 20 mm thick and has rivet holes of 4 mm in diameter with a spacing of 32 mm. The dimensions have been chosen based on [98]; this is the baseline for rib sheet manufacturing.

7.5.3. Strut Design

A negative g manoeuvre serves as the main driver for the strut redesign, due to the induced compressive load. Therefore, buckling is the primary design driver for the strut dimensions. The assumption of $C = 0.8$ falls in the upper limit of the fixed-to-pinned strut support. Moreover, the most frequent loading to which the strut is subjected is the on-ground bracing of the wing weight. The effective length L_e, therefore, can be quantified with reference to subsection 7.4.2 calculation of length and the C factor.

Since column buckling is the governing failure scenario in this case, this results in a required minimum moment of inertia resisting the buckling stemming from the Equation 7.25. The design will be a circular hollow tube. While a streamlined profile was considered, the hollow tube was ultimately chosen due to its simpler manufacturing and easier analysis.

$$P_{cr} = \frac{\pi^2 E I_{xx}}{(CL)^2} = \frac{\pi^2 E I_{xx}}{L_e^2} \tag{7.25}$$

A key design driver is the location of the strut attachment at 0.6*b/2 length of the wing. This location minimises the $\int |M(z)|$ value over the wing span, therefore leading to the potential for the most optimal weight saving made within the wing structure. This location was found via NVM calculation with the use of 0.05c length spacing. The main trade-off for this decision is the higher length of the strut and, as such, an increase in the required moment of inertia to support the buckling load. x

Table 7.8: Comprehensive strut material, geometric, and structural properties

Property	Value
Material	AA2024-T3
Effective Length (L_e)	3.184 m
Radius (r)	5.5 cm
Wall Thickness (t)	2.2 mm
Cross-sectional Area (A)	$7.60 \cdot 10^{-4}$ m^2
Area Moment of Inertia (I_{xx})	$1.15 \cdot 10^{-6}$ m^4
Slenderness Ratio (L_e/r)	81.87
Mass	8.503 kg

7.6. Wing Box Idealisation

A wing box is a primary torsional and bending-resistant structure within an aircraft wing, typically formed by the front and rear spars, the upper and lower skins, and the ribs. For preliminary design, this structure can be idealised, allowing iteration of spar cap area, stringer area, and skin thickness. To idealise, the actual continuous skin-stringer-spar configuration is reduced to a set of discrete booms that carry all axial stresses, while the thin skin is assumed to carry only shear stresses (torsion). This will be done for each cross-section that needs to be analysed, as some parts of the wing will need to sustain higher loads than others, and some cross-sections are tapered (leading to a different wing box size).

For the idealisation, the number and location of the booms need to be set. The spar locations along the chord were set in Section 7.5; therefore, the cap boom position was already known. When analysing the aerofoil profile for the stringer locations, it was determined that some simplifications could be made for faster analysis. Firstly, the upper and lower wing skins were simplified to be straight as the profile did not deviate much from this between the spars (see Figure 7.9). Secondly, the vertical positions of the spar and stringer booms could be assumed symmetric about the wing box centreline, resulting in a chordwise-symmetric wing box idealisation. This allows for a simple shear centre derivation and easier iteration of the number of stringers while barely deviating from the aerofoil shape. These assumptions can be reversed in future iterations when a more detailed design is necessary. Then, the number of stringers for the aircraft skin was chosen based on a typical stringer spacing (~10 cm [99]), which led to 6 evenly distributed booms along the wing skin.

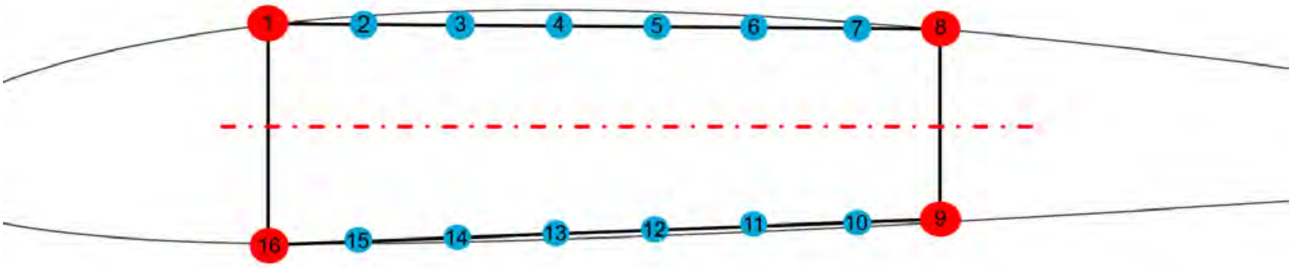

Figure 7.9: NACA2412 wing box idealisation. Red circles are spar booms, the red line is the axis of symmetry (in the x-direction), and the blue circles are stringer booms.

Now that the boom locations are known, their size/area needs to be determined. Using the spar design as a starting point, the initial spar boom's size could be set for each spar cap area, respectively. For each stringer boom, the area was preliminarily set to 40 mm^2 to reduce the number of unknowns. Finally, the skin was ignored in the first iteration as its contribution to the booms depends on the ratio of axial loads in adjacent stringer booms.

7.6.1. Boom Stress

The area moment of inertia about the x-axis must be found to determine the stresses in each boom. For this, it was assumed that the booms were point areas and only their parallel axis component contributed ($I_{xx}^{(i)} = B_i y^2$). Summing all the boom contributions yielded the wing-box area moment of inertia. To determine the load in the booms due to bending of the wing box, Equation 7.26 can be used with multiple loading conditions. Here, M_x is the moment about the x-axis, and y is notably the distance from the neutral axis of the wing box to the boom in the y-direction (not the distance from the chordline). Additionally, the wing box experiences high compressive load in regions 1 & 2 due to the presence of the strut. Typically, the compressive load is distributed equally among the booms, and the stress is found with the total area (compatibility, all booms need to deform equally). However, due to the spar caps being made of AA7075 compared to the AA2024 aluminium alloy of the other components, the load was distributed according to the boom's Young's modulus divided by the total boom area times Young's modulus (see Equation 7.27). This axial stress can then be summed with the bending stress (principle of superposition, Equation 7.28). This is done for the maximum positive and negative load factors (limit and ultimate) to find which pair of stresses produces the highest absolute total stress.

$$\sigma_{\text{bend}, i} = \frac{M_x y}{I_{xx}} \tag{7.26}$$

$$\sigma_{\text{axial}, i} = \frac{P E_i}{\sum_{i=1}^{16} (B_i E_i)} \tag{7.27}$$

Where P is the compressive load, E_i is the Young's Modulus of boom i, and B_i is its area.

$$\sigma_i = \sigma_{\text{bend}, i} + \sigma_{\text{axial}, i} \tag{7.28}$$

Four variants of this idealisation are needed for each region prescribed in Section 7.5, due to differences in spar size, wing loading and tapering of the chord length. For these regions, changes to the wing box were kept limited to facilitate easier manufacturing and assembly. The stringer spacing was kept the same to allow them to be continuous throughout the entire span. Additionally, when possible, the wing skin thickness will be kept the same since it is more complicated to produce compared to compensating with different stringers.

Table 7.9: Iteration 1, region 1, boom ultimate stresses under a bending moment of -6.6 kNm and axial load of -111 kN. Refer to Figure 7.9 for ID

Boom ID	**1**	**2**	**3**	**4**	**5**	**6**	**7**	**8**
$\sigma_{\text{ult total}}$ [MPa]	-20	-29	-33	-37	-41	-45	-49	-48
Boom ID	**16**	**15**	**14**	**13**	**12**	**11**	**10**	**9**
$\sigma_{\text{ult total}}$ [MPa]	-211	-212	-208	-204	-200	-196	-192	-183

In Table 7.9, the maximum stresses each boom must hold for the first iteration of region 1 are shown. Note that the loading from a negative load factor is not shown, since it does not result in a constraining loading condition. The negative load factor results in the strut causing a tensile load in regions 1 & 2, which, when summed with the bending, results in a smaller total stress in all booms. In the first iteration, the stress magnitude is unrealistic because the skin contribution has not yet been accounted for. However, with the boom stress values, the skin contribution can be derived using either Equation 7.29 for spar cap booms or Equation 7.30 for stringer booms. The difference is due to the spar caps having only one adjacent boom and, therefore, only one skin contribution. The stringer booms have two adjacent wing-skin sections and therefore two skin-contribution components. A represents the cross-sectional area of the stringer or spar cap without the skin, b is the distance between adjacent booms, i is the boom ID, and t_{skin} is the skin thickness.

$$(B_i)_{\text{spar cap}} = A_{\text{spar cap}} + \frac{t_{\text{skin}} b}{6}\left(2 + \frac{\sigma_{i\pm1}}{\sigma_i}\right) \qquad [100] \tag{7.29}$$

$$(B_i)_{\text{stiffener}} = A_{\text{stiffener}} + \frac{t_{\text{skin}}\, b}{6}\left(2 + \frac{\sigma_{i-1}}{\sigma_i}\right) + \frac{t_{\text{skin}}\, b}{6}\left(2 + \frac{\sigma_{i+1}}{\sigma_i}\right) \qquad [100] \tag{7.30}$$

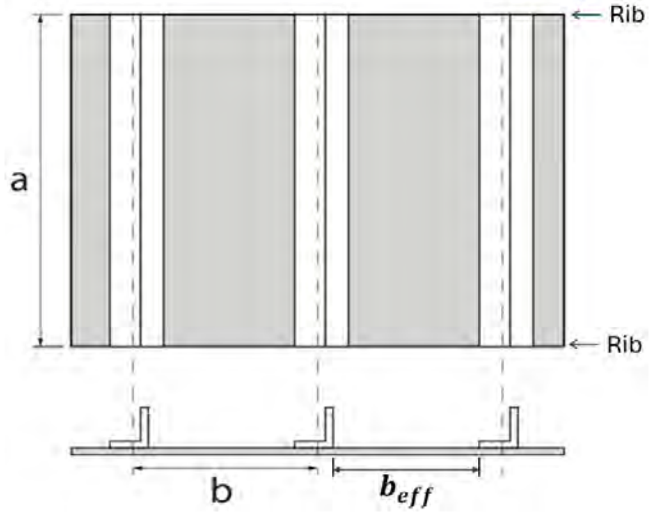

Figure 7.10: Simplified skin plate, a is the rib spacing, and b is the stringer spacing from centre to centre [100].

With the addition of the skin contribution and using a conservative skin thickness ($t = 2$mm), the next iteration could be completed for all regions. For this, it was chosen to keep the number of stringers the same and therefore their spacing. In addition, the changes made will stay symmetric on both the top and the bottom of the wing box to keep the bending neutral axis constant. This will allow for quicker iteration for this preliminary design. The skin contribution increased the total boom area by a factor of four and thereby equally decreased the stress through each boom (see Table 7.10).

Table 7.10: Iteration 2, region 1, boom ultimate stresses under a bending moment of -6.6 kNm and axial load of -111 kN. Refer to Figure 7.9 for ID

Boom ID	**1**	**2**	**3**	**4**	**5**	**6**	**7**	**8**
$\sigma_{\text{ult total}}$ [MPa]	-3	-5	-6	-7	-9	-10	-11	-10
Boom ID	**16**	**15**	**14**	**13**	**12**	**11**	**10**	**9**
$\sigma_{\text{ult total}}$ [MPa]	-53	-53	-52	-51	-50	-49	-48	-46

7.6.2. Skin Torsional Loading

Before proceeding to the next iteration, it is important to consider the wing box's many failure modes to determine whether stresses need to be reduced or increased. First, torsional loading will be considered to determine what wing skin thickness can withstand the shear loads. Using the maximum torsional moment, derived in subsection 7.4.3, the shear stress through the wing box's skin panels can be found using Equation 7.31. For this equation, the skin thickness is assumed to be much smaller than the distance from the torsional centre of the wing box, resulting in the shear flow, q_f, being constant throughout the skin. This assumption holds since the preliminary skin thickness is 2mm, while the shortest distance from the centre is around 40 times larger than this. As a result, the skin thickness must be at least 0.35 mm.

$$\tau = \frac{q_f}{t} = \frac{T}{2tA_{\text{encl}}} \quad \rightarrow \quad t_{\text{min}} = \frac{T}{2\sigma_{yield}A_{\text{encl}}} \qquad [100] \qquad (7.31)$$

7.6.3. Stiffened Panel Buckling

The next, and most important, failure mode is skin panel buckling. This buckling is relevant to the individual wing skin panels between stiffeners, which is visualised in Figure 7.10. Between adjacent stringers (or between a stringer and a spar cap), the thin wing skin is assumed to act as a flat plate supported along its edges. Under the compressive component of the total boom stress, these skin panels are susceptible to elastic buckling well before the material yield strength is reached. The purpose of the stiffeners (stringers) is to subdivide the skin into smaller panels, increasing the local buckling stress. However, the stiffeners themselves must also be checked against crippling between rib supports. The design must therefore ensure that neither local skin buckling nor stiffener crippling occurs at or below the limit load.

The critical buckling stress for a flat skin panel of thickness t and width b_{eff} is given by Equation 7.32, where C is the buckling coefficient that depends on b_{eff}/t and the type of stiffener used. In [101, p.460], a graph with two curves for values of C (depending on b_{eff}/t) for specifically stiffened panels is given. The curve for non-torsionally stiff stiffeners is chosen because the preliminary cross-sectional area of each stiffener is too low for easy manufacturing of hat stiffeners. Note that these curves and the equations require that the rib spacing, a, be at least 3 times larger than the stiffener spacing b, which is the case for all four regions. η_c is the plastic reduction factor; the value equals 1 since the loads induced in the wing box do not approach the yield stress of the alloy. b_{eff} is taken as the distance between stringer components for iterations 1 & 2.

$$\sigma_{cr,skin} = \frac{C\eta_c\pi^2 E}{12(1-\nu^2)}\left(\frac{t}{b_{eff}}\right)^2 \qquad \text{[101, p.458]} \tag{7.32}$$

Even if the skin does not buckle, the stiffener itself may fail by local crippling. Crippling is a local instability of the stiffeners free flange or web caused by the formation of halfwaves in the cross-section without the entire member bending globally. For a short column or a stiffener with closely spaced ribs, crippling often governs before Euler buckling. Equation 7.33 gives the crippling stress $\sigma_{cr}^{(i)}$ per stiffener segment of area A_i using an empirical Johnsontype formulation, where $alpha$, v, and n are alloyspecific constants (for AA2024, $\alpha = 0.85$, $v = 0.33$, $n = 0.5$ [94, 100]). The term (t_s/b_s) here is interpreted as the slenderness of each stiffener element (e.g., flange width over thickness). For the preliminary design, L-shaped stiffeners are chosen to quickly derive buckling for the iterative process and because the total stiffener cross-sectional area is the more important factor at this point in the design. Note that C here takes values from a different graph in [101] depending on if element of the stiffener has a free edge ($C = 0.425$) or not ($C = 4.00$). With both elements calculated, the final crippling stress of the stiffener can be found with Equation 7.34. Using an L-shaped stiffener with 2 segments of 10 mm x 2 mm, $\sigma_{cc} = 915$ MPa; since this is well above the ultimate stress, this failure mode will not constrain the design.

$$\sigma_{cc}^{(i)} = \frac{\alpha}{\sigma_y}\left[\frac{C}{\sigma_y}\frac{\pi^2 E}{12(1-\nu^2)}\left(\frac{t_s}{b_s}\right)^2\right]^{1-n} \qquad \text{[100]} \tag{7.33}$$

$$\sigma_{cc} = \frac{\sum \sigma_{cc}^{(i)} A_i}{\sum A_i} \qquad \text{[100]} \tag{7.34}$$

Even though the crippling stress of the current stiffeners is no constraint, the result can be used to find the effective width, b_{eff}, to iterate on the skin buckling. A portion of the skin adjacent to the stiffener of total width, $2w_e$, will carry additional load until the stiffener itself fails. Therefore, the skin panel between the stiffeners has a width smaller than the stiffener spacing, and this effective width can be determined using Equation 7.35. The calculation of $2w_e$, in Equation 7.36, uses yet again a different value of C, this time from [25, p.144]. This calculation reduced b from 0.103 m to 0.078 m, which increased the $\sigma_{cr,\text{skin}}$ from 55 MPa to 84 MPa. Note that this improvement has not been taken into account in the third iteration and therefore can be used in the future.

$$b_{eff} = b - 2w_e \tag{7.35}$$

$$2w_e = t\sqrt{\frac{C\pi^2}{12(1-\nu^2)}}\sqrt{\frac{E}{(\sigma_{cc})_{stiffener}}} \qquad \text{[100]} \tag{7.36}$$

7.6.4. Transverse Plate Loading

Finally, an additional loading condition on the skin panels arises from aerodynamic pressure differentials across the wing skin. During manoeuvres and gust encounters, the external pressure distribution on the upper and lower surfaces differs from the internal pressure (which is assumed to be vented to ambient through small holes). This pressure differential Δp induces a transverse bending stress in the skin panels acting perpendicular to the plane of the skin. The maximum stress due to this bending can be found with Equation 7.37, ρ was taken as 1.225 kg/m^3 [102], the sea level value along with the dive speed to derive the highest possible Δp. C_p is the local pressure coefficient obtained again from *XFOIL* with the same inputs as mentioned in subsection 7.4.3. The highest value, $C_p = -2.3$, on the wing box surface was found to be on the plate between boom 1 and 2, at the highest pre-stall angle of attack of 15°. This is a conservative assumption, as achieving this high angle of attack at the dive speed would exceed the physical strength of the pilot and/or the capability of the elevator. With the maximum value of $\Delta p = 12kPa$, the transverse stress can be calculated with Equation 7.38. $\beta = 0.72$ is found using a/b (rib spacing/stiffener spacing) and a table in [103, p.502].

The plate is also considered to be simply supported on all sides, which is conservative since [101] claims the ribs often provide more support; however, analysis is normally done with simply supported. The worst-case result, highest $\sigma_\perp = 107$ MPa, is achieved in region 3 with the highest a/b by also using b_{eff}. As a result, this failure mode does not drive the design by staying below the yield strength. On the other hand, this stress induces a deflection of the centre of the plate of 3 mm, which will have an undetermined impact on the flow. This should be investigated further (likely experimentally) to determine at what point the deflection becomes detrimental to the safe flight.

$$\Delta p = C_p \frac{1}{2} \rho V^2 \tag{7.37}$$

$$\sigma_{\perp} = \frac{\beta(|\Delta p|)b^2}{t^2} \qquad \text{[103, p.502]} \tag{7.38}$$

7.7. Wing Box Iteration 3 Results

After accounting for the failure modes, the final iteration has been performed for regions 1-3. Region 4 will be analysed in future stages of the design. From iteration 2 to 3, only 2 variables were changed: the skin thickness and the stiffener cross-sectional area. The values of these are found in Table 7.14; the reasons for keeping the other values constant are discussed throughout Section 7.6. The iteration is driven by two main constraints: the wing skin buckling should not occur before the limit load, and a minimum stringer area of 40 mm for manufacturing and assembly. For region 1, a skin thickness of 1.2 mm was found to be optimal, which was kept in region 2 for ease of manufacturing. Due to the higher loads in region 2, the stringer area had to be increased. For region 3, the load is significantly lower, and therefore, the minimum stringer area with a skin thickness of 0.9 mm was selected. This skin thickness maximised the load the wing could carry without buckling before the limit load.

Table 7.11: Iteration 3, region 1, boom ultimate stresses under a limit bending moment of -4.40 kNm, ultimate bending moment of -6.6 kNm, and axial load of -73.8 and -111kN. Refer to Figure 7.9 for ID

Boom ID	**1**	**2**	**3**	**4**	**5**	**6**	**7**	**8**
$\sigma_{\text{lim total}}$ [MPa]	-3	-5	-6	-7	-8	-9	-10	-10
$\sigma_{\text{ult total}}$ [MPa]	-5	-8	-10	-11	-13	-14	-15	-15
Boom ID	**16**	**15**	**14**	**13**	**12**	**11**	**10**	**9**
$\sigma_{\text{lim total}}$ [MPa]	-50	-50	-49	-48	-47	-46	-45	-43
$\sigma_{\text{ult total}}$ [MPa]	-75	-76	-74	-73	-71	-70	-68	-65

Table 7.12: Iteration 3, region 2, boom stresses under a limit bending moment of 9.53 kNm, ultimate bending moment of 14.3 kNm, and Axial load of -73.8 and -111 kN. Refer to Figure 7.9 for ID

Boom ID	**1**	**2**	**3**	**4**	**5**	**6**	**7**	**8**
$\sigma_{\text{lim total}}$ [MPa]	-54	-53	-52	-50	-49	-47	-46	-44
$\sigma_{\text{ult total}}$ [MPa]	-81	-80	-78	-75	-73	-71	-69	-65
Boom ID	**16**	**15**	**14**	**13**	**12**	**11**	**10**	**9**
$\sigma_{\text{lim total}}$ [MPa]	17	15	14	12	11	9	8	7
$\sigma_{\text{ult total}}$ [MPa]	26	23	20	18	16	14	11	10

Table 7.13: Iteration 3, region 3, boom stresses under a limit bending moment of 4.11 kNm and ultimate of 6.17 kNm, no axial stress. Refer to Figure 7.9 for ID

Boom ID	**1**	**2**	**3**	**4**	**5**	**6**	**7**	**8**
$\sigma_{\text{lim total}}$ [MPa]	-29	-28	-27	-25	-24	-23	-22	-21
$\sigma_{\text{ult total}}$ [MPa]	-44	-42	-40	-38	-36	-35	-33	-31
Boom ID	**16**	**15**	**14**	**13**	**12**	**11**	**10**	**9**
$\sigma_{\text{lim total}}$ [MPa]	29	28	27	25	24	23	22	21
$\sigma_{\text{ult total}}$ [MPa]	44	42	40	38	36	35	33	31

Table 7.14: Iteration 3 region dimensions, b is stringer pitch, and a is rib spacing.

Region	1	2	3
t_{skin} [mm]	1.2	1.2	0.9
A_{stringer} [mm^2]	40	130	40
b [cm]	10.3	10.3	10.3
a [cm]	37.5	40.0	30.0
σ_{cc} [MPa]	915	634	915
$\sigma_{cr,\text{skin}}$ [MPa]	55	55	32
$\sigma_{\perp}$ [MPa]	60	59	107

Table 7.14 shows the main final results of the structural design for this report, meeting all requirements. The main driver for the wing box design is the skin panel buckling stress, which constrains the skin thickness. Furthermore, it may be hard to manufacture the current skin thickness; if this needs to be increased, the spar cap area needs to be reduced.

7.8. Manufacturing and Assembly

This section describes how the Retrofitted electric Cessna wing structure is translated from structural sizing into a practical production and assembly route. The focus is on selecting manufacturing processes, tolerances, and joining methods that are repeatable for series production while preserving clear load paths and avoiding unnecessary weakening of highly loaded members.

7.8.1. Manufacturing Techniques for Electric Cessna Structural Components

Since the aircraft is intended for series production, the driving decisions in the manufacturing methods were chosen for repeatability and low cost at volume. All material is already supplied from the foundry in its final heat-treated temper AA2024 as T3 sheet and AA7075 as T6 plates or extrusion, as selected in the mid-term report. Joining is mechanical (riveting and bolting), since these high-strength aluminium alloys are not weldable, and adhesive bonding would violate the requirement of making the retrofitted Cessna recyclable. The manufacturing processes chosen are being dictated by the material allocation chosen for each structural component. Lastly, it is important to note that every part receives a to-be-determined coating and a primer for corrosion protection before assembly. Available manufacturing techniques are: extrusion, CNC machining, press-brake bending (sheet-metal bending), roll forming and press forming.

One more important consideration is the cost structure and volume of production for the choice of manufacturing process. For example, an extrusion carries a high one-time investment in the extrusion die. That only pays off at production volume, or if a standard off-the-shelf extruded section happens to fit the geometry. Machining has essentially no tooling cost, just stock and CNC time; therefore, it is chosen for complex variable geometry or critical parts at the price of a higher per-part cost.

Forming AA7075-T6 sheet metal is notoriously difficult due to its high strength and low ductility. Cold forming causes cracking, while hot forming risks losing the material's structural temper. For the spar caps, a heated AA7075 billet is forced through a die shaped like the cap profile, producing long, near-net sections in a single operation. The grain flows along the length of the cap, which aligns with the main (spanwise) load direction and gives good strength and fatigue performance, while the high cost of the extrusion die is spread across the whole production run. The only remaining operations are cutting to length, drilling the fastener holes, and machining the end fittings. Machining each cap from a solid plate would only be preferable for a one-off part, as it wastes material and machine time at volume.

The spar web is cut from a flat AA2024-T3 sheet to its outline and lightning-hole pattern using a CNC router. Stiffening flanges are then cold-formed along their edges on a press brake, and the web is riveted to the caps in an assembly jig. AA2024-T3 bends cleanly at room temperature, so no heating is required.

Ribs are made from flat AA2024-T3 blanks that are cut to shape and then pressed into their curved profile, with flanges bent around the edge for attachment to the skin and spar webs. The cut made needs to account for bending and be larger in size. Press forming is cheap and produces light, thin-walled parts, which suit the high production volume. The few highly loaded ribs, such as the root and the strut attaching, are to be CNC milled from a solid plate. This manufacturing decision results in better accuracy, highly required in this high stressed ribs and also manufacturing ease when working with thicker ribs for higher strength.

The stringers are long, thin L-shaped stiffeners cold-formed from AA2024-T3 sheet. For series production, roll forming is preferred, where the sheet passes continuously through a series of rollers that gradually build up the profile. They are then cut to length and drilled to match the rib spacing, which they are designed to support.

The strut carries axial bracing load; its structural core is simply an extruded AA2024 tube (round, oval, or streamlined) cut to length. The load-carrying end fittings are CNC-machined from a plate and fastened to the tube ends. As an improvement in the aerodynamic performance, a light sheet-metal fairing can be added over the circular tube to reduce aerodynamic drag, since the strut is largely exposed to the incoming airflow in cruise.

Table 7.15: Stock form and primary manufacturing process for each structural component.

Component	Material/T	Stock form	Primary process(es)
Spar caps	AA7075-T6	Extruded section	Extrusion, then CNC machining
Spar web	AA2024-T3	Sheet	Press-brake bending
Ribs	AA2024-T3	Sheet	Press forming
Stringers	AA2024-T3	Sheet	Roll forming
Lift strut	AA2024-T3	Extruded tube	Extrusion then CNC-machined fittings

Table 7.16: Manufacturing cost and CO_2 estimate for the wing structure.

Quantity	Full wing
Structural mass [kg]	157.6
From stock [kg]	236
CO_2 [kg CO_2]	3,546

7.8.2. Manufacturing Tolerances

Having discussed and traded off the manufacturing techniques, the designers had to update the provided dimensional reference values with manufacturing tolerance. All values presented in this report have already been updated with the values provided for the minimum tolerance value for the manufacturer. Therefore, the extrusion manufacturing method has a $\pm 0,1$ mm tolerance, as such an example lift strut could expect at a maximum a $+0.2$ mm increase in its wall thickness t of 2.2 mm, leading to the value of 2.4 mm. Where the manufacturer sets the 2.2 as the minimum value.

7.8.3. Assembly Approach

The assembly approach for the Cessna structure is of crucial importance. The assembly approach of the redesigned wing structure was selected with the aim of maintaining a clear load path while minimising stress concentrations in the most highly loaded structural members. The number of connections that at least should be considered are: rib to spar connection, ribs to wing skin and spar caps to spar web. The use of aluminium alloy rivets with an appropriate coating is used to join the components together, also avoiding galvanic coupling. While for the joining of the wing structure to the fuselage of the Retrofitted Cessna, stainless steel bolts are to be used. Those bolts carry the heaviest joining loads and are used in the most load-demanding section of joining the wings together, joining the wing to the fuselage and the strut to the fuselage.

Brackets join ribs and spars to each other via the use of brackets joining through the web. Ribs join due to the fillet around their outline into the skin via rivets. Finally, the connection of the two L-shaped spar caps connected with the spar web was made through horizontal riveting as depicted in Figure 7.11a and Figure 7.11b. This approach minimises the number of holes and therefore stress concentrations in the highly stressed caps.

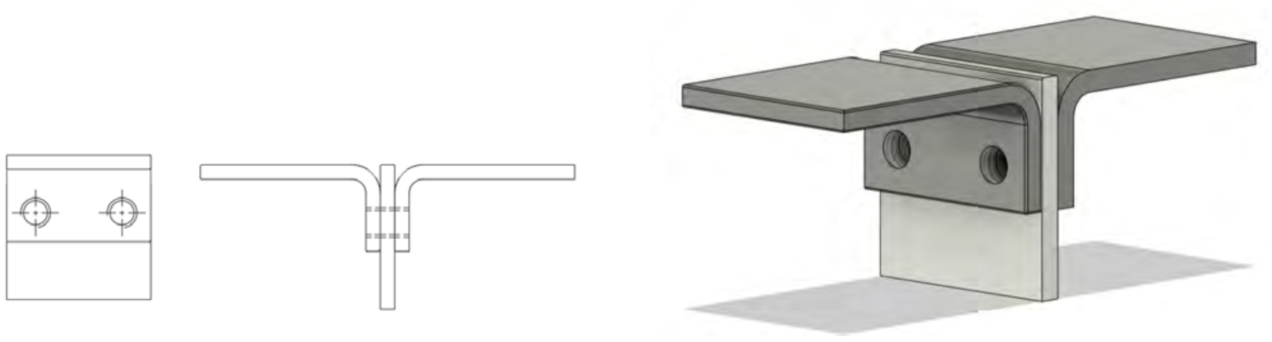

(a) Engineering drawing capturing the joint characteristics with 4 mm rivet holes at 12 mm spacing.

(b) Isometric View of the joint, with different colour shading capturing use of 7075 and 2024 AA.

Figure 7.11: Spar cap to web assembly

7.9. Tail Surface Resizing

Stability Criterion

For the conventional wing-tail arrangement, the longitudinal static stability is determined by the location of the stick-fixed neutral point, expressed as a fraction of the mean aerodynamic chord $\bar{c}$:

$$\frac{x_{np}}{\bar{c}} = \frac{x_{ac}}{\bar{c}} + \frac{C_{L_{\alpha_h}}}{C_{L_{\alpha_{A\text{-}h}}}}(1-\frac{d\varepsilon}{d\alpha})(\frac{V_h}{V})^2\frac{S_h l_h}{S\bar{c}} \tag{7.39}$$

here $x_{ac}/\bar{c}$ is the aerodynamic centre of the aircraft-less-tail, $C_{L_{\alpha_h}}$ and $C_{L_{\alpha_{A\text{-}h}}}$ are the lift gradients of the tail and the aircraft-less-tail, $d\varepsilon/d\alpha$ is the wing downwash gradient on the tail, V_h/V is the tail-to-wing speed ratio, S_h and S are the tail and wing areas, and l_h is the tail arm. The aircraft is statically stable only when the centre of gravity lies ahead of the neutral point by at least the required static margin SM:

$$\frac{x_{cg}}{\bar{c}} \leq \frac{x_{np}}{\bar{c}} - \text{SM} \tag{7.40}$$

Substituting Equation 7.39 into Equation 7.40 and grouping the tail contribution into a single slope term a gives the stick-fixed stability line:

$$\frac{x_{cg}}{\bar{c}} = (\frac{x_{ac}}{\bar{c}} - \text{SM}) + a\frac{S_h}{S}, \qquad a = \frac{C_{L_{\alpha_h}}}{C_{L_{\alpha_{A\text{-}h}}}}(1-\frac{d\varepsilon}{d\alpha})(\frac{V_h}{V})^2\frac{l_h}{\bar{c}} \tag{7.41}$$

Required Tail Area

The slope a is evaluated with the coefficients obtained from the DATCOM method for the lift gradients [104] and the Slingerland method for the downwash gradient [105], namely $C_{L_{\alpha_h}} = 3.576\,\text{rad}^{-1}$, $C_{L_{\alpha_{A\text{-}h}}} = 5.269\,\text{rad}^{-1}$, $d\varepsilon/d\alpha = 0.409$, a fuselage-mounted speed ratio $V_h/V = 0.85$ [100] and a tail arm $l_h = 4.60\,\text{m}$:

$$a = \frac{3.576}{5.269}(1-0.409)(0.85)^2\frac{4.60}{1.4935} = 0.892$$

Solving Equation 7.41 for the tail area ratio at the aft c.g. limit, with $x_{ac}/\bar{c} = 0.25$ and a required static margin of SM $= 0.05$, gives the minimum tail required for stability:

$$(\frac{S_h}{S})_{\min} = \frac{\frac{x_{cg}}{\bar{c}} + \text{SM} - \frac{x_{ac}}{\bar{c}}}{a} \tag{7.42}$$

$$(\frac{S_h}{S})_{\min} = \frac{0.379 + 0.05 - 0.25}{0.892} = 0.201$$

Multiplying by the new wing area yields the required tail area:

$$S_{h,\text{new}} = 0.201 \cdot 18.461 = 3.71\,\text{m}^2$$

The baseline tail of the original aircraft has an area of $S_{h,0} = 3.36\,\text{m}^2$, which provides a static margin of 5.1% at the aft limit of the original aircraft, but only 3.3% when placed on the enlarged electric wing, which is below the required 5%. The horizontal tail surface must therefore be increased by 10%. This corresponds to extending the stabiliser span from $3.43\,\text{m}$ to $3.60\,\text{m}$ at a constant tail aspect ratio.

$$\Delta S_h = S_{h,\text{new}} - S_{h,0} = 3.71 - 3.36 = 0.35\,\text{m}^2 = 10.4\%$$

7.10. CAD Model

The computer-aided design (CAD) model of the wing structure has been created to integrate the designed part components. The CAD seen in Figure 7.12 served a great value in verifying the design through its visualisation of the internal structure. While Figure 7.13 visualises the increase in wing area in comparison to the original wing and how the overall retrofitted green Cessna incorporates all design choices. One correction that has been spotted is the required angle and taper of the rear spar. The rear spar does not fit at 65% of the root chord length and had to be scaled to the local chord length.

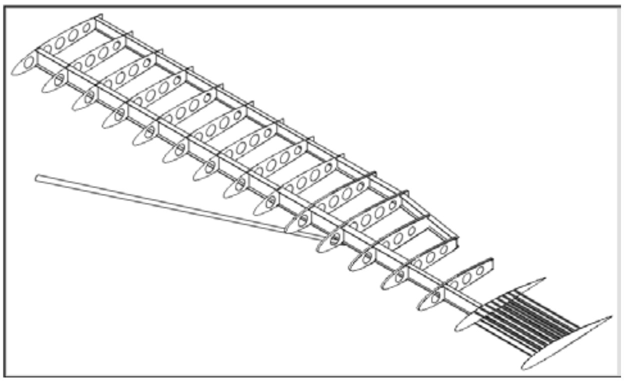

Figure 7.12: Internal Structure view, the stringers would go through the whole structure, but they would protrude the view of the ribs so they are showcased at the tip

Figure 7.13: CAD Model of the Green Cessna with the bigger tail wing proportionally and side comparison of the two wings showcasing the resize

7.11. Possibilities for Future Design Iterations

In future iterations, the useful properties of AA7075 alloys can be utilised by a reduction of the cross-sectional area of all components, so that higher loads can occur. There are many improvements that could be included in future iterations to reduce the wing's weight. Firstly, the wing-strut attachment point is not optimal due to minimum size constraints. The strut removes too much load from the outboard side of the wing, such that it is constrained by a minimum stringer and skin size instead of buckling loads. In addition, the strut induces very high compression loads on the inboard side of the wing, which, when summed together with bending, results in a low skin buckling stress. The latter will already be improved in future iterations without any changes by implementing the effective length from Equation 7.35; however, changing the strut positioning to be more inboard will have a higher impact. Furthermore, allowing the number of stringers to vary along the span and even within the same cross-section will enable weight optimisation. For example, the maximum stresses on the top and bottom of the skin vary heavily even when considering negative loading scenarios. It is therefore possible to have a non-symmetric cross-section to reduce the weight. This was not done in this preliminary phase due to the stringer pitch, b, being a variable in all failure modes and requiring a redesign of the wing box calculator itself.

For future iterations, it is recommended to redesign the wing box idealisation calculator to be an algorithm. This would allow for all design constraints to be input and a model to be trained to optimise. Furthermore, some assumptions should be reversed, such as the stringer booms lying in a straight line from spar to spar instead of following the wing skin. The latter assumption underestimates the bending stress along the stringers and wing-skin due to the distance from the neutral axis being lower. Furthermore, empirical book graphs should be converted into formulas such that changes in variables can be systematically computed without requiring user input. In addition, the idealisation does not account for additional weight from part assembly. For example, splitting the spar regions may be optimal in the current design; however, the mass of the required joints for load transfer may prove to be less weight-optimal. Finally, one of the more important drawbacks of the current idealisation is that the buckling is calculated with different loads in isolation. The wing skin is calculated to buckle with a pure compression load (Equation 7.32); however, it is simultaneously experiencing the transverse aerodynamic loading (Equation 7.38). [106] states that the presence of this transverse loading could increase the critical buckling stress; however, they are sceptical about accounting for this in design.

Moreover, the torsional stiffness of the wing box is only first-order and unverified. The wing box shape and non-symmetrical loading in the x-direction will result in induced torsion due to bending. This has not been evaluated in the report and must be considered in future iterations. Potential Lightning holes are placed in the web of the spar of region 1 and region 3, due to the low acting internal shear forces. The addition of lighting holes would be highly beneficial from the mass optimisation standpoint. The evaluation of lighting size dimensions would have to be backed up with higher-order analysis, preferably verified through a finite element analysis.

The preliminary design has not been performed with detailed fatigue calculations. However, the allocation of materials has been chosen with some consideration for fatigue. The overall structure will still have to be tested and validated, especially due to the values of fatigue strength provided for AA7075 and AA2024, being respectively 159 MPa and 138 MPa (500,000,000 loading cycles) [94]. Having inspected these values and compared them to the structure that has been designed with a safety factor of 1.5 (ultimate load) and stress to 460 MPa and 248 MPa of σ_y, one can clearly spot the need for further consideration of the produced spar design. However, when the spars are introduced into the wing box iterations, the stresses are at a maximum of 55 MPa and therefore, well below the fatigue strength. Future iterations will evaluate an appropriate maximum stress for each major wing component, depending on the number and magnitude of loading cycles they experience.

8

Cessna Propulsion and Power

In this chapter, the propulsion and power system design of the green retrofitted Cessna 172S Skyhawk will be discussed. A short rationale of previous work precedes the final design overview. Afterwards, the detailed design of the mission profile, weight and balance, battery, motor, aerodynamics, thermal management, and life cycle is presented.

8.1. Electric Propulsion Rationale

In terms of sustainability, it was not sensible to go through all the aluminium recycling effort just to have the demonstrated use case be a Cessna 172S with a fossil-fuel engine. Therefore, the requirement was set that the green Cessna should also have a green propulsion system, i.e. the aircraft should have no operational emissions. The trade-off procedure for the type of green system to use led to the selection of an electric propulsion system. The other hydrogen and hydrogen-electric hybrid options lost on criteria such as cost, risk, and sustainability, due to the safety concerns and grey production of hydrogen.

An initial conceptual design and sizing of the electric Cessna was followed to determine the feasibility of the concept. In this first iteration, the Maximum Take-Off Weight (MTOW) was still equal to that of the original Cessna. It was determined that removing the rear passenger seats would save weight. This was deemed acceptable as training flights almost exclusively require two passengers [107]. The battery mass and capacity were estimated to be sufficient to complete training flights following flight performance analyses. It was then determined that the MTOW could be increased by 10% to broaden the design space. The final detailed design of these last iterations is presented in this chapter. Starting with an overview of the final design in Section 8.2.

8.2. Design Overview

The green Cessna 172S Skyhawk is an electric retrofit of the original version. The retrofit aircraft will only use recycled aluminium alloys, and the redesigned wing allows for a 10% increase in MTOW. The fossil-fuel propulsion system of the original is replaced by an electric motor, batteries, and an improved thermal management system. To allow for more battery weight, the rear passenger hardware was removed, resulting in a two-seater configuration. A render of the retrofit can be seen in Figure 8.1. As determined in the market analysis, the largest market for Cessna 172S is training flights. It will compete against the smaller Pipistrel Velis Electro. However, the retrofit is designed to be capable of all private pilot license (PPL) necessary flights, which the Pipistrel Velis Electro cannot achieve. The retrofit has a cruise endurance of 100 minutes and a cruise range of 230 km, making it feasible for some leisure general aviation flights, not just training flights. Other performance parameters, such as take-off/landing distance, climb, stall, and top speed, are the same as or better than the original Cessna.

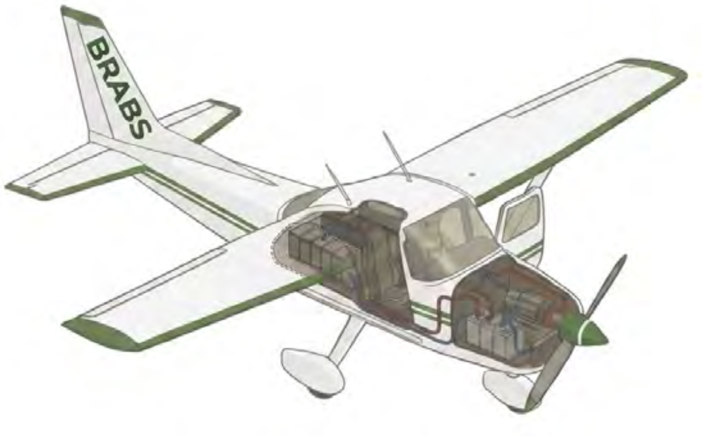

Figure 8.1: Render of the retrofit Cessna, highlighting the batteries, motor, thermals and two-seater configuration (AI-generated)

The electrical, thermal, and data flow of the retrofit components are shown in Figure 8.2. The high-voltage components primarily include the motor and battery packs. Notable are the power delivery unit, necessary to combine the power of the two battery packs, and the DC-DC converter to charge the low-voltage battery circuit. The charging controller manages fast recharging via an external ground charger. The low-voltage circuits include operational components such as the battery management system and vehicle control unit, which connect pilot input to the correct propulsion output. The thermal management system manages coolant flow and fan speed through the radiator to keep the motor and battery cool. The interactions between external systems are also shown, such as the heat exchange between the radiator and the environmental (flight) data captured by the avionics sensors.

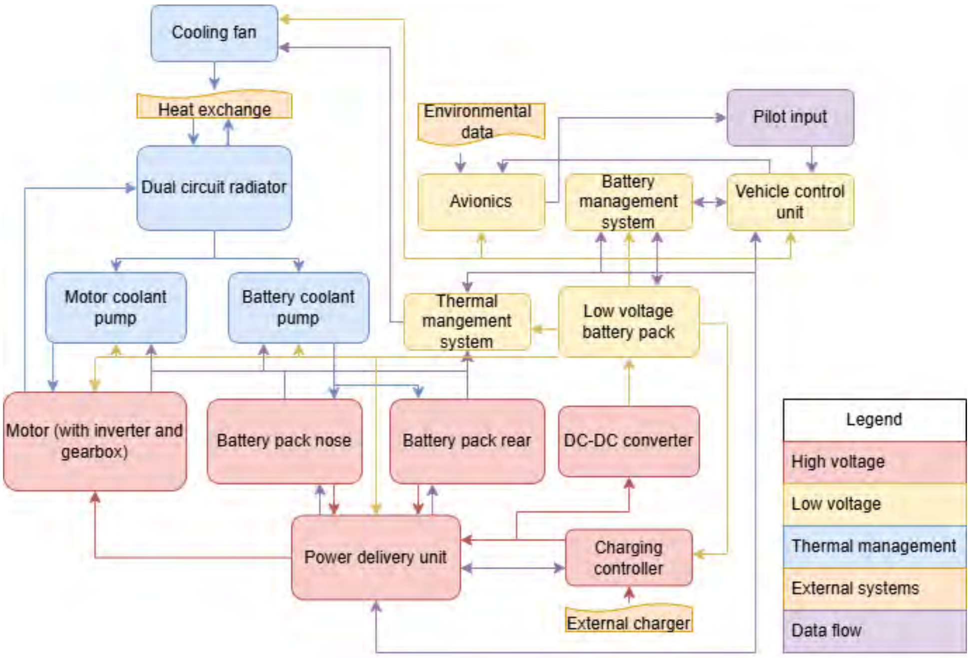

Figure 8.2: Electrical, thermal, and data block flow diagram for the retrofit Cessna

The following sections will describe the detailed design of the electric propulsion system.

8.3. Mission Profile

This and the following sections will describe the detailed design of the electric propulsion system. The sizing of this system is dependent on the mission profile, as it determines the required energy. In the market analysis, flight schools were identified as the largest market for the Cessna 172S. Therefore, the retrofit Cessna should be capable of all flights necessary to obtain a PPL. These flights can vary widely in mission profile, but a common mission profile will be determined [107].

8.3.1. Flight Data Analysis

Flight data from FlightRadar24[1] of 114 training flights (spanning April 2026 through June 2026) in the Cessna 172S aircraft across the US, Germany, France, and India were analysed. Due to uncertainty in the FlightRadar24 data, the dataset was filtered using the interquartile range to remove outliers. The distribution and median of flight duration, sea-level altitude, and typical cruise speed were determined across the flights, as shown in Figure 8.3.

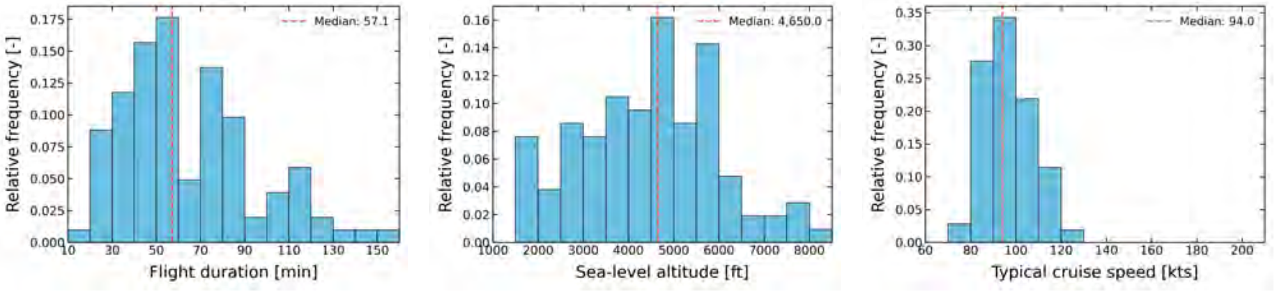

Figure 8.3: Relative frequency of flight parameters for flight data of 100 flights

---

[1] URL `https://www.flightradar24.com/`[cited on 11 June 2025]

This data, together with the European Union Aviation Safety Agency (EASA) PPL requirements [108], was used to construct two mission profiles: the common training flight and the cross-country flight. The latter is a solo flight, but to stay conservative, both profiles are modelled at MTOW. If both mission profiles can be completed, the aircraft can be used to obtain a PPL.

8.3.2. Common Training Flight Profile

The common training flight covers the start and middle of the PPL syllabus. The flight follows this procedure: taxi, take-off, climb, cruise, manoeuvres (e.g. deep stall, steep turns, slow flying, ground reference), cruise, descent, traffic pattern work (e.g. leg flying, go-around, touch-and-go), landing, taxi and a mandatory 30-minute reserve. As endurance is the limiting factor in electric aircraft, the mission profile (shown in Figure 8.4) has an 80-minute flight duration, which is more than 40% longer than the median. Therefore, most training flights are accounted for in the modelled mission profile. For altitude and cruise speed, the median is roughly followed. The aircraft still has the capability to fly higher or faster; however, this will decrease flight duration.

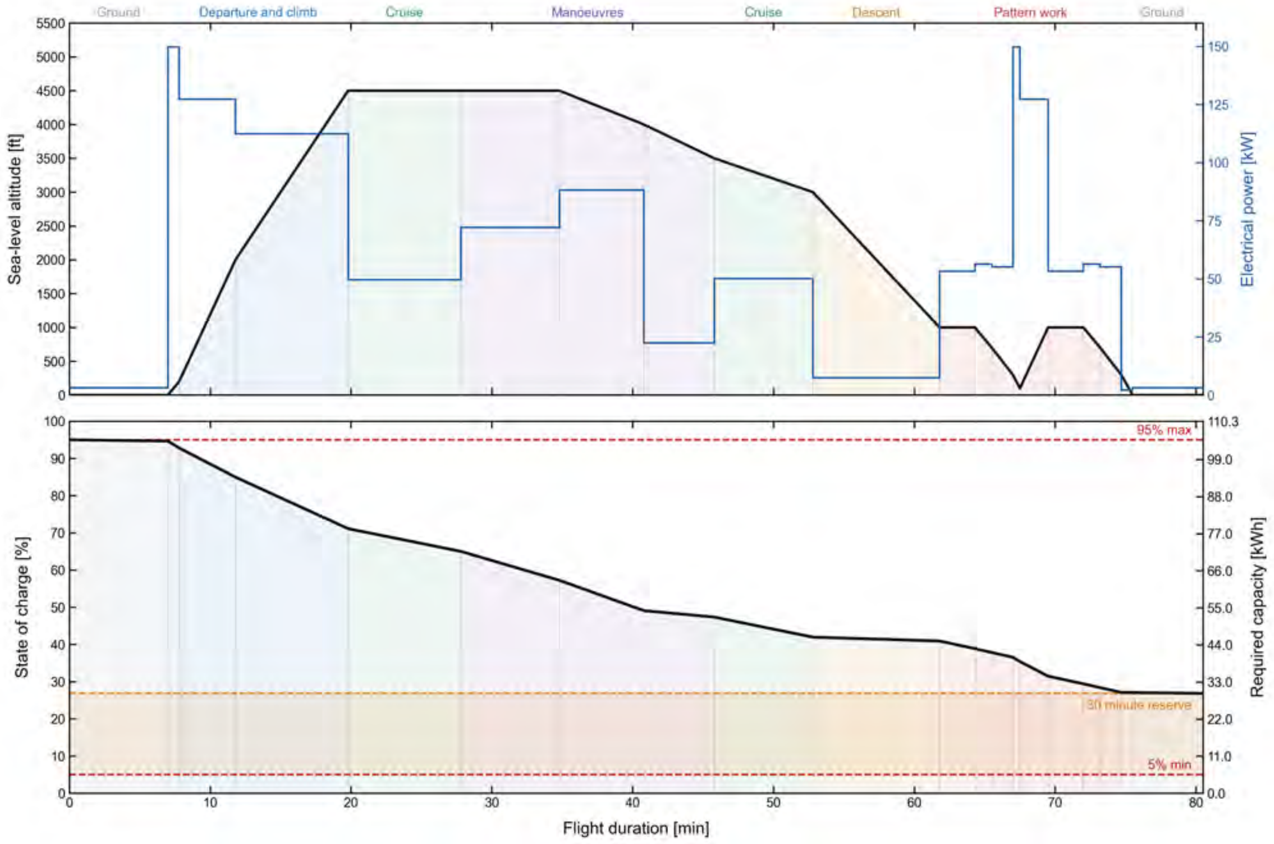

Figure 8.4: Common training flight mission profile

An important takeaway from Figure 8.4 is the required battery capacity of 106 kWh. This number is calculated based on aerodynamic, motor, and battery performance, which will be detailed in later sections. Furthermore, the reserve is critical, as it accounts for more than 20% of the State of Charge (SOC) budget. The take-off, climb, and go-around phases are crucial for battery and thermal analysis. The maximum electrical power (after efficiency losses) is 147 kW.

8.3.3. Cross-Country Training Flight Profile

The cross-country flight follows a different procedure: three direct flight legs of at least 50 nautical miles (93 km) with full stops in between the legs. The modelled mission profile shown in Figure 8.5 accounts for three legs of slightly more than 93 km, with the same altitude and cruise speed as before. The aircraft will not have sufficient capacity to fly all three legs consecutively; therefore, recharging is required.

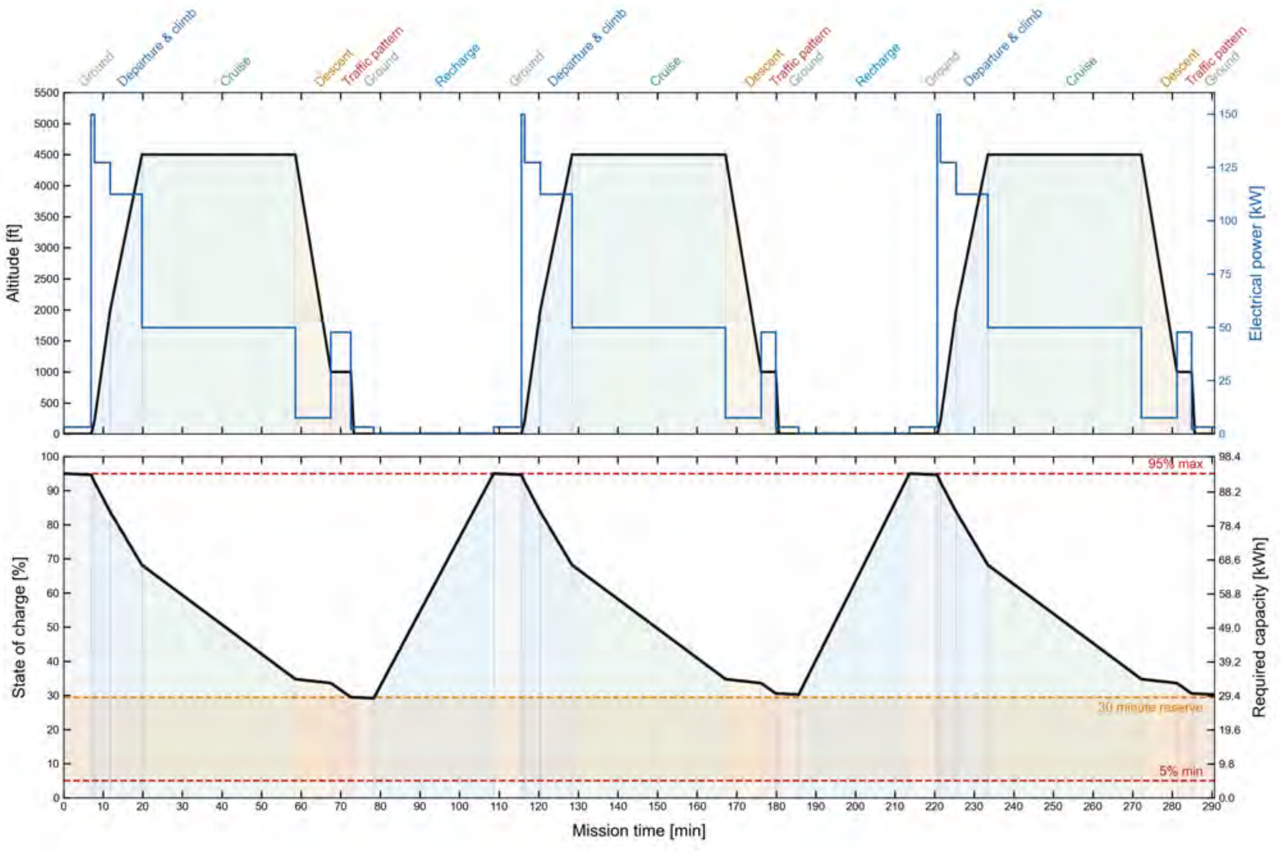

Figure 8.5: Cross-country training flight mission profile

An important takeaway from Figure 8.5 is, again, the required capacity: only 90 kWh. The same aerodynamic, motor and battery performance has been used for calculations. The reserve consumes 25% SOC, a significant portion of the energy budget. Furthermore, a new important parameter is the recharging time, which is 30 minutes. Recharging performance is also detailed in later sections. This is significantly longer than the usual stoppage times for these cross-country flights. Therefore, a slight adaptation from flight schools might be required to take longer breaks in between legs. However, from talking to flight schools, it was determined that, on average, this recharge time would not affect the number of lessons per day by a significant amount on average.

With the key findings from the mission profile, the sizing and performance analysis for the retrofit can be performed in the following sections. During the design process, the mission profile was updated iteratively with sizing and performance analysis until this converged design was reached.

8.4. Battery Sizing and Positioning

Battery sizing and positioning are crucial to determining the available battery capacity. As batteries have a much lower energy density than common fuels, this requires careful positioning to keep the aircraft balanced.

8.4.1. Available Battery Mass

The battery sizing procedure involves stripping the Cessna's basic empty weight (BEW) of unnecessary components. Most of this mass comes from the internal combustion engine (ICE), as seen in Table 8.1. The rear seats and some ICE-related electrical systems are also removed. Then the mass of the electrical systems (excluding batteries) is determined using the required retrofit components. These weights are shown in Table 8.2; specific weights of these systems are detailed in later sections.

From the stripped Cessna, the weight of the electric propulsion system is determined, and the available battery mass is calculated. For the battery, the Amprius SA02 cell is used [109]. This is a high-performance battery which offers a mix of sufficient specific energy and cycle life. The weight of this cell is 111.2 g, and the cell-to-pack ratio is assumed at 82% [110]. This is a common overhead used to estimate the mass of battery housing, cooling and integration. By increasing the MTOW by 10%, this total value becomes 1272 kg. From the MTOW, the stripped BEW (including the 32.5 kg wing weight increase), the electric propulsion system components, the student pilot and instructor, and the safety margin are subtracted to find the available battery mass, as shown in Table 8.3.

Table 8.1: Mass and moment arms of the stripped components

Stripped part	Mass [kg]	Arm [m]
ICE	145.51	-0.472
Seating and restraints	23.81	2.066
Electrical components	18.96	-0.225
Other	1.14	0.973
Total removed	**189.42**	**-0.119**

Table 8.2: Mass and moment arms of the added electric components

Added component	Mass [kg]	Arm [m]
Electric motor	16.00	-0.508
Thermal system	7.29	-0.381
High voltage management	16.50	0.356
Low voltage management	13.50	0.322
Total added	**53.29**	**-0.013**

Table 8.3: Available battery mass

Parameter	Mass [kg]
MTOW	1272.3
BEW	-587.9
Electric propulsion system	-53.3
Student and instructor (86 kg each [93])	-172.0
Safety margin	-20.0
Available battery mass	**439.2**

8.4.2. Battery Configuration

The available battery mass does not equal the implemented battery mass, as the battery cell configuration must be taken into account. Firstly, the assumed cell-to-pack ratio of 82% is applied to the available battery mass, which gives the available cell mass. Cells are configured in series and parallel; to find the best configuration for capacity, an optimisation process was conducted, shown in Figure 8.6. The voltage range is determined by the motor (detailed in a later section), which has a minimum bus voltage of 750 V to ensure peak power can be reached and a maximum of 850 V. Furthermore, increasing the number of cells in series is beneficial for thermal management.

The optimisation resulted in a configuration of 202 cells in series and 16 in parallel. Conveniently, this is also the best configuration for thermal considerations, as it has the highest number of cells in series. This configuration leads to a battery mass of 438 kg, leaving roughly 1 kg of available battery mass unused.

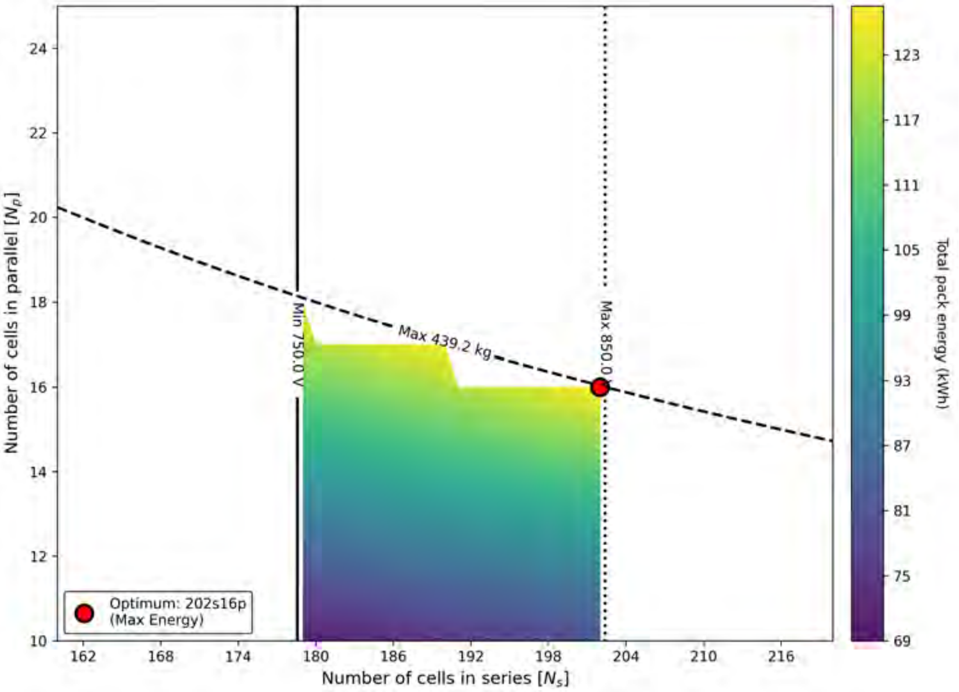

Figure 8.6: Capacity optimised series and parallel battery cell configuration

8.4.3. Battery Positioning and Balance

After determining the total battery mass and modifying components, the component positions are used to balance the retrofit aircraft. In Figure 8.7, an overview of the placement of all removed and added components is shown. It also includes the centre of gravity (CG) for an empty and fully loaded aircraft. The placement of these components was done using technical drawings from the original Cessna[2]. Conservative estimates of the nose and rear volumes were 400 and 1,000 L, respectively. The front battery pack volume is 65 L, and the rear battery pack is 84 L. Thus, there is enough room left for the other components; volume is not a critical factor in this retrofit.

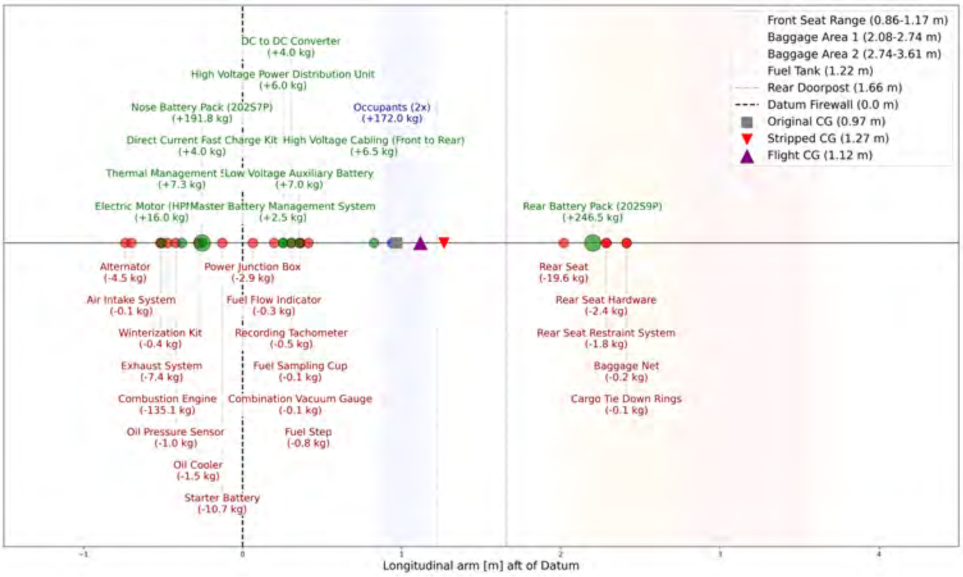

Figure 8.7: Component and battery mass and CG

Concurrently, the configuration was checked to be stable. The centre of gravity (CG) range was determined by extrapolating the CG moment envelope from the pilot operating handbook (POH) [93] to include the larger MTOW. The forward limit is bounded by elevator authority, and the aft limit by longitudinal static stability. Since these handling characteristics should be similar for the retrofit, extrapolation was used. The CG excursion for the three different loading cases is shown in Figure 8.8. The components were placed to sustain this loading within the safe flight envelope. Therefore, the retrofit Cessna will be longitudinally stable and controllable. The safety margin of 20 kg will increase the weight. This extra weight will be added longitudinally around the seats and therefore will extend the blue dotted line. Which will stay in the green region.

---

[2] URL `https://www.scribd.com/document/503597905/CESSNA-172-OSU-Correct-Panel-Angles-Drawing-v11` [cited on 12 June, 2026]

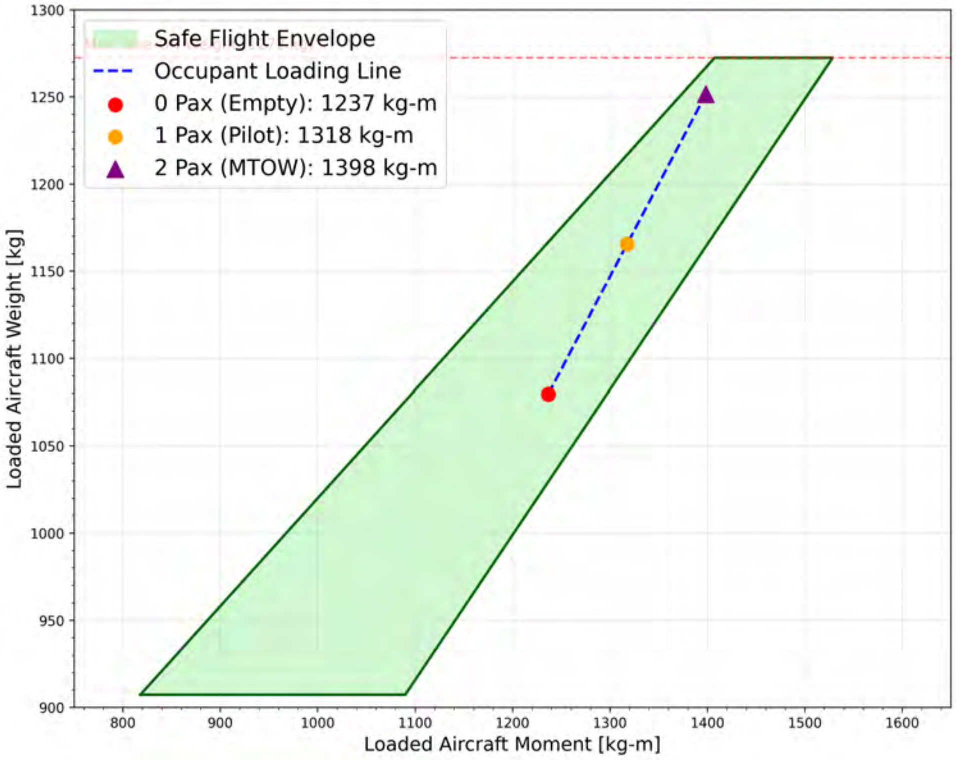

Figure 8.8: CG moment envelope extrapolated for the retrofit Cessna

8.5. Battery Performance

Battery performance is crucial to an electric aircraft. The previously determined battery weight and cell configuration provide the installed capacity. However, due to performance constraints and degradation, not all installed capacity is available for use.

8.5.1. Usable Battery Capacity

The chosen Amprius SA02 cell [109] is a high-performance lithium-ion cell; important specifications are shown in Table 8.4. To obtain the usable battery capacity, knockdown factors have to be applied to the new cell capacity, as shown in the waterfall chart in Figure 8.9. The new cell capacity equals the cell-specific energy multiplied by cell mass, which was determined previously.

The first knockdown factor, packaging, was also discussed, giving a cell-to-pack ratio of 82%. The second knockdown is the maximum depth of discharge (DOD), i.e. the SOC range that can be used without causing excessive degradation. This was determined to be 90%, from 95% to 5% SOC [111]. The last factor is the minimum state of health (SOH), i.e. the minimum battery capacity after degradation compared to new. This was found to be 90%, to balance between battery capacity and cycle life. The result is a new pack and an end-of-life (EOL) pack usable capacity of 115 kWh and 103 kWh, respectively. This is just 74% and 66% of the theoretical new cell capacity, respectively. Therefore, the retrofit can fulfil both mission profiles at the beginning of life; however, at EOL, the common training flight is slightly too demanding at 106 kWh. However, due to the largely differing training flight profiles, a difference of just 3 kWh is deemed acceptable to still complete most training flights near battery pack EOL.

Table 8.4: Important Amprius SA02 cell specifications [109]

Parameter	Comment	Value
Specific energy	= capacity (39.38 Wh) / weight (112.2 g)	351.6 Wh/kg
Cell voltage	Nominal	3.50 V
	Charge	4.20 V
	Discharge	2.50 V
Cell current	Max continuous discharge	33.0 A (3C)
	Max charge	11.0 A (1C)
Temperature range	Discharge	-20 to 55 °C
	Charge	0 to 55 °C
	Storage	-20 to 30 °C
Internal resistance	Alternating current (1 kHz @ 30% SOC)	$\lesssim$ 10 mΩ
Cycle life	+1C/-1C, 100% DOD to 80%	700 cycles
	+1C/-1C, 90% DOD to 80% SOH	1000 cycles

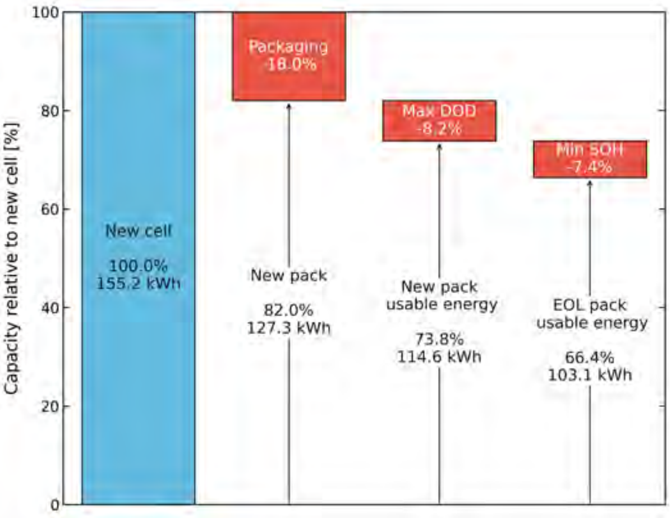

Figure 8.9: Waterfall chart showing the relationship between new cell capacity and EOL pack capacity

8.5.2. Battery Discharge Characteristics

The optimal battery layout was determined to be 202 cells in series and 16 in parallel. This battery pack will have a maximum voltage of 848 V and a maximum current of 528 A. From the mission profile, a maximum electrical power draw of 153 kW was determined, accounting for efficiency losses. The battery discharge efficiency was set at 98% [110], and the propeller and motor efficiency are discussed in the following section. The battery was modelled to maintain this power draw across all SOC levels, as shown in Figure 8.10. The voltage and current response under the constant power load are calculated with Equation 8.1 [112], which maps pack-level demands to individual cell constraints.

$$V_{\text{pack}} = N_{\text{series}} \cdot (V_{\text{oc}} - I_{\text{cell}} \cdot R_{\text{cell}}) \qquad I_{\text{pack}} = N_{\text{parallel}} \cdot \left(\frac{V_{\text{oc}} - \sqrt{V_{\text{oc}}^2 - 4 R_{\text{cell}} P_{\text{cell}}}}{2 R_{\text{cell}}} \right). \tag{8.1}$$

Where V_{pack} and V_{oc} are pack and open-circuit voltages; I_{pack} and I_{cell} are pack and cell currents; P_{cell} and R_{cell} are cell power and resistance; and N_{series} and N_{parallel} are the number of cells in series and parallel. The voltage at 100% SOC sags immediately due to the current draw necessary to produce the power. The current draw is highest at 0% SOC, which the battery should never experience, as 5% is the limit. However, the current is still below the pack maximum. Thus, the battery can comfortably provide the motor with the necessary power at any point in flight.

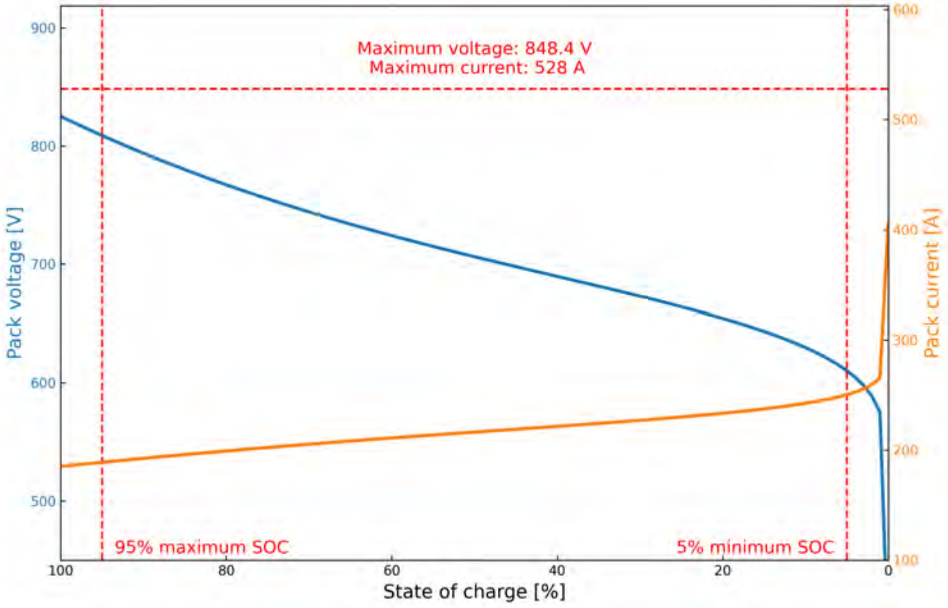

Figure 8.10: Battery discharge performance across SOC

8.5.3. Battery Degradation

The maximum battery capacity will degrade over its lifetime [110]. Because the aircraft is subjected to variable flight durations, the battery pack will experience distinct cyclic DOD depending on the scheduled lesson plan. To quantify the cumulative degradation of the battery pack across this non-uniform schedule, a degradation framework based on Miner's Rule was established [112]. The baseline cycle life of the cell was modelled as an exponential power-law function derived from empirical data points, at 700 cycles for 100% DOD and 1,000 cycles at 90% DOD (as seen in Table 8.4). To predict aircraft longevity, a discrete probability matrix was developed representing five distinct flight profiles at different DOD levels, shown in Figure 8.11.

A Monte Carlo simulation was implemented to track SOH degradation flight-by-flight, assuming a linear relationship between cycle life and fractional capacity drop. The relationship between mission frequency and degradation share is shown in Figure 8.11. The simulation reveals the large impact of high DOD flights on the total battery degradation. The 70% DOD flights occur half as often as 60% DOD flights, but have nearly the same share in battery degradation, as governed by Equation 8.2.

$$D_{\text{flight}} = \sum_i P(\text{DOD}_i) \cdot \frac{\Delta \text{SOH}_{\text{allowable}}}{N_{\text{life}}(\text{DOD}_i)} \quad \text{where} \quad N_{\text{life}}(\text{DOD}) = 700 \cdot \text{DOD}^{-3.3852} \tag{8.2}$$

Where D_{flight} is the per-flight damage, DOD_i is the i-th depth of discharge with probability $P(\text{DOD}_i)$, $\Delta\text{SOH}_{\text{allowable}}$ is the allowable state-of-health degradation, and N_{life} is the cycle life at that DOD. The resulting lifetime flight cycles, depending on SOH, are depicted in Figure 8.12. The battery pack can log more than 3,400 flights before reaching the decommissioning floor at 80% SOH. However, 90% SOH (roughly 1,700 flights) was chosen as the recommended replacement point to balance cycle life and battery capacity requirements.

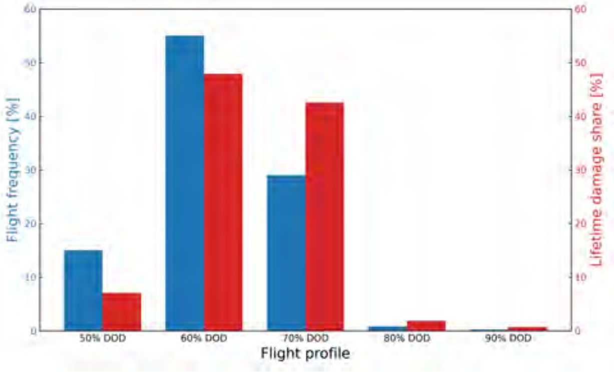

Figure 8.11: Comparison between mission frequency and lifetime degradation share

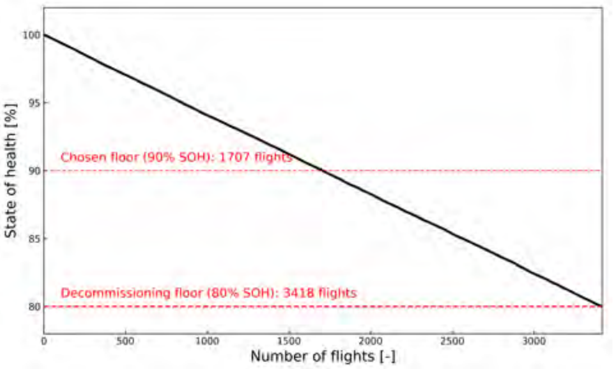

Figure 8.12: Battery SOH across number of flights

Depending on the preferences and needs of the user, they can choose their own decommissioning floor up to 80% SOH. Whilst operating at a 90% SOH, the battery packs possess enough residual capacity to support a high amount of training missions, especially the brief training missions. Therefore, if the user continues to use the battery pack longer, it would improve the cycle life of the batteries, reducing costs and emissions. Once the batteries reach their decommissioning floor, they are still high-quality battery cells for most applications. Thus, these decommissioned battery cells can be sold. This is further explained in the life cycle analysis section in Section 8.8. Once the batteries reach their operational battery EOL, they can be recycled back into their raw materials [113], further strengthening the circular aspect of the retrofit Cessna.

8.5.4. Battery Recharging Performance

The battery recharging performance is evaluated to determine ground turnaround constraints. The target recharge window spans from 5.0% to 95.0% SOC, requiring a net chemical energy storage of 115 kWh for a new pack to restore the full pack usable window. Based on a continuous cell charge rating of 11.0 A, see Table 8.4, the charge time requires roughly 58 minutes. This duration incorporates an empirical compensation factor of 1.15 to account for the current decay during the constant-voltage (CV) taper phase. The result is an average charging pace of 0.64 minutes per 1% SOC, or 0.5 minutes per 1 kWh of chemical storage.

The SOC, pack voltage, and pack current during the charge phase are shown in Figure 8.13. During the constant-current (CC) phase, the pack terminal voltage climbs steadily according to the internal resistance model [112]. At the boundary where the voltage hits its absolute ceiling of 848.4 V, the system transitions into the CV phase, keeping the terminal voltage locked while the pack current decays exponentially. The mathematical boundaries governing both the CC and CV phases are defined in Equation 8.3.

$$V_{\text{pack}}(t) = S \cdot [V_{\text{oc}} + I_{\text{cell,cc}} \cdot R_{\text{int}}] \qquad I_{\text{pack}}(t) = P \cdot \left[\frac{V_{\text{pack,max}} - S \cdot V_{\text{oc}}}{S \cdot R_{\text{int}}}\right] \tag{8.3}$$

Where V_{pack} and I_{pack} are pack voltage and current; S and P are the number of series and parallel cells; and V_{oc}, $I_{\text{cell,cc}}$, and R_{int} are cell open-circuit voltage, constant-current charge, and internal resistance, with $V_{\text{pack,max}}$ being the maximum pack voltage. To maintain this charging rate, the aircraft requires a DC delivery power of 142 kW. Accounting for thermal losses in the battery and a charger efficiency of 96.0% [114], the peak power demand drawn from the utility grid is 148 kW; over the full cycle, this results in an energy draw of 142 kWh (80.5% grid-to-battery efficiency). Usually, a full charge is not necessary, as the reserve is unused. Common charging times will range from 20 to 40 minutes. This is longer than refuelling for the original Cessna. However, with post- and pre-flight inspections and other flight school logistics usually taking up more than 30 minutes, this turnaround time is deemed acceptable.

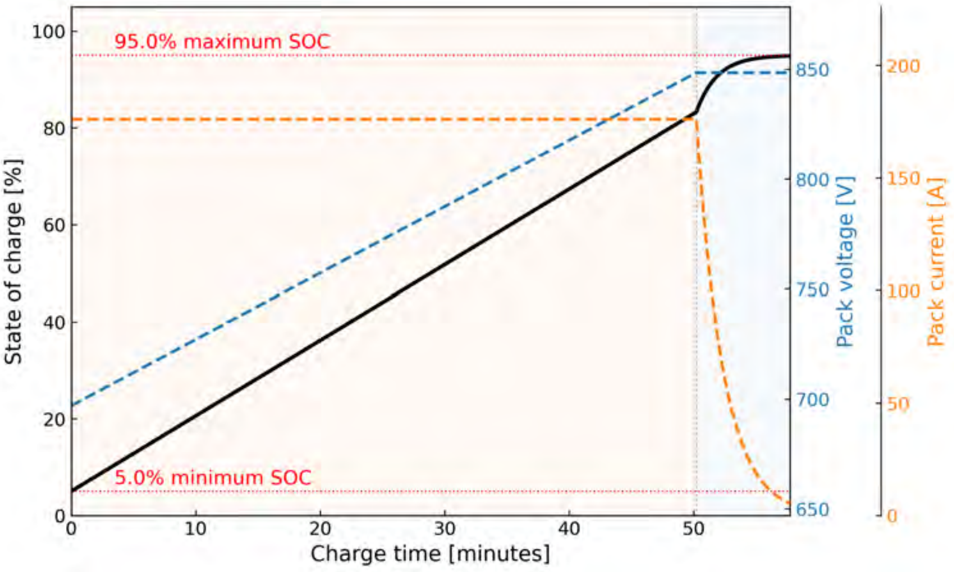

Figure 8.13: SOC, pack voltage, and pack current across a charge cycle (CC phase in orange and CV phase in blue)

Some battery performance parameters were influenced by motor performance, which is detailed in the next section. The final design was obtained by iteratively calculating design changes until convergence.

8.6. Motor and Aerodynamic Performance

The motor and aerodynamic performance are the second-to-last metrics necessary to complete the full retrofit design. The battery energy from the previous section can now be translated into actual aircraft performance metrics.

8.6.1. Motor Specifications and Aerodynamic Changes

The selected motor is an H3X HPDM-180R, a high-performance electric motor with an integrated gearbox and inverter; its important specifications are given in Table 8.5 [115]. The motor was chosen based on a combination of factors: sufficient power, an appropriate RPM range, low mass/volume, high efficiency, and a high bus voltage.

The redesigned wing structure, explained in the previous chapter, accounts for the 10% MTOW increase; its new parameters are given in Table 8.6. The other important aerodynamic change is the reduction in zero-lift drag, which is explained in the following subsection. Lastly, the shaft power requires a slight increase to account for the higher MTOW; this rationale is detailed in a later subsection. The propeller remains unchanged to keep the characteristics similar to the original; thus, the maximum RPM of 2,700 is also retained. Other performance parameters, such as take-off/landing distance, rate/angle of climb, and stall, are checked and designed to remain the same to keep the handling profile of the retrofit Cessna similar to the original, as seen in subsection 8.6.4.

Table 8.5: Important H3X HPDM-180R motor specifications [115]

Parameter	Value
Speed range	0 – 2,985 RPM
Continuous power	180 kW
Continuous torque	576 Nm
Peak efficiency	94.5%
Mass	16 kg
Volume	6 L
Max HVDC bus voltage	850 VDC
Operating temperature	-40 to 60 °C
Coolant type	50/50 WEG
Minimum coolant flow rate	25 LPM

Table 8.6: Important aerodynamic and powertrain specifications and changes [93, 116]

Parameter	Old value	New value
Wing area S	16.17 m^2	18.5 m^2
Aspect ratio AR	7.32	8.5
Zero-lift drag C_{D0}	0.029	0.024
Oswald factor e	0.78	0.78
Maximum shaft power	134 kW	136 kW
Propeller diameter	1.93 m	1.93 m
Peak propeller efficiency	85%	85%

8.6.2. Aerodynamic Drag Polar and Propeller Efficiency

The aerodynamic drag polar characterises the relationship between lift and drag across the flight envelope and follows the standard parabolic form given in Equation 8.4 [117]. Where C_D and C_L are drag and lift coefficients; C_{D0}, AR, and e are the zero-lift drag coefficient, aspect ratio, and Oswald efficiency factor. The retrofit benefits from a reduced $C_{D0} = 0.024$, compared to 0.029 for the original Cessna. This reduction is primarily due to the removal of the engine cowling air intakes and exhaust infrastructure, which is replaced by a smoother nose profile housing the electric motor, a battery pack and some thermal systems [118]. Since engine cowlings account for up to 15% of parasitic drag [119], and with the new thermal system requiring a far smaller, more aerodynamic inlet (see Section 8.7), this assumption is valid.

The resulting drag polar is shown in Figure 8.14. The electric variant achieves a maximum lift-to-drag ratio $L/D = 14.9$, compared to $L/D = 12.4$ for the original; this is a 20% aerodynamic efficiency improvement, caused by the C_{D0} reduction and the larger AR. The improved efficiency directly reduces the power required in cruise and therefore improves range and endurance.

Since the original McCauley fixed-pitch propeller is kept in the retrofit, its efficiency is a function of the advance ratio J, defined in Equation 8.5 [120]. Where J is calculated from velocity V, rotational speed n, and propeller diameter D. At the electric minimum power speed of 73 kts (explained in subsection 8.6.3), the propeller operates at $J = 0.59$ with an efficiency of $\eta = 0.81$, compared to $J = 0.56$ and $\eta = 0.77$ at the original minimum power speed of 80 kts. The electric system thus operates 5% more efficiently at its minimum-power condition, a direct consequence of the lower minimum-power speed. The propeller efficiency as a function of advance ratio is shown in Figure 8.15. Even though the propeller remains unchanged, the retrofit still shows a noise reduction due to the removal of combustion and exhaust noise. The Pipistrel Velis Electro showed a 50% reduction in perceived noise compared to its combustion counterpart, the Pipistrel Virus [121]. Demonstrating that similar results should be achievable for this Cessna retrofit.

$$C_D = C_{D0} + \frac{C_L^2}{\pi A R e} \tag{8.4}$$

$$J = \frac{V}{nD} \tag{8.5}$$

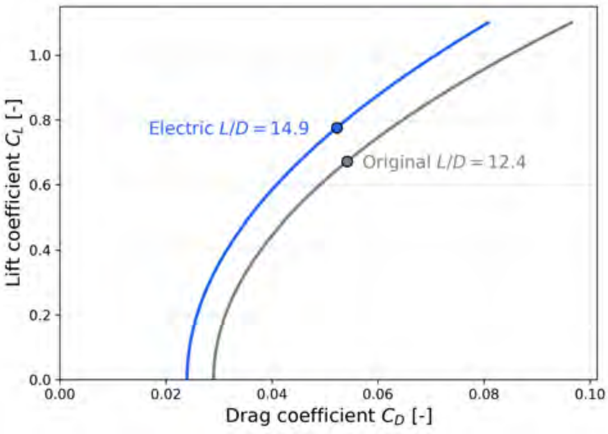

Figure 8.14: Drag polar comparison between the electric (blue) and original (grey) Cessna

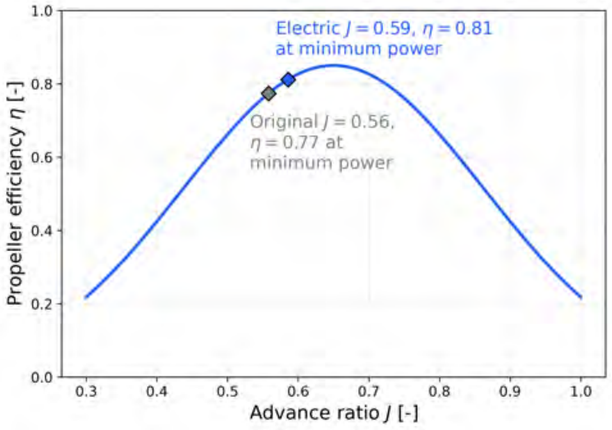

Figure 8.15: Propeller efficiency comparison between electric (blue) and original (grey) minimum power advance ratio

8.6.3. Power Required and Available

To evaluate the performance limits across the flight envelope, the steady-state shaft power required for steady level flight is modelled as shown in Equation 8.6 [122].

$$P_{\text{req}} = \frac{DV}{\eta_{\text{prop}}} = \frac{W}{(L/D)} \cdot \frac{V}{\eta_{\text{prop}}} \tag{8.6}$$

Where P_{req} is required power; D and L are drag and lift forces; W is aircraft weight; V is velocity; and η_{prop} is propeller efficiency, with L/D being the lift-to-drag ratio. The resulting power profiles for both configurations are mapped across the operational velocity spectrum in Figure 8.16 for a cruise altitude of 4,500 ft at 2,000 RPM. Driven by the improved aerodynamic efficiency and optimised propeller advance ratio, the electric retrofit has a minimum power requirement of 39 kW at a true airspeed of 73 kts. In contrast, the original internal combustion engine (ICE) baseline demands a minimum of 49 kW at 80 kts [93]. This yields a 20% reduction in power required at the maximum endurance speed, demonstrating how the structural wing and cowl optimisations successfully offset the weight penalties of the battery pack. This results in an endurance of 100 minutes and a range of 230 km for the retrofit Cessna.

Another operational advantage of the electric configuration is the decoupling of power available from aircraft forward airspeed. The electric motor power available remains constant across airspeed, whereas the original ICE's bell-shaped power available profile is constrained by atmospheric density and engine-RPM coupling that causes power to drop off steeply away from the rated cruise speed. The flat power characteristic of the electric drive ensures that maximum excess power remains available at low airspeeds, directly translating into superior take-off roll acceleration, climb performance, and maximum level speed [123], as will be explained in the following subsection.

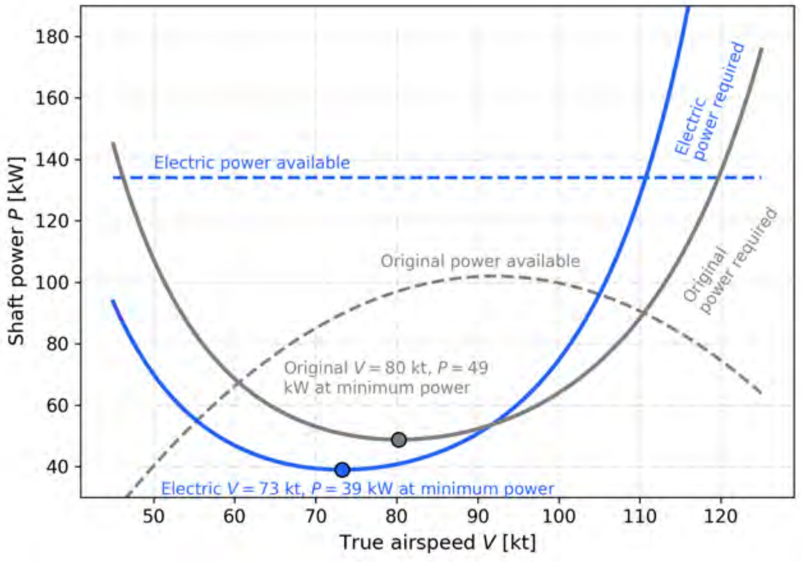

Figure 8.16: Shaft power required and available comparison between electric (blue) and original (grey) Cessna, for cruise altitude (4500 ft) and RPM (2000)

8.6.4. Performance Constraints and Required Power

To ensure that the retrofit Cessna has the same or better performance compared to the original Cessna, the retrofitted aircraft must match or exceed the most performance targets. These targets contain a clean stall speed, maximum level cruise speed, takeoff ground roll and 15 m obstacle clearance, maximum rate of climb (ROC), and landing from 15 m obstacle and roll [93, 116].

Stall Speed and Maximum Cruise Speed

The clean stall speed is determined by Equation 8.7 [117]. Where V_{stall} is the stall speed, which depends on the aircraft weight W, air density ρ, wing planform area S, and maximum lift coefficient $C_{L,\text{max}}$. The 10% MTOW increase is mitigated by the expansion in wing area (14% larger, as specified in Table 8.6). By lowering the net wing loading (W/S), the retrofitted airframe successfully decreases the clean stall speed from the original 53 kts to 51 kts.

Conversely, maximum cruise speed is mostly drag-limited and calculated by the power-balance relation detailed in Equation 8.8. Where P_{shaft} is the required shaft power at a maximum velocity V_{max} and drag coefficient C_D, adjusted by propeller efficiency η_{prop}. Due to the optimised, lower-drag airframe (17% decrease), the power required to overcome parasite drag at high velocity is reduced. As a result, matching the original maximum-level cruise speed target of 123 kts requires just 99 kW of shaft power, or the retrofit could achieve a maximum cruise speed of 132 kts.

$$V_{\text{stall}} = \sqrt{\frac{2W}{\rho S C_{L,\text{max}}}} \tag{8.7}$$

$$P_{\text{shaft}} = \frac{1}{\eta_{\text{prop}}}\left(C_D \frac{1}{2}\rho V_{\text{max}}^3 S\right) \tag{8.8}$$

Take-off Ground Roll and 15 m Obstacle Clearance

Take-off performance is split into ground-roll acceleration and the airborne 15 m obstacle clearance. Due to the flat torque profile of the electric motor, maximum thrust is available immediately at zero velocity. This provides significant initial acceleration, which yields a compliant ground roll of 265 m (compared to the 288 m of the original) under a standard 134.0 kW maximum power, as calculated via Equation 8.9. Where the ground roll distance S_{roll} is determined by liftoff speed V_{lo}, weight W, gravitational acceleration g, thrust T_{to}, average drag D_{avg}, average lift L_{avg}, and ground friction coefficient μ_{roll}.

However, the 10% mass penalty affects the subsequent airborne 15 m obstacle segment. At lift-off, the total horizontal distance required to clear the 15 m obstacle stretches out as a function of the climb trajectory, as expressed in Equation 8.10. Where the airborne distance S_{air} is a function of the climb angle γ, weight W, lift-off thrust T_{lo}, and drag D_{lo}. Because W resides in the denominator of the climb angle profile, the weight penalty flattens the initial path. When constrained to the stock 134.0 kW ceiling, the total distance required to clear the obstacle stretches to 524 m, failing the 514 m target. To shorten the airborne trajectory and meet the 514 m baseline, the required matching shaft power must be driven up to 136 kW.

$$S_{\text{roll}} = \frac{V_{\text{lo}}^2 W}{2g\left(T_{\text{to}} - D_{\text{avg}} - \mu_{\text{roll}}(W - L_{\text{avg}})\right)} \tag{8.9}$$

$$S_{\text{air}} = \frac{15}{\gamma} \approx \frac{15W}{T_{\text{lo}} - D_{\text{lo}}} \tag{8.10}$$

Maximum Rate of Climb

Once the aircraft transitions from the low-speed runway environment into a steady-state climb, the underlying physics shift from thrust-to-weight dominance to an excess power framework. The steady-state rate of climb is given by Equation 8.11 [122], while the forward climb airspeed scales with wing geometry according to Equation 8.12. Where the rate of climb ROC depends on propeller efficiency η_{prop}, shaft power P_{shaft}, drag D, velocity V, and weight W, while the climb velocity V_{climb} scales from a baseline $V_{\text{climb, base}}$ using current-to-baseline weight W/W_{base} and baseline-to-current wing area S_{base}/S ratios.

In this regime, the aerodynamic improvements lower the power required to overcome drag. Furthermore, by optimising propeller RPM during climb, the advance ratio is kept closer to peak efficiency. Consequently, when operating at the full standard 134.0 kW shaft power, the abundance of excess power yields a climb rate of 1,390 ft/min, significantly more than the target of 720 ft/min. To match the target, only 86 kW of shaft power is necessary.

$$\text{ROC} = \frac{\eta_{\text{prop}} P_{\text{shaft}} - DV}{W} \tag{8.11}$$

$$V_{\text{climb}} = V_{\text{climb, base}}\sqrt{\frac{W}{W_{\text{base}}}\frac{S_{\text{base}}}{S}} \tag{8.12}$$

Landing Ground Roll and 15 m Obstacle Clearance

Landing performance is decoupled from power and is governed by touchdown kinetic energy, passive aerodynamic drag, and braking deceleration. The physical rollout segment is modelled by Equation 8.13, while the approach and flare clearance distance from a 15 m height is defined by Equation 8.14. Where the landing ground roll $S_{\text{roll, land}}$ is determined by touchdown speed V_{td}, weight W, gravitational acceleration g, average landing drag $D_{\text{avg, land}}$, braking friction coefficient μ_{brake}, and average landing lift $L_{\text{avg, land}}$, while the landing airborne distance $S_{\text{air, land}}$ is a function of the approach lift-to-drag ratio $(C_L/C_D)_{\text{app}}$.

Despite the 10% mass penalty increasing the aircraft's kinetic energy at touchdown, the expanded wing area permits a lower approach speed, keeping energy growth within reasonable bounds. Mechanical braking successfully manages the landing ground roll within 123 m, which is within the 168 m target. The total calculated landing distance from a 15 m obstacle is 330 m, which also satisfies the 395 m target. This performance profile eliminates any need for design alterations to fulfil this requirement.

$$S_{\text{roll, land}} = \frac{V_{\text{td}}^2 W}{2g\left[D_{\text{avg, land}} + \mu_{\text{brake}}(W - L_{\text{avg, land}})\right]} \tag{8.13}$$

$$S_{\text{air, land}} = 15\left(\frac{C_L}{C_D}\right)_{\text{app}} \tag{8.14}$$

In conclusion, all performance requirements are exceeded except for the take-off 15 m obstacle clearance, which requires a maximum shaft power of 136 kW, as mentioned in Table 8.6. The motor performance, together with battery performance, can be used to evaluate the thermal management system.

8.7. Thermal Management

The thermal system must reject waste heat from the motor and battery pack across the full mission profile without exceeding component temperature limits. A sizing of the components is completed.

8.7.1. Thermal Loading Profile

The thermal loading profile, shown in Figure 8.17, is derived from the common training flight profile. The heat losses from the motor are calculated with efficiency losses, and the heat losses for the battery are derived from Joule heating based on internal cell resistance [112]. The most important thermal considerations are the take-off / touch-and-go peaks and the initial climb phase. As the thermal power output is either highest or sustained high level, making them the critical design points.

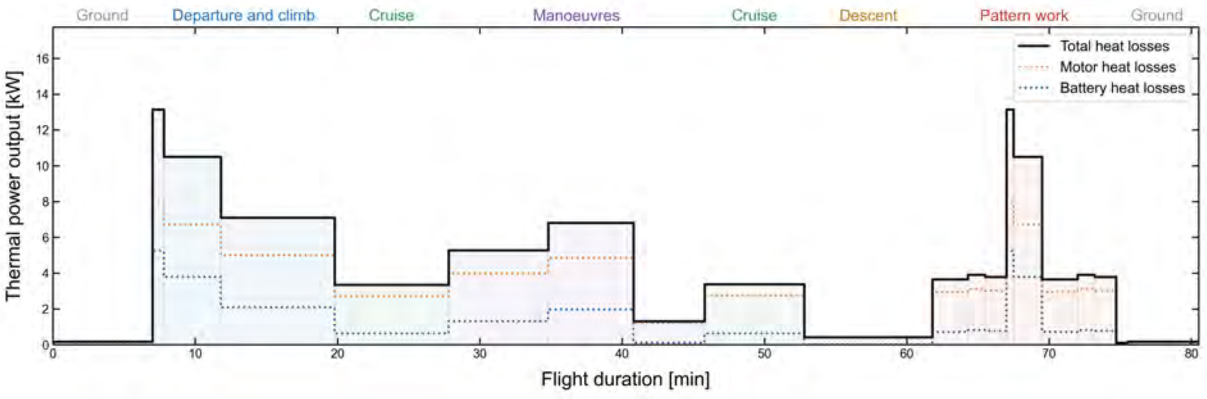

Figure 8.17: Motor and battery heat generation across the training mission

8.7.2. Thermal System Architecture

The thermal system is evaluated at $35°$C, which is standard ISA temperature ($15°$C) plus $20°$C [102]. A shared radiator core architecture is selected to avoid the weight and drag penalties of dual air ducts. Weaving the independent motor and battery coolant loops within a single radiator core allows both systems to utilise the full air-side face area, maximising heat transfer efficiency. Both loops utilise a 50/50 water-ethylene-glycol (WEG). The governing sizing relationships are described in Equation 8.15 [124].

$$\dot{m}_{\text{mot}} = \frac{Q_{\text{mot,des}}}{c_{p,\text{WEG}}\Delta T_{\text{mot}}} \qquad A_{\text{HX}} = \frac{Q_{\text{total,des}}}{\rho_{\text{air}} V_{\text{ram}} c_{p,\text{air}} \Delta T_{\text{air}}} \tag{8.15}$$

Where $\dot{m}_{\text{mot}}$ is the motor loop coolant mass flow rate, $Q_{\text{mot,des}}$ and $Q_{\text{total,des}}$ are the design heat rejection rates for the motor and total system, $c_{p,\text{WEG}}$ and $c_{p,\text{air}}$ are the specific heat capacities of the fluid and air, ΔT_{mot} and ΔT_{air} are the fluid and air temperature changes, ρ_{air} is the air density, V_{ram} is the ram air velocity, and A_{HX} is the total air-side heat exchanger core area. The primary design parameters and resulting system specifications are summarised in Table 8.7. The physical face area ensures adequate surface area to reject the peak sustained continuous flight load at initial climb. The total radiator volume is roughly 12 L, which easily fits next to the motor and batteries in the nose volume calculated previously. The airflow is supplied via a very compact inlet, which significantly optimises cooling-drag compared to the original Cessna. Where each engine cowling has a capture area of roughly 400 cm^2, this results in an 80% decrease of capture area for the retrofit Cessna. Two separate coolant loops are used to balance individual component requirements: the motor loop is set to satisfy manufacturer minimum operational thresholds, while the battery loop is regulated to absorb transient surges. This integrated cooling solution minimises thermal system weight while maintaining peak temperatures safely below the thermal operational limits of the battery and motor. The power consumption of the cooling system is deemed negligible compared to that of the motor.

Table 8.7: Key design and sizing parameters for the cooling system

Parameter	**Value**
Sustained design heat load Q_{total}	10.7 kW (initial climb)
Radiator core face area A_{HX}	2,360 cm^2
Aerodynamic inlet capture area	164 cm^2 $(200 \cdot 80$ mm)
Motor loop coolant flow rate	25 LPM
Battery loop coolant flow rate	5.7 LPM
Peak motor / battery temperature	51 / 40 °C
Total thermal system mass	7.21 kg

8.7.3. Thermal Transient Analysis

To track core component temperatures, a 1-second step-resolved transient thermal model was constructed using a lumped-parameter differential framework shown in Equation 8.16 [125].

$$M_{\text{mot}}c_{p,\text{mot}}\frac{\mathrm{d}T_{\text{mot}}}{\mathrm{d}t} = Q_{\text{motor}} - \frac{T_{\text{mot}} - T_{\text{fluid,in}}}{R_{\text{mot}}} \qquad M_{\text{bat}}c_{p,\text{bat}}\frac{\mathrm{d}T_{\text{bat}}}{\mathrm{d}t} = Q_{\text{batt}} - \frac{T_{\text{bat}} - T_{\text{fluid,in}}}{R_{\text{bat}}} \tag{8.16}$$

Where M_{mot} and M_{bat} are the motor and battery masses; $c_{p,\text{mot}}$ and $c_{p,\text{bat}}$ are their respective specific heat capacities; $\mathrm{d}T/\mathrm{d}t$ represents the transient temperature changes over time t; Q_{motor} and Q_{batt} are the internal heat generation rates; T_{mot} and T_{bat} are the component temperatures; $T_{\text{fluid,in}}$ is the coolant inlet temperature; and R_{mot} and R_{bat} are the respective thermal resistances to the fluid. The resulting temperature profiles across the training mission are shown in Figure 8.18. The inlet temperature is set $5°$C higher than ambient as a margin. The battery's high thermal inertia effectively dampens brief take-off and touch-and-go spikes, keeping cells well below their $55°$C limit and closer to an efficient operating temperature of $40°$C. The motor temperature climbs during sustained climbs but stabilises safely below its $60°$C operational ceiling, validating the design margins and showing the good performance of the thermal system.

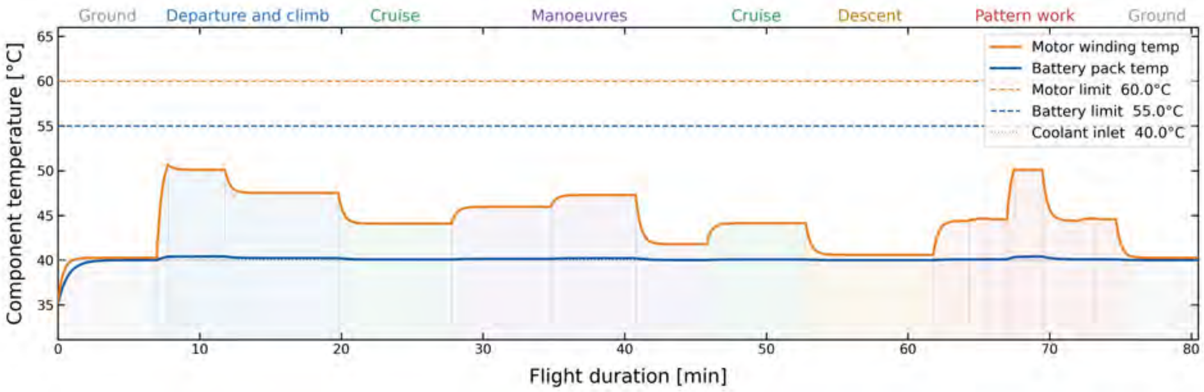

Figure 8.18: Component temperature transient response across the continuous flight profile segments

8.7.4. Recharging Thermal Management

Recharging introduces a critical condition: high-rate current from the charges generates a sustained internal battery Joule heating load of $Q_{\text{charge}} = 5.66\,$kW over a 60-minute cycle. Because the aircraft is stationary, a dedicated electric puller fan is necessary to provide airflow. The radiator core face area is kept fixed from the flight design, and the fan is spun up to pull the required air mass flow. The required fan face velocity is calculated using Equation 8.17 [126]. This results in a fan face velocity of 1.3 m/s, which is easily achievable without significant weight. By isolating the battery circuit to utilise the full radiator face area while the motor loop is inactive, safe cell temperatures are maintained during fast charging without increasing the aircraft's aerodynamic cross-section.

$$V_{\text{fan,charge}} = \frac{\dot{m}_{\text{air,charge}}}{\rho_{\text{air}}A_{\text{HX}}} \tag{8.17}$$

Where $V_{\text{fan,charge}}$ is the fan-induced air velocity during charging, $\dot{m}_{\text{air,charge}}$ is the required air mass flow rate, ρ_{air} is the air density, and A_{HX} is the heat exchanger core area. Apart from recharging, another ground operation that must be considered is heating on cold days. Fortunately, the battery can be kept until $-20°$C. Normal operational procedure will include charging the aircraft before flight, as batteries are best stored at the lowest charge for longer periods of time [110]. However, the minimum battery charging temperature is $0°$C, therefore, an external heating solution must be used for these rare extremely cold days. At temperatures higher than that, the battery will warm to a more efficient temperature during charging.

8.8. Emission and Cost Analysis

During its lifetime, the electric Cessna will have significant differences in emissions and costs with respect to the original Cessna. The operational lifetime of the Cessna is assumed to be 20 years, with 3.5 flights per day for 250 operating days a year. This is equal to 17,500 flights and 23,275 flight hours over its lifetime. The 62% average DOD per flight was taken from the battery degradation profile, resulting in 79 kWh per 80-minute flight.

8.8.1. Emission Analysis

This emission analysis accounts for the production, operations, and EOL CO_2 emissions for both Cessna versions. For the production of the Cessna, the CO_2emissions of the aluminium structure are taken.

In the production of primary aluminium, 10.1 kg of CO_2 is emitted per kg of aluminium. For recycled aluminium, this value is reduced to 1.04 kg CO_2 per kg of aluminium. During its operations, the electrical Cessna uses several battery packages. Battery production accounts for 54 kg of CO_2 equivalents per kWh of storage capacity [127]. However, during its operational lifetime, the electric Cessna has low emissions, especially when using green electricity. The combustion engine, on the other hand, uses AVgas, which produces 3 kg CO_2 per litre [128].

For the full carbon lifecycle assessment of the electric Cessna, a recycling rate of 85% for the aircraft structure and a 30% were end-of-life credit for the batteries was assumed. The result of this assessment was a reduction of 2,052,986 kg CO_2 or an 84% reduction over its lifetime compared to the conventional Cessna.

Table 8.8: Comparison of original and electric retrofit Cessna 172S lifecycle CO_2-emissions

Life cycle phase	**Original [kg CO_2]**	**Electric retrofit [kg CO_2]**
Production	5,610	611
Battery packs (11x)	-	75,535
Operational lifetime	2,443,875	343,262
EOL structure	-4,277	-4,527
EOL battery packs	-	-22,661
Total	**2,445,207**	**392,221**

8.8.2. Cost Analysis

The cost analysis follows a similar procedure. The calculation is done from a consumer's perspective. The price of a new Cessna 172 is approximately €387,000[3]. To find the price for the green retrofit Cessna, the profit margin is removed first. Textron Aviation reported this to be 11% [129]. Then the engine is removed, which costs €82,783[4]. It is assumed that the remaining aircraft components are of the same value for both aircraft. However, since the MTOW is increased by 10%, the cost is multiplied by this factor. Removing the engine and accounting for the mass increase, the cost is €287,811.04. By adding the electric engine and battery costs, the final costs are found. The electric engine costs €40,747, which is calculated using Equation 8.18 [130]. In this formula, the CPI stands for consumer price index, which had a value of 1.301 from 2019 until now [5].

$$\text{EngineCost} = 174 \cdot N_{\text{engine}} \cdot P_{\text{ICE}} \cdot CPI \tag{8.18}$$

The price of the battery is determined by using the price per kWh at the cell level. This is €150.5 [131]. To convert this to pack level, a price conversion of 1.4 is used, which derives from the electric car industry [6]. With this conversion, the battery pack price per kWh is €210.70. Which resulted in a battery price of €26,793.39. Using this value, the cost of the retrofit Cessna is found to be €355,351.75. Using the same profit margin as Textron Aviation, this would result in a selling price of €394,953. Purchasing these alloys at a production cost of €5.13 /kg during manufacturing would reduce the final aircraft production cost; however, this was not taken into account.

The price of the battery pack is €26,793.39. During the lifetime of the Green Cessna, the batteries are replaced ten times. Thus resulting in a total cost of €267,933. However, these costs are offset by a low electricity price compared to the relatively high price of AVgas. Electricity costs €0.25 euro per kWh and one liter of AVgas costs approximately €2.75 in Europe[7][8]. The AVgas price in the US is around €1. Both of these prices will be used in the cost comparison.

During its lifetime, the battery packs used by the Green Cessna are replaced when they are degraded to 90% of the total capacity. This results in a total battery pack capacity of 114.57 kWh. The second-hand value of this battery type is 20.9% of its new price [132]. This results in a rest value of €55,703 for each battery pack. In addition to the battery, both of the aircraft also contain large amounts of aerospace-grade aluminium alloys. This has a scrap value of €1.77. With all life-cycle phases quantified, the overall cost can be found in Table 8.9.

---

[3] URL `https://epicflightacademy.com/cost-of-a-cessna-172/` [cited on 15 June 2026]

[4] URL `https://www.airpowerinc.com/io-360-l2a` [cited on 16 June 2026]

[5] URL `https://www.cbs.nl/nl-nl/visualisaties/dashboard-economie/inflatie` [cited on 17 June 2026]

[6] URL `https://about.bnef.com/insights/clean-energy/lithium-ion-battery-pack-prices-hit-record-low-of-139-kwh/` [cited on 15 June 2026]

[7] URL `https://ec.europa.eu/eurostat/statistics-explained/index.php?title=Electricity_price_statistics` [cited on 15 of June 2026]

[8] URL `https://aviation-fuel-prices.com/airport-info/` [cited on 15 June 2026]

Table 8.9: Comparison of original and electric retrofit Cessna 172S lifecycle costs

Life cycle phase	Original [€]	Electric retrofit [€]
Purchasing cost	387,000	394,953
Battery pack replacements (10x)	-	267,933
Operational lifetime	814,625 - 2,240,218	343,262
EOL structural value	-836	-885
Total EOL battery value	-	-55,703
Total cost	**1,200,789 - 2,626,382**	**949,560**

The most prominent difference can be seen in the operation costs for the combustion Cessna. This is due to the different cost of gas between Europe and North America. If the electric Cessna were used in Europe, it would create a 64% cost reduction. However, in North America, the lower price of AVgas reduces this benefit to 21%.

An overview of the cost and CO_2 emissions during the Cessna 172 lifetime in Europe and America compared to the Green Cessna can be found in Figure 8.19, showing the major advantages of the Green Cessna.

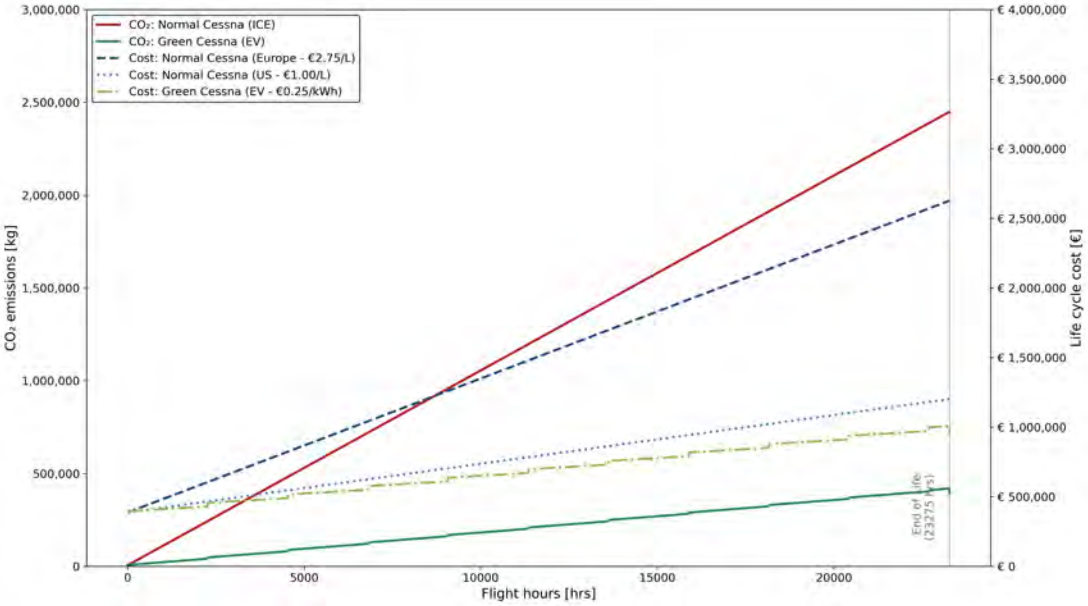

Figure 8.19: Life cycle analysis on CO_2 and cost of the Cessna 172 and Green Cessna

9

Technical Risk Assessment

In this chapter, a technical risk assessment is performed. Firstly, in Section 9.1, a SWOT analysis is performed. Then in Section 9.2, the risks are identified, analysed, and treated. In Section 9.3, risk matrices are created and a rationale is provided. Finally, in Section 9.4, the reliability, availability, maintainability, and safety of the process are described and evaluated.

9.1. SWOT Analysis

In this section, a SWOT analysis is performed. The strengths and weaknesses are internal factors, whilst the opportunities and threats are external. The SWOT analysis is shown in Table 9.1

Table 9.1: SWOT Analysis of Recycled Aluminium and Green Cessna

STRENGTHS	**WEAKNESSES**
▪ High-quality, closed-loop recycling: traditional dismantlers downcycle the aircraft alloys into lower-grade materials. This process preserves the aerospace-grade quality. By doing this, the material can compete with expensive virgin aluminium alloys. ▪ High environmental savings: recycling consumes much less energy. ▪ Strategic sourcing: by operating within the EU, low-carbon power grids are available, keeping the carbon emissions of the entire process low. ▪ Innovative disassembly process: using diamond wire sawing with a computer allows for precise cutting while avoiding cutting through rivets. This reduces the amount of iron contamination and prevents degradation of the material properties. ▪ Green upcycling product: by creating a 'green Cessna 172' with an electric propulsion system, the operational emissions are eliminated. By creating it specifically for training flights, it is tailored to the current market for Cessnas.	▪ Contamination and quality risks: by cutting using a steel-substrate diamond wire, iron debris can contaminate the cut face. This contamination could ruin the melt if it is not cut away. Also, switching between different alloy families can cause alloy cross-contamination. ▪ Complex waste management: both the removal of the chromium coating and the refining of the aluminium alloys create harmful waste. This type of waste requires proper handling and is expensive to get rid of. ▪ High upfront costs: setting up the entire process requires high investments in equipment and infrastructure. ▪ Strict certification constraints: the financial viability depends highly on the certification of the material. This creates an overhead cost of approximately €2,500 per batch and scraps that need to be cycled back into the loop. ▪ Alloy contamination: if the alloys are mixed up after sorting, a mismatch of alloys contaminates the melt. This reduces the quality and causes the alloys to be downgraded. This leads to massive profit reductions.
OPPORTUNITIES	**THREATS**
▪ Phasing out of free EU carbon permits: the EU is gradually phasing out free CO_2 permits for primary aluminium smelters. This shift in regulation could create a shift in baseline costs, causing a competitive edge for the 'green' recycling process. ▪ 'Green premium' introduction: major global companies are more willing to pay a premium for 'green' materials to appeal to eco-conscious customers and to fulfil their sustainability ambitions. It also provides a more sustainable solution than difficult-to-recycle composite materials. ▪ Aerospace feedstock backlog and market growth: the aluminium market is expected to grow significantly. This is mainly driven by the aerospace and automotive sectors. Since a global aircraft retirement wave is expected, the number of available carcasses for recycling is high. ▪ Beneficial EU legislation and funding: the EU's introduction of legislation of the 'Green Deal', 'Circular Economy Action Plan ', and the 'Critical Raw Materials Act' could help create an economically viable business plan by providing a grant and fast-tracking permits.	▪ Severe feedstock competition and sourcing uncertainty: Disassembling companies such as AELS and Tarmac Aerosave are already established companies in the industry and own massive shares of the current market. Since the project is highly dependent on acquiring enough carcasses, this competition could threaten economic viability. ▪ Chromium exposure: the retired aircraft have a highly toxic chromium(VI) coating. Disassembly techniques could vaporise these coatings. This requires closed-off filtration environments, automation or PPE to ensure compliance with health regulations. ▪ Future composition changes: future retiring aircraft will be composed of a higher percentage of composites. This could threaten the longevity of the current set-up. ▪ Energy market fluctuations and Geopolitics: unpredictable legislation changes like tariffs can have a massive impact on the energy market. These spikes in energy costs can cut into the profit margins.

9.2. Risk Identification, Analysis and Treatment

In this section, risks are given identifiers and a short description in the table seen below. Then they are given a risk score and both mitigative and reactive measures. The post-mitigative risk (remaining risk RR) is always lower than the initial value; however, since the likelihood and consequences are given in a range, the values can reduce within a level or shift entire levels.

To find the risk levels, the likelihood is multiplied by the consequence. The levels of likelihood and consequences are defined as follows:

Likelihood

- 0.2: less than 1% likely
- 0.4: 1–10% likely
- 0.6: 10–50% likely
- 0.8: 50–80% likely
- 1: 80–100% likely

Consequences

- 0.2: Small restructuring
- 0.4: Adaptations necessary
- 0.6: Serious adaptations/minor injuries
- 0.8: Multiple adaptations/human injuries
- 1: Project failure/serious harm or death

Table 9.2: Risk Identification, Analysis and Treatment

ID	Risk Item	WP	Score	Mitigative Measure (Proactive)	Reactive Measure (Contingency)	RR	Responsible Person
RSK-CRE-1	Aluminium leaks from smelter	Foundry	0.2	Build underground safety spaces or spill paths.	Activate barriers to contain the melt, stop the remelting process, and start emergency cooling.	0.2	Chief Foundry Engineer
RSK-CRE-2	Chemical Exposure	Foundry	0.16	Mandatory use of specialised PPE, strict closed handling procedures for alkaline cleaners and acids.	Emergency eyewashes or showers and execute hazardous spill containment protocols.	0.04	Chief Foundry Engineer
RSK-CRE-3	Dross formation	Foundry	0.8	Implement compaction and optimised thermal pre-treatments during aluminium scrap recycling.	Adjust material recovery rate in business case, clean alloys more thoroughly	0.24	Chief Foundry Engineer
RSK-CRE-4	Injury due to vapour release from heated baths	Foundry	0.8	Install local exhaust ventilation systems above heated processing baths.	Evacuate the affected area, ramp up ventilation, and provide medical aid.	0.16	Chief Foundry Engineer
RSK-CRE-5	Hydrogen generation during NaOH stripping	Foundry	0.2	Implement strict ignition controls and continuous forced ventilation in stripping zones.	Isolate power sources, trigger gas venting systems, evacuate the floor.	0.04	Chief Foundry Engineer
RSK-SRT-1	Alloy mix-ups	Sorting	0.6	Preliminary sorting, strict sorting using LIBS and routine checks for alloy purity	Sell contaminated melt as waste and audit to find issues within the process	0.4	Chief Engineer Foundry
RSK-DIS-1	Aluminium dust fire/explosion	Disassembly	0.6	Use wet or inert cutting techniques, eliminate ignition sources	Activate localised facility isolation.	0.2	Disassembly Engineer
RSK-DIS-2	Hexavalent chromium (Cr(VI)) exposure	Disassembly	1.0	Use robotic/remote cutting enclosures and monitor continuously.	Immediate operational shutdown, upgrade PPE, perform medical screening.	0.2	Decoating Engineer
RSK-DIS-3	Uncontrolled section drop/collapse	Disassembly	0.8	Design individual segment cradles and enforce strict, pre-defined cutting sequences. Using a rotator for the fuselage to ease cutting	Use of PPE for workers	0.16	Disassembly Engineer
RSK-DIS-4	Diamond-wire breakage and snapback	Disassembly	0.8	Install blast guarding/deflectors and create physical operator exclusion zones.	Engage emergency wire brakes, initiate remote-system lockouts.	0.16	Disassembly Lead

ID	Risk Item	WP	Score	Mitigative Measure (Proactive)	Reactive Measure (Contingency)	RR	Responsible Person
RSK-DIS-5	Cutting into residual fluids / pressurised parts	Disassembly	0.2	Mandate strict stripping steps and complete hazardous component mapping.	Activate secondary spill containment kits, deploy specialised containment teams.	0.04	Disassembly Engineer
RSK-LOG-1	Lack of aircraft	Logistics	0.8	Secure sourcing contracts early; source a diverse, mixed fleet to guarantee baseline supply.	Source alternative aircraft brands or modify project scheduling.	0.24	Business Manager
RSK-LOG-2	Fuel price increase	Logistics	0.4	Secure fuel price agreements or execute bulk-purchase supply contracts.	Optimise transportation routing, adjust budget allocations, and baseline costs.	0.2	Business Manager
RSK-CRT-1	Certification failure	Certification	0.8	Conduct early and frequent internal tests.	Engage external regulatory consultants, design an immediate compliance recovery plan.	0.24	Chief Foundry Engineer
RSK-PRP-1	Battery malfunction	Electric Propulsion	0.2	Integrate two decoupled, independent battery packs to ensure system redundancy.	Isolate failed pack, switch system to the operational backup pack.	0.04	Electrical Engineer
RSK-PRP-2	Engine malfunction	Electric Propulsion	0.2	Design and verify safe aircraft gliding performance profiles during the design phase.	Execute standard forced-glide landing procedures, deploy emergency transponder.	0.04	Propulsion Engineer
RSK-PRP-3	Battery overheating	Electric Propulsion	0.2	Implement conservative thermal margins in battery layout alongside active cooling systems.	Trigger emergency liquid cooling loop flush, reduce propulsion power draw.	0.04	Propulsion Engineer
RSK-PRP-4	Unexpected battery degradation	Electric Propulsion	0.2	Integrate real-time state-of-health tracking algorithms into the battery management system.	Enforce strict predictive maintenance and replace battery frequently	0.04	Electrical Engineer
RSK-PRP-5	Control difference from Cessna	Electric Propulsion	0.48	Design flight control software and control surface gearing to mimic traditional feel.	Deploy firmware patches to adjust control law sensitivity.	0.12	Chief Design Engineer
RSK-PRP-6	Too long charging time	Electric Propulsion	0.12	Integrate high-power fast charging batteries	Use less capacity of the battery at once.	0.04	Electrical Engineer
RSK-DES-1	Underestimating aeroloads	Cessna Design	0.6	Use validated CFD models backed by empirical flight data and structural safety margins.	Recalculate stress loads, integrate local structural reinforcements.	0.12	Structural Engineer
RSK-DES-2	Model inaccuracies	Cessna Design	0.8	cross-examine analytical models with wind tunnel testing and historical datasets.	Apply conservative design coefficients across affected structures.	0.16	Structural Engineer

9.3. Risk Matrices and Rationale

The risks identified earlier are placed in a matrix, which provides a clear overview of the criticality of all risks. In all matrices, the bottom-left (light green) indicates that the risk level is low (the risk may be worth accepting when it remains monitored). The darker green and light yellow risks require a level of management, mitigation, and monitoring. The top right corners (dark yellow, red and dark red) require extensive management, monitoring, mitigation and in the case of dark red, senior management involvement. The inherent risk matrix (before mitigative measures) is shown in Table 9.3, the residual risk matrix follows the same structure as the previous risk matrix. The mitigative actions result in a downward and leftward shift, which shows that the mitigative actions were effective. For all risks, the value for the likelihood or probability is on the vertical axis and the consequence on the horizontal axis.

Seven risks fall into the dark red region. This makes them critical risks, causing them to require active management. The mitigative measures are briefly explained below.

A primary risk is alloy mix-ups. The high-quality of the alloys is a driving factor for the project. Without this, the financial viability of the project is endangered, and the loop is not closed. This risk is mitigated by disassembling the aircraft carefully and using LIBS after decoating to sort the material once more. This moves the risk from a probability of 0.6 to 0.4, thus outside of the critical zone. However, it is still high risk and requires active monitoring. The contingency plan includes regular in-house testing and internal audits. Secondly, chromium exposure (RSK-DIS-2) is considered. By using automation, this risk is entirely avoided, but in case humans are involved, mandatory use of PPE and handling procedures are implemented. This decreases the likelihood of injury from the chromium coating from 1 to 0.2 and is considered low-risk. Then, certification failure is considered (RSK-CRT-1). By not being able to certify the material, the price goes down drastically and makes the entire process unfeasible. Mitigative measures include early and frequent in-house testing. A reactive measure is to create a recovery plan. By frequently testing in-house, the likelihood is decreased to 0.4. Although out of the critical zone, this is still a medium-high risk and will require active monitoring. Thirdly, the collapse of the aircraft carcass is looked at (RSK-DIS-3). Since this can cause significant human injury, it is a critical risk. By implementing a strict cutting plan and rotating the fuselage to ease cutting, the risk of collapse is significantly reduced to 0.2. Reactive measures include PPE, but the consequences of collapse are still significant, so the risk should be monitored. Then, design risks are looked at. The underestimation of aerodynamic loads is critical as it could cause failure during flight (RSK-DES-1). Using validated models and safety factors, the likelihood of failure of the aircraft decreases massively, from 0.8 to 0.2. Model inaccuracies can also be detrimental to the performance of the aircraft. By cross-examining the models with wind tunnel testing and historical datasets, this risk is mitigated effectively and falls within the low-risk zone. Also, the disassembly of the aircraft generates significant amounts of fine aluminium metal dust. When this is suspended in a confined space this poses a severe explosion and fire hazard (RSK-DIS-1). This risk is mitigated by installing continuous wet-scrubber dust extraction systems. When combining these with spark-detection systems and automated explosion suppression barriers, the probability of a dust explosion shifts from 0.6 down to 0.2. This successfully places this risk well within the low-risk zone.

Finally, not being able to source enough aircraft endangers the economic feasibility of the project (RSK-LOG-1). If the amount is too low, the non-recurring costs cannot be paid back. By making agreements with lessors and getting contracts early on, this potential risk is effectively mitigated. Since it is not guaranteed that these lessors want to work together and may work with potential competitors, this risk is still medium-high and requires active monitoring.

Table 9.3: Comparative Pre-Mitigative and Residual Risk Matrices

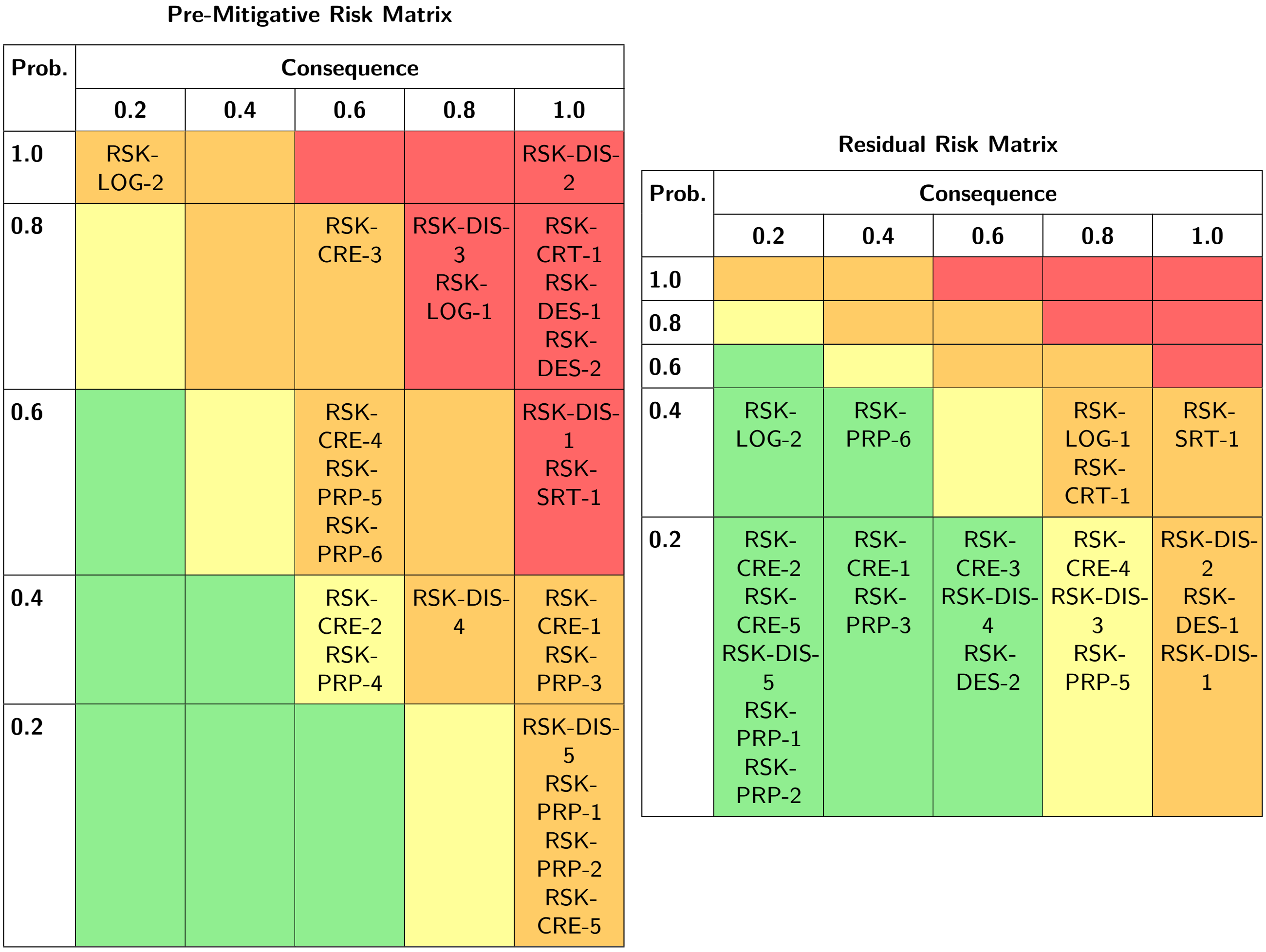

Pre-Mitigative Risk Matrix

Prob.	Consequence				
	0.2	0.4	0.6	0.8	1.0
1.0	RSK-LOG-2				RSK-DIS-2
0.8			RSK-CRE-3	RSK-DIS-3 RSK-LOG-1	RSK-CRT-1 RSK-DES-1 RSK-DES-2
0.6			RSK-CRE-4 RSK-PRP-5 RSK-PRP-6		RSK-DIS-1 RSK-SRT-1
0.4			RSK-CRE-2 RSK-PRP-4	RSK-DIS-4	RSK-CRE-1 RSK-PRP-3
0.2					RSK-DIS-5 RSK-PRP-1 RSK-PRP-2 RSK-CRE-5

Residual Risk Matrix

Prob.	Consequence				
	0.2	0.4	0.6	0.8	1.0
1.0					
0.8					
0.6					
0.4	RSK-LOG-2	RSK-PRP-6		RSK-LOG-1 RSK-CRT-1	RSK-SRT-1
0.2	RSK-CRE-2 RSK-CRE-5 RSK-DIS-5 RSK-PRP-1 RSK-PRP-2	RSK-CRE-1 RSK-PRP-3	RSK-CRE-3 RSK-DIS-4 RSK-DES-2	RSK-CRE-4 RSK-DIS-3 RSK-PRP-5	RSK-DIS-2 RSK-DES-1 RSK-DIS-1

9.4. Reliability, Availability, Maintainability and Safety

Using a reliability, availability, maintainability and safety (RAMS) framework creates project viability, minimises uncertainties, ensures the health and safety of both employees and the environment, and the project. This framework is applied to all parts of the process and is illustrated in subsequent subsections.

9.4.1. Disassembly Processes

To ensure RAMS compliance, a stock of spare parts is in place. Replacement parts are available in sufficient quantity to cover maintenance operations and predicted consumables for one year. During disassembly, there are two main operation-related consumables: diamond wire and laser cutter nozzles. The nitrogen used for laser cutting is produced on-site, so it is not necessary to keep a stock. To size the need for maintenance-related consumables and spare parts, manufacturers' guidelines and suggested best practices are used.

The wire saw cutting will not be operative when employees enter the cutting zone. Therefore, once the machine is in operation, no employees are allowed to go within 5 m of the saw. Furthermore, due to airborne metal generated during wire-saw operations, all employees within 20 m of the saw are required to wear PPE.

The laser cutters use high-powered lasers to cut chromium-coated parts. Due to the heat produced by the laser, the chromium coating vaporises and becomes airborne. The room requires ventilation to remove these fumes from the working area. The laser reflects the cutting surface and could result in eye injury. Therefore, the machine should be approached only with a respirator and suitable eye protection.

9.4.2. Chemical Decoating Systems

The RAMS characteristics of the chemical decoating stage are modelled around a specialised immersion bath system. Because this process uses heated chemical baths, aggressive alkaline solutions, multiple rinsing stages, drying stations, and contaminated coating waste streams, the system layout is engineered to prioritise reliability while strictly limiting operator and surrounding ecosystem exposure risks.

The operational reliability of the coating removal process depends on the synchronised performance of several subsystems. These include chemical tank enclosures, immersion racks, drying ovens, and heating elements.

To optimise system reliability, the process incorporates real-time chemical bath monitoring, isolated multi-stage rinsing, easily replaceable filtration units, and dedicated waste collection systems for each discrete chemical stream. Crucially, implementing multiple parallel bath lines enhances reliability and system availability by eliminating single-point vulnerabilities. If an immersion line requires maintenance, the remaining parallel lines continue to operate at reduced capacity, preventing a complete operational stoppage. Furthermore, by using commercially established chemical stripping and surface treatment equipment, the technical uncertainty of this stage is minimised.

The decoating architecture is designed to enable independent inspection, servicing, and isolation of components. This simplifies both scheduled and unscheduled maintenance protocols. Routine, preventative maintenance checks are applied to ensure machinery integrity and process safety. These checks monitor chemical concentrations, pH levels, temperature sensors, heating elements, fluid agitators, tank seals, filtration media, ventilation fans and drying ovens. Conversely, corrective, non-scheduled maintenance protocols are clearly defined if events such as chemical leakages, abnormal bath temperature fluctuations, incomplete coating removal, drying oven failures, or drops in ventilation performance occur.

The most critical functions of chemicals are chemical containment, heating, ventilation, safe part transfer, and segregated waste handling. Structural containment is paramount to mitigate the risk of leaks, spills, and employee exposure. As the stripping baths operate at elevated temperatures, vapour and fume generation is suppressed and controlled using sealed, instrumented tank covers. Source capture ventilation hoods are positioned directly above the tanks to control fume dispersion. To eliminate manual exposure to hazardous chemicals, parts are transferred via specialised baskets, structural racks, and automated overhead hoists. Operators are required to wear PPE during loading, unloading, bath inspection, and physical maintenance tasks.

The process is redundant, with parallel lines, focusing on the most time-critical bath operations. For secondary subsystems, redundancy is created by keeping a stock of replaceable components, such as spare pumps, inline filters, redundant sensors, and emergency safety equipment. Ultimately, redundancy is deployed especially if component failure would severely impact personnel safety or annual processing throughput.

9.4.3. Aluminium Refining and Structural Redesign

Aluminium refining is a highly mature, heavily researched domain. Substantial research and development funding has been channelled into optimising scrap refinement. Consequently, modern refining machinery features low maintenance requirements, minimal recurring costs, and high operational reliability validated by decades of industrial deployment.

The refining process relies on downstream supply lines from the disassembly and decoating stages, receiving a steady, sorted influx of alloys to process distinct AA2024 and AA7075 batches. Personnel safety within this capital-intensive sector is highly regulated; annual industry-wide incident reports, such as those compiled by the Aluminium Association [133], drive continuous improvements in occupational safety standards.

The post-casting sheet production of recycled aluminium and subsequent thermomechanical treatments are outsourced to external suppliers. Sheet manufacturing is a massive, highly standardised global sector. As a result, its reliability, maintainability, and safety protocols are strictly regulated by entities such as the Aluminium Association and comprehensive ISO certifications, keeping technical risk to a minimum.

The structural output of the retrofitted Cessna, particularly the redesigned wing structure, is evaluated with RAMS to address critical fatigue concerns. Reliability is achieved when all components respond to loads in a predictable manner, as monitored during testing and certification of the retrofit Cessna. The availability of the structure is determined by the ability to integrate recycled aluminium alloys. Maintainability focuses on components being accessible for non-destructive inspection, routine repair and replacement. Safety is guaranteed by using sufficient safety margins and checking for crack propagation.

9.4.4. Electric Propulsion Integration

Although electric propulsion is a recent application within the aviation sector, the underlying technology has a Technology Readiness Level (TRL) of 9[1]. This maturity rating indicates that the propulsion system is commercially viable, fully developed, and inherently reliable for flight operations.

To improve in-flight safety, two independent and isolated battery packs are used. These battery packs are separated in the front by the firewall, and in the back, an additional firewall will be added. For the safety of the passengers. The system is configured to maintain an average Depth of Discharge (DOD) of 61.7%. This conservative operational profile ensures that if one battery pack suffers a sudden, catastrophic failure, the remaining operational pack retains a

---

[1] URL `https://www.rvo.nl/sites/default/files/2026-04/brochure-milieulijst-2026-0104206.pdf` [cited on 15 June 2026]

robust energy reserve. This configuration prevents the cells from being pushed to their physical limits while ensuring the pilot has ample endurance to execute a safe emergency diversion and landing.

Compared to conventional internal combustion engine (ICE) aircraft, the electric Cessna's powertrain requires less maintenance. Data from the automotive sector indicates that electric motors incur approximately 50% lower maintenance costs than equivalent ICE variants [134]. This trend is assumed to carry over into electric aviation. In addition to being cost-effective, shorter scheduled repairs limit maintenance downtime, thereby maximising operational availability.

Despite these operational benefits, the widespread adoption of electric aviation is limited. Currently, only one certified electric aircraft exists on the commercial market, which has an endurance of 50 minutes[2]. Because of its limited market share, airports have not yet broadly deployed the infrastructure required to support a large-scale introduction of electric aircraft.

9.4.5. Logistics and Operations

The process is designed to provide RAMS throughout the sourcing, certification, testing and transport stages. Reliability is achieved by sourcing aircraft from French boneyards and by contracting with large lessors, creating a steady supply. Also, applying standardised testing and certification procedures to verify alloy composition and material quality before further processing reduces the risk of producing low-quality material. Availability is increased by operating within the EU, by well-developed transport networks, and by regulations that support an efficient supply chain. Maintainability is assisted by using accredited testing laboratories, standardised certification procedures, and existing logistics infrastructure. Safety is ensured by complying with European regulations governing aircraft dismantling, hazardous material handling, laboratory testing, and freight transport. This protects workers, local communities, and the process of recycling aerospace materials throughout the supply chain.

---

[2] URL `https://www.pipistrel-aircraft.com/products/velis-electro/` [cited on 15 June 2026]

10

Sustainability Assessment

The recycling process is done to create a closed-loop system for aluminium alloys. In addition, a 'green' retrofit electric Cessna is designed to demonstrate that recycled aluminium alloys can be used in aerospace applications. An explanation of this strategy is done based on three separate perspectives: social sustainability in Section 10.1, economic sustainability in Section 10.2 and environmental sustainability in Section 10.3.

10.1. Social Sustainability

From a social perspective, the proposed recycling process contributes to employment, workforce development, community engagement and responsible sourcing. Unlike current industry practices, where aircraft aluminium is often dismantled and processed without any alloy-specific sorting, the proposed process requires a high degree of material separation during disassembly. This creates opportunities for skilled employment in aircraft dismantling, material identification and metallurgical processing. To support these activities, investments will be made in human capital through targeted employee training programs. This also contributes to the development and retention of technical expertise within the European aerospace and recycling sectors.

The disassembly activities are expected to take place in France or Spain. Although aircraft storage and dismantling facilities are often located in remote areas, the infrastructure and accessibility of these locations reduce challenges related to employee housing and transportation compared to more isolated aircraft boneyards. Employee well-being will be prioritised through monitoring and managing both physical and mental health conditions, ensuring a safe and sustainable working environment throughout the recycling process.

In addition, the project focuses on community engagement and transparency. Information regarding project activities and potential environmental impacts will be actively communicated to nearby residents and stakeholders. This is particularly relevant for facilities involved in chromium(VI) removal, aluminium melting operations and aircraft disassembly. By maintaining transparent communication, the project aims to improve public trust, enhance perceived safety and reduce potential resistance from local communities.

Finally, although the resulting Cessna aircraft will be fully electric, the batteries required for propulsion rely on raw materials that are often associated with unsafe working conditions, human rights concerns and exploitation within global mining supply chains [135]. To address these risks, a transparent supply chain and responsible sourcing policy will be implemented for all battery procurement activities. Compliance with the European Union Battery Regulation will be required to ensure that environmental, social and human rights considerations are incorporated throughout the battery value chain.

10.2. Economical Sustainability

Currently, aerospace aluminium is downcycled into the automotive industry, where it competes with mixed alloy scrap aluminium. Since the recycled aluminium will be aerospace-grade, it will compete with virgin aluminium. This will significantly increase its market price. The material's recyclability raises the market price slightly, driven by a 'green premium', as it helps companies achieve their sustainability goals.

Early-stage testing is crucial to prevent project failure, as low-quality alloys cannot be certified as aerospace-grade. To ensure the project's longevity and stabilise against market volatility, a buy-back arrangement should be set up with major lessors, such as AerCap or Avolon, to close the loop. Demonstrating a stable supply chain is also required for European grant applications.

Additionally, raw material prices are highly sensitive to geopolitics. Recycled aluminium is much less vulnerable to this because it can be produced wherever aircraft fly or are stored. While the electric Cessna has high upfront battery costs, these are offset by lower recurring operational and maintenance costs.

Logistically, sourcing the retired aircraft directly in France and executing the energy-intensive smelting phase locally creates an efficient setup. By keeping the entire operation within the EU, complex cross-border import duties are avoided. Furthermore, using electric melting furnaces directly on the low-carbon French electricity grid, carbon credit expenses are cut drastically, which have risen consistently since their initial introduction.

The aircraft currently stored in boneyards can be used in the recycling process, but these will run out if the project is scaled up. It is essential to the company's longevity that it also recycle the fleet that will retire over the next 10 years. In addition, the use of sustainable energy will reduce carbon credit costs, which have been rising steadily since their introduction in 1997.

Looking beyond the next 10-15 years, future planning must account for the fact that retiring airframes will contain a significantly higher percentage of composite materials.

10.3. Environmental Sustainability

Recycling aluminium comes with significant environmental benefits. The process is measured directly against two metrics defined earlier in the process: embodied energy consumption and embodied carbon intensity. The first aspect is adhered to by producing recycled aluminium, which requires approximately 95% less energy than the production of virgin aluminium. The second aspect is adhered to by using the French electricity grid. Since recycling on a large scale still demands significant energy, especially during the smelting phase, using this 95% green grid reduces emissions sufficiently.

Another aspect is waste reduction. By preserving the high structural quality of the aerospace alloys, a closed-loop system is established. Ensuring a high recovery rate prevents the material from being downcycled into lower-value automotive products. Substituting virgin aluminium alloys with recycled material limits the expansion of bauxite mines. This limitation prevents more local habitat degradation, prevents deforestation, and stops the generation of "red mud" which frequently causes severe water pollution and river contamination [136].

Furthermore, the implementation of an electric instead of a fuel-powered aircraft delivers environmental advantages. This switch eliminates direct operational greenhouse gas emissions. When a renewable charging grid charges this aircraft the entire lifecycle carbon footprint is minimized.

11

Business case

11.1. Technical Resource Budgets

Mass Budget

The mass budget tracks where the mass of an end-of-life aircraft goes as it passes through the recycling process, from the whole-aircraft input to the final output streams. It is constructed as a conservation balance: the mass of every output stream sums back to the operating empty weight (OEW), so no mass is created or lost unaccounted for. All figures are averages per aircraft, calculated as outlined in Chapter 11.

Table 11.1 gives the resulting per-aircraft mass budget. About 35% of the OEW is recoverable structural aluminium (20,538 kg). Of this, the recovered fraction passes through the foundry: 7,536 kg (13% of OEW) leaves as saleable product, (12,918 kg, 22% of OEW) leaves as lower-value downcycled scrap, and a small dross loss ($\sim 0.2\%$) is skimmed in melting. The remaining mass is the non-aluminium structure (15%: steel, titanium, fasteners and composites) and the non-structural components (50%: engines, landing gear, systems, interiors, and residual fluids), which are removed before sectioning and routed to component reuse, separate material recycling, or disposal. These are outside the aluminium recovery line but are included here to balance the books.

Table 11.1: Per-aircraft (average) mass budget

Stream	Mass [kg]	% OEW
Aluminium product (sold)	7,536	12.84
Aluminium scrap (sold)	12,918	22.01
Dross / melt loss	84	0.14
Non-aluminium structure	8,802	15.00
Non-structural components	29,340	50.00
Total (OEW)	**58,680**	**100.00**

Table 11.1 presents average mass results for the aircraft expected to be recycled, weighted by the proportions of narrow- and wide-body airframes in the retiring fleet. A more detailed description of the used approach can be found in Section 11.2.

Energy Budget

In order to assess the energy needs of the recycling process, its performance against primary aluminium alloy production, and check that the project requirements are met, the following Table 11.2 is compiled. The table summarises the energy required by each step of the process, normalised per kilogram of sold aluminium. Transport does not use electricity and is thus ignored in this budget.

Table 11.2: Energy budget

Process	**Energy** [kWh/kg]
Diamond wire sawing	0.046
Wing Laser cutting	0.041
Fuselage Laser cutting	0.037
Sorting	0.017
Decoating	0.736
Refining & Casting	2.50
Sheet production (Rolling & Heat treating)	2.61
Transport	0.207
Total	**6.19**

Refining thus largely drives the energy need of the full recycling chain, followed by the most energy-intensive processes for the production of the final product: sheet production.

Emissions Budget

In order to assess the environmental impact of the recycling process, its performance against primary aluminium alloy production, and check that the project requirements are met, the following Table 11.3 is compiled. The table summarises the emissions produced by each step of the process, normalised per kilogram of sold aluminium. All emissions are reported in CO_2eq, with conversion factors [91] used when applicable.

Table 11.3: Emissions budget

Process	**Emissions** [CO_2eq/kg]
Diamond wire sawing	0.00124
Wing Laser cutting	0.00110
Fuselage Laser cutting	0.0021
Sorting	0.00046
Decoating	0.0200
Melt refining	0.0675
Sheet production	0.0705
Transport	0.0516
Total	**0.215**

Sheet-making and casting are thus driving the emissions of the recycling chain, with transport also accounting for a significant portion of them.

Comparison with primary production

Table 11.4: Key performance metrics comparing primary and recycled aerospace-grade aluminium alloys.

Metric	**Primary**	**Recycled**	**% reduction**
Carbon footprint (Europe, incl. imports)	10.1 kg CO_2e/kg [137]	0.215 kg CO_2e/kg	– 98%
Process energy (excl. transport)	14.8 kWh/kg [138]	6.19 kWh/kg	– 58%

On the key metrics of environmental footprint and energy consumption, recycled aluminium alloys greatly outperform primary production. They record an almost 98% reduction in emissions, and energy consumption for production is slashed by 58%. For the estimated 600 t yearly throughput, a total of 129 t of CO_2e emissions are therefore saved, the equivalent of taking 30 cars off the road [1].

11.2. Cost Budget

The objective of the cost budget is to determine the minimum number of aircraft that must be processed per year for the dismantling and aluminium alloy recovery operation to be financially viable. Because the supply of retired aircraft is uncertain and competed for, throughput is treated as the central decision variable: the model sweeps the annual number of processed aircraft and recomputes the full budget at each value, rather than assuming a single operating point. All monetary values are in euros.

The business case runs on a fleet-weighted-average airframe (OEW 58,680 kg). Two empirical inputs are imported from single-aircraft worked examples and assumed to scale: the structural-aluminium recovery fraction from the A310 (Chapter 4), and the per-kilogram carcass price 1.77/kg benchmarked on a Boeing 747 (subsection 3.3.2). No single physical aircraft has all three properties; the average airframe is a modelling construct. The 19% figure in Sec. 3.3.3 is a fraction of OEW used only to convert the 55,000 carcass into the 1.77/kg acquisition price; the recovery fraction is a fraction of structural aluminium and governs saleable mass. They measure different things and are not meant to match.

Model Structure

The operation is decomposed into several unit processes (cutting, decoating, sorting, the foundry chain, sheet production, sourcing, logistics, certification and the facility). For each process, the budget separates capital expenditure (CAPEX) from three operating-expenditure (OPEX) channels, so that each cost scales appropriately:

---

[1] URL `https://www.epa.gov/energy/greenhouse-gas-equivalencies-calculator-calculations-and-references` [cited 15 June 2026]

- per-kg OPEX: mainly energy and consumables that scale with the mass processed
- per-aircraft OPEX: costs incurred once per airframe (e.g. handling, inspection)
- fixed OPEX: volume-independent costs such as labour, rentals and transport contracts

Mass Bases

It must be noted that, for the per-kg figures, the reference masses vary for each process depending on how much material has left the recycling loop at a given point. Three bases are used (also summarised in Table 11.6):

- The sold mass $m_{\text{sold}} = 7,536,$kg per aircraft is the mass of aerospace-grade aluminium sold
- The recovered mass $m_{\text{rec}} = m_{\text{sold}}/\text{MRR}$ is the aluminium fed into the foundry before melt losses, where the foundry metal-recovery rate $\text{MRR} = 0.989$ accounts for the 1.1% lost as dross and oxidation. This is the basis for the per-kg costs of foundry processes and everything downstream of it
- The Operating Empty Weight (OEW) is used for the two processes that act on the entire airframe: aircraft acquisition and wire sawing.

Revenue

Two revenue streams are modelled. The primary stream is the sale of the recycled aluminium alloys at price p_{Al} on the sold mass basis. The second is scrap revenue from the sale of unsorted aircraft material for downcycling purposes, as is already done by some dismantling companies such as AELS or Tarmac Aerosave. With the aircraft assumed to be acquired for scrap price, the structural weight accounting for roughly 50% of the OEW, it only being roughly 70% aluminium, and the recycled fraction about 37.1% of the structural weight, about $0.5 \cdot 0.7 \cdot (1 - 0.371) \approx 22\%$ of OEW by mass; reselling it as scrap recovers a corresponding share of the per-kilogram acquisition outlay.. Annual revenue at a throughput n is therefore

$$R(n) = n\left(m_{\text{sold}}\,p_{\text{Al}} + m_{\text{rec}}\,p_{\text{scrap}} + \text{OEW}p_{\text{green}}\right), \qquad p_{\text{scrap}} = p_{\text{acq}}, \tag{11.1}$$

with p_{acq} the per-kg acquisition price and p_{green} the green premium presented in Chapter 2.

To compute the revenue for recycled aluminium, an average sold mass of alloys and an average sale price are defined. The sold mass m_{sold} is computed using the empirically determined ratio of recovered aluminium to OEW for the Airbus A310, multiplied by the weighted average OEW for planes expected to retire. The weights in this average are the proportions of narrowbody, widebody and regional aircraft to be retired [139]. This number is then multiplied by the foundry MRR to obtain m_{sold}. Similarly, the sale prices for the aluminium alloys recycled by this project (AA2024 and AA7075) are weighted by their prevalence in aircraft [140] to obtain a single figure for the average sale price p_{Al}.

Capacity-driven CAPEX

Each process can only handle a finite number of aircraft per year per unit of equipment. Exceeding that capacity "triggers" an additional block of capital investment, capturing the step-wise nature of scaling such an industrial process. For process a p with base CAPEX C_p^0, a per-unit capacity of κ_p aircraft per year, and incremental block cost ΔC_p, the effective CAPEX at a throughput n is

$$C_p(n) = C_p^0 + \max\Big(0,\ \lceil n/\kappa_p \rceil - 1\Big)\,\Delta C_p. \tag{11.2}$$

The total upfront investment is $C(n) = \sum_p C_p(n)$ and is assumed to be spent all at once at $t = 0$. CAPEX is expensed by straight-line depreciation over each asset's economic life L_p, giving an annual depreciation expense of $D(n) = \sum_p C_p(n)/L_p$. The depreciation periods for each item are established according to IRS guidelines [19].

Profit and Cash Flow

The annual accounting (accrual) profit Π and operating cash flow CF thus are

$$\Pi(n) = R(n) - \text{OPEX}(n) - D(n), \tag{11.3}$$

$$\text{CF}(n) = R(n) - \text{OPEX}(n), \tag{11.4}$$

Depreciation is a non-cash expense and is therefore excluded from cash flow, as it is simply the accounting spread of the CAPEX over the entire depreciation period.

Financial assumptions

In order to account for the time value of money and define a minimum viable number of aircraft to be dismantled, a discount rate and payback period must be set.

Discount Rate (WACC)

Future cash flows are discounted at a weighted average cost of capital (WACC) built from the inputs summarised in Table 11.5.

Table 11.5: WACC inputs

Input	Value	Source
Risk-free rate R_f	3.06%	10-yr German Bund (lowest risk bond)[2]
Equity risk premium ERP	4.2%	Damodaran, mature Europe [141]
Unlevered beta β_u	0.81	Env. & Waste Services [3]
Size premium SP	3.4%	assumed based on Banz [142]
Pre-tax cost of debt R_d	6.27%	R_f + B-rating spread [4]
Tax rate t	25%	French corporate tax [143]
Debt/equity weights	$30/70$	assumed from comparable ventures

The cost of equity follows the Capital Asset Pricing Model, $R_e = R_f + \beta_L\,\text{ERP} + \text{SP}$, with the unlevered sector beta $\beta_L = \beta_u\,[1+(1-t)\,D/E]$ relevered to a $30/70$ debt/equity structure. A micro-cap size premium SP is added because the venture is a small, single-asset operation rather than a diversified listed firm [142]. Combining the cost of equity with an after-tax cost of debt $R_d(1-t)$ at the chosen weights gives

$$\text{WACC} = \tfrac{E}{V}R_e + \tfrac{D}{V}R_d(1-t) \approx 9\%. \tag{11.5}$$

Payback Target and Horizon

A discounted payback target of 5 years is imposed, reflecting the roughly 20-year window over which the retired aircraft targeted by this project are expected to be available, and a longer payback would mean capturing fewer retirements, significantly hurting return on investment (ROI). On the other hand, the project life used for the cash-flow and return analysis is 20 years, accounting for the full expected lifetime of this venture.

Viability Criteria

A throughput is deemed viable only if it satisfies both:

(A) Steady-state profitability: $\Pi(n) \geq 0$, meaning a normal operating year covers or exceeds OPEX and depreciation.

(B) Payback: the discounted payback period is at most 5 years. With CAPEX at $t = 0$ and constant cash flow, this is equivalent to a non-negative 5-year net present value (NPV). Thus, the criterion can be written as $\text{NPV}_5(n) = -C(n) + \sum_{t=1}^{5} \text{CF}(n)/(1+\text{WACC})^t \geq 0$.

The minimum viable fleet is the smallest number of processed aircraft n meeting both. In practice, results show that criterion (B) is binding, as accounting profitability is reached at a much lower volume than cash recovery.

Results

At the assumed inputs, the contribution margin is positive at €66,253 per aircraft (revenue of €121,244 less variable cost of €54,991), so scale is able to absorb the €1.78 M/yr of fixed cost. Accounting break-even (criterion A) is reached at about 35 aircraft/year, but the 5-year payback (criterion B) raises the requirement to a minimum viable fleet of 77 aircraft per year. The key outcomes are summarised in Table 11.7 and visualised in Figure 11.1, and the input parameters to the model are compiled in Table 11.6.

---

[2] URL `https://tradingeconomics.com/germany/government-bond-yield` [cited on 10 June 2026]

[3] URL `https://pages.stern.nyu.edu/~adamodar/New_Home_Page/datafile/Betas.html` [cited on 15 June 2026]

[4] URL `https://pages.stern.nyu.edu/~adamodar/New_Home_Page/datafile/ratings.html` [cited on 15 June 2026]

Table 11.6: Key input assumptions and finance parameters

Symbol	Quantity	Value	Basis / source
m_{sold}	Aluminium sold per aircraft	7,536 kg	weighted retiring fleet estimate
MRR	Foundry metal-recovery rate	0.989	melt-loss estimate
m_{rec}	Recovered (melt-input) mass	7,620 kg	$m_{\text{sold}}/\eta_{\text{MRR}}$
OEW	Operating empty weight	58,680 kg	weighted by retiring types
p_{Al}	Aluminium product price	€9.93 / kg	market price [5]
p_{scrap}	Scrap credit	€1.77 / kg	p_{acq}
WACC	Discount rate	9%	Equation 11.5
–	Payback target	5 yr	availability window
–	Project horizon	20 yr	IRS guidelines [19]
p_{green}	Green premium	€0.40/kg	Chapter 2

Table 11.7: Results at the minimum viable throughput.

Quantity	Value
Contribution margin	€66,253 / aircraft
Fixed costs	€1.78 M / yr
Accounting break-even (A)	≈ 35 aircraft/yr
Minimum viable fleet	**77 aircraft/yr**
Total upfront investment	€12.9 M
Discounted payback	5.0 yr
Annual profit (steady state)	€2.71 M
20-yr ROI (cash)	416% total (≈ 21%/yr)

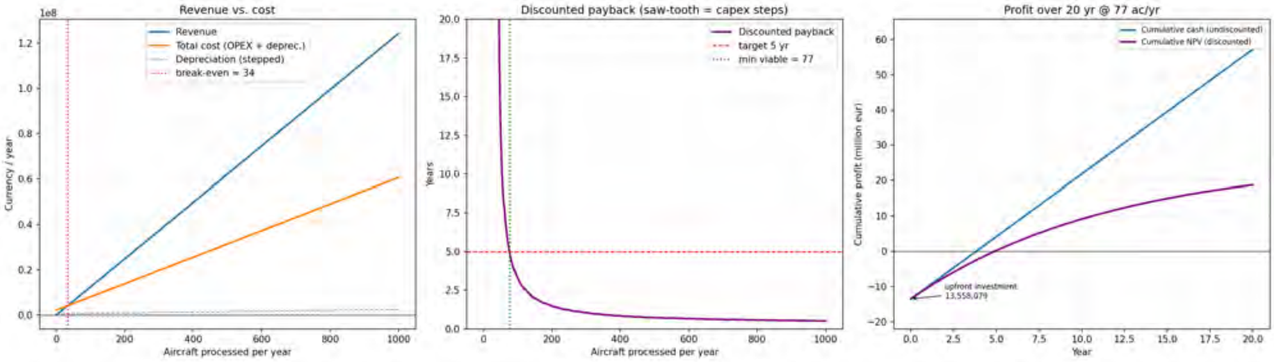

Figure 11.1: Left: annual revenue versus total cost as a function of throughput, with the accounting break-even marked. Centre: discounted payback versus throughput; the saw-tooth reflects the capacity-driven CAPEX steps of Equation 11.2, and the minimum viable fleet is where payback meets the 5-year target. Right: cumulative cash position over the 20-year life at the viable fleet, starting from the €12.9 M upfront investment; the discounted curve crosses zero at the 5-year payback.

Cost drivers

A breakdown of annual cost by process at the viable throughput, together with a $\pm 20\%$ "tornado" on each process's total cost, shown in Figure 11.2, identifies the dominant drivers. Sheet production, aircraft sourcing and decoating account for the large majority of cost, with sheet production alone being the single largest item and the input to which the required fleet is most sensitive. The remaining foundry sub-processes are individually negligible drivers of the result.

Sensitivities

The result is robust to the discount rate (the minimum viable fleet moves only modestly across 4% $<$ WACC $<$ 20%), but much more sensitive to the aluminium sale price: holding the scrap credit fixed, the viable fleet throughout doubles below about €6/kg and the required fleet falls steeply at higher prices. Sale price is therefore the dominant external risk, and a dedicated sensitivity analysis for it is shown in Figure 11.2.

---

[5] URL `https://solitairesteelllp.com/aircraft-aluminum-sheet-supplier/` [cited on 15 June 2026]

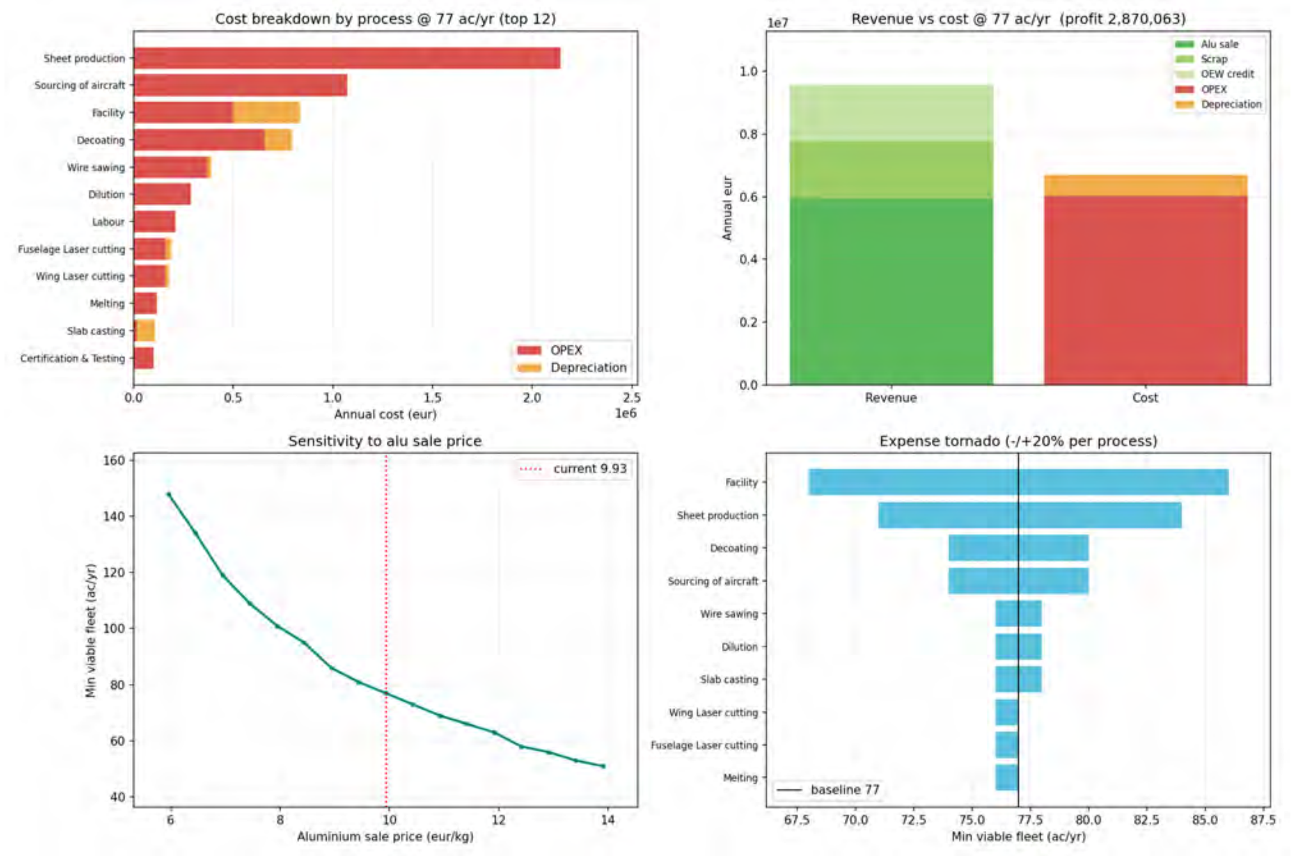

Figure 11.2: Top-left: annual cost by process (OPEX and depreciation) at the viable throughput. Top-right: revenue versus cost streams. Bottom-left: sensitivity of the minimum viable fleet to the aluminium sale price (scrap credit held constant). Bottom-right: expense tornado – the minimum viable fleet at $\pm 20\%$ of each process's total cost.

Return attractiveness

A project is conventionally judged attractive when its internal rate of return exceeds the hurdle rate (here the 9% WACC)[6]. By construction, the minimum viable fleet sits exactly at this hurdle, but at operating volumes above 77 aircraft/year, the return rises well clear of it. While somewhat higher than for comparable recycling projects, the 5-year payback is due to the facility's high capital intensity.

The modelled net margin ($\approx 29\%$) and 21%/yr average ROI are well above the $\approx 4.8\%$ net margin typical of commodity scrap-metal recycling[7]. This gap is attributable to the high value-added product that is aerospace alloys: the operation is priced as a producer of a wrought aluminium sheet product rather than a seller of bulk scrap. The risk of generating an excess supply of aluminium alloy is also negligible: extracting 7.76t of aerospace-grade aluminium alloys from each of the 77 aircraft processed per year results in a roughly 600t annual output, posing no stability risk to a total market seeing hundreds of thousands of tonnes traded each year [144].

Finally, the dominant non-financial risk is supply: while a minimum viable fleet of 77 aircraft/year represents a reasonable share of global annual *projected* retirements (roughly 12% of them), if these projections were to be overestimated, the project could face much larger hurdles in acquiring the aircraft. Securing sufficient feedstock is thus the largest constraint on the concept.

11.3. Business expansion

To show a real-life application for the recycled aluminium alloys, a retrofit of the Cessna 172 is designed. In Chapter 7, the aluminium alloys are used to design a wing structure. However, the amount of aluminium alloys used in a Retrofit Cessna is roughly 587.9 kg as mentioned in subsection 8.4.1. With an annual sales volume of 28 aircraft in the first three to five years, this will require approximately 17 tonnes of aluminium alloys.

The profit margin on the retrofit Cessna is €40,000, this cost calculation is shown in subsection 8.8.2. Multiplying this by the expected amount of 28 annual sales results in a total profit of roughly €1,120,000. This would increase the total annual profit to 4 million euros. This is a substantial increase.

---

[6] URL `https://corporatefinanceinstitute.com/resources/valuation/internal-rate-return-irr/` [cited on 15 June 2026]

[7] URL `https://www.ibisworld.com/united-states/industry/scrap-metal-recycling/5391/` [cited on 15 June 2026]

However, the upfront development was not taken into account; testing and certifying for a CS-23 can go up to 50 million dollars [8]. To pay back this upfront cost, 1250 retrofit Cessnas would have to be sold. The sales forecast for the upcoming 5 to 20 years is shown in Figure 11.3. The green line follows the growth of the electrical aircraft market of 18.7%[9]. With this growth and a maximum sales amount of 150 aircraft. The total sales would be around 1600 aircraft. This covers the high upfront cost; however, in this case, only 88 tonnes of aluminium alloys are used, whilst 600 tonnes are produced by the foundry process.

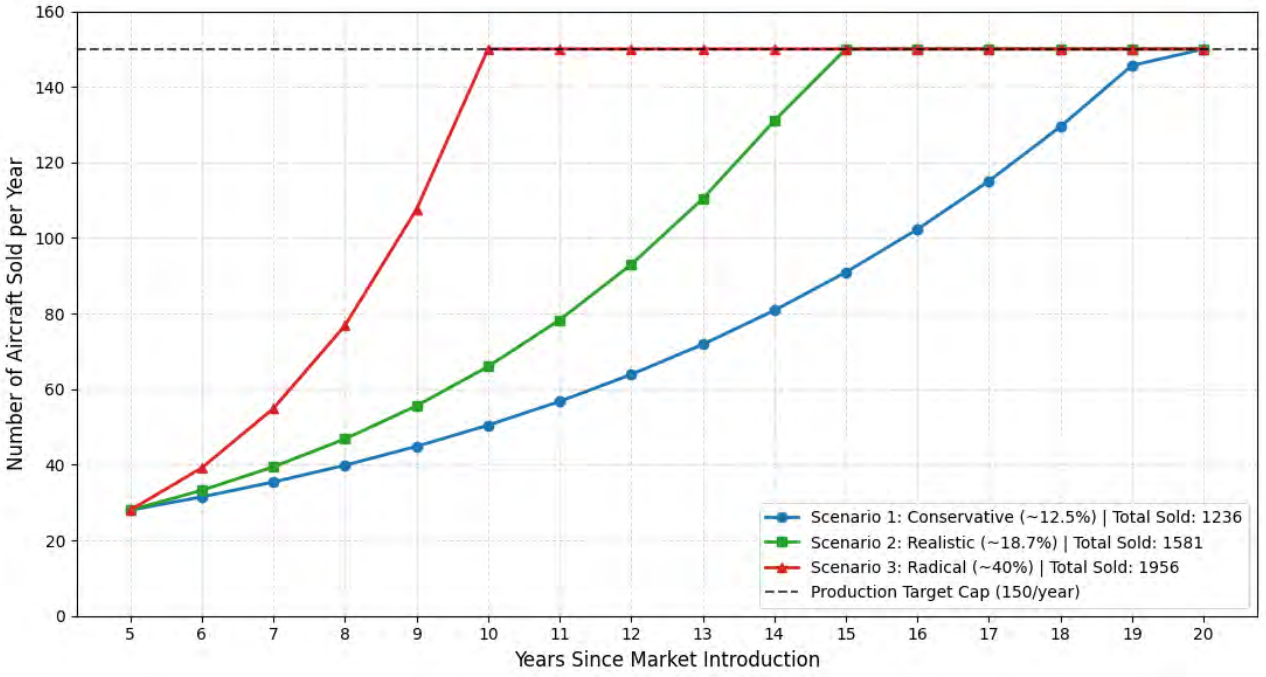

Figure 11.3: Sales forecast of the Electrical Cessna

The electric aviation market has a lot of potential, especially once cell capacity increases and the electric aircraft range can compete with that of fuel-powered aircraft. It can then target the rest of the 1600 single-engine propeller aircraft market, mentioned in Chapter 2. But currently, the high upfront costs, lack of infrastructure and low required amount of aluminium alloys make it a less appropriate business expansion.

11.4. Key assumptions and limitations

This financial analysis rests upon a few key assumptions and also has its limitations that are worth highlighting:

- The budget evaluates a single representative steady-state year; CAPEX is taken at $t = 0$, and constant volume is assumed (no ramp-up).
- Depreciation is straight-line at each asset's economic life; equipment replacement at end-of-life (reinvestment) is not modelled.
- The minimum viable fleet assumes the corresponding share of retirements can actually be sourced.
- Viability is assessed while assuming 13,000 aircraft will be retired over the next 20 years [1], and the retirements are uniformly distributed.
- Recovery fraction and carcass price are each calibrated on one worked example and assumed constant across types.

---

[8] URL `https://generalaviationnews.com/2012/09/09/the-cost-of-certification/` [cited on 23 June 2026]

[9] URL `https://www.vantagemarketresearch.com/electric-aircraft-market` [cited on 23 June 2026]

12

Verification and Validation

This chapter establishes the verification and validation framework.

12.1. Software Verification

Closing the loop on aircraft aluminium, covering key stages such as disassembly, refining, and Cessna manufacturing, can require substantial software development, most of which is done in-house using languages such as Python. To ensure that these scripts do not contain any calculation errors and produce the correct end result, each will be extensively verified. This can be done with tests such as unit tests and system tests throughout the script, and will be detailed in this section.

12.1.1. Dilution Calculator

The dilution calculator calculates the upper bounds for each alloying element in each alloy type, and graphs the amounts of virgin pure and alloy aluminium required to dilute the melt to within AMS limits. Following an update to the maximum virgin melt proportion that can be added, to stay below some requirements as detailed in subsection 6.3.3, the code will verify the following:

- Not more than 7% of the total melt mass after dilution is virgin aluminium.
- All alloying elements shall have their wt% within AMS limits.

For now, it is not known what kind of virgin material will be used for dilution. The dilution ingots will be tested with an OES analyser, but for now, the pure and alloy aluminium compositions were assumed to follow two rules: if AMS specifies a range, the value is assumed to be slightly higher than the middle of said range; if the AMS specifies a maximum value, the value is assumed to be around half of said maximum.

Firstly, the `unit test` framework embedded into Python was used to bypass the user interface part of the script, isolating the core mathematical framework. It provides a foundation for writing and organising tests. Then, three different tests were run. In the first test, the model is fed a very high wt% of titanium and tested to see whether it correctly outputs that the dilution is mathematically impossible. The second test uses a slightly out-of-spec recycled melt composition to verify that the model adds a positive amount of virgin aluminium to the melt. Lastly, the third test evaluates the model against a wide range of element concentrations, up to the maximum value the model can dilute to AMS limits. This is to ensure that the model can find the critical limits without missing important points or falling into an infinite loop. When running `python aluminium_boundary_plotter.py -test` in the terminal, it will output the running time along with 'OK' if all tests ran successfully.

12.1.2. Diamond Wire Sawing Cutting Model

The diamond wire saw is sized, and its key metrics are evaluated using the Python script `diamond_wire_calculator`.

Unit tests: Each calculation is checked against a hand-computed value (Table 12.1). For example, the power-limited cut rate is $A = (P\eta_{\text{util}}/u_s)/k$, which for the reference parameters ($P = 20\,\text{kW}$, $\eta_{\text{util}} = 0.6$, $u_s = 17.38\,\text{J/mm}^3$, $k = 10.3\,\text{mm}$) must equal $4,022\,\text{mm}^2/\text{min}$; the labour cost per aircraft is $n_{\text{op}} \cdot h \cdot d \cdot r / N = 2 \cdot 10 \cdot 250 \cdot 35/400 = e437.5$.

Table 12.1: Unit tests for the wire-saw calculator

Target	Case	Expected
`fuselage_slice_count`	$\lceil 33.5/6 \rceil$	6
`wing_slice_count`	$\lceil 21.95/3 \rceil$	8
material k-factor	2024-T3 / 7075-T6	1.0 / 0.8
cut rate (power)	defaults	$4,022\,\text{mm}^2/\text{min}$
cut rate (areal)	defaults / 7075-T6	25,000 / 20,000
fuselage cut area	$\pi D t f_{\text{str}} \cdot n$	hand calc
labour cost	defaults	€437.5

System tests: These confirm accurate model output on full calculator runs based on known properties:

- **Wire-speed independence (power mode)**: the power-limited rate is invariant to wire speed (wire speed cancels in throughput).
- **Fixed-cost spreading**: labour cost per aircraft falls as the annual throughput rises, and the number of saws is non-decreasing in throughput.
- **Self-consistency**: cutting time = area/rate, the total cost equals the sum of its components, and emissions scale linearly with throughput.

12.1.3. Cutting Heat Field Model

To check the maximum temperature reached at the cut face, a moving heat source field is simulated in Python with the script `cut_thermal.py`. The model is checked for physicality against known laws and expected outcomes.

Unit tests.

- **Feed-rate formula**: the reported feed equals $v_f = \mathrm{MRR}/k \cdot t_{\text{skin}})$.
- **Stability and physicality**: the explicit scheme produces a finite field with no values below ambient (the source only heats).
- **Linear calibration**: because the heat equation is linear in the source term, doubling the target peak (above ambient) doubles both the calibrated source power and the field's temperature rise
- **Source kinematics and placement**: the source advances monotonically within the domain, and the hottest cell of each frame lies on the cut line at the wire contact location.
- **Lateral decay**: along the source column the temperature peaks on the cut line and decays to the clamped ambient boundaries on both sides.

System test. The figure routine runs end-to-end and returns a heat-affected-zone width that is positive and bounded by the domain height.

12.1.4. Structure

A series of verification procedures was undertaken for the structural design. For the structural design, the most crucial calculations were done in Excel to ensure a clear overview. The calculation workbook is independently checked for formula errors, broken links, unit consistency, input control and agreement between the sheet name and the $+15\%b$ configuration.

Hands-on calculation of the "Crucial Cells" has been written at the top row, from which interpolation was used for rows further down. Therefore, a single hand calculation was performed to ensure these single crucial cells were calculated correctly.

Instead of using raw cell references (e.g., A1*B2), input cells are named so the formulas read like actual structural equations. This is done to expose "Black box" formulas and code.

Formula auditing was done using Excel's built-in 'Evaluate Formula' tool to step through and check complex calculations.

Self-Checking uses conditional formatting or IF statements to visually flag "PASS/FAIL" or when code limits are exceeded.

12.1.5. Business Case Cutting Model

The main business viability analysis tool is the Python script `dismantling_economics.py`, which sweeps the annual number of processed aircraft and computes the cost budget, minimum viable fleet, payback, NPV, IRR, and sensitivity analyses, as shown in Chapter 11.

Unit Tests. Each function is tested against a hand-computable expected value. For example, `npv(100, 50, 0, 2)` must return 0 (an undiscounted outlay of 100 recovered by two cash flows of 50), and `irr(100, 100, 2)` must return the golden-ratio root ≈ 0.618. Table 12.2 summarises the unit-test cases.

Table 12.2: Unit tests for `dismantling_economics.py`.

Function	Input	Expected output
`blocks_needed`	$(100,50)$ / $(101,50)$ / $(50,50)$	2 / 3 / 1
`process_capex`	base 100k, cap 50, block 40k @ 51	140k
`npv`	$(100,50,0,2)$	0.0
`discounted_payback`	$(100,100,0)$; cash flow ≤ 0	1.0 ; ∞
`irr`	$(100,100,2)$	≈ 0.618
`irr` (guard)	cash flow · horizon < CAPEX	NaN
`economics_at`	trivial single-process config	matches hand calculation
`economics_at`	`sale_price` / `cost_mult` override	only intended term changes
`find_breakeven`	profit array crossing zero	interpolated crossing
`cost_breakdown`	sum over processes	equals `economics_at` total

System tests. The model as a whole on configurations with a known outcome:

- **Known infeasible**: with a negative unit margin (sale price far below OPEX), the tool must report no viable fleet, "never" payback and a NaN IRR. A viable result here would indicate a bug.
- **Closed-form single process**: for one process with no scaling or fixed cost, the minimum viable fleet has the analytic value $n \geq \max\big(C/(L\,M(p-o)),\ C/(M(p-o)\,A_5)\big)$, where A_5 is the 5-year annuity factor; the numerical result must match.
- **Monotonicity**: with a positive margin and no CAPEX steps, payback must decrease and NPV must increase with throughput.
- **Internal equivalence**: $\mathrm{NPV}_5(n) \geq 0$ must hold exactly when discounted payback ≤ 5 years, at every volume.
- **Conservation**: profit = revenue − OPEX − depreciation, cash flow = revenue − OPEX, and the per-process breakdown reconciles to the totals.

12.1.6. Decoating Cost and Time Optimisation

To optimise the amount of Kemstrip bath scaling up and the rest of the lines, a capacity vs cost trade-off has been applied by increasing the amounts of both Kemstrip and the rest baths for each case, then adding the corresponding costs for each scenario. Following the indices that increase the number of Kemtrip and rest baths, two plots are made. The first plot indicates the number of aircraft that can be processed per year with the given capacity, and the second plot indicates the corresponding cost for the configuration.

Unit tests: The unit test verification utilises pytest function in python. The unit tests work by verifying each input by checking it with the expected output. In total 16 tests were applied, some of them are summarised in the following table Table 12.3. The unit tests verify if the given calculations, corresponding effective process times, the capacity per year and total costs of the known cases. Each result is compared with the expected result, and each block is verified following this path. All unit tests passed for this code, and further verify the conclusions drawn from the plots and respective tables in Chapter 5.

Table 12.3: Software verification unit tests for the capacity cost trade-off.

Function	Input	Expected output
`calculate_capacity_tradeoff`	KEMSTRIP bath range $K = 1\ldots12$, rest-line range $R = 1\ldots8$	Dataframe contains $12 \cdot 8 = 96$ rows
`calculate_capacity_tradeoff`	Default input parameters	Required output columns are present
`calculate_capacity_tradeoff`	$R = 2$, $K = 4$, $t_{\mathrm{rest}} = 1.33$ h, $t_{\mathrm{KEM}} = 4$ h	Effective time per basket is 1.665 h
`calculate_capacity_tradeoff`	8760 h/year, 53 baskets/aircraft, $R = 2$, $K = 4$	Capacity is approximately 99.34 aircraft/year
`calculate_capacity_tradeoff`	Full line cost $= 495{,}000$ €, KEMSTRIP bath cost $= 20{,}000$ €, $R = 2$, $K = 4$	Total cost is $1{,}030{,}000$ €
`calculate_capacity_tradeoff`	Same known capacity and cost case	Cost per aircraft/year capacity is approximately $10{,}369$ €/(aircraft/year)
`calculate_capacity_tradeoff`	Target capacity $= 100$ aircraft/year	Feasible combinations are identified based on the target capacity
`calculate_capacity_tradeoff`	$K = \{1,2,4,8\}$ with fixed $R = 2$	Capacity increases as the number of KEMSTRIP baths increases
`calculate_capacity_tradeoff`	$R = \{1,2,4,8\}$ with fixed $K = 4$	Capacity increases as the number of rest process lines increases
`calculate_capacity_tradeoff`	$K = \{1,2,4,8\}$ with fixed $R = 2$	Total cost increases as the number of KEMSTRIP baths increases
`calculate_capacity_tradeoff`	$R = \{1,2,4,8\}$ with fixed $K = 4$	Total cost increases as the number of rest process lines increases
`calculate_capacity_tradeoff`	Target capacity $= 100$ aircraft/year	Cheapest eligible configuration reaches the target capacity

System Tests:

- **Bottleneck of the process:** The code and optimisation plots should run in a way such that when KEMSTRIP baths are low, the process time should be dominated by the immersion time for KEMSTRIP, and the rest of the process lines should not be as influential. Thus, when the number of KEMSTRIP lines increases, the overall process time should be determined by the number of rest lines.
- **Optimisation and cost consistency:** The configurations that satisfy the processed target aircraft configuration, and then choose the minimum cost within the viable options.
- **Capacity parallelisation:** The capacity of baskets that can be processed should increase with the increasing number of baths, thus simultaneously, the effective processing time should decrease.

12.1.7. Retrofit Propulsion System

Verification ensures that the in-house Python scripts used for all retrofit propulsion calculations, such as aircraft sizing, mission simulation, battery degradation, and thermal management, contain no calculation errors. A dedicated verification suite was developed using the `pytest` framework. The suite combines two complementary levels of testing:

- Unit tests, which isolate individual formulas (e.g. the ISA atmosphere model, lift and drag coefficients, propeller efficiency, battery pack energy and C-rate calculations, weight and centre-of-gravity arithmetic) and compare their output against independently derived reference values.
- System tests, which execute each script end-to-end and check that the resulting outputs are internally consistent (e.g. energy budgets summing correctly, monotonic battery state-of-health degradation) and that all expected output figures are produced.

As an example, there is a unit test verifying the maximum lift-to-drag ratio computed by the sizing script against its closed-form aerodynamic expression. In total, the verification suite comprises 64 automated tests spanning all eight scripts. Following correction of the calculation errors identified during development, all 64 tests now pass, confirming that the scripts are free of the calculation errors they were designed to detect.

12.2. Software Validation

Now that all software has been verified, it should also be validated to ensure the end product works as intended. A product can have correct formulas throughout, but if it does not complete the required task, it is useless. In this case, User Acceptance Testing (UAT) will ensure that all Python scripts are verified. Each script's UAT will be described in its own subsection, demonstrating that it works as intended.

12.2.1. Dilution Calculator

The dilution calculator model also needs to be validated to ensure it accurately reflects reality in a foundry. First, some physical sanity checks will be performed to verify that the model behaves as expected in real-world conditions. Next, the model's physical simplifications will be analysed, leading to either a valid model or key takeaways for future improvements. Lastly, UAT will analyse the intuitiveness of the model and how easily the user interface can be integrated on a casthouse floor.

Verification tests where the melt was diluted to copper concentrations below the AMS limit already function as physical sanity checks. They show physical bottlenecks within the system such as too diluted elements and trace elements too concentrated in the melt. Key assumptions should also be reviewed, notably the following:

- The downstream material losses due to e.g. oxidation and fluxing are not taken into account.
- The concentration of the alloying elements in the virgin material is assumed to be around the upper half of the range specified by AMS and elements with a maximum value such as iron assumed to have a concentration between 0.05 and 0.15 wt%, see an example presented in subsection 6.3.3 for the AA2014 virgin alloy.

Table 12.4: Table showing the element concentrations in the dilution material according to industry practices

Element	Fe	Cu	Mg	Zn	Mn	Si	Cr	Ti
AMS limits [wt%]	0.7max	3.9-5.0	0.2-0.8	0.25max	0.4-1.2	0.5-1.2	0.1max	0.15max
Chosen value [wt%]	0.10	4.5	0.55	0.10	0.85	0.90	0.05	0.10

The first assumption could compromise material quality, as some element evaporation and reactions with added elements, such as fluxes, could occur. This will be addressed by adding those elements back into the melt, for example, replacing lost magnesium by adding a calculated mass of a pure magnesium ingot. The second assumption follows an engineering intuition about the manufacturing of aluminium ingots. If a factory wants to follow certain standards, such as the Six Sigma standards[1], it would make sense to aim for the upper half of a certain range and to minimise the wt% of an element with a maximum AMS value.

With the assumptions holding, the last step is to ensure the software can be implemented on a foundry floor. The code produces a clear graph, as shown in subsection 6.3.3, and allows the composition of both the recycled and virgin melts to be altered. Using a package such as pandas, the code could easily be adapted to have a CSV file as input, enabling it to work seamlessly with the output from the OES melt analyser. Lastly, the code outputs exactly how much virgin pure and alloy aluminium to add, giving clear instructions to a machine or floor operator.

12.2.2. Wire Cutting Models

Both scripts `cut_thermal.py` and `diamond_wire_calculator.py` modelling the wire cutting procedure are also validated by:

- **Cross-model consistency**: the saw model's mass-removal rate ($\approx 690\,\text{mm}^3/\text{s}$) is the same figure used to drive the moving source in `cut_heatmap.py`, so the two models are mutually consistent.
- **Literature and physical bounds**: the specific cutting energy ($\sim 5\text{–}40\,\text{J/mm}^3$ for abrasive regimes), the grid carbon intensity and the predicted heat-affected-zone width are checked against published ranges and engineering expectation.
- **User acceptance testing**: the disassembly / thermal team confirm that the cut plan, throughput, cost split and heat-field extent match their manual assessment; validation is achieved when they agree the tools reflect the real process.

12.2.3. Business Case Budget Model

Validation confirms that the tool `dismantling_economics.py` captures real budget behaviour rather than merely executing its code correctly (the latter being the scope of the unit and system tests above). It is achieved through:

- **Cross-tool comparison**: the Python outputs (revenue, OPEX, CAPEX, depreciation, profit) are compared cell-for-cell against an independent Excel budget at several throughputs; agreement within rounding validates a faithful implementation of the agreed model.
- **Independent hand calculation**: a team member computes one full operating year at one throughput by hand and compares.
- **Benchmark plausibility**: the resulting margin, payback and ROI are checked against published figures for order-of-magnitude consistency.
- **User acceptance testing (UAT)**: each process owner reviews the cost-driver breakdown and confirms that their process's OPEX/CAPEX figures, and the resulting minimum viable fleet, are consistent with their judgement. Validation is achieved when all owners agree that the tool reflects the real budget.

12.2.4. Decoating Time and Cost Optimisation:

To validate that the code runs as expected, the input data used and the following calculations with respect to the calculations are validated to ensure the model works as expected.

- **Hand calculations** have been performed for several configurations to ensure they return the expected values for total cost, capacity, and processing time.
- **Literature and supplier validation** for the cost, immersion time and process sequence, for instance the amount of rinse and chemical immersion steps are compared with technical data sheets and literature research.
- **Extreme case check** The extreme cases for the number of baths have been checked using different configurations for the maximum and minimum number of baths, and their respective cost.

12.2.5. Retrofit Propulsion System

The retrofit propulsion system software should also be validated so that the toolchain as a whole fulfils its intended purpose. For each script, a set of real-world acceptance criteria were defined and automatically checked, covering aspects such as whether the aircraft remains within its (new) maximum take-off weight and centre-of-gravity envelope, whether take-off and landing performance meets or exceeds the original POH figures, whether cruise range and ground-recharge time are operationally useful, and whether motor and battery temperatures remain within their design limits throughout a full mission.

As an example, it was checked that the peak transient battery temperature predicted by the cooling-system sizing script remains below the Amprius SA02 cell's $55\,^{\circ}\text{C}$ limit. Of the 34 acceptance criteria evaluated, 33 passed outright.

---

[1] URL `https://sixsigmastandards.org` [cited on 16 June 2026]

The single remaining case was the take-off distance to clear 15 m, which exceeds the original POH figure by roughly 10 m (<2%). However, in another script, the shaft power was increased to account for failing this criterion; therefore, the criterion was also accepted. The validation process therefore confirms that the toolchain not only computes correctly but also produces a physically realistic and operationally viable aircraft design.

12.3. Compliance Matrix

To verify the project as a whole, all stakeholder, mission and system requirements are compiled in a compliance matrix. They are then investigated individually, and if the requirement is met, a checkmark is added to the third column; the fourth column provides a brief explanation for the respective row. That row typically shows a section or subsection referring to another part of the report, or provides a certain value coming from the report. Lastly, some requirements are out of scope for the project, such as SH-USR-02, which concerns an inspection strategy; these are given a question mark and sometimes are left with a TBD. They require a deeper dive into certain topics like the certification, which fall outside the scope of the project.

Requirement ID	**Requirement**	**Check**	**Reference**
SH-USR-02	The designed aircraft shall include an inspection strategy.	?	Scope
SH-USR-03	The design shall demonstrate a safe life limit of 10,000 flight hours.	✓	Chapter 7
SH-USR-04	The system shall have less environmental impact than current standards.	✓	-97%
SH-USR-05	The green Cessna shall be as expensive as or cheaper than the current Cessna.	X	Green premium
SH-USR-06	The system shall use EOL aircraft to produce new aerospace-grade aluminium.	✓	Disassembly and smelting
SH-REG-01	The green Cessna shall be airworthy under the EASA CS-23 / FAA Part 23 airworthiness requirements.	✓	Regulations
SH-REG-02	The system shall comply with the local government regulations.	✓	Legal business
SH-REG-03	The composition of each recycled alloy shall be compliant with the guidelines set by the Aluminum Association and European Aluminium.	✓	subsection 6.3.2
SH-REG-04	The alloy provenance of each structural component shall be fully documented from aircraft disassembly to final part installation as to FAA 8130-3/EASA Form 1 requirements.	X	Unnecessary
SH-REG-05	The de-coating process shall comply with REACH Regulation (EC) No 1907/2006 with respect to CrVI handling and disposal.	✓	Chapter 5
SH-REG-06	All hazardous waste streams generated by the process shall be managed in compliance with EU Waste Framework Directive 2008/98/EC.	✓	Section 5.4
SH-REG-07	The aluminium produced shall meet the aerospace quality requirements as stated in the ASM specifications.	✓	subsection 6.3.2
SH-REG-08	The system should adhere to the workplace regulations in the country (France) where the system will be deployed.	✓	Legal business
SH-CSN-01	The system and process shall comply with all intellectual property regulations.	✓	Regulations
SH-PIL-01	The handling characteristics of the Green Cessna 172 shall not noticeably deviate from those of the standard Cessna 172 as defined in the Pilot Operating Handbook.	?	Scope
SH-OEM-01	The airframe shall be compatible to the other Cessna 172 systems.	✓	Original airframe
SH-INV-01	The company shall become economically profitable within ten years.	✓	5 years
SH-INV-02	The selling price of the Green Cessna 172 shall not exceed the market price of an equivalent primary-alloy Cessna 172 at industrial scale.	X	€394,953

Requirement ID	Requirement	Check	Value
MS-REG01-AIR-01	The aircraft shall have aerospace-standard safety margins on its structural components.	✓	1.5 margin
MS-REG01-AIR-02	There should be a plan to reach a certified aircraft.	✓	subsection 6.3.11
MS-USR03-AIR-01	The aircraft shall have at least 10,000 flight hours	✓	Chapter 7
MS-USR03-AIR-02	All non-critical components with a design life of less than 10,000 flight hours shall be replaceable.	?	Scope
MS-USR04-REC-01	The mission shall provide recycled aluminium alloys with lower emissions output than its virgin alloy counterpart.	✓	Section 11.1
MS-USR04-REC-02	All aluminium material from the feedstock that cannot be recycled shall be downcycled.	✓	Sold as scrap
MS-USR04-REC-03	All material that cannot be down-cycled shall be disposed of.	✓	Disposed of
MS-USR04-REC-04	95% of the new aircraft must be recyclable.	?	Scope
MS-USR04-AIR-01	The Green Cessna 172 shall have lower environmental impact then the normal Cessna 172.	✓	Electic propulsion
MS-USR05-BUD-02	The market price of the recycled aerospace-grade aluminium shall be within 1.1 times the price of virgin aerospace-grade aluminium.	✓	Section 11.2
MS-USR06-REC-01	The system shall define a process for attaining an EOL aircraft.	✓	Section 3.3
MS-USR06-REC-02	The system shall be able to disassemble an EOL aircraft.	✓	Chapter 4
MS-USR06-REC-03	The system shall be able to decoat aluminium parts.	✓	Chapter 5
MS-USR06-REC-04	The system shall be able to sort aluminium scrap based on alloy composition.	✓	Section 6.2
MS-USR06-REC-05	A detailed strategy for the extraction of contaminants from the alloys shall be planned.	✓	Section 6.3
MS-USR06-REC-06	The metal recovery rate of the foundry process shall have a grade level separation of at least 92%.	✓	98.9%
MS-REG01-AIR-01	The aircraft shall adhere to the structural integrity regulations as set by EASA C-23 or FAA part 23	✓	Chapter 7
MS-REG01-AIR-02	The aircraft shall adhere to the performance regulations as set by EASA C-23 or FAA part 23	✓	Chapter 8
MS-REG01-AIR-03	The aircraft shall adhere to the flight characteristic regulations as set by EASA C-23 or FAA part 23	✓	Chapter 7 and Chapter 8
MS-REG01-AIR-04	The aircraft shall adhere to the system design regulations as set by EASA C-23 or FAA part 23	✓	Entire design
MS-REG02-SYS-01	The system shall comply with French regulations.	✓	Legal business
MS-REG03-REC-01	The recycled aluminium shall be given the name as in accordance with the specification sheet.	✓	subsection 6.3.8
MS-REG04-REC-01	The origin of all recycled aluminium shall be documented.	✓	subsection 6.3.10
MS-REG04-REC-02	When the recycled aluminium is processed and made into bars, a material passport shall be kept up to date.	✓	subsection 6.3.10
MS-REG05-SFT-01	A chemical safety assessment shall be conducted.	✓	subsection 5.1.2
MS-REG05-SFT-02	A chemical risk assessment for controlling the risk associated to working with chemicals shall be made.	✓	Section 9.2
MS-REG06-WAS-01	Before being disposed of, all waste shall be properly stored in accordance to the EU waste framework directive.	✓	Legal business
MS-REG06-WAS-02	All waste shall be properly disposed in accordance to the EU waste framework directive.	✓	Legal business
MS-REG06-WAS-03	All industrial waste shall be properly documented in accordance to the EU waste framework directive.	✓	Legal business
MS-REG07-ALM-01	All aluminium shall be tested for compliance with the ASM specifications.	✓	subsection 6.3.11

Continued on next page...

Table 12.6 – Continued from previous page

Requirement ID	**Requirement**	**Check**	**Value**
MS-REG08-SFT-01	All required safety equipment shall be on site.	✓	Legal business
MS-REG08-SFT-02	All employees shall posses all necessary certification.	✓	Legal business
MS-REG08-SFT-03	The system shall have the correct danger signage.	✓	Legal business
MS-REG08-OPR-01	All employ schedules shall adhere to the local workplace regulations.	✓	Legal business
MS-CSN01-REG-01	The green aircraft shall carry the logos of Cessna the same as the old Cessna 172	✓	Intellectual property
MS-PIL01-AIR-01	The aircraft shall not require any additional training, next to that of the C172, in order to fly the aircraft.	✓	Private pilot license
MS-PIL01-AIR-02	The aircraft shall have the same aerodynamic profile as the Cessna 172 Skyhawk.	✓	Same wing
MS-PIL01-AIR-03	The aircraft shall have the same load diagram as the Cessna 172.	✓	Same loads
MS-PIL01-AIR-04	The aircraft shall remain a training aircraft.	✓	Training aircraft
MS-PIL01-AIR-05	*The aircraft final empty weight must be within ±2% of its original empty weight.*	X	+10%
MS-OEM01-AIR-01	The Cessna engine should be integrated into the airframe.	✓	Original airframe
MS-OEM01-AIR-02	The Cessna instruments should be integrated into the airframe.	✓	Original airframe
MS-OEM01-AIR-03	The Cessna flight controls shall be integrated Cessnas into the airframe.	✓	Original airframe
MS-OEM01-AIR-04	The safety equipment shall be integrated into the airframe.	✓	Original airframe
MS-OEM01-AIR-05	The aircraft shall carry the loads produced by an engine of a Cessna 172.	✓	Original airframe
MS-INV01-COM-01	The company shall produce and sell green Cessnas to turn a profit.	✓	Section 11.2
MS-INV01-COM-02	The business case shall not rely exclusively on carbon pricing or subsidies to be profitable.	✓	Section 11.2
MS-INV01-COM-03	The company shall be able to recover from a financial hit.	✓	Buffer
MS-INV01-COM-04	The business shall be resilient to year-over-year fluctuations of ±15% in feedstock	✓	Buffer
MS-INV02-COM-01	The production cost of the Green Cessna shall not exceed the current production cost of the Cessna 172 airframe.	X	Unverifiable

Requirement ID	**Requirement**	**Check**	**Value**
SYS-OEM01-AIR05-WNG-01	The system shall be able to carry a thrust load of 2700 N.	✓	Original airframe
SYS-PIL01-AIR02-WNG-01	The wing shall have a NACA 2412 airfoil.	✓	NACA 2412
SYS-PIL01-AIR02-WNG-02	The wing configuration shall be high-wing.	✓	high winged
SYS-PIL01-AIR02-WNG-03	The wing configuration shall be strut-braced.	✓	Strut braced
SYS-PIL01-AIR02-WNG-04	The wing shall have a dihedral of 1.5°.	?	scope
SYS-PIL01-AIR02-WNG-05	The wing tips shall have washout.	✓	Same wingtip
SYS-PIL01-AIR02-WNG-06	The wing shall be compatible with the flaps from the original Cessna.	✓	Same airframe
SYS-PIL01-AIR03-FLP-01	The aircraft shall stall at a speed of 24.72 m/s.	✓	26.64 m/s

Continued on next page...

Table 12.7 – Continued from previous page			
Requirement ID	**Requirement**	**Check**	**Value**
SYS-PIL01-AIR03-FLP-02	*The airframe shall withstand a positive 3.8 g acceleration.*	✓	4.6 g
SYS-PIL01-AIR03-FLP-03	*The airframe shall withstand a negative 1.5 g acceleration.*	✓	-2.6 g
SYS-PIL01-AIR03-FLP-04	The aircraft shall have a maximum cruise speed of at least 123 kts.	✓	132 kts
SYS-PIL01-AIR03-FLP-05	The aircraft shall have a maximum climb rate of at least 720 ft/min.	✓	1,391 ft/min
SYS-PIL01-AIR03-FUS-01	Thickness of components/panels can only be increased/decreased towards the interior direction.	✓	Thickness inside
SYS-PIL01-AIR04-FRM-01	The aircraft shall be able to transfer two passengers.	✓	two passengers
SYS-PIL01-AIR04-CSN-01	The retrofit Cessna shall be able to full fill a average trainings flight.	✓	Section 8.3
SYS-PIL01-AIR04-CSN-02	The retrofit Cessna shall have at least 136 kW peak power.	✓	180 kW
SYS-PIL01-AIR04-CSN-03	The Green Cessna shall be able to refuel in 60 minutes.	✓	58 minutes
SYS-PIL01-AIR05-FRM-01	The airframe weight shall be within 2% of the original Cessna's airframe weight.	X	10% increase
SYS-REG01-AIR01-FRM-02	The airframe shall provide protection for all occupants, accounting for likely flight, ground, and emergency landing conditions. [145].	✓	Same airframe
SYS-REG01-AIR01-FRM-03	The airframe, during emergency landing conditions, shall not generate loads experienced by the occupants, which exceed established human injury criteria for human tolerance due to restraint or contact with objects in the aircraft [145].	✓	Same airframe
SYS-REG01-AIR02-CER-01	The system shall provide steps towards certification.	✓	Section 6.3
SYS-REG01-AIR02-CER-02	The budget for certification shall not exceed 2.5 million dollars.	✓	subsection 6.3.11
SYS-USR03-AIR01-FRM-01	The main airframe and load bearing critical components shall have a design life of at least 10,000 flight hours.	?	Scope
SYS-USR03-AIR01-FRM-05	Critical structures shall be designed so that the residual strength of the airframe remains above the limit load even in the presence of cracks up until **TBD** mm.	?	Scope
SYS-USR03-AIR01-FRM-06	All parts and assemblies shall be fully documented to support maintenance procedures, including identification, disassembly, reassembly, lubrication, and inspection steps.	✓	Section 9.4
SYS-USR03-AIR02-FRM-01	All non-critical parts shall be accessible without the removal of critical structures.	?	Scope
SYS-USR04-REC01-SUS-01	The system shall output a maximum of 3 kg CO_2 per kg of aluminium produced.	✓	Section 11.1
SYS-USR04-REC01-SUS-02	The foundry process shall have 90% lower greenhouse gas emissions than its virgin counterpart.	✓	Section 11.1
SYS-USR04-REC01-SUS-03	The foundry process must stay below 2.5 kWh/kg, resulting in a 70% reduction in embodied energy compared to primary smelting.	✓	subsection 6.3.12
SYS-USR04-REC02-FND-01	All purely aluminium waste from the foundry process shall be collected, sorted and downcycled.	✓	Chapter 6
SYS-USR04-REC03-FND-01	The system shall have a waste-disposal plan.	✓	Section 5.4
SYS-USR04-REC04-FRM-01	The airframe shall contain at least 85% of secondary alloys.	✓	max 15% dillution

Continued on next page...

Table 12.7 – Continued from previous page

Requirement ID	Requirement	Check	Value
SYS-USR04-REC04-FRM-02	The new airframe shall consist of at least **TBD**% reusable fasteners.	?	Scope
SYS-USR04-REC04-FRM-03	The new airframe shall not be coated with a carcinogenic coating.	✓	subsection 7.8.1
SYS-USR04-REC04-FRM-04	The new airframe shall consist of a maximum of 5 different aluminium alloys.	✓	2 alloys
SYS-USR04-AIR01-CSN-01	The green Cessna shall have no CO2 emissions during flight.	✓	No emissions
SYS-USR05-BUD01-BUD-01	The manufacturing cost of the airframe shall be less than 95% of the selling price.	✓	subsection 8.8.2
SYS-USR05-BUD01-BUD-02	The integration cost of the different aircraft systems into the airframe shall be less than **TBD**% of the selling price.	?	Scope
SYS-USR05-BUD02-BUD-01	The cost of the aluminium recycling process shall be at least 10% lower than the selling price of virgin aluminium.	✓	11% profit margin
SYS-USR06-REC01-FND-01	The system shall be able to remove any non-carcass-related parts of an aircraft.	X	Outsource
SYS-USR06-REC01-BUD-01	The EOL aircraft shall not cost more than the value of the aluminium extracted from the EOL aircraft.	✓	Section 3.1
SYS-USR06-REC02-FND-01	The system shall be able to identify different alloys of aluminium.	✓	XRF
SYS-USR06-REC02-FND-02	The system shall be able to extract different alloys from the carcass.	✓	3 melt streams
SYS-USR06-REC02-FND-04	The system shall deliver chunks smaller than 0.25 m^2.	✓	0.2 max
SYS-USR06-REC02-BUD-01	The extraction process shall not cost more than 90% of the value of the extracted recycled aluminium.	✓	Section 11.2
SYS-USR06-REC03-FND-01	The system shall be able to remove coating from chunks of aluminium of 0.25 m^2 and smaller	✓	Decoating
SYS-USR06-REC03-FND-02	The decoating method shall not result in a Cr(VI) concentration of more than 1 mg/m^3 in an environment where humans are present.	✓	Regulations
SYS-USR06-REC03-FND-03	The system shall be able to decoat in under 8 hours.	✓	5.33 h
SYS-USR06-REC03-BUD-01	The decoating shall not cost more than €2,000,000 per year	✓	€1,861,888.89
SYS-USR06-REC04-FND-01	*The system shall be able to sort with 99.5% accuracy in separating different alloys series.*	✓	99.9%
SYS-USR06-REC04-FND-02	The system shall be able to sort all aluminium from the aircraft in at least 24 hours	✓	12 hours
SYS-USR06-REC04-BUD-01	The upfront cost for the sorting process shall not cost more than €150,000	✓	€113,031
SYS-USR06-REC05-FND-02	The system shall verify the chemical composition of every melt batch with non-destructive testing.	✓	OES Test
SYS-USR06-REC05-FND-03	The system shall introduce less than 15% of virgin aluminium into the alloys.	✓	No more then 15%
SYS-USR06-REC05-FND-04	The system shall verify that every batch is aerospace-grade.	✓	Correct limits
SYS-USR06-REC05-FND-05	Recycled batches must show maximum of 3% variance in tensile strength compared to virgin standards.	✓	max 3%
SYS-USR06-REC06-FND-01	The metal recovery rate of the foundry process shall have a grade level separation of at least 92%.	✓	98.9%
SYS-USR04-AIR03-FRM-01	A fatigue test shall be performed on all components to ensure fatigue resistance.	✓	Test done

Continued on next page...

Table 12.7 – Continued from previous page

Requirement ID	Requirement	Check	Value
SYS-USR04-AIR03-FRM-02	A fatigue test shall be performed on all components to ensure corrosion immunity.	✓	Test done
SYS-REG01-AIR01-AIR-02	The structure shall be able to withstand the limit loads with a safety margin of 1.5 for at least 3 seconds.	✓	three seconds
SYS-REG01-AIR01-AIR-03	The system shall determine all structural design loads in the airframe that may occur in flight, on the ground or when its parked.	✓	Flight envelope
SYS-REG01-AIR02-AIR-01	The manufacturer shall determine the maximum rate of climb for various configurations.	✓	1,391 ft/min
SYS-REG01-AIR02-AIR-03	The aircraft shall remain controllable and manoeuvrable during all phases of flight, including landing flares and go-arounds.	?	Scope
SYS-REG01-AIR02-AIR-04	The aircraft shall provide the pilot with a clear and distinctive stall warning.	✓	Original avionics
SYS-REG01-AIR02-AIR-05	The aircraft shall allow for a safe recovery without exceptional piloting skill.	✓	Original avionics
SYS-REG01-AIR02-AIR-08	The performance data shall be published in airplane flight manual (AFM).	✓	Included
SYS-REG01-AIR02-AIR-09	The performance data in the AFM shall be adjusted for pressure altitude, ambient temperature and runway slope/surface conditions.	✓	Included
SYS-REG01-AIR03-AIR-01	The aircraft shall be safely controllable during take-off, climb, cruise, descent and landing.	✓	Stable
SYS-REG01-AIR03-AIR-02	The aircraft shall be able to complete a landing without causing substantial damage or serious injury using the steepest approved approach gradient.	✓	Stable
SYS-REG01-AIR03-AIR-03	The aircraft shall be able to maintain a constant flight condition (hands-off) during normal operations.	✓	Stable
SYS-REG01-AIR03-AIR-04	Trim shall be available for any lateral, directional and longitudinal forces within the design envelope.	✓	Stable
SYS-REG01-AIR03-AIR-05	If the speed is disturbed, the aircraft shall naturally return to its original trimmed speed.	✓	Stable
SYS-REG01-AIR03-AIR-06	The airframe shall be positively stable, meaning it is naturally slip and skid resistant.	✓	Stable
SYS-REG01-AIR03-AIR-07	During stall, the aircraft shall not exhibit any uncontrollable rolling and pitching.	✓	Stable
SYS-REG01-AIR03-AIR-08	During stall, the aircraft shall be able to be recovered with only standard control inputs.	✓	Stable
SYS-REG01-AIR03-AIR-09	The airframe shall be free from vibration and buffeting that could interfere with control.	✓	Stable
SYS-REG01-AIR03-AIR-10	The airframe shall be free from flutter, which could cause structural damage at any speed until the V_{NE} (never exceed speed).	✓	Stable
SYS-REG01-AIR04-AIR-02	A failure in one system shall not cause a catastrophic failure in another.	?	Scope
SYS-REG01-AIR04-AIR-03	Critical systems shall remain operational even after a single failure.	?	Scope
SYS-REG01-AIR04-AIR-04	Catastrophic failures shall be extremely improbable.	?	Scope
SYS-REG01-AIR04-AIR-05	The system shall be protected against high-intensity radiated fields and lightning strikes.	✓	Original airframe
SYS-REG01-AIR04-AIR-06	Systems shall be designed to minimise the risk of ignition.	✓	Fire shield
SYS-REG01-AIR04-AIR-07	Systems shall be designed to contain a fire if one occurs.	✓	Fire shield

Continued on next page...

Table 12.7 – Continued from previous page

Requirement ID	Requirement	Check	Value
SYS-REG01-AIR04-AIR-08	The power supply shall provide sufficient power for all essential loads during normal and emergency operations.	✓	Mission profile
SYS-REG01-AIR04-AIR-09	Equipment shall function within the defined temperature and altitude.	✓	Thermal performance
SYS-REG01-AIR04-AIR-10	The system shall provide clear and timely warnings regarding any system malfunctions.	✓	Original avionics
SYS-REG02-REC01-SYS-01	The system should follow the French laws.	✓	Located in France
SYS-REG03-REC01-FND-01	Every aluminium part should have the correct naming according to the specification of ASM.	✓	Foundry process
SYS-REG04-REC01-FND-01	When dismantling, the exact location of the part shall be documented.	X	Not needed
SYS-REG04-REC02-FND-01	The system shall document for every melting batch which input the certain batch have.	X	Not needed
SYS-REG04-REC02-FND-02	The system shall document the chemical composition of every batch.	✓	Regulations
SYS-REG04-REC02-FND-03	The system shall document the refinement steps of every batch.	✓	Regulations
SYS-REG05-SFT01-ALL-01	The system shall provide a chemical safety assessment for all chemicals used during the systems operation according to EU REACH regulations.	✓	Chapter 5
SYS-REG05-SFT02-ALL-01	The system shall provide access to Safety Data Sheets (SDS) for each chemical in all languages spoken by employees.	✓	Regulations
SYS-REG06-WAS01-FND-01	The recycling system shall store hazardous waste in sealed, labelled, bundled containers separate from non-hazardous waste.	✓	Chapter 5
SYS-REG06-WAS02-FND-01	The recycling system shall dispose of hazardous waste only through a waste carrier and facility holding permits under the EU Waste Shipment Regulation (EC).	✓	Regulations
SYS-REG07-ALM01-FND-01	All aluminium alloys shall have the material properties by the standards set by ASM.	✓	Regulations
SYS-REG07-ALM01-FND-02	All aluminium alloys shall undergo heat treatments set by the standards of ASM.	✓	Outsource
SYS-REG08-SFT01-FND-01	All local fire regulations shall be met.	✓	Regulations
SYS-REG08-SFT02-FND-01	All persons working with hazardous materials shall be in possession of proper HAZWOPER or CHMM certification.	✓	Regulations
SYS-REG08-SFT02-ALL-02	All persons working at heights shall be in possession of proper MEWP certification.	✓	Regulations
SYS-REG08-SFT02-ALL-03	All persons working with heavy machinery shall have a TCVT or the respective operator certificate.	✓	Regulations
SYS-REG08-SFT03-FND-01	The recycling system shall post hazard signs (GHS pictograms) at each process zone.	✓	Regulations
SYS-REG08-OPR01-ALL-01	The working hours shall be between 9.00 and 18.00 hours.	✓	Regulations
SYS-CSN01-REG01-AIR-01	The aircraft shall carry the official Cessna logo on its tail and fuselage.	✓	Intellectual property
SYS-OEM01-AIR01-AIR-01	The airframe shall tolerate the same vibrations as all certified C172 engine models without failing.	?	Scope
SYS-OEM01-AIR02-AIR-01	The instrument panel shall include the original pitot static pressure system from the Cessna 172.	✓	Original avionics
SYS-OEM01-AIR02-AIR-02	The instrument panel shall include the original gyro instruments from the Cessna 172.	✓	Original avionics

Continued on next page...

Table 12.7 – Continued from previous page

Requirement ID	Requirement	Check	Value
SYS-OEM01-AIR03-AIR-01	All flight control cable shall be routed through identical, co-located holes in the airframe as in the original Cessna 172.	✓	Original lay-out
SYS-OEM01-AIR03-AIR-02	All mounting locations of control surfaces shall remain at the same location relative to the original Cessna 172.	✓	Original control surfaces
SYS-OEM01-AIR03-AIR-03	The elevator control force curve shall remain within 5% of the original C172's control force below cruise velocity.	✓	Original control surfaces
SYS-OEM01-AIR04-AIR-01	The airframe shall be able to include a safety harness for all persons onboard.	✓	Original seats
SYS-OEM01-AIR04-AIR-02	The airframe shall be able to include a fire shield between the engines and the cockpit.	✓	Included
SYS-INV01-COM01-AIR-01	The company shall sell more than **TBD** green Cessna's after 10 years.	?	Scope
SYS-INV01-COM01-AIR-02	The selling of the aircraft shall include a 10% profit margin.	✓	11%
SYS-INV01-COM02-ALL-01	The system must be able to scale-up to a minimum annual throughput of 30% of all available feedstock.	?	Scope
SYS-INV01-COM04-AIR-01	The company shall keep a backup of feedstock to continue producing airframes for a minimum of **TBD** months.	?	Scope

Rationale

The rationale for all stakeholder requirements

- SH-USR-02 - A precise inspection strategy is too detailed for preliminary design, thus it is said to be out of scope.
- SH-USR-03 - The structure is designed in Chapter 7 to have a safe life of at least 10,000 hours.
- SH-USR-04 - As described in Section 11.1, the total reduction in emissions is 97%.
- SH-USR-05 - When selling the aluminium, a green premium can be added onto the price as seen in Section 2.7 without losing demand. Thus making it illogical to price the aircraft lower.
- SH-USR-06 - The process of disassembling and melting is made such that the newly acquired aluminium is aerospace-grade.
- SH-REG-01 - To be completely airworthy under the regulations, rigorous testing needs to be done, which is described in subsection 6.3.11.
- SH-REG-02 - To operate a legal business, all regulations are met.
- SH-REG-03 - Before being able to sell the aluminium, the precise composition and structure need to adhere to the ASM guidelines as laid down in subsection 6.3.2.
- SH-REG-04 - Before selling the material, it is important to keep a material passport. However, this only needs to start at the smelting process and not at the disassembly. Starting the passport at the smelting is thus done.
- SH-REG-05 - During the entire decoating process as described in Chapter 5 all regulations are met.
- SH-REG-06 - The entire waste stream is described in Section 5.4, where all regulations regarding disposal are met.
- SH-REG-07 - Before being able to sell the aluminium, the precise composition and structure need to adhere to the ASM guidelines as laid down in subsection 6.3.2.
- SH-REG-08 - To be a legal business, all workplace laws and regulations need to be followed.
- SH-CSN-01 - As the green Cessna is heavily based on the original Cessna 172 all intellectual property laws need to be followed to become a legitimate business.
- SH-PIL-01 - Handling characteristics cannot be modelled until detailed design has been completed.
- SH-OEM-01 - The airframe is kept the same as the original, thus compatible with all other systems.
- SH-INV-01 - As explained in Chapter 11, the projection is to be profitable within five years of the initial investment.

- SH-INV-02 - The selling price of a regular Cessna is €387,000 and that of the green Cessna is €394,953 as described in subsection 8.8.2 thus failing the requirement.

The rationale for all mission requirements

- MS-REG01-AIR-01 - The structure will use a 1.5 safety margin as described in Section 7.2
- MS-REG01-AIR-02 - In subsection 6.3.11 the certification steps are laid out.
- MS-USR03-AIR-01 - The structure is designed in Chapter 7 to have a safe life of at least 10,000 hours.
- MS-USR03-AIR-02 - The replaceability of components does not lie within the scope of the structural design as laid out in Chapter 7.
- MS-USR04-REC-01 - As described in Section 11.1, there will be a reduction in emissions of 97.87%.
- MS-USR04-REC-02 - When aluminium is not recycled, it is sold as scrap material to scrappers.
- MS-USR04-REC-03 - If the material is not able to be downcycled or sold as scrap, it will be disposed of.
- MS-USR04-REC-04 - As only a preliminary design is made, the recyclability is not taken into account, and is deemed out of scope for this project.
- MS-USR04-AIR-01 - The aircraft will have electric propulsion as laid out in Chapter 8, thus lowering the environmental impact.
- MS-USR05-BUD-02 - As described in Section 11.2, the market price will be within 1.02 of the original price.
- MS-USR06-REC-01 - The method used to obtain EOL aircraft is described in Section 3.3.
- MS-USR06-REC-02 - Chapter 4 describes the method used to disassemble EOL aircraft.
- MS-USR06-REC-03 - Details on the decoating of aluminium parts can be found Chapter 5.
- MS-USR06-REC-04 - The sorting method which is used, is described in Section 6.2.
- MS-USR06-REC-05 -The detailed strategy for contaminant extraction can be seen in Section 6.3.
- MS-USR06-REC-06 - The metal recovery rate is calculated in subsection 6.3.9 to be 98.9%.
- MS-REG01-AIR-01 - In Chapter 7, all regulations are taken into account and met during the structural design process.
- MS-REG01-AIR-02 - While designing the propulsion system in Chapter 8 all regulations are taken into account.
- MS-REG01-AIR-03 - The flight characteristic regulations are taken into account while designing the structure and propulsion system in Chapter 7 and Chapter 8.
- MS-REG01-AIR-04 - During the entire design process, the system design regulations are taken into account and adhered to.
- MS-REG02-SYS-01 - To create and operate a legal business, all laws and regulations are met.
- MS-REG03-REC-01 - To sell the aluminium, it is given the correct name in accordance with the specification sheet as described in subsection 6.3.8.
- MS-REG04-REC-01 - The origin of the material is documented as described in subsection 6.3.10.
- MS-REG04-REC-02 - The material passport is added to the bars during the smelting as is described in subsection 6.3.10.
- MS-REG05-SFT-01 - A chemical safety assessment is made in subsection 5.1.2.
- MS-REG05-SFT-02 - In Section 9.2 all chemical risks and the treatment is listed.
- MS-REG06-WAS-01/02/03 - All waste is handled in accordance with these directives to ensure compliance with legal and environmental standards for safe waste handling, disposal, and documentation within the EU as described in Section 5.4.
- MS-REG07-ALM-01 - The aluminium is tested to comply with ASM standards as described in subsection 6.3.11.
- MS-REG08-SFT-01/02/03 - To ensure a safe and legal business, these conditions are all met.
- MS-REG08-OPR-01 - When operating a legal business all employment regulations must be met.
- MS-CSN01-REG-01 - As during the design process the intellectual property of Cessna is used, the logos of Cessna must be carried and a deal must be closed with Cessna.
- MS-PIL01-AIR-01 - After obtaining a private pilot license, it is possible to fly any single piston aircraft, which the new green Cessna still is as described in Section 8.3.
- MS-PIL01-AIR-02 - During the design process in Chapter 7, the entire aerodynamic profile stayed the same.
- MS-PIL01-AIR-03 - All the loads have been determined in Section 7.4.

- MS-PIL01-AIR-04 - The aircraft still serves the purpose of a training aircraft as described in Section 8.3
- MS-PIL01-AIR-05 - To add more leeway into the design, a weight increase of $\pm 10\%$ has been allowed.
- MS-OEM01-AIR-01/02/03/04/05 - The original airframe for the Cessna 172 has been kept, thus all parts can still be integrated into the design.
- MS-INV01-COM-01/02 - As described in Section 11.2, the main revenue stream is that of the producing and selling of green aluminium alloys and green Cessnas.
- MS-INV01-COM-03/04 - The company will have a large enough buffer to keep operations moving, even when there is a financial setback.
- MS-INV02-COM-01 - The production cost of the original Cessna is unverifiable due to it being a company secret.

The rationale for all system requirements

- SYS-OEM01-AIR05-WNG-01 - The system will keep the original airframe, thus the original loads can still be carried as described in Chapter 7.
- SYS-PIL01-AIR02-WNG-01 - In Chapter 7, it has been chosen to use the NACA 2412 airfoil.
- SYS-PIL01-AIR02-WNG-02 - In Section 7.2, it has been decided that the aircraft will be a high-wing configuration.
- SYS-PIL01-AIR02-WNG-03 - In Section 7.2 it has been decided that the aircraft wings will be strut-braced.
- SYS-PIL01-AIR02-WNG-04 - Out of scope for the preliminary wing design as shown in Chapter 7.
- SYS-PIL01-AIR02-WNG-05 - Out of scope for the preliminary wing design as shown in Chapter 7.
- SYS-PIL01-AIR02-WNG-06 - The aircraft frame will remain the same as the original airframe manufactured by Cessna, as shown in Section 7.2.
- SYS-PIL01-AIR03-FLP-01 - The aircraft will have a stall speed of 26.64 m/s as calculated in Section 7.4.
- SYS-PIL01-AIR03-FLP-02 - The aircraft is designed to withstand 4.6 g in normal flight, see subsection 7.5.3.
- SYS-PIL01-AIR03-FLP-03 - The aircraft is designed to withstand -2.6 g in normal flight, see subsection 7.5.3.
- SYS-PIL01-AIR03-FLP-04 - The cruise speed is calculated to be 65 m/s as in Section 7.4.
- SYS-PIL01-AIR03-FLP-05 - The propulsion system can deliver nearly double the amount of climb rate.
- SYS-PIL01-AIR03-FUS-01 - In Section 7.2 it has been decided that there will only be a thickness increase towards the inside.
- SYS-PIL01-AIR04-FRM-01 - In Section 8.2, it has been decided that the green Cessna will carry two passengers.
- SYS-PIL01-AIR04-CSN-01 - In Section 8.3 this is discussed.
- SYS-PIL01-AIR04-CSN-02 - The motor has a power overshoot of 44 kW.
- SYS-PIL01-AIR04-CSN-03 - The charging time is 58 minutes, as can be seen in Section 8.5.
- SYS-PIL01-AIR05-FRM-01 - To make sure the aircraft can still achieve a reliable mission profile, the weight increase has been adapted to 10% as can be seen in Section 7.2.
- SYS-REG01-AIR01-FRM-02 - The aircraft frame will remain the same as the original airframe manufactured by Cessna, as shown in Section 7.2.
- SYS-REG01-AIR01-FRM-03 - The aircraft frame will remain the same as the original airframe manufactured by Cessna, as shown in Section 7.2.
- SYS-REG01-AIR02-CER-01 - In subsection 6.3.11 the certification process is explained.
- SYS-REG01-AIR02-CER-02 - From subsection 6.3.11 it is known that the total cost of certification will be less than 2.5 million dollars.
- SYS-USR03-AIR01-FRM-01 - Out of scope for the preliminary wing design as shown in Chapter 7.
- SYS-USR03-AIR01-FRM-05 - Out of scope for the preliminary wing design as shown in Chapter 7.
- SYS-USR03-AIR01-FRM-06 - Inspection and repair will be accounted for in the detailed design phase.
- SYS-USR03-AIR02-FRM-01 - Out of scope for the preliminary wing design as shown in Chapter 7.
- SYS-USR04-REC01-SUS-01 - As explained in Section 11.1 the system will output 0.215 kg CO_2eq.
- SYS-USR04-REC01-SUS-02 - From Section 11.1 it is known that a reduction of 97.9% in carbon equivalent emissions is achieved.

- SYS-USR04-REC01-SUS-03 - In Section 11.1 it is given that the foundry will have an energy consumption of 2.5 kWh/kg.
- SYS-USR04-REC02-FND-01 - Chapter 6 gives the method of how all aluminium waste is used and recycled.
- SYS-USR04-REC03-FND-01 - In Section 5.4 a waste disposal plan is introduced.
- SYS-USR04-REC04-FRM-01 - In subsection 6.3.3 the refining method is laid out, here no more than 15% dilution is used, making 85% of the material secondary.
- SYS-USR04-REC04-FRM-02 - Out of scope for the preliminary wing design as shown in Chapter 7.
- SYS-USR04-REC04-FRM-03 - The coating selection shall be done during detailed wing design.
- SYS-USR04-REC04-FRM-04 - As described in subsection 7.8.1, only two alloys are used in the production of the green Cessna, namely 2024 and 7075.
- SYS-USR04-AIR01-CSN-01 - Due to the electric propulsion system, no CO2 will be emitted during flight as laid out in Chapter 8.
- SYS-USR05-BUD01-BUD-01 - From subsection 8.8.2 it is known that the aircraft's manufacturing cost are 89% of the total selling price
- SYS-USR05-BUD01-BUD-02 - Out of scope for this project, pertains to detailed design
- SYS-USR05-BUD02-BUD-01 - This is a necessary condition to obtain a profit margin, and thus a profitable business.
- SYS-USR06-REC01-FND-01 - To make the system more economically viable, it has been decided in subsection 3.3.2 that an empty carcass will be bought directly from another company. Meaning there is no need for the system to strip the aircraft from the non-carcass parts.
- SYS-USR06-REC01-BUD-01 - Paying more than the extracted value would result in an unprofitable business.
- SYS-USR06-REC02-FND-01 - The alloy identification process is laid out in Section 6.2, here the different alloys are sorted into their respective groups with the help of XRF.
- SYS-USR06-REC02-FND-02 - With a combination of Chapter 4 and Section 6.2, it is possible to retrieve three different melt streams from the end-of-life aircraft.
- SYS-USR06-REC02-FND-04 - The system will retrieve pieces with a maximum size of 0.2 m^2, which is described in subsection 4.4.6.
- SYS-USR06-REC02-BUD-01 - This is a necessary condition to obtain a profit margin, and thus a profitable business.
- SYS-USR06-REC03-FND-01 - In Chapter 5 the entire process of Cr(VI) decoating is laid down, which is applied to pieces smaller than 0.25 m^2.
- SYS-USR06-REC03-FND-02 - Limits mandated by French and European regulation, compliance is necessary to run a business.
- SYS-USR06-REC03-FND-03 - From subsection 5.3.2 it is known that the time it will take to decoat all the aluminium will be 5.33 hours.
- SYS-USR06-REC03-BUD-01 - After the cost calculations in Section 5.5, the total cost of the decoating process will be €1,861,888.89.
- SYS-USR06-REC04-FND-01 - From a conversation with the manufacturer, the machine will have an accuracy of 99.8% as seen in Section 6.2.
- SYS-USR06-REC04-FND-02 - All aluminium from the aircraft will be sorted in 12 hours as laid out in Section 6.2.
- SYS-USR06-REC04-BUD-01 - From Section 6.2 it is known that the sorting process will cost €113,031.
- SYS-USR06-REC05-FND-02 - During the process, OES spark testing is used to verify the chemical composition, as described in Section 6.3.
- SYS-USR06-REC05-FND-03 - The system will, as a maximum introduce 15% of new or alloyed aluminium, as noted down in Section 6.3.
- SYS-USR06-REC05-FND-04 - After Chapter 6, the aluminium is tested and found to be within the range for either 2024 or 7075, meaning it is within aerospace-grade limits.
- SYS-USR06-REC05-FND-05 - The new aluminium outputted by Chapter 6 is within the correct range of 2024 and 7075, meaning there will always be a maximum variance of 3%.
- SYS-USR06-REC06-FND-01 - The metal recovery rate is calculated in subsection 6.3.9 to be 98.9%

- SYS-USR04-AIR03-FRM-01 - Fatigue resistance testing will be done as laid out in subsection 6.3.11.
- SYS-USR04-AIR03-FRM-02 - Corrosion immunity testing will be done as laid out in subsection 6.3.11.
- SYS-REG01-AIR01-AIR-02 - In Section 7.2, it has been determined that the structure shall withstand limit loads for three seconds, in compliance with FAA regulations.
- SYS-REG01-AIR01-AIR-03 - All the loads have been determined in Section 7.4.
- SYS-REG01-AIR02-AIR-01 - The rate of climb is set at 1,391 ft/min in Chapter 8
- SYS-REG01-AIR02-AIR-03 - The precise controllability lies outside the scope of this project.
- SYS-REG01-AIR02-AIR-04 - An important assumption is that no avionics will be changed during the redesign of the aircraft. Thus, as this is already included in the original Cessna, it will also be in the new version.
- SYS-REG01-AIR02-AIR-05 - Here, the assumption of original avionics is used, and thus, this is still identical to the original Cessna.
- SYS-REG01-AIR02-AIR-08 - The data will be published in the AFM.
- SYS-REG01-AIR02-AIR-09 - The adjusted data will be included in the AFM.
- SYS-REG01-AIR03-AIR-01 - Due to the tail resizing in Equation 7.9 and the newly calculated centre of gravity in Section 8.4, the aircraft will be safely controllable.
- SYS-REG01-AIR03-AIR-02/03/04/05/06/07/08/09/10 - As the tail is resized in Equation 7.9 and a new centre of gravity in Section 8.4 is calculated, the aircraft is deemed stable. The aircraft is also equipped with the original control surfaces, thus it will achieve all stability and control requirements.
- SYS-REG01-AIR04-AIR-02 - Will be accounted for in detailed wing design.
- SYS-REG01-AIR04-AIR-03 - Will be accounted for in detailed design.
- SYS-REG01-AIR04-AIR-04 - Will be accounted for in detailed design.
- SYS-REG01-AIR04-AIR-05 - The aircraft will have the same airframe as the original Cessna, which has protection against both high-intensity radiated fields and lightning strikes.
- SYS-REG01-AIR04-AIR-06/07 - In the aircraft, a fire shield is installed, which is described in subsection 8.4.3 to reduce fire risks.
- SYS-REG01-AIR04-AIR-08 - The aircraft has been designed to fly its mission profile in Section 8.3 with enough power, including reserves.
- SYS-REG01-AIR04-AIR-09 - In Section 8.7, the thermal performance is laid out, and the system is designed to function within this thermal range.
- SYS-REG01-AIR04-AIR-10 - The aircraft has the original avionics, meaning it gives clear warnings.
- SYS-REG02-REC01-SYS-01 - As described in Section 3.3, the main company will be in France, thus all French laws are followed to establish a legal company.
- SYS-REG03-REC01-FND-01 - During the foundry process in Chapter 6 the alloys will be made into either 2024 or 7075, following the ASM specifications.
- SYS-REG04-REC01-FND-01 - To get aerospace-grade material, the origins of the material need to be documented. But the documenting only starts at the smelting process, thus it is not necessary to start documenting the disassembly process.
- SYS-REG04-REC01-FND-02 - To get aerospace-grade material, the origins of the material need to be documented. But the documentation is not needed for the specific input into the smelting process.
- SYS-REG04-REC02-FND-02/03 - For the production of aerospace-grade material, it is important to document the chemical composition and the refinement steps, and thus it is done during the process explained in Section 6.3.
- SYS-REG05-SFT01-ALL-01 - To comply with French law, a chemical safety assessment of the products used must be performed, as described in Chapter 5.
- SYS-REG05-SFT02-ALL-01 - Safety Data Sheets are mandatory and must be understandable by employees.
- SYS-REG06-WAS01-FND-01 - To comply with French law, all waste management regulations must be met to operate a business.
- SYS-REG06-WAS02-FND-01 - To comply with French law, all waste management regulations must be met to operate a business.
- SYS-REG07-ALM01-FND-01 - To achieve 2024 and 7075 alloy the material needs to be within the correct ASM set range. This is done in Section 6.3.

- SYS-REG07-ALM01-FND-02 - From subsection 6.3.8 it is known that all alloys will undergo heat treatment as set by ASM regulations.
- SYS-REG08-SFT01-FND-01 - To comply with French law, all fire regulations must be met to operate a business.
- SYS-REG08-SFT02-FND-01 - To comply with French law, all labour laws must be met to operate a business.
- SYS-REG08-SFT02-ALL-02 - To comply with French law, all labour laws appropriate with working with heights must be met to operate a business.
- SYS-REG08-SFT02-ALL-03 - To comply with French law, all labour laws appropriate with working with heavy machinery must be met to operate a business.
- SYS-REG08-SFT03-FND-01 - To comply with French law, all labour laws must be met to operate a business.
- SYS-REG08-OPR01-ALL-01 - To comply with French law, all labour laws must be met to operate a business.
- SYS-CSN01-REG01-AIR-01 - When redesigning a Cessna aircraft, the intellectual property laws still have to be followed in order to market the newly designed aircraft.
- SYS-OEM01-AIR01-AIR-01 - Out of scope for the preliminary structural design as shown in Chapter 7.
- SYS-OEM01-AIR02-AIR-01/02 - The aircraft will still have the same avionics as the original aircraft.
- SYS-OEM01-AIR03-AIR-01/02/03 - The aircraft will still have the same lay-out and control surfaces as the original aircraft.
- SYS-OEM01-AIR04-AIR-01 - The aircraft will have the original seats as the Cessna, thus a safety harness is included.
- SYS-OEM01-AIR04-AIR-02 - The aircraft will have a fire shield as described in Chapter 8
- SYS-INV01-COM01-AIR-01 - Only looked into the scale for the first 3 to 5 years.
- SYS-INV01-COM01-AIR-02 - The profit margin used is 11% as discussed in subsection 8.8.2
- SYS-INV01-COM02-ALL-01 - Too much in depth for the project, out of scope.
- SYS-INV01-COM04-AIR-01 - Too much in depth for the project, out of scope.

13

Future Project Development

13.1. Production, Manufacturing and Assembly Plan

The production, manufacturing and assembly plan is divided into three main stages: the foundry and recycling process, part manufacturing, and final assembly. The current project entails the recovery of aluminium from end-of-life aircraft, applying the stages for disassembly, decoating, sorting, refining, melting, slab casting, sheet manufacturing and alloy certification. The output of the project is the certified aluminium sheets that are to be used for the part manufacturing of the wing design and structural design. Furthermore, the wing, battery, power and propulsion design specifications will also be delivered. These outputs are then handed over to Cessna, where structural component production, propulsion system integration and final aircraft assembly would be carried out in future project phases. The process cycles can be mostly held in batches, where the foundry part follows a linear route for the recycling. Each process step operates simultaneously through feeding the system with the upcoming batches that will be dismantled. After recycled aluminium sheets are produced, the part manufacturing and assembly of the individual parts will be applied in collaboration with Cessna. The following section elaborates on how the production phase of the foundry and recycling process is held, the design specifications for the part manufacturing, and assembly considerations.

Foundry and Recycling process begins with the acquisition of the end-of-life aircraft, followed by a detailed dismantling process in which the aluminium components are separated from non-aluminium materials and prepared for further processing through laser cutting. After the disassembly process, the parts are cut in similar dimensions, being 50x50 cm and, 70x15 cm of plates and stringers. This prepares the parts for the decoating stage, where parts are placed in vertical racks in groups according to their specific parts. For instance, ribs, parts, stringers, skin and frame parts are grouped and immersed simultaneously with their corresponding class. After the decoating process the parts will be ready for the smelting and refining stages. The refining process aims to remove the impurities that might occur during the part's lifetime, for instance, due to its contact with other metal parts, aluminium oxidation during melting or further dissolved gases that might be present. Thus, the refining process applies a detailed plan to remove the possible impurities that the aluminium melt could include and pose a risk to the purity of the alloy.

After the aluminium melt is refined, it is slab cast and sheet manufactured to be transported to the external alloy testing facilities, where the alloying structure and the microstructural properties of the recycled aluminium can be certified and verified. After the recycled parts are certified, it can be proceeded with the part manufacturing of the structural and frame parts of the green Cessna.

Part Manufacturing entails the manufacturing of structural parts from the recycled aluminium sheets. This process considers several shaping and manufacturing techniques to comply with the material-specific alloy properties and their corresponding requirements. For instance, as mentioned in subsection 7.8.1, the 7xxx series requires manufacturing with extrusion, CNC machining, press brake bending, roll forming, and press forming. This stage of manufacturing focuses on the spar webs, flanges, and ribs. The further elaboration of the part manufacturing considerations can be found at subsection 7.8.1. Wing frame components, ribs, stringers, and skin are manufactured in parallel at this stage and prepared for the assembly of the parts. For future stages of the project, a detailed manufacturing and production considerations plan, including the detailed wing and part design considerations outlined in Section 7.2, will be delivered to Cessna to finalise the production of structural parts for wing production. In parallel with the wing part design, the proposed electric propulsion subsystem design will be delivered to Cessna for the acquisition of parts and the manufacturing of specific parts.

Assembly is held simultaneously within the subsystems, for their respective parts. The wings, fuselage and frame assembly are held by Cessna following the wing design given in Chapter 7 and battery design given in Chapter 8. For the assembly of the battery packs, the given specifications for the subsystem integration will be considered.

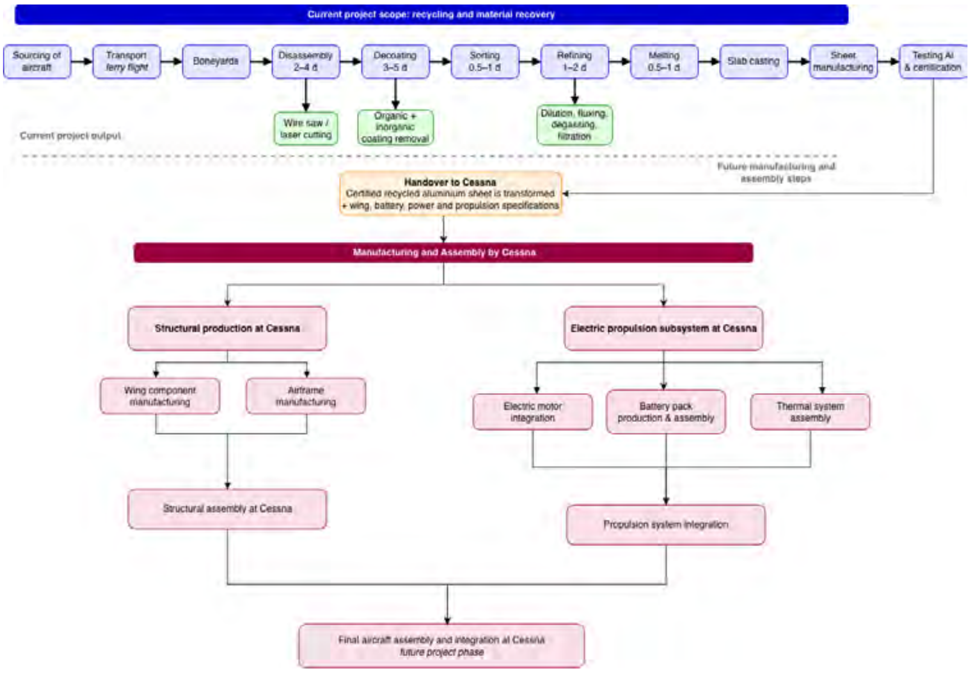

Figure 13.1: Production Assembly and Manufacturing Plan

13.2. Project Design & Development Logic

The Project Design & Development (PD&D) logic shows the chronological order of activities after the research phase of the project is finished. The diagram is split up into 5 sections: phase 1A (in light blue) tests the foundry processes at the micro-scale and is scaled up during the last phase, called macro-scale refining (light green), phase 1B (pink) tests the electric Cessna design with virgin material and verifies the assembly plan. This is followed by the Cessna handover package (yellow), which lists all information critical to a successful handover, and phase 2 (purple) details the production of parts using recycled materials.

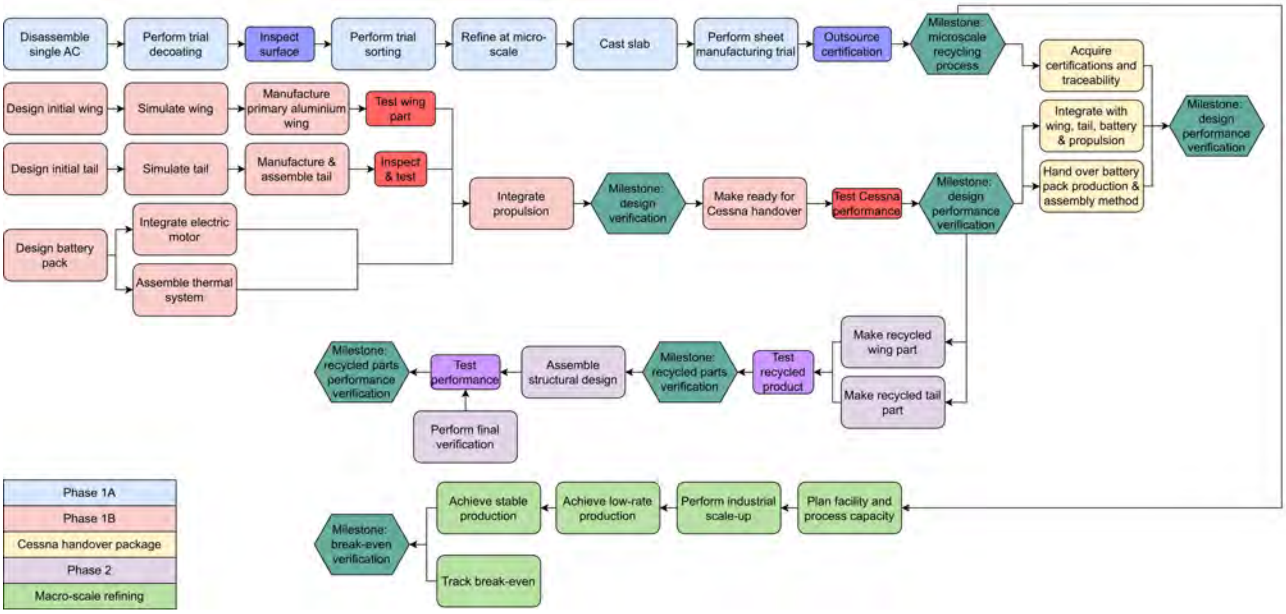

Figure 13.2: The project design & development logic diagram, showing the future steps of the project.

13.3. Project Gantt Chart

The five-year project Gantt Chart presents the significant milestones for the project, and the timelines of corresponding tasks. The chart shows the transition from the verification of the recycling process in the first phase, then provides design verification processes and finally the Cessna handover stages and production of the Green Cessna.

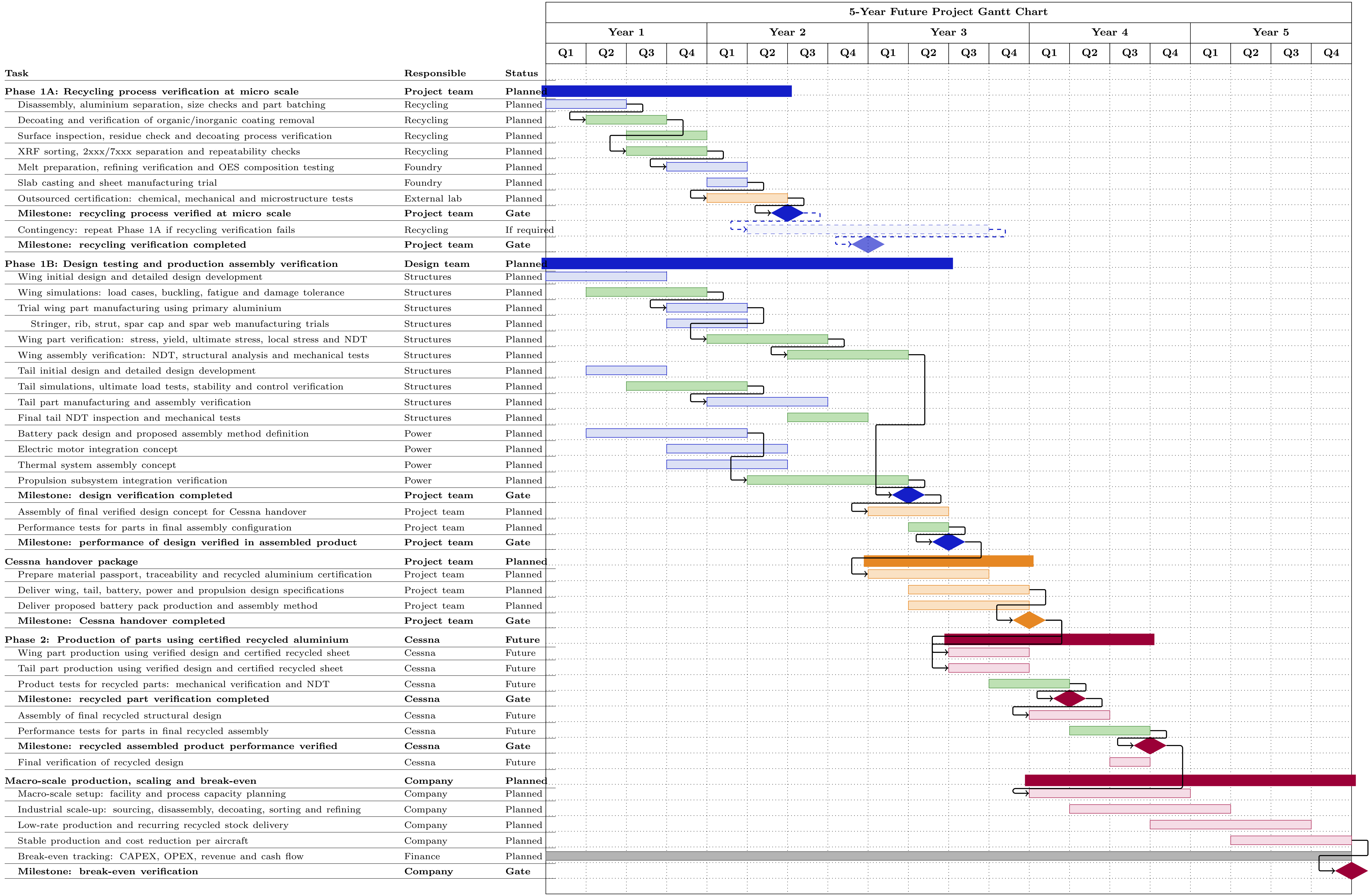

Task	Responsible	Status
Phase 1A: Recycling process verification at micro scale	**Project team**	**Planned**
Disassembly, aluminium separation, size checks and part batching	Recycling	Planned
Decoating and verification of organic/inorganic coating removal	Recycling	Planned
Surface inspection, residue check and decoating process verification	Recycling	Planned
XRF sorting, 2xxx/7xxx separation and repeatability checks	Recycling	Planned
Melt preparation, refining verification and OES composition testing	Foundry	Planned
Slab casting and sheet manufacturing trial	Foundry	Planned
Outsourced certification: chemical, mechanical and microstructure tests	External lab	Planned
Milestone: recycling process verified at micro scale	**Project team**	**Gate**
Contingency: repeat Phase 1A if recycling verification fails	Recycling	If required
Milestone: recycling verification completed	**Project team**	**Gate**
Phase 1B: Design testing and production assembly verification	**Design team**	**Planned**
Wing initial design and detailed design development	Structures	Planned
Wing simulations: load cases, buckling, fatigue and damage tolerance	Structures	Planned
Trial wing part manufacturing using primary aluminium	Structures	Planned
Stringer, rib, strut, spar cap and spar web manufacturing trials	Structures	Planned
Wing part verification: stress, yield, ultimate stress, local stress and NDT	Structures	Planned
Wing assembly verification: NDT, structural analysis and mechanical tests	Structures	Planned
Tail initial design and detailed design development	Structures	Planned
Tail simulations, ultimate load tests, stability and control verification	Structures	Planned
Tail part manufacturing and assembly verification	Structures	Planned
Final tail NDT inspection and mechanical tests	Structures	Planned
Battery pack design and proposed assembly method definition	Power	Planned
Electric motor integration concept	Power	Planned
Thermal system assembly concept	Power	Planned
Propulsion subsystem integration verification	Power	Planned
Milestone: design verification completed	**Project team**	**Gate**
Assembly of final verified design concept for Cessna handover	Project team	Planned
Performance tests for parts in final assembly configuration	Project team	Planned
Milestone: performance of design verified in assembled product	**Project team**	**Gate**
Cessna handover package	**Project team**	**Planned**
Prepare material passport, traceability and recycled aluminium certification	Project team	Planned
Deliver wing, tail, battery, power and propulsion design specifications	Project team	Planned
Deliver proposed battery pack production and assembly method	Project team	Planned
Milestone: Cessna handover completed	**Project team**	**Gate**
Phase 2: Production of parts using certified recycled aluminium	**Cessna**	**Future**
Wing part production using verified design and certified recycled sheet	Cessna	Future
Tail part production using verified design and certified recycled sheet	Cessna	Future
Product tests for recycled parts: mechanical verification and NDT	Cessna	Future
Milestone: recycled part verification completed	**Cessna**	**Gate**
Assembly of final recycled structural design	Cessna	Future
Performance tests for parts in final recycled assembly	Cessna	Future
Milestone: recycled assembled product performance verified	**Cessna**	**Gate**
Final verification of recycled design	Cessna	Future
Macro-scale production, scaling and break-even	**Company**	**Planned**
Macro-scale setup: facility and process capacity planning	Company	Planned
Industrial scale-up: sourcing, disassembly, decoating, sorting and refining	Company	Planned
Low-rate production and recurring recycled stock delivery	Company	Planned
Stable production and cost reduction per aircraft	Company	Planned
Break-even tracking: CAPEX, OPEX, revenue and cash flow	Finance	Planned
Milestone: break-even verification	**Company**	**Gate**

13.4. Cost breakdown structure (CBS)

The Cost Breakdown Structure (CBS) shown in Figure 13.3 identifies all cost elements that contribute to the development and production of the aircraft dismantling and aluminium recovery facility designed during the DSE. It is organised as an AND-tree: the total project cost at the top is the sum of its branches, and each branch is in turn the sum of its child elements, so the leaves together form a complete, non-overlapping decomposition of the cost. The structure follows the PD&D logic and serves as the basis for the cost estimate.

The cost is split into three branches. The development branch covers the non-recurring effort required to take the preliminary design to a realised facility, including detailed design and engineering, permitting and certification, prototyping and testing, and project management. The capital investment branch contains the non-recurring CAPEX of the facility and its processing equipment, grouped by sub-system (disassembly, decoating, sorting, foundry and casting, quality and testing). The operations branch contains the recurring OPEX of running the facility, covering feedstock acquisition, energy, consumables, labour, maintenance, logistics, recurring certification and overhead. The capital investment and operations branches correspond directly to the CAPEX and OPEX elements quantified by the cost model of Chapter 11, while the development branch captures the additional non-recurring cost incurred after the DSE in bringing this project to life.

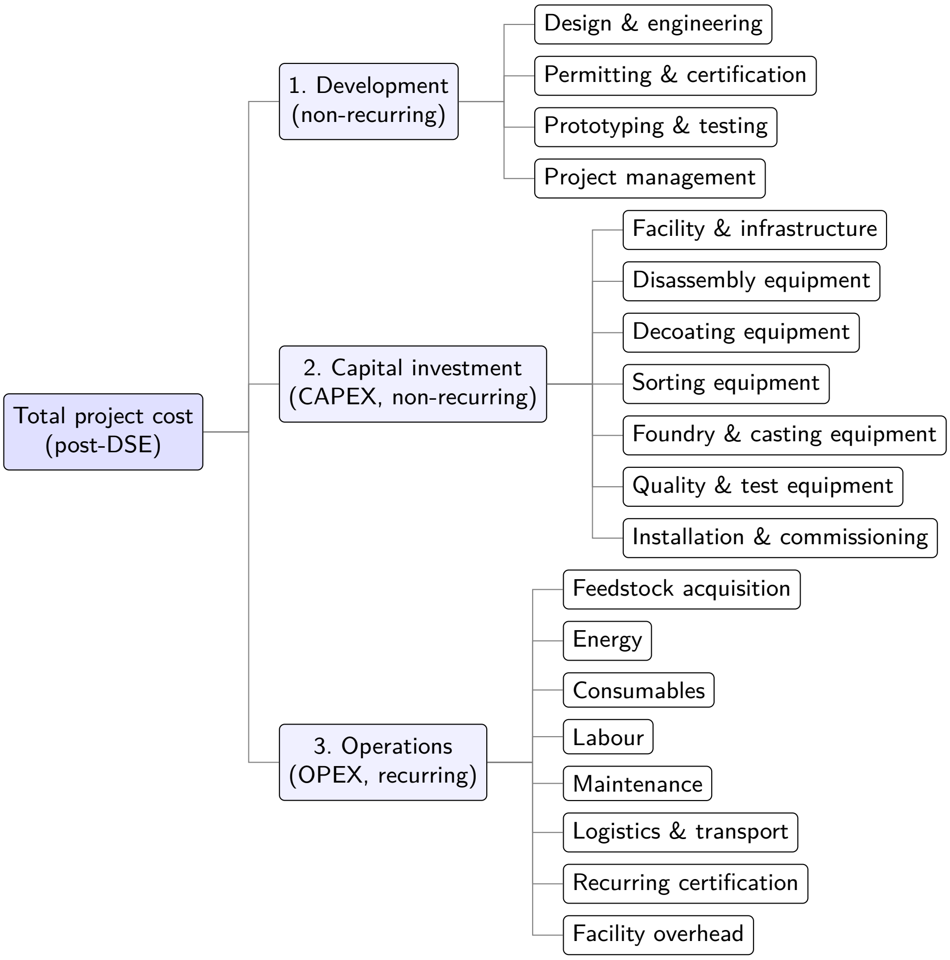

Figure 13.3: Cost Break-down Structure (CBS) of the post-DSE development and production cost

14

Conclusion

The aim of this final report was to design a comprehensive closed-loop recycling process for aerospace-grade aluminium alloys from end-of-life aircraft, and to demonstrate the viability of this approach through the preliminary design of a green, electric, retrofitted Cessna 172S. Hundreds of aircraft are retired and parked in boneyards each year, and this report has presented a viable method of recycling this lost metal into new aircraft. In addition, a market analysis and business case is evaluated to show the viability and requirements for a potential start-up company providing these services. To reach the production of aerospace-grade aluminium alloys, seven steps are followed from aircraft acquisition to alloy testing, including disassembly, decoating, and sorting of commercial end-of-life aircraft. Finally, an electric propulsion system and accompanying larger wing are retrofitted on the Cessna 172S to demonstrate the viability of the alloys in aircraft design.

Through rigorous analysis, optimal methods for each stage of the recycling process were identified and refined. Firstly, it was decided to start with bulk sectioning of the carcass to make smaller, more accurate cuts in a controlled environment rather than on the aircraft itself. The diamond wire sawing was selected as the primary bulk sectioning technique, demonstrating safe and efficient cutting while maintaining temperatures well below the aluminium softening threshold. For this, a preliminary design for a bespoke machine was developed, capable of sectioning all transport aircraft types. From the technique, three main component categories are obtained: wing planform, empennage, and fuselage. From all of these, some parts need further processing or downcycling due to the presence of composites, adhesives, or a large number of rivets. Secondly, the remaining cut-outs are further processed on a laser-cutting rig within an indoor facility. The laser is equipped with computer vision systems to detect a rivet with an accuracy of 98% allow for precise rivet-line identification. The process up until this point recovers over 10.7 tonnes of aluminium per A310-class aircraft, representing 37.1% of the structural aluminium present in the carcass, establishing a baseline recovery figure with the potential for additional yield.

The decoating process employs a sequential chemical-bath immersion system to effectively remove hazardous chromium (VI) coatings. Since components and their fasteners are coated on all sides, this process is performed after disassembly to prevent contamination of the melt. Each part is sequentially submerged into 9 baths, with the setup and number of baths designed for maximum part throughput. This accounts for the time spent in each bath, cleaning of the baths, and drying of the parts in between. Each aircraft will require 55 batches in two different rack types, with each batch having a process time of 5.33 hours.

For the refining, three melt streams were determined: one for AA2024, one for AA7075, and a third stream isolates zirconium-containing alloys. Each alloy type can only be introduced into its respective melt stream to ensure the final product stays within its required chemical composition. To sort these alloys into their streams, X-ray Fluorescence technology was selected, achieving 99.8% accuracy in distinguishing between alloys at a rate of 3-5 seconds per plate. This technique was selected for its low cost and ease of use, while allowing for sufficient processing speed on the designed conveyor belt sorter. Then the streams undergo a five-step purification sequence, which yields a 98.9% metal recovery rate to achieve the desired composition. This includes a calculated dilution step that adds up to 7% virgin aluminium to reduce metallic contaminants such as iron and titanium within the melt.

The structural design of the retrofitted Cessna 172S successfully accommodates a 10% increase in maximum take-off weight through a 15% wing span extension, while maintaining handling characteristics similar to the original aircraft. A spar design was established across four regions, resulting in a structure utilising 7075-T6 aluminium for spar caps and 2024-T3 for spar webs. Two I-beam spars were selected for half the span, reducing to zero spars towards the wing tip. The strut-braced wing configuration, with the strut attached at 60% of the semi-span, was optimised to minimise bending moments. Rib spacing was determined to prevent spar column buckling, with spacings ranging from 300 mm to 400 mm across the inboard regions. The wing skin thicknesses and stringer area were iterated in different regions of the span to the main constraint of skin panel buckling at limit load conditions. This resulted in the skin thickness of 0.9-1.2 mm and a stiffener area of either 40 or 130 mm^2, depending on loads in each region.

The electric propulsion system was designed around a 180 kW motor and a battery pack capacity of 115 kWh, resulting in a cruise range of 230 km and endurance of 100 min. The mission profiles for common training and cross-country flights were established, requiring 106 kWh. Battery degradation modelling predicted over 1,700 flights before reaching

90% state-of-health, balancing cycle life and capacity requirements. The thermal management system incorporates a shared radiator core with independent coolant loops, maintaining motor and battery temperatures safely below their operational limits of 60 °C and 55 °C, respectively, throughout the mission profile and during rapid recharging.

Finally, the business case was evaluated with the costs and emissions of the entire process. This included all components of the recycling process (such as cutting machines, sorters and baths) to determine the capital investment and operating costs required per aircraft. The analysis revealed a minimum viable throughput of 77 aircraft per year to achieve a five-year discounted payback, with an annual profit of 2.87 million and a total 20-year return on investment of 422% at this throughput. Despite the high upfront investment of 13.6 million, the operation has a positive contribution to environmental sustainability, with 97% lower emissions and 60% lower energy consumption than primary production.

Recommendations

Based on the findings of this report, several recommendations are proposed for future development of both the recycling process and the retrofitted Cessna design. For disassembly, it is recommended to proceed to the detailed design of bespoke machinery. The costs of aircraft acquisition and the decoating process require further research, as they are currently based on industry standards and/or averages from ranges. In addition, chemical solution consumption and wastewater treatment may vary with coating condition, affecting electricity, water, and chemical usage. It is recommended to perform real-world tests to obtain more accurate figures and size the process accordingly. For the refining of the melts, the current dilution calculated only recommends adding pure or alloyed aluminium; however, this could be expanded to include the melt used to clean downstream machines and pure elements. In addition, the flux processes require further research to understand what occurs at the microscopic scale. For the Cessna wing structure, the wing-box idealisation requires many more iterations and a redesign to accommodate greater variability within an optimisation algorithm. Afterwards, detailed design needs occur with the addition of finite element analysis to verify the design requirements. For the propulsion system, the battery degradation and thermal management need to be evaluated in real-world conditions to confirm that the calculated efficiency is met. Furthermore, airports currently lack large-scale electric charging infrastructure, which causes a barrier to entry; this needs to be evaluated in the business case.

Bibliography

[1] Page, H., Griffiths, C., and Thomas, A., "Economic and Environmental Analysis of Aluminium Recycling from Retired Commercial Aircraft," *Sustainability*, Vol. 17, 2025, p. 8556.

[2] Fastmarkets, "Valuing lower carbon emission steel and aluminium: a look at regional premium fragmentation," Tech. rep., Fastmarkets, 2026.

[3] Page, H., Griffiths, C. A., and Thomas, A. J., "Economic and Environmental Analysis of Aluminium Recycling from Retired Commercial Aircraft," *Sustainability*, Vol. 17, No. 19, 2025, p. 8556.

[4] General Aviation Manufacturers Association, "2025 General Aviation Aircraft Shipment and Billing Report," Annual report, GAMA, 2026.

[5] Cole, W., Frazier, A. W., and Augustine, C., "Cost Projections for Utility-Scale Battery Storage: 2023 Update," Tech. Rep. NREL/TP-6A40-85332, National Renewable Energy Laboratory (NREL), Golden, CO, 2023.

[6] The Aluminum Association, "International Alloy Designation and Chemical Composition Limits for Wrought Aluminum and Wrought Aluminum Alloys," Tech. rep., The Aluminum Association, 2015.

[7] Turkensteen, M., "The computation of carbon emissions due to the net payload on a truck," Working Paper 2017-3, Aarhus University, Department of Economics and Business Economics, Cluster of Operations Research And Logistics (CORAL), 2017.

[8] Xu, Z., Huang, H., Cui, C., Liao, X., Wu, M., and Xue, Z., "Complex-Shaped Metal Parts High Efficiency Sawing with Diamond Wire," *International Journal of Mechanical Sciences*, Vol. 250, 2023, p. 108306. doi:10.1016/j.ijmecsci.2023.108306.

[9] van Leeuwen, T., Dowdy, R., Guerrero, A., and Gannon, P., "Reactive evaporation and condensation of chromium: A review," *Journal of Power Sources*, 2023.

[10] Airbus S.A.S., *A330 Aircraft Characteristics – Airport and Maintenance Planning*, Airbus S.A.S., Customer Services, Technical Data Support and Services, 31707 Blagnac Cedex, France, Aug. 2022. Revision 31, Aug 01/22. Original issue Jan 01/93.

[11] Malkin, S., and Guo, C., "Thermal Analysis of Grinding," *Manufacturing Technology*, 2007.

[12] Wang, Y., Song, L.-X., Liu, J.-G., Wang, R., and Zhao, B.-C., "Investigation on the sawing temperature in ultrasonic vibration assisted diamond wire sawing monocrystalline silicon," *Materials Science in Semiconductor Processing*, 2021.

[13] Carslaw, H., and Jaeger, J., *Conduction of Heat in Solids*, 2nd ed., Oxford University Press (Clarendon Press), Oxford, 1959.

[14] Rowe, W., *Principles of Modern Grinding Technology*, 2nd ed., William Andrew (Elsevier), Oxford, 2014.

[15] Rumble, J., *CRC Handbook of Chemistry and Physics*, 104th ed., CRC Press, Boca Raton, FL, 2023. Thermal properties of diamond (thermal conductivity, density, specific heat).

[16] ASM International, *Properties and Selection: Nonferrous Alloys and Special-Purpose Materials*, ASM Handbook, Vol. 2, ASM International, Materials Park, OH, 1990. Thermal properties of aluminium alloys (conductivity, density, specific heat).

[17] Jaeger, J. C., "Moving sources of heat and the temperature at sliding contacts," *Journal and proceedings of the Royal Society of New South Wales*, 1942.

[18] Rosenthal, D., "The Theory of Moving Sources of Heat and Its Application to Metal Treatments," *Transactions of the American Society of Mechanical Engineers*, Vol. 68, No. 8, 1946, pp. 849–866.

[19] Internal Revenue Service, *Publication 946 (2025): How To Depreciate Property*, United States Internal Revenue Service, 2025.

[20] Kaufman, J. G., "Properties of Pure Aluminum," *Aluminum Science and Technology*, 2018.

[21] Kovacik, J., Marsavina, L., and Linul, E., "Poisson's ratio of closed-cell aluminium foams," *Materials*, 2018.

[22] Liu, Z., Forsyth, D. S., Marincak, A., and Vesley, P., "Automated rivet detection in the EOL image for aircraft lap joints inspection," *NDT&E International*, Vol. 39, 2006, pp. 441–448.

[23] Amosov, O. S., Amosova, S. G., and Iochkov, I. O., "Deep Neural Network Recognition of Rivet Joint Defects in Aircraft Products," *Sensors*, Vol. 22, 2022.

[24] Jackson, P., *Jane's All the World's Aircraft*, Macdonald and Jane's, 2013.

[25] Niu, M. C.-Y., *AIRFRAME STRUCTURAL DESIGN*, Conmilit Press Ltd., 1988.

[26] Airbus Industrie, *A310 Structural Repair Manual*, Airbus Industrie, 1996.

[27] Roskam, J., *Airplane Design Part V: Component Weight Estimation*, DAR Corparation, 1999.

[28] Bennett, J. S., et al., "Hexavalent Chromium and Isocyanate Exposures during Military Aircraft Painting under Crossflow Ventilation," *Journal of Occupational and Environmental Hygiene*, Vol. 13, No. 5, 2016, pp. 356–371. doi:10.1080/15459624.2015.1116696.

[29] Carlton, G. N., England, E. C., and Moorman, W. J., "Hexavalent chromium exposures during full-aircraft corrosion control," *AIHA Journal*, Vol. 64, No. 5, 2003, pp. 668–672. doi:10.1202/527.1.

[30] Giannis, S., Adams, R., Clark, L., and Taylor, M., "Investigation of the water and fuel exposure characteristics of aircraft fuel tank sealants and the effect on their glass transition temperature," *Journal of Applied Polymer Science*, Vol. 108, No. 5, 2008, pp. 3073–3091.

[31] Farrier, L. M., and Szaruga, S. L., "Sample preparation and characterization of artificially aged aircraft coatings for microstructural analysis," *Materials Characterization*, Vol. 55, No. 3, 2005, pp. 179–189. doi:https://doi.org/10.1016/j.matchar.2005.04.009.

[32] Liu, J., Chen, K., Zhang, Y., Zhou, L., Wang, F., Xiang, X., and Wu, H., "Study on the chemical bonding at the interface between epoxy primer and polyurethane topcoat," *Progress in Organic Coatings*, Vol. 196, 2024, p. 108677.

[33] Zhao, J., "Unleashing the Power of Organic Corrosion Inhibitors in Aircraft Coating Design," Dissertation, Delft University of Technology, 2025.

[34] Titu, A. M., Ravai-Nagy, S., and Pop, A. B., "Research on the Influence of Coating Technologies on Adhesion Anti-Corrosion Layers in the Case of Al7175 Aluminum Alloy," *Coatings*, Vol. 13, No. 6, 2023. doi:10.3390/coatings13061054.

[35] Sunderland, R., "Analysis of Chromate Conversion Coatings on Aluminum," *Japanese Journal of Applied Physics*, Vol. 13, 1974, p. 347.

[36] European Space Agency, "Assessment of Chemical Conversion Coatings for the Protection of Aluminum Alloys," Tech. Rep. ESA STM-276, European Space Agency, 2008. Accessed: 2026-06-22.

[37] Campestrini, P., Terryn, H., Hovestad, A., and de Wit, J., "Chromate Conversion Coating on Aluminum Alloys. I. Formation Mechanism," *Journal of The Electrochemical Society*, Vol. 151, No. 2, 2004, pp. B59–B70.

[38] Ardelean, M., Lascau, S., Ardelean, E., and Josan, A., "Surface treatments for aluminium alloys," *IOP Conference Series: Materials Science and Engineering*, Vol. 294, 2018, p. 012042. doi:10.1088/1757-899X/294/1/012042.

[39] Monette, D., "10 - Coating removal techniques in the aerospace industry," *Corrosion Control in the Aerospace Industry*, edited by S. Benavides, Woodhead Publishing Series in Metals and Surface Engineering, Woodhead Publishing, 2009, pp. 225–247.

[40] Advisory Group for Aerospace Research and Development, "Environmentally Safe and Effective Processes for Paint Removal," AGARD Lecture Series AGARD-LS-201, North Atlantic Treaty Organization, Advisory Group for Aerospace Research and Development, Neuilly-sur-Seine, France, 1995.

[41] Nyarko, E., "Determination of the Relative Activity of Selected Paint Stripping Components with Epoxy and Polyurethane Aerospace Coatings," 2011. OhioLINK Electronic Theses and Dissertations Center.

[42] Callington, "Aircraft paint strippers," Tech. rep., Callington, 2026.

[43] Young, C., Clayton, C., Yesinowski, J., Wynne, J., and Watson, K., "Physicochemical investigation of chemical paint removers: Interactions of methylene chloride with polyurethane coatings," *Progress in Organic Coatings*, Vol. 77, No. 1, 2014, pp. 232–241.

[44] Hans, H. B., "Paint Stripping with Nontoxic Chemicals," *Metal Finishing*, Vol. 93, No. 4, 1995, pp. 34–38. doi:10.1016/0026-0576(95)95844-7.

[45] Young, C., Clayton, C., Wynne, J., Yesinowski, J., and Daniels, G., "Physicochemical investigation of chemical paint removers. II: Role and mechanism of phenol in the removal of polyurethane coatings," *Progress in Organic Coatings*, Vol. 88, 2015, pp. 212–219.

[46] Fremont Industries, "Paint Stripping Guide," , n.d. Accessed: 2026-06-16.

[47] UK Health Security Agency, "Sodium Hydroxide: Incident Management," , nov 2024.

[48] Johnson, P., "A Non-Chromium, Non-Heavy Metal Deoxidizer System for Aluminum Alloys," , n.d. Accessed: 2026-06-16.

[49] European Integrated Pollution Prevention and Control Bureau, "Reference Document on Best Available Techniques for the Surface Treatment of Metals and Plastics," Bref, European Commission, Joint Research Centre, 08 2006. Surface Treatment of Metals and Plastics BREF.

[50] Cee-Bee, "Cee-Beeő E-3000," Tech. rep., Cee-Bee, 2024.

[51] Bonderite, "BONDERITE C-IC DEOXDZR 6 MU," Tech. rep., Bonderite, 2019.

[52] ASM International, "Surface Engineering of Aluminum and Aluminum Alloys," *ASM Handbook, Volume 5: Surface Engineering*, edited by C. M. Cotell, J. A. Sprague, and F. A. Smidt, ASM International, 1994, pp. 784–804. Accessed 5 June 2026.

[53] Small Business Environmental Assistance Program, "Pollution Prevention for the Electroplating and Metal Finishing Industry," , 2026. Accessed: 2026-06-22.

[54] OECD, "Emission Scenario Document on Transport and Storage of Chemicals," , 2009. ENV/JM/MONO(2009)26.

[55] Cee-Bee, "Eldorado PR-5044," Tech. rep., Cee-Bee, 2024.

[56] Cee-Bee, "Cee-Beeő E-3000M," Tech. rep., Cee-Bee, 2021.

[57] U.S. Environmental Protection Agency, "Wastewater Technology Fact Sheet: Chemical Precipitation," , Sep 2000. Accessed 4 June 2026.

[58] Electric Power Research Institute, "Metal Finishing: A Small Business Guide," Tech. Rep. TR-106676-V6, Electric Power Research Institute, Palo Alto, CA, 1996.
[59] Li, S., Yue, X., Li, Q., Peng, H., Dong, B., Liu, T., Yang, H., Fan, J., Shu, S., Qiu, F., and Jiang, Q., "Development and applications of aluminum alloys for aerospace industry," *Journal of Materials Research and Technology*, Vol. 27, 2023, pp. 944–983.
[60] Rambabu, P., Eswara Prasad, N., Kutumbarao, V., and Wanhill, R., *Aluminium Alloys for Aerospace Applications*, Springer Singapore, Singapore, 2017.
[61] Reichert, W., Kenn, D., Sannikow, V., Tonnesen, T., and Telle, R., "Influence of modern aluminium alloys on the reaction behavior of refractory linings," *Ceramic Engineering & Science*, 2022.
[62] Wang, Y., Fang, C., Zhou, L., Hashimoto, T., Zhou, X., Ramasse, Q., and Fan, Z., "Mechanism for Zr poisoning of Al-Ti-B based grain refiners," *Acta Materialia*, Vol. 164, 2019, pp. 428–439.
[63] Li, X., and Starink, M., "Identification and analysis of intermetallic phases in overaged Zr-containing and Cr-containing AlZnMgCu alloys," *Journal of Alloys and Compounds*, Vol. 509, 2011, pp. 471–476.
[64] Hiroyuki Ida, S. T., Takao Segawa, and Kawai, J., "Reactive evaporation and condensation of chromium: A review," *Journal of Power Sources*, 2023.
[65] Osawa, Y., Takamori, S., Kimura, T., Minagawa, K., and Kakisawa, H., "Morphology of Intermetallic Compounds in Al-Si-Fe Alloy and Its Control by Ultrasonic Vibration," *Materials Transactions*, Vol. 48, No. 9, 2007, pp. 2467–2475. doi:10.2320/matertrans.F-MRA2007874.
[66] Adtech, "Features of Smelting Aluminum Alloys," , 2019.
[67] NASA, "Environment Enhanced Fatigue of Advanced Aluminum Alloys and Composites," Tech. rep., NASA, 1990.
[68] Xhanaria, K., and Fingar, M., "Organic corrosion inhibitors for aluminum and its alloys in chloride and alkaline solutions: A review," *Arabian Journal of Chemistry*, Vol. 12, 2016, pp. 4646–4663.
[69] Capral Aluminium, "Lower-Carbon Aluminium for Australian Manufacturers," Tech. rep., LocAl, 2024.
[70] Zumdahl, S., and Zumdahl, S., *Chemistry*, 8th ed., Brooks/Cole Pub Co, 2008.
[71] Milani, V., and Timelli, G., "Solid Salt Fluxes for Molten Aluminum ProcessingA Review," *Metals*, Vol. 13, 2023, p. 832.
[72] Zhang, Z., "Covering flux for smelting aluminum and a process for its preparation," U.S. Patent US5762722A, 11 1995.
[73] Vesuvius, "Flussum SW 2-Datasheet," Tech. rep., Vesuvius, 2025.
[74] Wang, M., Zhang, S., Du, S., Wang, J., and Liu, B., "A review of the upcycling of aluminum scrap and dross using molten salt electrolysis," *Resources, Conservation and Recycling*, Vol. 220, 2025, p. 108352.
[75] Vesuvius, "Flussum 111-Datasheet," Tech. rep., Vesuvius, 2024.
[76] Adtech, "Online degassing equipment," Tech. rep., Adtech, 2025.
[77] Liquide, A., "Chlorine (Cl2)," Tech. rep., Air Liquide, 2026.
[78] Wang, Y., Que, Z., Hashimoto, T., Zhou, X., and Fan, Z., "Mechanism for Si Poisoning of Al-Ti-B Grain Refiners in Al Alloys," *Metallurgical and Materials Transactions A*, Vol. 51, 2020, pp. 5743–5757.
[79] McClelland, T., "'Apex' rolling ingot casting technology benefits casthouses and rolling mills," Tech. rep., Wagstaff, 2021.
[80] ABB, "AL-EMS electromagnetic stirring solutions: Improving aluminium furnace performance," Tech. rep., ADD AB, 2024.
[81] Scamans, G., Li, H.-T., Nebreda, J. L., Patel, J., Stone, I., Wang, Y., Yang, X., and Fan, Z., "Chapter 8 - Advanced Casting Technologies Using High Shear Melt Conditioning," *Fundamentals of Aluminium Metallurgy*, edited by R. Lumley, Woodhead Publishing Series in Metals and Surface Engineering, Woodhead Publishing, 2018, pp. 249–277.
[82] Kore, K., Deshmukh, A., Thakur, B., Mane, S., Dhekane, T., Mane, A., and Totla, N., "Comparative Analysis of Aluminum Alloy Grades: Properties, Applications, and Performance," *Journal of Information Systems Engineering and Management*, Vol. 9, 2024.
[83] Liao, J., Sharma, A., and Cooper, D., "The Effect of Composition, Geometry and a Novel Tool Design on Metal Recovery During Aluminum Process Scrap Remelting," *Proceedings of the ASME 2022 17th International Manufacturing Science and Engineering Conference*, Vol. Volume 1: Additive Manufacturing; Biomanufacturing; Life Cycle Engineering; Manufacturing Equipment and Automation; Nano/Micro/Meso Manufacturing, ASME, 2022, p. V001T03A002.
[84] Onyekwere, O. S., Orji, C. I., and Uyanga, K. A., "Determination of percentage zinc loss during melting of zinc scrap in a crucible furnace," *Global Journal of Engineering and Technology Advances*, Vol. 1, No. 1, 2019, pp. 22–26.
[85] Vallejo-Olivares, A., Gertjegerdes, T., Høgåsen, S., Friedrich, B., and Tranell, G., "Effects of Compaction and Thermal Pre-treatments on Generation of Dross and Off-Gases in Aluminium Recycling," *Journal of Sustainable Metallurgy*, Vol. 10, No. 1, 2023, pp. 69–82.
[86] Committee, A. I. H., *ASM Handbook, Volume 16 - Machining*, ASM International, 1989.
[87] Kalpakjian, S., and Schmid, S., *Manufacturing Engineering and Technology*, 8th ed., Pearson, Boston, MA,

2020.

[88] Commercial Testing Laboratory Index, "Aerospace Metallurgical and Mechanical Testing Rate Schedule Assessment," Industrial pricing review, Global Material Testing Aggregates, 2026.

[89] Hartlieb, M., and Wittbecker, G., "Minimizing the Carbon Footprint of A356 Castings," Tech. rep., Modern Casting, 2021.

[90] Kuenen, J., Berdowski, J., van der Most, P., Mulder, W., Bloos, J. P., Pacyna, J., Rentz, O., Oertel, D., Woodfield, M., Pulles, T., and Appelman, W., "2.C.3 Aluminium production," Tech. rep., European Environment Agency, 2013.

[91] City of Winnipeg, "Emission factors in kg CO2-equivalent per unit," Tech. rep., City of Winnipeg, 2026.

[92] Gotten, F., Finger, F., Havermann, M., and Braun, C., "On the Flight Performance Impact of Landing Gear Drag," DGLR, 2018.

[93] Cessna Aircraft Company, *Pilot's Operating Handbook and FAA Approved Airplane Flight Manual: Cessna Model 172S Skyhawk SP (Nav III)*, Cessna Aircraft Company, Wichita, Kansas, USA, 2021.

[94] ASM International, "Specifications Sheet Aluminum 2024-T3," , 2001.

[95] International Civil Aviation Organization, "Manual of the ICAO standard atmosphere," Tech. Rep. Doc 7488/3, ICAO, 1993.

[96] Garg, G., "Design and analysis of an aircraft rib," *International Journal of Advances in Mechanical Engineering*, 2014.

[97] G, and Loveleen, "Preliminary Sizing Procedure of Rib of an Aircraft," *International Journal of Aerospace and Mechanical Engineering*, Vol. 1, 2014, pp. 31–33.

[98] ThomasNet, *Sheet Metal Design Handbook*, 1998.

[99] Arunkumar, K., Lohith, N., and Ganesha, B., "Effect of Ribs and Stringer Spacings on the Weight of Aircraft Structure for Aluminum Material," *Journal of Applied Sciences*, Vol. 12, 2012, pp. 1006–1012.

[100] Rans, C. D., and Melkert, J. A., "AE2135-I Structural Analysis & Design," TU Delft, 2023.

[101] Niu, M. C. Y., *Airframe Stress Analysis and Sizing*, 2nd ed., Conmilit Press Ltd., 1997.

[102] International Civil Aviation Organization, "Manual of the ICAO Standard Atmosphere," Doc. 7488-CD, International Civil Aviation Organization, Montreal, Canada, 1993.

[103] Young, W. C., and Budynas, R. G., *Roark's Formulas for Stress and Strain*, 7th ed., McGraw-Hill Companies, Inc, 2001.

[104] Torenbeek, E., *Synthesis of Subsonic Airplane Design: An Introduction to the Preliminary Design of Subsonic General Aviation and Transport Aircraft, with Emphasis on Layout, Aerodynamic Design, Propulsion, and Performance*, Springer, 1982.

[105] Yahyaoui, M., "A New Method for the Prediction of the Downwash Angle Gradient," *International Journal of Aviation, Aeronautics, and Aerospace*, Vol. 6, No. 3, 2019.

[106] Teixeira, A., and Guedes Soares, C., "Strength of compressed rectangular plates subjected to lateral pressure," *Journal of Constructional Steel Research*, Vol. 57, No. 5, 2001, pp. 491–516.

[107] Wilson, N., Archer, L., Guthridge, R., Roesler, J., and Lents, M., "Technical and Regulatory Factors of Adopting Electric Training Aircraft in a Collegiate Aviation Setting," *Collegiate Aviation Review International*, Vol. 41, No. 1, 2023, p. Article 5.

[108] European Union Aviation Safety Agency (EASA), "Easy Access Rules for Aircrew (Regulation (EU) No 1178/2011)," , November 2025. Revision from November 2025; accessed June 2026.

[109] Amprius Technologies, "Product Portfolio Q2 2026," [Catalogus], 2026.

[110] McDonald, R., "Batteries are not Fuel," [Samengesteld artikel, oorspronkelijk gepubliceerd op LinkedIn], January 2023.

[111] de Vries, R., Wolleswinkel, R. E., Rosen Jacobsen, D., Bonnema, G. M., and Thiede, S., "Battery Performance Metrics for Large Electric Passenger Aircraft," *Proceedings of the 34th Congress of the International Council of Aeronautical Sciences (ICAS 2024)*, International Council of Aeronautical Sciences, Florence, Italy, 2024.

[112] Plett, G. L., *Battery Management Systems, Volume I: Battery Modeling*, Artech House, Boston, MA, 2015.

[113] Rezaei, M., Nekahi, A., Kumar, M. A., Nizami, A.-S., Li, X., Deng, S., Nanda, J., and Zaghib, K., "A review of lithium-ion battery recycling for enabling a circular economy," *Journal of Power Sources*, Vol. 630, 2025, p. 236157.

[114] Society of Automotive Engineers, "Power Quality Requirements for Plug-In Electric Vehicle Chargers," Standard SAE J2894/1_201901, SAE International, 2019.

[115] H3X Technologies Inc., *HPDM-180R Preliminary Datasheet*, version 2 ed., 2025. [Datasheet].

[116] Vidal, G., "Cessna 172 Flight Simulation Data," , August 2021. doi:10.13140/RG.2.2.24231.88481, Accessed: 2026-06-15.

[117] Anderson, J. D., *Introduction to Flight*, 8th ed., McGraw-Hill Education, New York, 2016.

[118] Torenbeek, E., *Advanced Aircraft Design: Conceptual Design, Analysis and Optimisation of Subsonic Civil Airplanes*, John Wiley & Sons, Chichester, 2013.

[119] Raymer, D. P., *Aircraft Design: A Conceptual Approach*, 6th ed., American Institute of Aeronautics and

Astronautics, Reston, VA, 2018.

[120] McCormick, B. W., *Aerodynamics, Aeronautics, and Flight Mechanics*, 2nd ed., John Wiley & Sons, New York, 1995.

[121] von den Hoff, B., Merino-Martínez, R., Yupa Villanueva, R. M., and Snellen, M., "Noise Emissions and Noise Annoyance of a Single-propeller Electric Aircraft During Flyover," *Proceedings of the 30th International Congress on Sound and Vibration*, edited by W. van Keulen and J. Kok, Society of Acoustics, Amsterdam, The Netherlands, 2024.

[122] Gudmundsson, S., *General Aviation Aircraft Design: Applied Methods and Procedures*, Butterworth-Heinemann, Oxford, 2014.

[123] Bogdanov, A., and Laskaridis, P., "Propeller Performance Considerations for Electric Aircraft Propulsion," *Aerospace Science and Technology*, Vol. 132, 2023, p. 108051. doi:10.1016/j.ast.2022.108051.

[124] Kays, W. M., and London, A. L., *Compact heat exchangers*, 3rd ed., Krieger Publishing Company, Malabar, FL, 1984.

[125] Incropera, F. P., Dewitt, D. P., Bergman, T. L., and Lavine, A. S., *Fundamentals of heat and mass transfer*, 7th ed., John Wiley & Sons, Hoboken, NJ, 2011.

[126] Fox, R. W., McDonald, A. T., and Pritchard, P. J., *Introduction to fluid mechanics*, 8th ed., John Wiley & Sons, New York, NY, 2011.

[127] Bieker, G., "A global comparison of the life-cycle greenhouse gas emissions of combustion engine and electric passenger cars," White paper, International Council on Clean Transportation (ICCT), 2021.

[128] International Civil Aviation Organization, "Methodology for Actual Life Cycle Emissions," ICAO Document 07, International Civil Aviation Organization (ICAO), nov 2025.

[129] Textron Inc., "2024 Fact Book," Fact book, Textron Inc., 2025.

[130] Finger, D. F., Goetten, F., Braun, C., and Bil, C., "Cost estimation methods for hybrid-electric general aviation aircraft," *Proceedings of the 11th Asia-Pacific International Symposium on Aerospace Technology (APISAT 2019)*, Engineers Australia, 2019, pp. 265–277.

[131] de Vries, R., Wolleswinkel, R. E., Rosen Jacobson, D., Bonnema, M., and Thiede, S., "Battery Performance Metrics for Large Electric Passenger Aircraft," *Proceedings of the 34th Congress of the International Council of the Aeronautical Sciences (ICAS)*, Florence, Italy, 2024.

[132] Bach, A., Reichelstein, S. J., Onori, S., and Zhuang, J., "Fair Market Valuation of Electric Vehicle Batteries in Second Life Applications," , aug 2024. Working paper, University of Mannheim and Stanford University.

[133] Richter, R., "Annual Summary Report on Molten Metal Incidents in 2024," Tech. rep., The Aluminum Association, 2025.

[134] Harto, C., "Electric Vehicle Ownership Costs: Today's Electric Vehicles Offer Big Savings for Consumers," Tech. rep., Consumer Reports, Oct 2020.

[135] PBL Netherlands Environmental Assessment Agency, "Social impacts of mining critical raw materials: Challenges and entry points for governance," Tech. Rep. PBL publication 5740, PBL Netherlands Environmental Assessment Agency, 2025.

[136] Hansen, A. M., Larsen, S. V., Steenholdt, N. C., Aaen, S. B., Graugaard, N. D., and Kollias, K., "Social impacts of bauxite mining and refining: A review," *The Extractive Industries and Society*, Vol. 14, 2023, p. 101264.

[137] European Aluminium, "Environmental Profile Report 2024 V.2.0," Technical report, European Aluminium, 2025.

[138] International Aluminium Institute, "Inventory Analysis Report of Scrap Melting for Wrought Material," Technical report, International Aluminium Institute, 2023.

[139] Scheelhaase, J., Müller, L., Ennen, D., and Grimme, W., "Economic and Environmental Aspects of Aircraft Recycling," *Transportation Research Procedia*, Vol. 65, 2022, pp. 3–12.

[140] Li, S., Yue, X., Li, Q., Peng, H., Dong, B., Liu, T., Yang, H., Fan, J., Shu, S., Qiu, F., and Jiang, Q., "Development and applications of aluminum alloys for aerospace industry," *Journal of Materials Research and Technology*, 2023.

[141] Damodaran, A., "Equity Risk Premiums (ERP): Determinants, Estimation, and Implications — The 2023 Edition," Tech. rep., Stern School of Business, New York University, 3 2023.

[142] Banz, R. W., "The Relationship Between Return and Market Value of Common Stocks," *Journal of Financial Economics*, Vol. 9, No. 1, 1981.

[143] Public Finances Directorate General (DGFiP), *French Tax Law*, République Française, Finances Publiques, 2023.

[144] Markets Report World, "Aluminum for Aerospace Market Size, Share, Growth, and Industry Analysis, By Type (High Strength Aluminum, Aerospace Aluminum Alloys), By Application (Aerospace Manufacturing, Aircraft Production, Aerospace Engineering), Regional Insights and Forecast to 2033," Tech. rep., Markets Report World, 2025.

[145] Federal Aviation Administration, *Title 14 Code of Federal Regulations, Part 23: Airworthiness Standards: Normal, Utility, Acrobatic, and Commuter Category Airplanes*, U.S. Department of Transportation, Apr 2026.